École Doctorale des Sciences de la Matière, du Rayonnement et de l'Environnement (ED – SMRE)

Unité de recherche : Unité Matériaux et Transformations (UMET)

Thèse N° 118224

présentée par

Marco Alejandro EZEQUIEL ALVARADO

pour obtenir le **Grade de Docteur** en **Physique** de l'Université de Lille

Spécialité : Milieux denses, matériaux et composants

Mechanisms of liquid metal embrittlement of Cu-Zn alloys by the liquid Ga-In eutectic

Mécanismes de fragilisation d'alliages Cu-Zn par l'eutectique Ga-In

Soutenue le 28 février 2023 devant le jury composé de :

Dr Eric Charkaluk	Président du jury	École Polytechnique
Pr Bernard Viguier	Rapporteur	Université de Toulouse
Dr Isabelle Aubert	Rapporteur	Université de Bordeaux
Pr Marie-Laurence Giorgi	Examinateur	CentraleSupélec
Pr José Gonzalo Gonzalez Reyes	Examinateur	Universidad Nacional Autónoma de México
Dr Anna Hojna	Examinateur	Centrum výzkumu Řež
Dr Ingrid Proriol Serre	Directrice de thèse	Université de Lille
Dr Thierry Auger	Co-encadrant de thèse	Arts et Metiers ParisTech
Dr Eva Héripré	Co-encadrante de thèse	Arts et Metiers ParisTech

École Doctorale des Sciences de la Matière, du Rayonnement et de l'Environnement (ED – SMRE)

Unité de recherche : Unité Matériaux et Transformations (UMET)

Thèse N° 118224

présentée par

Marco Alejandro EZEQUIEL ALVARADO

pour obtenir le **Grade de Docteur** en **Physique** de l'Université de Lille

Spécialité : Milieux denses, matériaux et composants

Mechanisms of liquid metal embrittlement of Cu-Zn alloys by the liquid Ga-In eutectic

Mécanismes de fragilisation d'alliages Cu-Zn par l'eutectique Ga-In

Soutenue le 28 février 2023 devant le jury composé de :

Dr Eric Charkaluk	Président du jury	École Polytechnique
Pr Bernard Viguier	Rapporteur	Université de Toulouse
Dr Isabelle Aubert	Rapporteur	Université de Bordeaux
Pr Marie-Laurence Giorgi	Examinateur	CentraleSupélec
Pr José Gonzalo Gonzalez Reyes	Examinateur	Universidad Nacional Autónoma de México
Dr Anna Hojna	Examinateur	Centrum výzkumu Řež
Dr Ingrid Proriol Serre	Directrice de thèse	Université de Lille
Dr Thierry Auger	Co-encadrant de thèse	Arts et Metiers ParisTech
Dr Eva Héripré	Co-encadrante de thèse	Arts et Metiers ParisTech

«A smooth sea never made a skilled sailor.»

To all my mentors: I will follow your steps…

Acknowledgements

I have two kinds of acknowledgements: those coming from the head and the heart.

From the first, I thank all the members of the jury. Thanks to Eric Charkaluk, president of the jury. Thanks to Bernard Viguier and Isabelle Aubert for reviewing the manuscript and writing the reports. Thanks to Marie-Laurence Giorgi, José Gonzalo Gonzalez Reyes, and Anna Hojna for exanimate the thesis. Thanks to the jury for the stimulating discussion during my thesis defence; I enjoyed every question and exchange. I also thank my supervisors, but more of that is below.

I thank the financial support of the French National Research Agency (ANR) under the project ANR GauguIn (N° ANR-18-CE08-0009-01). I thank the Chevreul Institute. I thank the three laboratories where I did my experiments: the Unité Matériaux et Transformations (UMET) laboratory that was practically my house, the Laboratoire de Mécanique Paris-Saclay (LMPS), and the Procédés et Ingénierie en Mécanique et Matériaux (PIMM) laboratory.

I want to thank all the technical support given by several persons: Jocelyn Golek for the mechanical tests, Nicolas Nuns for the ToF-SIMS analysis, Loïc Perriere for the fabrication of the Cu-20%Zn and Cu-25%Zn alloys, Jean-Baptiste Marijon for the DIC analysis, and Vincent Magnier for access to the ABAQUS license. Finally, transitioning to the acknowledgements in the intersection head/heart: thanks to Damien Creton for his tireless patience and help with the metallographic preparation; his attention and care give a lot of life to the laboratory.

I am thankful for the supervision I received during my thesis. Without my supervisors, I could not have done this work. First, I thank Ingrid Proriol Serre for all the mentoring these 3 years. Thanks to her, I learned a lot about being a good researcher, treating people, managing projects, and many other things without forgetting the human side. Ingrid was an excellent example, and I expect that someday I will be a good researcher like her. Thanks to Thierry Auger for being one mentor in my life; although keeping his rhythm was not always easy, I always enjoyed our discussions. I thank Eva Héripré for being a mentor; even if our interactions were short, I tried to learn the most I could; thanks, Eva, for the most exciting experiments of my thesis.

And now my dear colleagues, to all those PhD students that shared the journey with me: Adithya Nair, Sabrina Macaluso, Mourtada Aly, Rana Bchara, Lais Avila, Mahira Cota; also those that are still on it: Manisha Behera, Kevin Dourgaparsad, Jan Ruzicka, François Quinzin, and Jules L'Hostis; thanks to all. Special thanks to Arthur Boidot and Aleksandra Cieplak for their friendship, letting me sleep on their couch when necessary, and taking care of Chisu. I will always be thankful for the help that Thibault Lesage, Beline Lesage, and Cyril Nicard gave me at the worst of times; their friendship and companionship made it possible for me to finish this thesis. Finally, I thank Jorge Salgado for his friendship that arrived late in the PhD but fulfilled this need of having a latino friend; thanks to him and Ségolène Jean for their support.

Out of the lab, many essential persons make this project reach an end. First, I enormously acknowledge the work of my psychologist Leslie Acuña who accompanied me almost thorough all my PhD; without her, it would be even more challenging to overcome all my intern problems

that manifested wildly during the confinement. Thanks, Leslie, for making me a person with more tools to face the future.

With some bitterness in my words, I thank Niguina Raja-Delettre. She was a keystone in my life during this PhD; thanks to her for all the love and care; life was not simple nor painless, but our relationship made me stronger, and she will always have a space in my memory. Chisu, my little love dog, I will miss her forever.

Now my heart is willing to express all my gratitude to my family and friends. First of all, I thank my mother for how she educated me from the beginning and especially for how she gives an extraordinary example of everyday discipline, organisation, strength, and above all, love. Love, gratitude and patience are core words in my heart, and all three come from my mother; I hope I will continue making her proud of me. To my father, who taught me to solve problems by thinking outside the box, this tool helped me a lot during my PhD; also, his stoicism with life has taught me a lot. To my sisters, I feel guilty for not being able to fulfil my role as a brother; they are growing so fast. I hope I'm giving them a good example, and I'm happy that they are following their paths and not my steps blindly. She is a very strong woman, and how she faces life problems inspire me to continue fighting; thanks to Paola for her love and motivation. Mariana, keep going; she has many challenges in her future. I will try to show with the example that it is possible to overcome them with love and perseverance.

Thanks to the Mexicans I met in France: Luis Salazar, Ismael Arroyo, Angella Velazquez, Alejandra Velazquez, Rebeca Cedeño, Tarek Maylaa, and Louis Meunier; the two last are not really Mexicans, but they were part of this warm group. Also, thank my Mexican friends in México: Rodrigo Villalobos, Oscar Pérez, Miguel Rios, Alfonso Sereno, Victor Hernández, Miguel Ramirez, Miguel Abad, Pamela Jimenez, Kenia Ramirez, Itzel Calixto, José Guzmán; their unconditional friendship exist across continents and give me the motivation to continue.

Index of content

Index of figures

Index of tables

Introduction

The contact of a solid metal with a liquid metal can induce different phenomena that are detrimental to the mechanical properties of the solid, such as liquid metal corrosion or grain boundary penetration of the liquid metal, which can happen spontaneously. In contrast, liquid metal embrittlement (LME) is a phenomenon that can occur only when a solid metal undergoes plastic deformation in contact with a liquid metal and results in modifying the solid's fracture that becomes brittle. This brittleness implies the change of the solid's fracture mode from ductile to brittle, which often manifests as a decrease in the ductility and fracture stress of the solid and can be quantified by the diminution of the solid's fracture toughness, which is significant and leads to fast crack propagation.

In the growing fields that attain the contact of solid metals with liquid metals, such as soldering/welding, heat-resistant alloys, and nuclear applications, the practical implications of this phenomenon are critical since the sudden unexpected failure of a component with the fast crack propagation could lead to catastrophic consequences. To prevent these scenarios, the LME must be understood.

Numerous researchers have studied the LME on several solid/liquid couples under many conditions. Although many studies concern LME, no available theory explains this phenomenon for the whole spectrum of solid/liquid couples presenting LME. For instance, an obsolete approach for studying the LME is to catalogue the solid/liquid couples based on their sensitivity to LME. The fact that the number of possible solid/liquid couples is practically infinite makes this approach unbearable. Moreover, researchers found that some couples previously catalogued as not sensitive presented LME when tested under specific conditions. Instead, further research identifies the conditions that could impede or enhance the LME apparition.

The conditions that influence the LME apparition fall into two categories. On one side, there are the intrinsic properties of the metals. The chemical composition of the solid and the liquid, the microstructural state of the solid, and the physicochemical properties of the solid and the liquid are among the most critical intrinsic parameters. On the other side, some external conditions influence the LME occurrence, such as the temperature of the solid and the liquid and the strain rate and stress magnitudes applied to the solid.

There are general tendencies on the effect of these parameters on the LME, but their influence does not follow uniform tendencies, i.e., there are often exceptions where the parameters do not affect the LME sensitivity or where there is an effect opposite to the general tendency.

Several available models explain the LME phenomenon and propose mechanisms that lead to embrittlement. The explanations given by these models are very varied, and there are disagreements between them regarding the mechanisms behind the LME and the parameters' effect on the LME sensitivity. None of these models can explain the effect of all the parameters and confidently predict the LME sensitivity of all possible couples under all possible conditions. In addition, the proposed mechanisms are difficult to confirm since the corresponding phenomena occur at small scales, and the usual conditions of LME, such as high temperatures, make difficult their *in-situ* observation.

One key issue to advance the understanding of the LME is establishing a predictive methodology of the intrinsic LME sensitivity for a given system. Therefore, working on a reference system could bring decisive progress towards the predictive methodology, which could apply to the many industrial systems showing fracture at interfaces in the presence of liquid metals. Indeed, the main issue of the ANR GauguIn (French National Research Agency program: Liquid metal embrittlement occurrence: phenomena and prediction – applied to the Cu-alloys/Ga-In system - N° ANR-18-CE08-0009-01), in which this thesis work takes place, is to determine a methodology on a reference system able to predict the propagation conditions of a brittle fracture in the presence of liquid metal.

This thesis aims to expand the comprehension of the LME by studying Cu and alpha brasses in contact with the liquid eutectic Ga-In (EGaIn). The liquid metal of this study is liquid at room temperature, is not toxic, and has a low vapour pressure; these characteristics expand the experimental possibilities since there is no need for heating devices or special precautions in handling the liquid metal. The solid metals of this study are monophasic metals or alloys with no precipitation of second phases and relatively simple microstructure; these characteristics simplify the interpretation of the results and allow a clearer understanding of the phenomena involved. Moreover, preliminary research on Cu and Cu-30 wt.%Zn in contact with Ga showed an apparent transition of the LME sensitivity related to the chemical composition of the solid. Additionally, these solid metals present the intermetallic $CuGa_2$ when in contact with Ga-based alloy at room temperature. The intermetallic formation is considered a phenomenon that generally impedes the LME apparition, and there are not many LME studies on systems with intermetallics; for instance, Steel/Zn and Steel/Sn. The study of a system that presents LME, even if there is intermetallic formation, would allow us to expand the understanding of the role of the intermetallic on the LME.

The main objective of this thesis is to study, at the macroscopic, mesoscopic, and microscopic scales, the LME occurrence on pure Cu and alpha brasses in the presence of the liquid eutectic Ga-In (EGaIn). The study quantifies the contact quality between the solid and the liquid and analyses their resultant interactions. In addition, the work includes identifying some conditions that influence the LME occurrence using different mechanical tests in air and in the presence of liquid metal, which includes the analysis of their fracture surfaces and cracking paths. Finally, the work quantifies the phenomenon by measuring the critical stress intensity factor reduction, especially by performing *in-situ* tests at microscopic scales.

The thesis manuscript divides into four chapters that address the different aspects of the study.

Chapter I presents an overview of the literature on the LME, including the reported effects of the parameters on the LME apparition and the most relevant models available, with their corresponding mechanisms. Additionally, the chapter shows the pertinent literature on Ga-based alloys, the Cu and alpha brasses, and the interactions between Cu and alpha brasses with Ga-based alloys. Moreover, the chapter assesses the LME studies on systems closely related to the system studied in this work.

Chapter II presents the study of the interface and the interactions resulting from the contact between Cu and the alpha brasses with the liquid EGaIn. The study of this interface includes measuring the contact angle, which gives us information on the quality of the wettability; hence the chapter starts with a brief review of this measurement and shows the results of the wetting measurements of EGaIn on Cu and alpha brasses with different Zn content. The chapter continues with the study of the intermetallic, which includes using the Scanning Electron Microscope (SEM) and Energy Dispersive X-ray Spectrometry (EDS) to characterize the composition, morphology and kinetics of the intermetallic. Furthermore, the study uses the Time-of-Flight Secondary Ion Mass Spectrometry (ToF-SIM) technique to measure the presence of the different elements in the material's depth. The chapter concludes with a proposition of the solid /liquid interface and interactions.

Chapter III presents the study of the parameters that influence the apparition of the LME on Cu and the alpha brasses with different Zn content in contact with the liquid EGaIn. This study implements two mechanical tests: the Small Punch Test (SPT) and the bending test. The chapter briefly explains each test and presents the principal results obtained on the different solid compositions under different mechanical conditions. The results of these tests include fractography analysis using SEM. Then, the chapter presents the mechanical tests' finite element modelling (FEM) and relates the results obtained with the calculated mechanical conditions. Finally, the chapter discusses the phenomenological mechanisms that explain the LME sensitivity for the studied system.

Chapter IV presents the quantification of the LME phenomenon with the fracture toughness measurement. The chapter begins with using the 3-point bending test results to calculate the fracture toughness and analyse its limitations. Later, the chapter presents the use of *in-situ* micro-bending tests to measure the fracture toughness of the Cu-30 wt.%Zn alloy in contact with the EGaIn. Before presenting the results of the micro-bending tests, the chapter briefly reviews the use of the micro-mechanical tests to measure fracture toughness. The chapter ends with calculating the fracture toughness using the FEM of the micro-bending tests.

The manuscript ends with some general conclusions and perspectives.

I. Relevant literature review

This chapter presents some relevant literature to understand the pertinence of the research and the approach presented in this work. First, the chapter presents the available literature on the liquid metal embrittlement phenomenon (LME), including the reports on the parameters that influence the LME sensitivity and the models and mechanisms that explain the LME. Then, the chapter describes the relevant properties of the Cu-Zn alloys, the liquid Ga-based alloys and the works that study their interactions. Finally, the end of the chapter presents the literature on the LME on solid/liquid metallic couples related to the Cu-Zn alloys and the eutectic Ga-In (EGaIn).

I.1. Liquid Metal Embrittlement

Liquid Metal Embrittlement (LME) is a phenomenon that can be present when a solid metal or alloy undergoes plastic deformation in contact with a liquid metal or alloy. The main effect of the LME is a detrimental change in the solid's mechanical properties, often observed as a loss in ductility and a change in its fracture mode. A ductile material that undergoes mechanical loading in contact with a liquid metal will present a brittle fracture mode when there is LME [1]–[4].

LME is in the category of environmentally assisted cracking; however, there are several essential differences between LME and other phenomena in the same category [5]–[7]. For instance, the embrittlement mechanisms of stress corrosion cracking and hydrogen embrittlement differ from those of LME, although they share similar effects, such as the propensity for brittle intergranular fracture [8]. In addition, liquid metal corrosion, grain boundary penetration, and high-temperature corrosion differ from LME because failure involves bulk chemical or structural modification of the solid metal.

Some authors differentiate LME from liquid metal-induced embrittlement (LMIE). The LMIE happens when there is spontaneous liquid metal penetration into the grain boundaries of a solid, i.e., without applying any stress on the solid. This phenomenon leads to the reduction of the mechanical properties of the solid metal [9]. In some cases, after a sufficiently long time of contact between the solid and the liquid metals, liquid metal stores into the grain boundaries, which is sufficient for the system to present embrittlement even if the liquid metal is retired from the surface of the solid, e.g., Al-Ga, Ag-Hg, and Cu-Hg [10].

In contrast with LMIE, for LME to happen, there must be stress during the contact with the liquid metal for the embrittlement to occur, i.e., if the solid separates from the liquid, its properties recover. Indeed, initial contact usually does not affect the occurrence of LME; hence, LME is not sensitive to the time of exposure of the solid by the liquid metal [11], [12]. There are some exceptions, such as the case of the T91 steel embrittled by the liquid eutectic Pb-Bi (LBE), where a pre-exposure favoured the corrosive effects that modified the solid's surface, enhancing the LME phenomenon [13], [14].

Another critical characteristic of LME is that the presence of liquid metal does not affect the yield strength of the solid. Furthermore, there are instances where the flow behaviour of the solid metal is not affected, only the fracture stress and strain [15]. Figure I–1 illustrates this effect on Cu embrittled by Bi [16]. There are other instances of LME where there is a modification of the solid's plastic behaviour, such as the 316 L austenitic steel embrittled by the eutectic Ga-In during a notched tensile test (Figure I–2) [17]. In this case, a local effect of the liquid metal in the notch could have generated the apparent change in the plastic regime, or it could have been due to a slight variation in the sample notching.

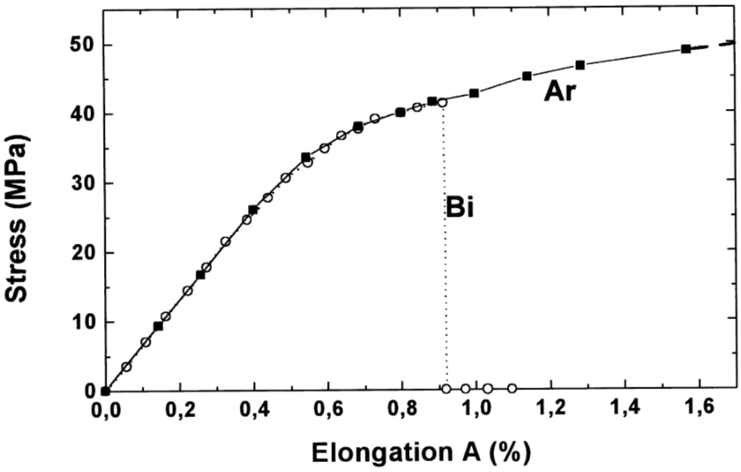

Figure I–1 Comparison of tensile curves of Cu at 300 °C under Ar and in liquid Bi for a strain rate = 10^{-4} s^{-1} [16].

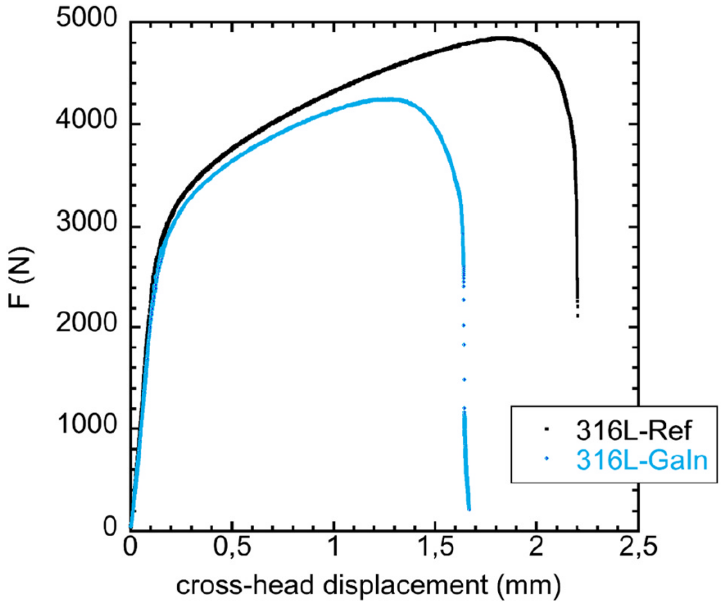

Figure I–2 Force versus crosshead displacement graph at room temperature of 316 L austenitic steel reference and tested in EGaIn (crosshead speed of 3.33 ×10−7 m s^{-1}*)* [17].

Because of the detrimental effects on solid metals, the study of LME attains many fields, such as soldering/welding, liquid metal-assisted superplasticity, heat-resistant alloys, and nuclear and military applications, among others [18]. For instance, various Zn-coated steels may suffer LME during resistance spot welding, which generates cracks that are difficult to observe directly and that reduce the mechanical resistance of the component, especially their ductility [19], [20]. Other practical examples are illustrated elsewhere [3].

There have been several attempts to predict the appearance of LME. For instance, one of these attempts is using the term specificity to catalogue the solid/liquid couples that present LME. With this, a simple table would indicate whether a couple presents LME. However, the apparition of LME depends strongly on several parameters, including the testing conditions, which implies that specificity is not an intrinsic parameter of LME and it is not reliable [3], [21], [22]. An example of this: Old stated that the couple Fe/Na did not present LME and was included as not embrittled in specificity tables [23]; however, further work by Hilditch et al. presented evidence of LME on this couple [24].

I.1.1. Parameters influencing LME

Indeed, the apparition of the LME depends not only on the solid and liquid in contact but on other parameters. Furthermore, small parameter changes can trigger LME susceptibility; hence any declaration of immunity to LME should be taken carefully and only for the presented conditions [6]. Studying these parameters has led to a better understanding of this phenomenon. However, several parameters influence LME, and their interrelations are complex.

To systematically discuss the parameters' effect, let us divide them into intrinsic and external. The intrinsic parameters are all those conditions related to the properties of the metals or alloys in contact. The external parameters include the experimental variables and all other external conditions that modify LME.

- Intrinsic parameters
    - Chemical compositions of the liquid and the solid
    - Metallurgical state of the solid
    - Physicochemical properties of the interface between the solid and the liquid
- External parameters
    - Strain rate of the mechanical solicitation
    - Temperature of the solid and the liquid in contact
    - Stress applied to the solid in contact with the liquid metal

The separation and classification of these parameters allow us to have a structured view of their impact on LME. However, these parameters are interdependent, and most are tightly connected.

I.1.1.1. Intrinsic parameters

The inherent characteristics of the solid and liquid in contact define the intrinsic parameters. Some of them are modifiable, for example, via heat treatment or surface treatment.

I.1.1.1.1. Chemical compositions

The chemical composition of the solid metal and the liquid metal can affect the severity of LME, the propagation rate of the crack, the strain to rupture, and other parameters linked to the LME [5], [12], [25].

For instance, a change in the composition of the liquid metal can change the temperature range at which LME occurs, as in the case of the couple Al/Hg, where Ga additions increase the brittle to ductile transition temperature [26]. Furthermore, a change in the composition of the liquid can also affect the severity of LME. Figure I–3 illustrates that adding other elements to liquid Hg decreases the stress and strain to fracture of pure Al. Westwood et al. related this phenomenon with electronegativity but stated that its fundamental significance was not established [25], [27].

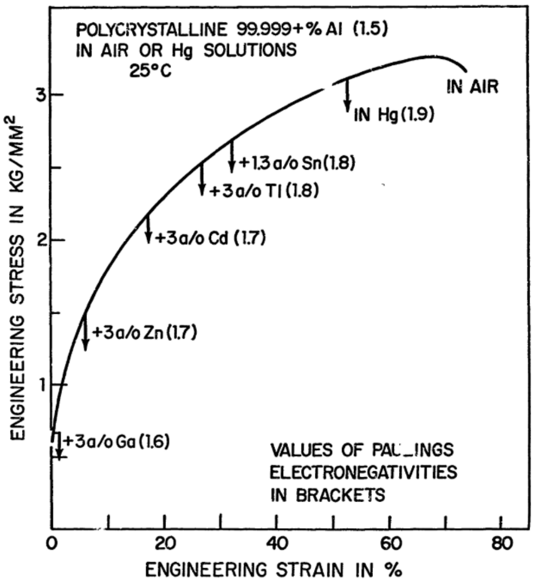

Figure I–3 Embrittlement of polycrystalline pure Al by various Hg solutions [27].

Also, the liquid metal may act as a medium to transfer impurities such as oxygen from the atmosphere to the solid's surface [12]. For example, in the T91 steel deformed in contact with LBE, Serre et al. concluded that the oxygen in the liquid eased the adsorption of Pb in the solid [28]. They propose that the Pb-O couple is preferentially attracted to the solid's oxide layer, this couple then dissociates, and the Pb atoms are absorbed in the oxide layer and then in the solid metal.

Adding alloying elements to the solid can modify the severity of LME. For example, Figure I–4 shows how adding different solutes enhances Zn's embrittlement by liquid Hg [27].

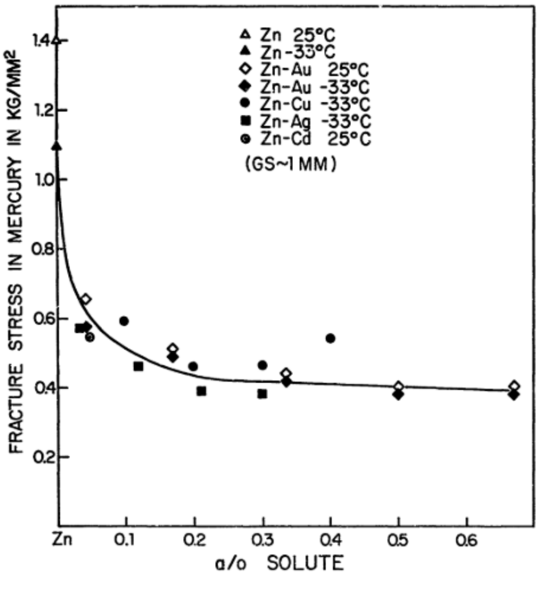

Figure I–4 Effects of small solute element additions on the susceptibility of polycrystalline Zn to embrittlement by Hg [27].

Shea and Stoloff stated that the solutes' influence on the degree of embrittlement comes from these solutes' effect on the solid's stacking fault energy. They state that the degree of plasticity of a solid in contact with a liquid metal linearly depends on the ease of cross-slip [29].

The chemical composition correlates strongly with the other parameters that modify the LME phenomenon. For instance, the chemical composition delimits the solid's microstructure and physicochemical properties and influences its metallurgical state. Consequently, the study of the impact of the chemical composition on LME can be complex.

I.1.1.1.2. Metallurgical state

Materials with a higher hardness generally present a more severe LME; an example is T91 steel embrittled in contact with LBE [30]. The hardness of the material can depend strongly on its chemical composition since the usual effect of alloying elements is to induce a solid solution, hence enhancing the LME sensitivity. In face-centred cubic (FCC) solids like Al, this effect correlated with a lowering of the stacking fault energy (SFE) [5]. However, the alloying elements do not always lower the SFE; for example, austenitic stainless steel lowers its SFE at a higher %Cr, but a higher %Ni have the opposite effect [31].

Moreover, hardness depends on the grain size of the solid, and since LME fractures are commonly intergranular, the grain size and grain boundary chemistry play an essential role in its apparition [5]. Equation (1) expresses the effect of the grain size. This equation was postulated by analyzing the dislocation model for initiating a brittle crack and evidenced experimentally in a 70/30 brass wetted with mercury [32].

$$T_c \propto \ln(d) \tag{1}$$

where T_c is the transition temperature, and d is the average grain diameter.

There is also a linear relation between $d^{-1/2}$ and the tensile strength of the solid. An increase in the grain size increases the strain hardening rate and reduces the relaxation capacity, which explains this linear relation [33].

Nevertheless, there are examples of opposing consequences of the change in grain size: an increase in grain size in the system Cu/Hg enhanced LME, while prestrained Al in contact with Hg-3%Zn presented the opposite tendency [5].

I.1.1.1.3. Physicochemical properties of the interface

Interfacial energy is a critical parameter of the LME phenomenon, and most of the models that describe LME include this energy in their formulation, along with the grain boundary energy [34]. This property also depends strongly on the chemical compositions of the solid and liquid metals, as observed in the system Cu/Bi-Pb [35].

On the other hand, for LME to happen, there should be good contact between the liquid and the solid. If this contact is interrupted, LME will not occur, or it will stop if it has already started. Therefore, oxide films and intermetallics play a role in LME since they can modify the contact between the liquid and the solid [3], [11], [36], [37].

Some works claim that there should be no intermetallic formation between the metals during the contact for LME to happen [2], [5]. Nonetheless, Clegg and Jones reported the apparition of LME despite the formation of intermetallics in En19 steel/Sn [38]. However, they did not describe the intermetallic's role in the LME sensitivity, and the study focused on the steel dissolution in Sn.

The appearance of intermetallics can change the kinetics of crack growth. For example, in the case of Cu embrittled by Bi, when there is an addition of Sb to the liquid Bi, there are compounds formed between Cu and Sb that generate a crack growth alternating with stops, which correspond to the rupture and reformation of the Cu-Sb intermetallics [39].

A widely studied system that presents LME, although it presents intermetallic compounds, is Fe/Zn. In this system, the formation of the intermetallics drastically changes the strain-rate dependence of the ductile-to-brittle transition. Kang et al. explain this relation by stating that whenever there is enough time to form intermetallics with a higher melting point than pure Zn, there will not be any available liquid metal to trigger LME [20].

Another critical issue of the solid/liquid interface is the presence of oxides. Some authors stated that LME is present only on oxide-free surfaces [11], [15]. However, researchers have observed LME on surfaces covered with oxide films. For instance, the 91-grade steel can have an oxide film that cracks during the application of stress while in contact with liquid lead; this allows contact between the liquid lead and the oxide-free surface of the steel, consequently enabling LME [40]. Moreover, Auger et al. studied the role of the oxide nature and the thickness on the occurrence of LME in the system T91/Pb-Bi [41]. They exhibited that, despite a thick oxide, LME is possible, and no oxide can guarantee protection from LME.

The solubility of the solid on the liquid is also an essential parameter for studying LME, as dissolution processes may blunt the crack. This effect can difficult the crack propagation; hence, low solubility favours the LME [5], [42]. Nevertheless, solubility cannot be a criterion of whether or not LME will occur on a specific system because there are several conflicting results, e.g., Fe/Cd [15]. Still, several models consider this parameter in their formulation.

I.1.1.2. External parameters

In contrast with the intrinsic parameters, the external parameters can vary a lot through modifications of the experimental settings. Furthermore, they are also intimately interconnected and interact with the intrinsic properties of the system.

I.1.1.2.1. Temperature

The LME phenomenon occurs above an initial temperature (T_E), at which there is a drop in ductility, and a final temperature (T_R), at which the initial ductility restores [5]. The range between these temperatures is named "ductility trough"; Figure I–5 schematizes it.

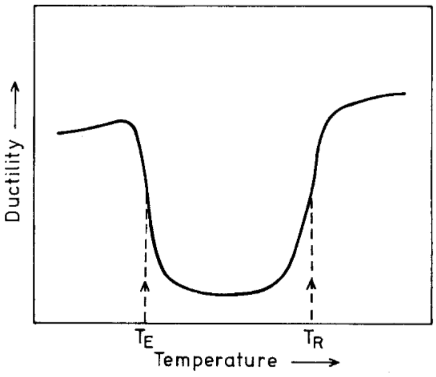

Figure I–5 The effect of LME on the variation of ductility with temperature (schematic) [5].

The initial temperature (T_E) is often the melting point of the liquid metal. In some systems, embrittlement occurs below this temperature; however, this is not LME but solid metal-induced embrittlement (SMIE) [43], [44]. Also, there are systems such as Fe/In and Alumina Forming Austenitic steel/Pb where the LME starts at temperatures higher than the melting point [5], [45].

When the LME generates intergranular fractures, the TE may depend on a transition temperature TW at which conditions are favourable for grain boundary wetting, i.e., replacing the grain boundaries with a liquid film. For the grain boundary wetting to occur, the energy of the exposed grain boundaries must be higher than double the solid/liquid interface energy ($\gamma_{GB} > 2\ \gamma_{SL}$). Both energies decrease at higher temperatures, but γ_{SL} decreases at a higher rate since the solid dissolves into the liquid phase; Figure I–6 schematizes these phenomena. In most cases, T_W is too high, and the supplementary energy of a mechanical loading will trigger LME [3].

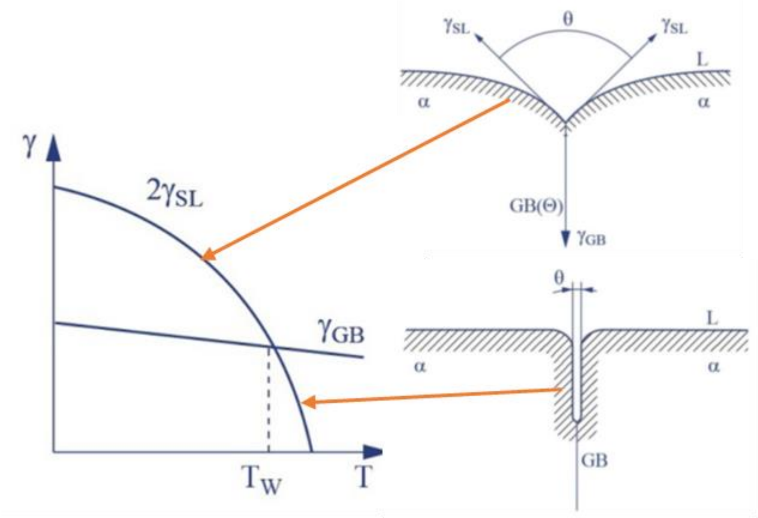

Figure I–6 Qualitative evolution of the temperature of Gibbs energy of a grain boundary and a solid-liquid interface. T_W is the transition temperature [3].

The LME disappearance above T_R can be due to the thermally activated plasticity that counteracts embrittlement [12]. In the case of En19 steel/Sn, Clegg and Jones proposed that T_R correspond to the point where the dissolution of the surface is sufficient to remove the crack nucleation [38].

I.1.1.2.2. Strain rate

The strain rate in the solid metal directly influences two aspects of LME: crack propagation and stress relaxation. For instance, in the Cu/Bi system, the crack propagation rate increases almost linearly with the increase of the strain rate [46]. On the other hand, slow strain rates allow stress relaxation in the system, and hence, the only effect of the adsorbed liquid metal is to ease plastic flow, which inhibits LME. In other words, high strain rates often produce increased LME [5], [11].

Generally, increasing the strain rate decreases the brittle-ductile transition temperature (T_R). Fernandes et al. reported that in the alpha-beta brass in contact with liquid Ga, the strain rate heavily affects the width and the depth of the "ductility trough" and may even lead to its disappearance [11], [47]. Figure I–7 illustrates their findings. However, they did not consider the formation of the $CuGa_2$ intermetallic, which could have inhibited the LME at lower strain rates.

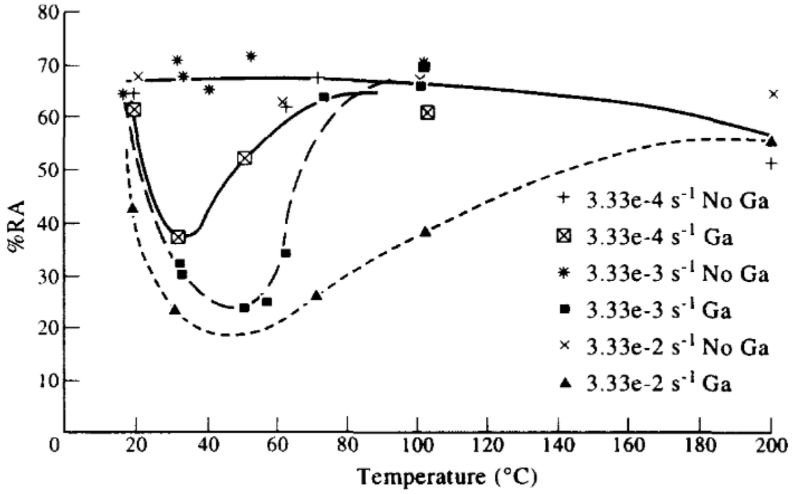

Figure I–7 Plot of the percentage reduction in cross-sectional area at failure %RA as a function of temperature at various strain rates for Cu-40 wt.%Zn [21].

A system with the opposite tendency is the T91 steel in contact with LBE, which showed more LME sensitivity at lower strain rates. Ye et al. explained this by suggesting that low strain rates enhanced the rate of adsorbed liquid metal atoms at fresh surfaces that enter into the solid's bulk at favourable sites, favouring the liquid metal's penetration [48].

I.1.1.2.3. Stress

Stress in the solid is necessary for the apparition of liquid metal embrittlement. The stress can enhance the liquid metal penetration by straining the bonds on the grain boundaries, increasing the free volume along with the interface; higher local stress will result in a more severe LME [12]. Some authors report a stress threshold or a stress-intensity factor threshold below which there is no LME, or there is a so-called "delayed fracture" [36], [37], [49].

Early works on LME used the tensile test on smooth samples; however, introducing a notch in solid samples increases the sensibility of tensile tests to LME by introducing a higher degree of local stress and a severe triaxial stress state [12]. For example, on the couples Cu-30 wt.%Zn/Ga [47] and T91/Pb [40], [50] LME was not present on unnotched tensile specimens; however, on notched tensile specimens, there was an apparition of LME.

With the information on the influence of the intrinsic and external parameters, researchers have developed models that aim to extrapolate the tendencies to other solid/liquid systems. Moreover, they aim to explain the apparition of this phenomenon by proposing several mechanisms that lead to the LME. The following section presents the most relevant models and mechanisms.

I.1.2. Models and mechanisms

Several mechanisms and models are available to explain and predict the LME phenomenon. However, no mechanisms or models still describe the phenomenon comprehensively. The lack of a comprehensive model comes from the phenomenon's complexity, the limited experimental data, and the differences in the mechanisms for each couple [4], [11], [12].

Several surveys of the models are available [6], [7], [12]. In particular, the one published by Joseph et al. includes a helpful graphic representation of the mechanisms involved for some of the LME models (Figure I–8) [11]. This image lets us quickly identify the proposed mechanisms occurring simultaneously to produce LME according to the different models. Similarly, Figure I–9 shows another helpful diagram proposed by Razmpoosh et al. [4]. In the diagram, they illustrate the principal mechanism proposed in each model and also show a categorization of these models. The reader can use both diagrams to support the explanations of the different models in the following pages.

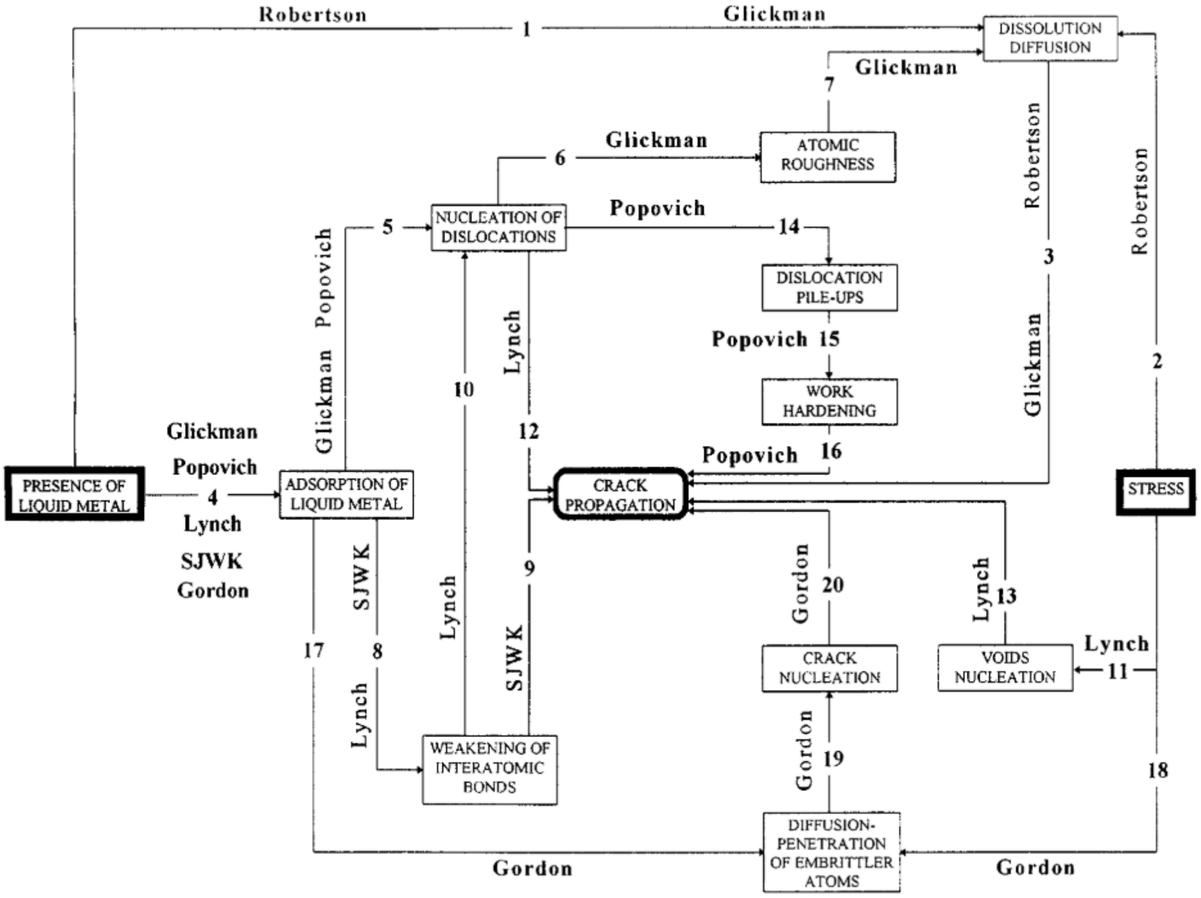

Figure I–8 Diagram illustrating the elementary steps involved in the different LME models [11].

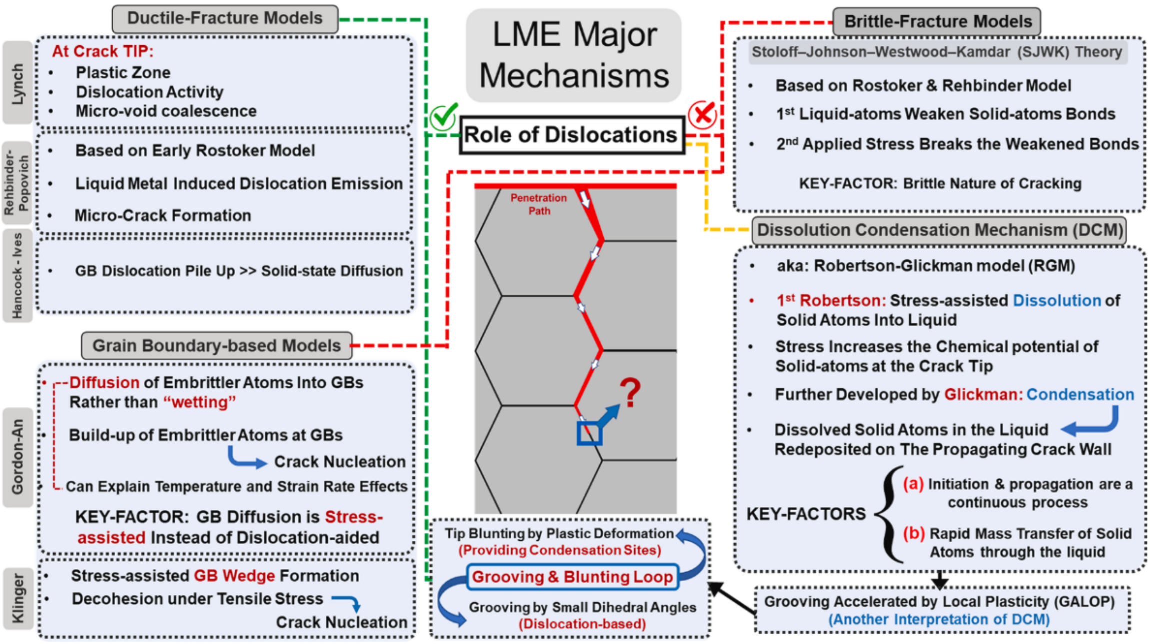

Figure I–9 Summary of the proposed LME mechanisms emphasizing the major contribution of dislocations at the crack-tip [4].

The available LME models use different mechanisms to explain LME, but often their central point is the reduction of the free surface energy of a solid caused by the adsorption of the surrounding medium, also known as the Rebinder effect [51].

I.1.2.1. Robertson-Glickman Model

Robertson was the first to develop this model [52]. For him, the solid metal at the crack tip dissolves in the liquid and then diffuses away from the crack, promoting further crack propagation; stress and capillarity enhance these phenomena. Robertson formulated an expression (Eq. (2)) for the crack growth rate:

$$\upsilon = \left(\frac{C_o D \Omega^2 \gamma_{SL}}{kT}\right)\frac{1}{r^2}\left(\frac{2L\sigma_a^2}{E\gamma_{SL}} - 1\right) \tag{2}$$

where C_o is the equilibrium concentration, D is the diffusion coefficient of the solute in the liquid, Ω is the atomic volume of the solid, γ_{SL} is the solid-liquid interfacial energy, k is the Boltzmann constant, T is the temperature, r is the radius of the tip, $2L$ is the length of the crack, σ_a is the applied stress, and E is Young's modulus. The -1 in Eq. (2) accounts for the capillarity effect and provides a stress threshold for crack propagation.

Similarly, Robertson derived an equation (Eq. (3)) for the maximum velocity of the crack:

$$v_{max} = \frac{C_o D \Omega^2 E}{2kdT} \tag{3}$$

This equation predicts maximum crack rates that concord with some systems, e.g., Cu-Hg. However, the effect of the variables on the degree of embrittlement does not agree with practical observations [11].

Glickman continued to develop the model by considering the redeposition of the dissolved atoms on the stress-free walls of the crack. He considers that LME is similar to stress-corrosion-cracking and that the role of the liquid is to act as a fast transport medium. Moreover, the dislocations generated during plastic deformation create atomic roughness at the interface, thus enhancing solid atoms' dissolution. Following these processes, there is rapid diffusion of solid metal atoms that precipitate at defined distances from the crack walls [39], [53].

For Glickman, there are three kinetic stages of failure. First, selective dissolution in the liquid metal initiates the crack at the points where the grain boundaries exit to the surface. Then, the controlling stage of failure is called crack precritical propagation; in this stage, the rate of subcritical growth of cracks does not depend on the length (L) or time (τ) but on the crack mobility (α), the applied stress (σ), and the threshold stress of subcritical growth (Δ); as depicted in Eq. (4).

$$v = \frac{\partial L}{\partial \tau} \approx \alpha(\sigma - \Delta) \tag{4}$$

Finally, supercritical crack propagation occurs when there is certain critical deformation near the crack tip; the transition to this stage corresponds to the constant value of the product between the critical stress and the critical length ($\sigma_c l_c$) [39].

Additionally, Glickman associates the accelerated fracture of LME with two factors: the fast removal of dissolved atoms from the crack tip due to the high diffusional permeability of the melt in the crack; and the degree of atomic roughness due to the high dissolution rate because of the low specific surface energy at the interfaces.

For the systems with low solubilities, such as Ti alloys-Hg and Al alloys-Hg, Glickman states that the mechanisms still operate at very low solubility due to impurities, which react with the solid metal to form compounds that are soluble in the melt.

Contrary to other models, the Robertson-Glickman model assumes that the liquid metal does not modify the failure mechanisms of the solid but only accelerates the diffusion-controlled process of subcritical crack growth [53].

I.1.2.2. GALOP

Glickman also developed another model based on a dissolution-condensation mechanism only applicable to intergranular failures: Grooving Accelerated by Local Plasticity (GALOP) [49]. He bases this model on the Mullins grain boundary grooving and considers that the crack propagates by a repetitive sequence of grooving-blunting events under tensile stress; Figure I–10 illustrates this mechanism.

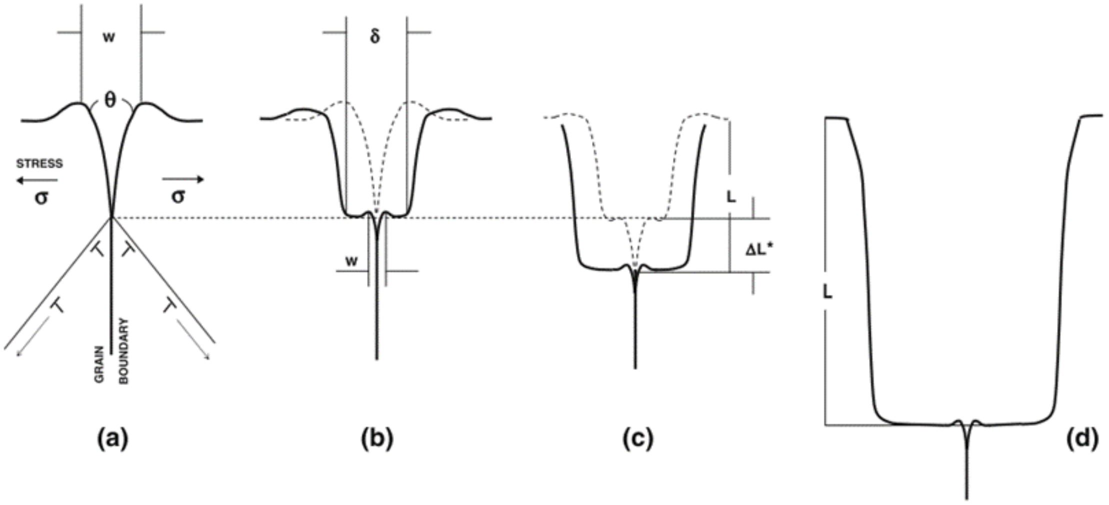

Figure I–10 GALOP mechanism of grain boundary LME [49].

First, a sharp grain boundary groove filled with liquid metal concentrates the stress (Figure I–10 (a)). The groove extends further, and the solid redeposits onto the shelf surface (Figure I–10 (b)). When the crack propagation reaches a "blunting distance", ΔL*, there is a new blunting event (Figure I–10 (c)). The final length of the crack, L, will be L=n × ΔL* (Figure I–10 (d)).

For Glickman, a massive dislocation emission from the tip of the crack generates the blunting of the grain boundary crack. Moreover, atomic defects may assist the process by acting as stress-strain concentrators. In this scenario, the blunting distance ΔL* depends on the distance between these atomic defects [49].

Considering the classical Mullins kinetics, Glickman gives an equation of the threshold of the stress intensity factor (K_{TH}) in Eq. (5) and the effective velocity (V_∞) in Eq. (6):

$$K_{TH}^2 = \varphi \Delta \mathrm{L}^* \mathrm{tg}\left(\frac{\theta}{2}\right)(\sigma_Y E) \tag{5}$$

$$V_\infty = \frac{C}{\Delta L^{*2}}\left[\mathrm{tg}\left(\frac{\theta}{2}\right)\right]^3 \tag{6}$$

where φ is a numerical factor in the range $10 \leq \varphi \leq 50$, σ_Y is the yield strength, E is the elastic modulus, θ is the equilibrium dihedral angle, and C is the concentration.

Indeed, the GALOP model reproduces the evolution of the stress intensity factor qualitatively as a function of the crack velocity, i.e., a sharp stress intensity factor threshold (K_{TH}) and the plateau of velocity (V_∞). The calculation of these two quantities for the Al7075-Hg couple gives a good agreement with the experimental results when adjusting the parameter ΔL^* to 1 nm [49].

I.1.2.3. SJWK

This model is named after Stoloff, Johnson, Westwood and Kamdar [25], [54]. The authors based the model on a particular case of the brittle fracture theory, the weakening of interatomic bonds due to liquid metal's adsorption on the solid's surface. Figure I–11 supports the explanation of the elementary mechanisms of this model. In this illustration, a liquid metal atom (B) reduces the solid's surface energy, weakening the interatomic bond A-A_0. Applied stress may exceed the reducing breaking stress, breaking the bond and propagating the crack and the liquid metal atom to the next solid atom (A_1). The process repeats until the material fails or the liquid metal cannot keep up with the crack propagation [27].

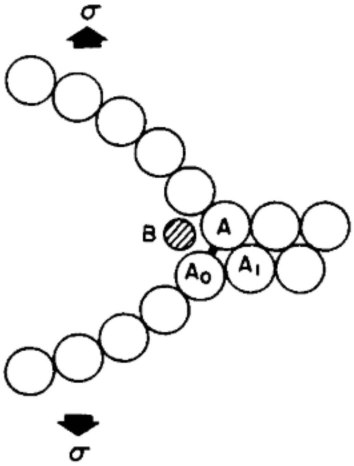

Figure I–11 Displacement of atoms at the tip of a crack. The bond $A-A_0$ *constitutes the crack tip, and B is a liquid metal atom* [42].

The authors of this model also used an expression of the maximum stress (σ_m) to break the interatomic bond A-A_0. They did this by equating the work done in breaking the interatomic bonds with the surface-free energy of the subsequently created fracture surface (γ). Equation (7) contains this expression, where E is the Young modulus and a_0 is the radius of an elastic crack.

$$\sigma_m = \left(\frac{E\gamma}{a_0}\right)^{\frac{1}{2}} \tag{7}$$

Consequently, reducing the surface energy by the liquid atom will reduce the interatomic bond's strength and the shear strength. Adsorption of the liquid atom in preferential sites, such as the vicinity of piled-up groups of dislocations at high-angle boundaries, will facilitate crack initiation [42].

Other authors have criticized using brittle fracture theory to model LME; e.g., Popovich claims that LME is a ductile phenomenon at a microscopic level [1].

I.1.2.4. Lynch

Lynch based his model on metallographic observations in hydrogen and liquid metal embrittlement. Like the SJWK model, Lynch based his model on the interatomic bonds weakening by the adsorption of atoms from the environment. However, the crack propagation mechanisms in Lynch's model differ from the SJWK model and explain the ductility at a micro-level. In Lynch's model, the weakening of the interatomic bonds leads to the nucleation of dislocations on the crack tip and promotes intensive slip, which leads to the creation and coalescence of voids, advancing the crack [8], [36]. Figure I–12 illustrates these LME mechanisms and compares them with an inert environment.

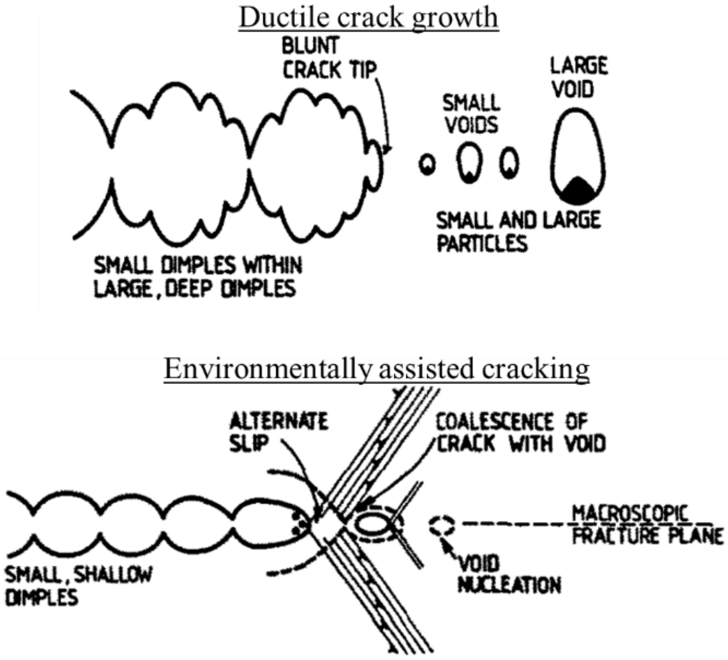

Figure I–12 Schematic diagrams illustrating the mechanism of ductile crack growth and environmentally assisted cracking [8].

In an inert environment, a large plastic zone with voids generates when a crack advances. According to Lynch, dislocations are not injected from the crack tip to any extent in this environment. In contrast, the presence of liquid metal atoms in the crack weakens the interatomic bonds and facilitates the dislocation nucleation at the crack tip. In this case, there is a small plastic zone since only minor strains are required to link up crack tips with the voids that nucleate ahead of the crack [8].

For Lynch, the fractures of embrittled solids are sometimes dimpled/fluted at a microscopic scale. This hypothesis does not match the experimental observations of the transgranular fractures. Moreover, Gordon underlines that the Lynch model does not explain delayed failure [37], and Kamdar claimed that the adsorption effects on dislocations would be secondary in importance compared with the interatomic bond breaking [42].

I.1.2.5. Popovich

The model proposed by Popovich has some similarities with the Lynch model; for instance, its elementary mechanisms begin with the adsorption of liquid metal atoms [1], [55]. For Popovich, this adsorption promotes plastic flow and results in a more critical outlet of dislocation to the surface; this may lead to pile-ups in grain boundaries or activation of slip planes; however, the adsorption always generates enhanced work hardening in a localized region, leading to the crack propagation and premature failure.

Alternatively, the large number of dislocations generated by the adsorption may transfer the strain to other grains by crossing grain boundaries, increasing overall ductility. Popovich explains the ductility trough by stating that at high temperatures and low strain rates, the relaxation processes may be significant, restoring the ductility and impeding LME. Regarding the grain size, he explains the experimental data by stating that in fine-grain structures, the dislocations can move easily as a result of the presence of a multitude of grain boundaries with high disorientation energy; hence adsorption-induced LME would be more severe on solids with high average grain size [33].

I.1.2.6. Gordon

In his model, Gordon proposes a period of crack incubation that starts when liquid metal atoms adsorb on the solid. Then, they penetrate the solid through stress-aided diffusion and possibly dislocation-aided diffusion. The liquid atoms have preferential paths for penetration, usually grain boundaries. In contrast with the Lynch model, Gordon claims that the zones with liquid atoms decrease crack resistance and dislocation movement. When a penetration zone reaches critical concentration and depth, crack nucleation occurs and propagates [37], [43].

Gordon's approach can explain the experimentally observed delayed fracture. For him, the nucleation time depends on two steps: the dissolution of the liquid atoms on the surface and its diffusion and penetration on the solid. Equation (8) expresses this dependence [37]:

$$t_n \sim \exp\left(\frac{\Delta G_S}{RT}\right)\exp\left(\frac{\Delta G_d}{RT}\right) \tag{8}$$

where ΔG_S and ΔG_d are the activation energies for each step, R is the ideal gas constant, and T is the temperature.

According to Gordon, there is a threshold stress below which no LME failure occurs. Figure I–13 schematizes the relation of the stress, temperature and time to produce penetration zones. This figure includes an example of a stress vs time curve of a sample tested at a temperature T_4 that illustrates the use of the graph. In this example, if the curve reaches the stress value σ_{i4}, the sample will fail instantaneously. If the stress reaches a value below σ_{th4}, the sample will not fail regardless of the time of the test. If the solid reach a stress magnitude between σ_{i4} and σ_{th4}, for example, σ_i at a time $t_{\sigma i}$, the material will fail after reaching the time t_i.

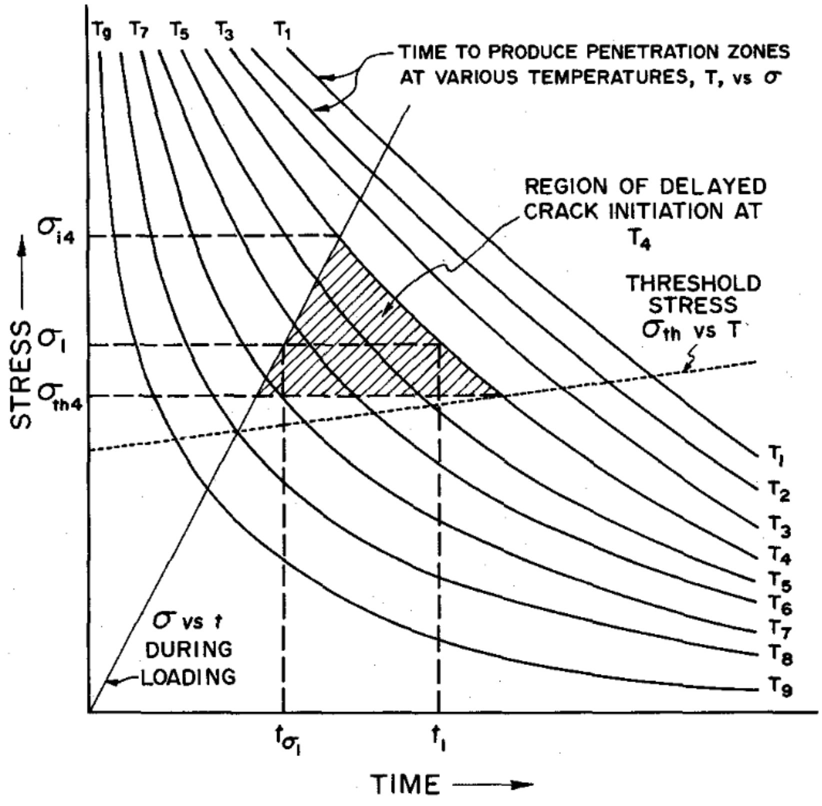

Figure I–13 Schematic diagram showing time to develop penetration zones as a function of stress and temperature of the test and its relationship to crack initiation time [37].

In his model, Gordon also discusses the crack propagation stage. He states that the LME phenomenon needs a liquid metal supply on the crack tip. However, bulk liquid flow ensures this supply, so the liquid metal supply does not determine the crack rate. For him, the reinitiation of the crack along the crack path is also necessary and could be slower than the liquid metal transport, making this the rate-determining step.

Gordon's model can explain several characteristics of LME, such as delayed failure, strain rate effects, solute effects, grain size effects, and cold work effects. On the other hand, it does not deal with the atomic details of the nucleation process, and it only mentions that the stress threshold is associated with the movement of dislocations [37].

The literature review on LME in this thesis gives us perspectives on which parameters and mechanisms could be relevant to our study. To comprehend the phenomena involved in the LME of Cu and alpha brasses by the eutectic Ga-In (EGaIn), it is necessary to have an insight into some of their relevant properties, which the following section will describe.

I.2. The Cu-Zn/EGaIn system

I.2.1. The solid metal: Cu and Cu-Zn alloys

Copper and Cu-alloys are two of the most commercial metals due to their electrical and thermal properties, outstanding resistance to corrosion, ease of fabrication, and good mechanical resistance. There are six Cu-alloys families, each of which has different alloying elements. The most used alloying elements are those that form a solid solution with copper since the resulting alloy will present high mechanical resistance without the brittleness related to the second phases and compounds.

Brass is one of the Cu-alloys family and has Zn as their only alloying element. Their typical applications include pipes, valves, fitting systems carrying fluids, and electronic components [56].

As observed in the Cu-Zn phase diagram in Figure I–14, there are two phases: the alpha phase, which presents an FCC structure and the beta phase, which has a body-centred cubic (BCC) structure. Indeed, brasses are named alpha brass, alpha-beta brass, or beta brass according to the presence of these phases in the alloy. This work studies pure Cu and different alpha brasses and focuses on their mechanical properties.

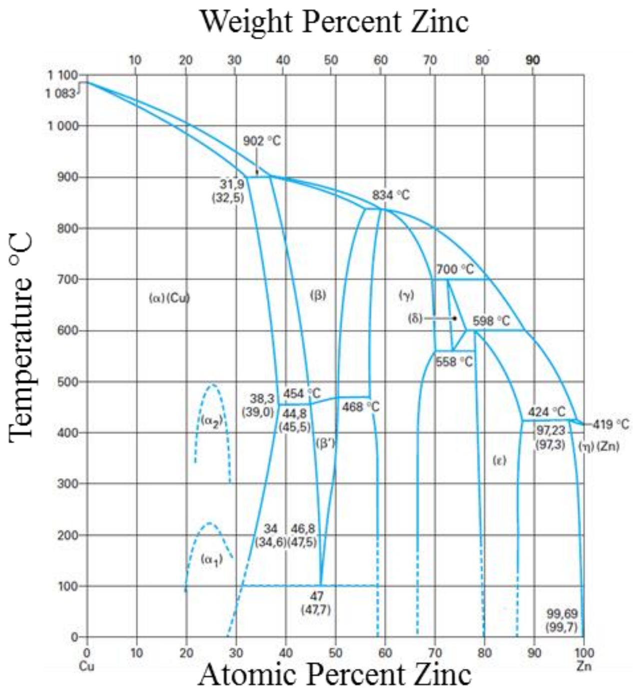

Figure I–14 Cu-Zn binary phase diagram [57].

I.1.1.1. Mechanical properties of Cu and alpha brasses

In alpha brasses, the primary role of Zn is to induce solid solution strengthening; hence, their mechanical behaviour depends strongly on the Zn content. For instance, Table I–1 shows the nominal composition and the range of some mechanical properties of commercial alpha brasses and commercial pure Cu.

Table I–1 Properties of wrought copper and brasses (the ranges are from softest to hardest commercial forms) [56].

Alloy number	**Nominal composition (wt.%)**	**Tensile strength (MPa)**	**Yield strength (MPa)**
C10200	99.95 Cu	221 - 455	69 - 365
C21000	95.0 Cu, 5.0 Zn	234 - 441	69 - 400
C22000	90.0 Cu, 10.0 Zn	255 - 496	69 - 427
C22600	87.5 Cu, 12.5 Zn	269 - 669	76 - 427
C23000	85.0 Cu, 15.0 Zn	269 - 724	69 - 434
C24000	80.0 Cu, 20.0 Zn	290 - 862	83 - 448
C26000	70.0 Cu, 30.0 Zn	303 - 896	76 - 448

It is possible to cold reduce copper almost limitlessly without annealing, but Cu-alloys usually harden by cold working rapidly and thus require annealing to re-soften the material before further cold working. In single-phase Cu-alloys such as the alpha brasses, annealing transforms the deformed and highly stressed crystals through recovery, recrystallization, and grain growth. Indeed, the grain size affects the strength, workability, control of directionality, and surface roughness of the alloys [56].

The mechanical properties of these alloys depend strongly on their thermo-mechanical history, which is why in Table I–1, the mechanical properties of the Cu-alloys vary a lot among the same composition. For instance, Figure I–15 shows the differences in some of the mechanical properties of an alpha brass with 30 wt.%Zn with different degrees of rolling reduction and different temperatures of recrystallization [58].

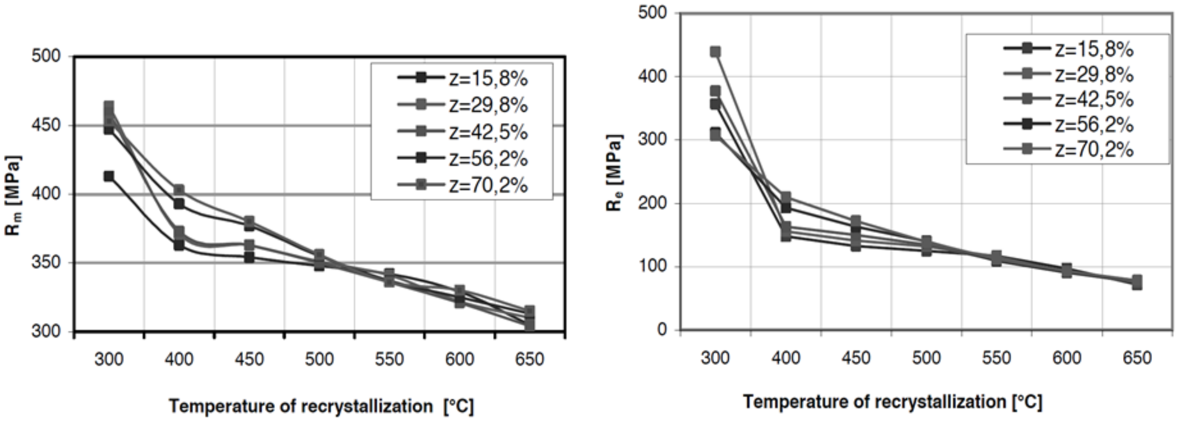

Figure I–15 Influence of the temperature of recrystallization and the degree of the rolling reduction (z) on the tensile strength (R_m) and the yield point (R_e) of Cu-30 wt.%Zn [58].

I.2.1.1. Deformation mechanisms

As for most metals, dislocations are the principal source of plastic deformation. Cu and alpha brasses have an FCC structure, so the slide systems are {111}<110> at room temperature. Additionally, the {110}<110> slide system also activates above 550 °C [59].

Alternatively, there is also plastic deformation by twinning. In the case of FCC metals, alloying decreases the stacking fault energy, which makes them prone to twinning during low-temperature deformation [60]. To illustrate, Figure I–16 shows the reported values of the stacking fault energies of some Cu-Zn alloys.

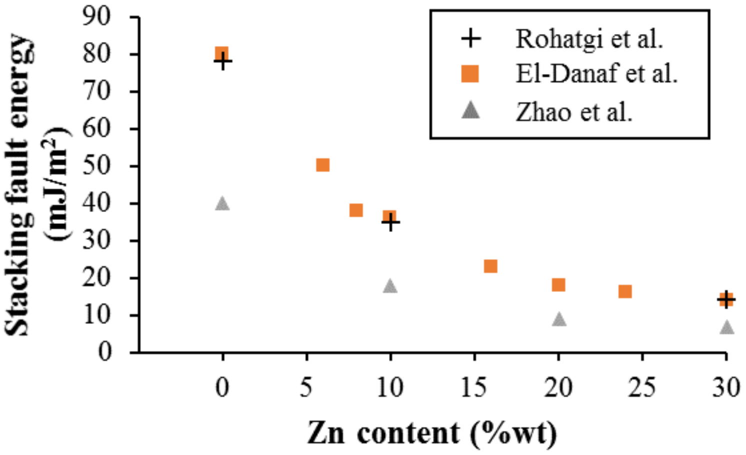

Figure I–16 Evolution of the stacking fault energy with the Zn content in alpha brasses [61]–[63].

The reported values are slightly different between the sources, but there is always a decrease in the stacking fault energy at higher Zn contents. This tendency relates to the fact that Cu does not twin at regular strain rates while brass shows extensive twinning, and it is often believed that a low stack fault energy promotes twinning [63], [64].

El-Danaf et al. explained this tendency by stating that reducing the stacking fault energy promotes strain hardening and reduces grain breakup. However, they stated that the stacking fault energy has only an indirect effect on twinning and that the microstructural variables that directly control the deformation twinning on polycrystalline FCC metals are the dislocation density and the average homogenous slip length [62].

I.2.1.2. Oxides

Apart from the mechanical behaviour, the surface properties of the solid are also relevant for studying LME. As explained in the previous section, oxides play an essential role in its apparition.

Copper oxides rapidly, even at low temperatures. This oxidation is not self-protective, and the oxidation rate is fast. First, the copper oxidates to form Cu_2O at a rate that dependents strongly on the temperature and the oxygen partial pressure. Then, Cu_2O oxides into CuO, which oxidation rate is approximately independent of the oxygen pressure [65].

Qiu and Leygraf studied the oxidation of an alpha brass with 20 wt.%Zn by humidified air [66]. They found that an amorphous Cu_2O-like oxide forms with ZnO that grows locally in Zn-rich zones. They did not observe the formation of CuO, which agrees with another study that reports only ZnO and Cu_2O in alpha and beta brasses at ambient temperature and the further apparition of CuO at higher temperatures [67].

Different acids, such as hydrochloric acid, sulfuric acid, nitric acid and citric acid, can dissolve CuO. Hydrochloric acid has the highest dissolution efficiency, and the correspondent reaction is as follows [68]:

$$\mathrm{CuO} + 2\mathrm{HCl} \rightarrow \mathrm{CuCl_2} + \mathrm{H_2O}$$

For instance, Colombeau et al. used hydrochloric acid to dissolve the Cu oxide to enable the wetting of Cu by liquid mercury [69], and Froemel et al. did the same with citric acid to enable the bonding of Cu with Ga [70].

I.2.2. The liquid metal: EGaIn

Metals with low melting points are attractive due to their unique properties. However, these metals usually present problems such as radioactivity (Cs and Fr), short half-life (Fr), violent chemical properties (Cs and Rb), and toxicity (Hg) [71]. Liquid Ga-based alloys are promising alternatives to these metals [71].

Compared with Hg, the most commonly used liquid metal at room temperature, Ga-based alloys are superior in most applications, mainly due to their low toxicity [72], [73]. Also, because of their low vapour pressure, they do not produce inhalable metal vapour under room conditions [74].

The unique properties of Ga-based alloys made them good candidates for several applications. Due to their low melting points and wetting properties, Ga-based alloys are attractive for applications such as film coating, electronic interconnects, and contrast agents for grain boundaries and microcracks [75]. Likewise, some researchers have proposed these alloys as potential coolants in nuclear power plants as an alternative to Na [71]. The biocompatibility of the Ga-based alloys makes them attractive for biological applications, such as drug delivery, bio-imaging, contrast media and biosensor [76]. In addition, the capacity of these alloys to form intermetallic compounds at low temperatures makes them promising for joining materials in microelectronics [77].

There are three principal Ga-based alloys: pure Ga; EGaIn, which is a Ga-In alloy with 24.5 wt.%In; and Galinstan, which is a Ga-In-Sn alloy with 21.5 wt.%In and 10.0 wt.%Sn. Table I–2 shows some physical properties of these Ga-based alloys, along with Hg, for comparison.

Table I–2 Physical properties of gallium (Ga), Ga-based alloys, and mercury (Hg) [71].

Parameter	**Ga**	**EGaIn**	**Galinstan**	**Hg**
Melting point (°C)	29.76	15.5	-19	-38.8
Boiling point Tb (°C)	2403	2000	>1300	356
Density at 20 °C (g/cm^3)	5.9	6.28	6.44	13.533
Vapour pressure (Pa)	1 at 1037 °C	<1.33 × 10^{-10} at 300 °C	<1.33 × 10^{-6} at 500 °C	1 at 42 °C
Specific heat (J/kg/K)	410	404	295	140
Electrical conductivity (W/m/K)	6.73 × 10^{6}	3.40 × 10^{6}	3.46 × 10^{6}	1.04 × 10^{6}
Thermal conductivity (W/m/K)	29.3	26.6	16.5	8.5
Viscosity µ (kg/m/s)	1.37 × 10^{-3}	1.99 × 10^{-3}	2.4 × 10^{-3}	1.526 × 10^{-3}

This work studies the EGaIn alloy, which name comes from "eutectic Ga-In", and its composition corresponds to the eutectic point in a Ga-In phase diagram obtained experimentally in 1938 [78]. However, further studies drew a phase diagram with a eutectic composition of 21.4 wt.%In (Figure I–17) instead of 24.5 wt.%In [79]. Despite this redefinition of the Ga-In eutectic, the composition of the EGaIn is still considered worldwide as having 24.5 wt.%In.

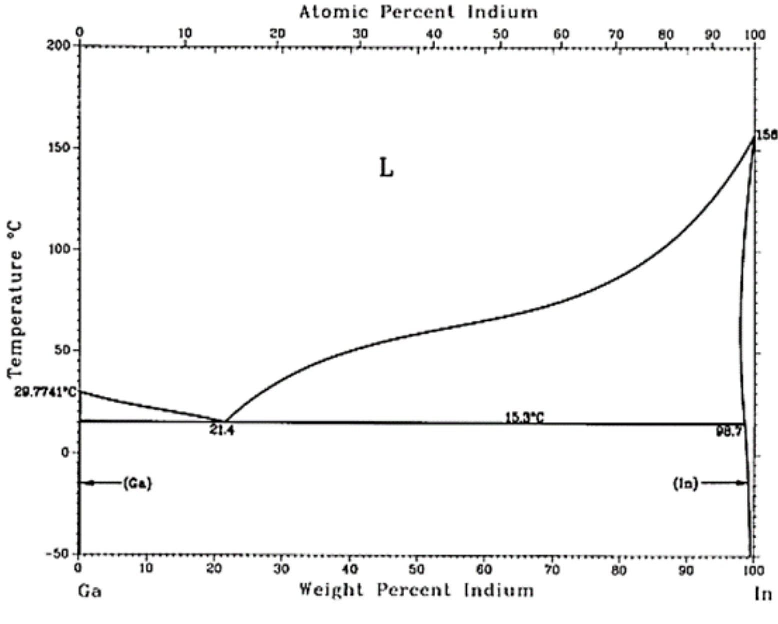

Figure I–17 Ga-In binary phase diagram [79].

At ambient conditions, the surface tension of EGaIn is approximately 624 mN/m [80], and it decreases to approximately 444 mN/m during exposure to HCl, presumably because it dissolves the oxide layer [72]. For comparison, pure Ga in an HCl bath has a surface tension of approximately 695 mN/m at 50 °C [75], and Galinstan, in oxygen-free conditions, has a surface tension of approximately 535 mN/m at 28 °C [81]. For comparison with other common liquid metals; the surface tension of Pb, Bi, and LBE at their corresponding melting points 328, 271, and 125 °C, is 374, 451, and 416 mN/m, respectively [82]; and Hg has a surface tension of approximately 476 at 25 °C [83].

I.2.2.1. Oxides

Whenever the EGaIn comes into contact with the oxygen in the environment, an oxide skin covers its surface and confines the liquid inside it. This skin prevents EGaIn from reflowing into the shape with the lowest interfacial energy [84]. Indeed, the liquid metal surface is so reactive that it can readily oxidize even under high vacuum conditions [85]. This oxide skin allows EGaIn to be "moldable" on the microscopic scale [72], which means that the form of the drop can be changed when applying an external force; Figure I–18 illustrates this phenomenon [84].

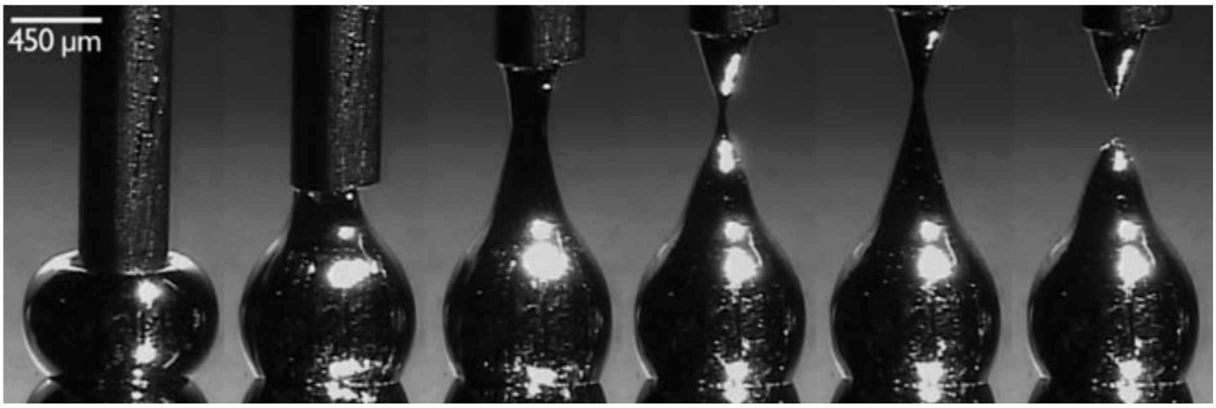

Figure I–18 A series of photographs of the formation of a conical tip of EGaIn [84].

Other liquids, such as Hg or H_2O, do not present an external oxide skin, but this skin is not exclusive to EGaIn. Other Ga-based alloys present this oxide skin, such as Galinstan (the Ga-In-Sn eutectic alloy) [86] and pure Ga [85].

In those Ga-based liquid alloys, the skin is composed of Ga oxides, and the bulk is composed of liquid metal with the corresponding composition (Ga, Ga-In, or Ga-In-Sn) [87]. Furthermore, in pure Ga, the oxide skin is likely amorphous and has a well-defined value of the thickness of 0.5 nm, which does not change with oxygen dosage or temperature, indicating that the Ga oxide acts as a passivating film [85]. According to Dickey et al., this last property also applies to the EGaIn, although they did not measure the thickness of the oxide layer [72].

On the other hand, Scharmann et al. studied the oxide layer in Galinstan and reported an oxide layer of approximately 2 nm in thickness [86]. They also claimed that the oxide skin contains Ga_2O_3 and Ga_2O, although the first is the most stable oxide. However, they clarified that they could not measure the presence of GaO due to their inability to distinguish that phase from Ga_2O in the photoelectron spectra.

There are studies on the deoxidization of Ga-based alloys. For instance, Dumke et al. described the behaviour of EGaIn after sputtering to retire the oxide skin [88]. They quantified that after the sputtering, the first monolayer of the liquid metal is approximately 97 at.%In. In the same deoxidation situation, there is a surface enriched with In. Moreover, when EGaIn is in contact again with oxygen, gallium oxides cover the surface yet again [72].

These observations agree with Scharmann et al., who reported that oxidation strongly influences Ga atoms more than In and Sn atoms in the Galinstan alloy [86]. They also support that In does not oxidize as fast as Ga, which agrees with Toastmann et al., who also reported that In oxide does not form a passivating film as Ga does [89]. There is a similar behaviour in Galinstan due to Ga_2O_3 being thermodynamically more stable than In_2O_3 [87].

Additionally, Dickey et al. described how the oxide skin dictates the rheological behaviour of EGaIn [72]. First, they observed that the skin has both elastic and viscous characteristics. Then, they observed that the resistance to flow only arises from such skin. According to them, this skin cannot support stresses larger than 500 mN/m, which is close to EGaIn surface tension; above this value, there is minimal resistance to flow since bulk EGaIn has a low viscosity. The contribution of the solid oxide layer to the stress supported is two orders of magnitude larger than the viscous contribution of the bulk [75].

Because of the oxide skin's role in the Ga-alloys' behaviour, there are studies regarding its control and elimination. Zrnic and Swatik used an HCl solution to remove the oxide skin on EGaIn and then measured its surface tension with the ring removal and the sessile drop methods, obtaining values of 397 and 435 mN/m, respectively [80]. Much later, Xu et al. studied the effect of HCl concentration on the mechanical properties of Ga and EGaIn [75]. They found that the same critical acid concentration controls the mechanical properties, which confirms that the mechanical properties depend on the oxide skin; in this sense, they reported that Ga reaches a pure liquid state when washing the metal with HCl with a concentration higher or equal to 0.5 M.

Likewise, Kim et al. developed an HCl vapour treatment to eliminate the oxide skin on Galinstan [90]. After using this treatment, they found evidence of the $GaCl_3$ formation as a reaction product between the Ga oxides and HCl. Similarly, they observed the $InCl_3$ formation due to the reaction of the In, which is below the surface, with HCl; Figure I–19 schematizes these findings. Besides, they report that the modified surface slightly reoxidizes when it enters into contact again with the air environment, but the chlorides remain on the surface. They did not report any reaction involving Sn, which remains in the liquid metal's core.

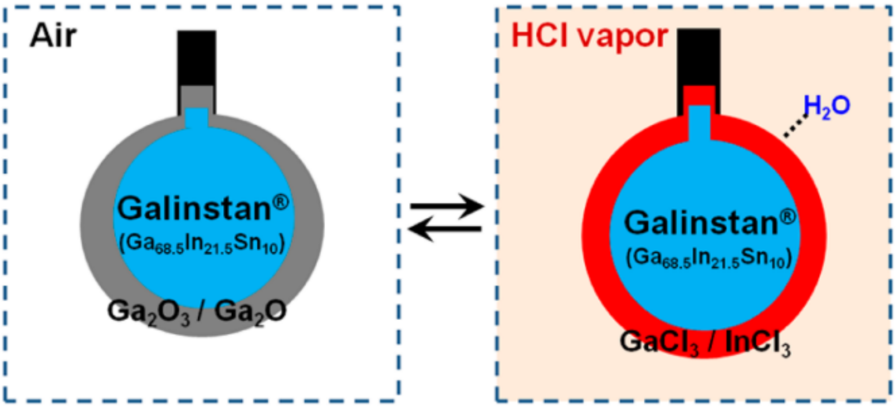

Figure I–19 Schematic diagram of the chemical reaction with HCl vapour. The phase of oxides (Ga2O3/Ga2O), chlorides ($GaCl_3$/$InCl_3$), and water is solid, aqueous, and liquid, respectively [90].

Doudrick et al. also studied the effect of deoxidization by focus ion beam and observed the changes in the wetting capacity on non-metallic substrates [87]. They also studied the morphology of the drops of Galinstan after an HCl vapour treatment and reported that a thick shell of approximately 1 µm made of Cl, Ga, and O replaced the oxide skin. In contrast with Kim et al., they did not report the apparition of In on the surface [90].

Alternatively, a NaOH solution can be used along with an external voltage to remove the oxide of EGaIn in contact with Cu. However, this method introduces water to the liquid metal [91].

I.2.2.2. Interfaces with Ga

Since there is contact between solid/liquid in virtually all applications of liquid metals, the interfacial interactions between the Ga-based alloys are essential. For instance, Ga reacts quickly with Al, Fe, Ni, and Cr [92].

Table I–3 summarizes the products of reactions of Ga-based alloys in contact with different metal foils. These reaction products correspond to conditions of high temperatures and long contact times and do not include any cases where there is Cu. The following section shows some cases of Ga-based alloys in contact with Cu at conditions closer to our study, i.e., lower temperatures and short contact time.

Table I–3 Summary of reactions between liquid Ga-based alloys and substrates other than Cu [71].

Liquid Phase	**Solid Phase**	**Reaction Condition**		**Products**	**Reference**
		Temperature	**Time**		
Ga	Ni	300 °C	24-3000 h	Ni_2Ga_3, $NiGa_4$	[93]
Ga	Fe	300 °C	24-3000 h	$FeGa_3$	[93]
Ga	Cr	300 °C	24-3000 h	$CrGa_4$	[93]
Ga	Pd	≈25 °C	8 days	$PdGa_5$	[94]
Ga	Au	≤ 50 °C	10 min	$AuGa_2$	[95]
Ga	Stainless steel 316	400 °C	24-3000 h	$FeGa_3$, $CrGa_3$, Ni_2Ga_3	[93]
Ga	Inconel 625	400 °C	24-3000 h	$CrGa_4$	[93]
Galinstan	Ni	500 °C	24 h	$Ga_{65}Ni_{35}$, $In_{50}Ga_{25}Sn_{20}Ni_5$, $In_{55}Sn_{41}Ga_4$	[96]
Galinstan	Ti	500 °C	24 h	$Ga_{75}Ti_{25}$, $Ga_{72}In_{12}Ti_9Sn_7$	[96]
Galinstan	Cr	500 °C	24 h	$Ga_{70}In_{13}Cr_9Sn_8$, $Cr_{84}Ga_{13}In_3Sn$	[96]
Galinstan	W	500 °C	24 h	No reaction layer	[96]
Ga-45 wt.%Al	a Ni foil	700 °C	20 min	Ni_3Ga	[97]
Ga-45 wt.%Ni-15 wt.%Al	a Ni foil	700 °C	20 min	Ni_3Ga	[97]

I.2.3. The couple: Cu-Zn/EGaIn

It is helpful to know the correspondent phase diagrams to understand what happens whenever Cu-Zn alloys enter into contact with the liquid EGaIn. Figure I–14 shows the Cu-Zn phase diagram, and Figure I–17 that of Ga-In. Figure I–20 illustrates the other binary phase diagrams.

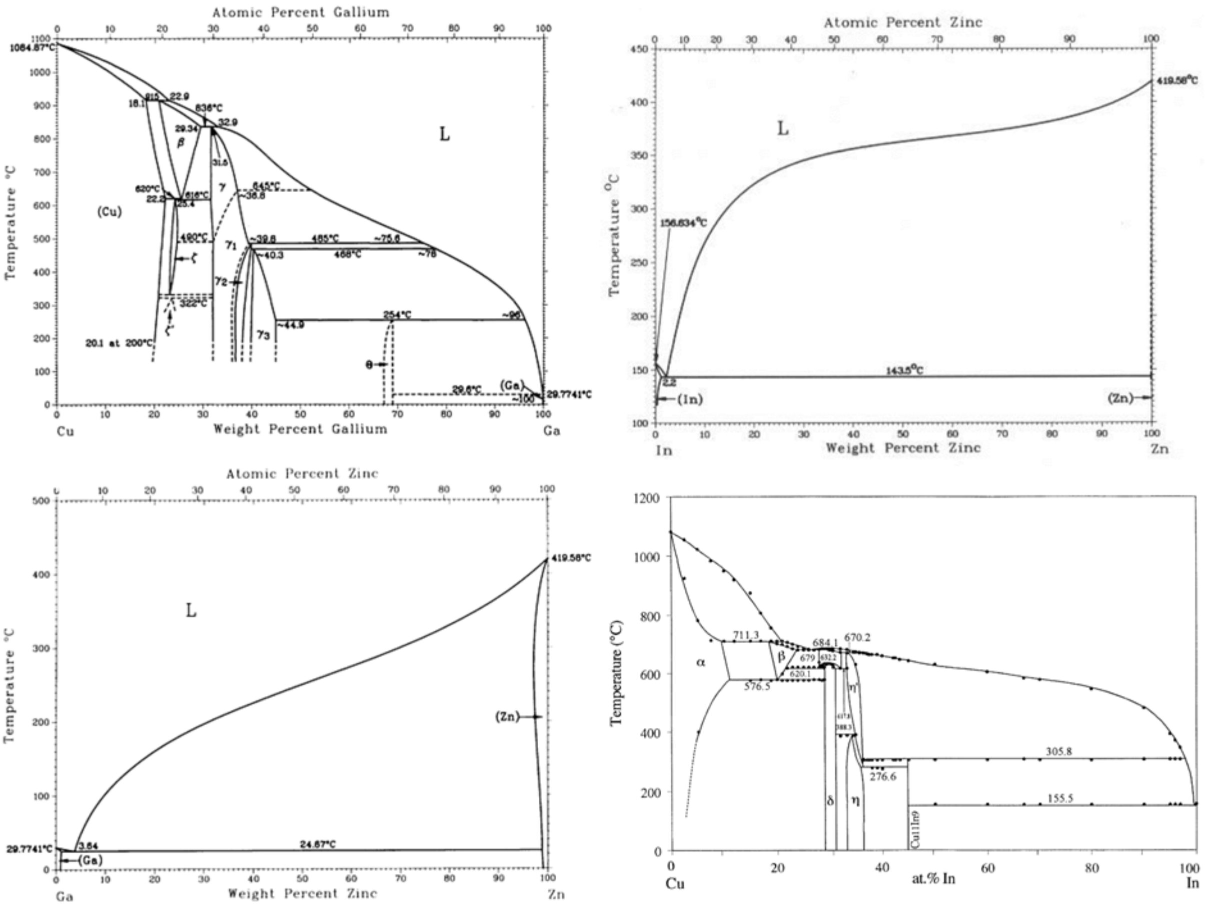

Figure I–20 Binary phase diagrams of the systems Cu-Ga, In-Zn, Ga-Zn [98]*, and Cu-In* [99].

Furthermore, to consider some of the critical properties that concern the study of the LME, Figure I–21 compiles some of the relevant properties of the system.

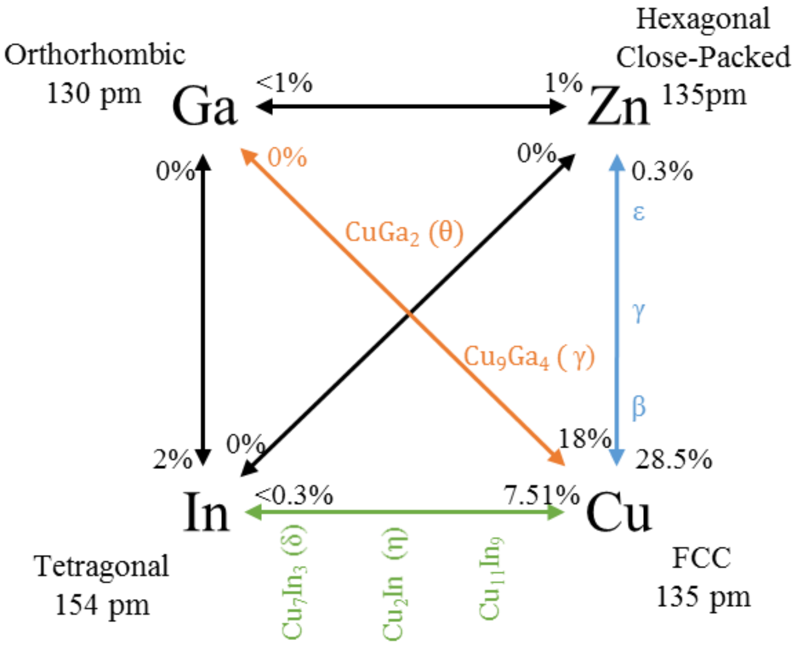

Figure I–21 Some relevant properties of the system Ga-Zn-In-Cu by couples (at room temperature): crystallographic structure when pure, atomic radii, intermetallic compounds, and maximum solubilities.

This diagram shows that Cu is the only element that forms intermetallics with the other metals. The ternary or quaternary phase diagrams are necessary to have this certainty. However, to the author's knowledge, no information is available about the experimental investigation of the other ternary systems, nor on the quaternary Cu-Zn-Ga-In. Also, no known compounds exist between Zn, Ga, and In. The only information available is on the Cu-Ga-In ternary system.

For the Cu-Ga-In ternary system, the usual phases reported are the $Cu_{16}In_9$ and Cu_9Ga_4 phases, along with the $Cu_9(Ga,In)_4$ and $Cu_{16}(Ga,In)_9$ ternary solid solutions, but there are no ternary compounds reported [100], [101].

On the other hand, Cu is a good choice as a structural material in many thermal and electronic devices, among other application fields; this is why several works study the interaction between Ga-based alloys and Cu [102].

There are two examples of potential applications of Ga-based alloys that involve Cu. One is the TransM^{2}ixes, an amalgam of EGaIn and Cu particles. The amalgam has semiliquid/semisolid behaviour and has potential applications in flexible electronics and thermal interface materials [91]. Another example is a self-powered copper wire oscillator that consists of a copper wire in contact with the liquid $GaIn_{10}$ alloy pre-fueled with aluminium submerged in a NaOH solution [103]. Another application is the joining of materials in microelectronics [77].

I.2.3.1. Intermetallics

Cu reacts with Ga to form intermetallic compounds. A series of articles reported the products of the reactions of different powders, mostly Cu-based, in contact with Ga-based alloys [104]–[108]. They used planetary ball-milling in an argon atmosphere to obtain these powders and found that when mixing pure Cu or Cu_9Ga_4 with liquid Ga, $CuGa_2$ is the main product of the interaction at room temperature [71].

Similarly, Tikhomoriva et al. described the interaction between Cu particles and liquid Ga at 100 °C [109]. They found that on the particles' surface, first, there is a formation of a layer made of Ga and enriched with Cu (2 - 2.5 wt.%), and then, there is the formation of the $CuGa_2$ intermetallic. However, the Cu-enriched layer remained between pure Ga and $CuGa_2$ until the liquid portion of the mixture vanished.

In the same work, they modelled the growth rate of the $CuGa_2$ phase with a power law (Eq. (9)),

$$x^2 = A\tau \tag{9}$$

where x is the compound layer thickness (mm), τ is the time (min), and A is a parameter proportional to the diffusion coefficient (mm^2/min) [109]. Applying physical and geometrical considerations, they found the value of A to be $(2.822 \pm 0.660) \times 10^{-8}$ (mm^2/min).

On the other hand,Table I–4 summarizes the reaction products of Ga-based alloys in contact with Cu foils [71].

Table I–4 Summary of reactions between liquid Ga-based alloys and Cu substrates [71].

Liquid Phase	**Solid Phase**	**Reaction conditions**		**Products**	**Reference**
		Temperature	**Time**		
Ga	Cu foil	200 °C	3-24 h	$CuGa_2$	[110]
Ga	Cu	160-240 °C	3-48 h	$CuGa_2$, Cu_9Ga_4	[111]
Ga	Cu	280-300 °C	3-48 h	Cu_9Ga_4	[111]
Ga on a 50 nm Au seed layer	Cu	90 °C	10 min	$CuGa_2$, Cu_9Ga_4, $AuGa_2$	[70]
Sn-32 wt.%Bi-6 wt.%Ga	Cu	158 °C	1-8 min	$CuGa_2$	[112]
Ga-10 wt.%Zn	Cu	150 or 200 °C	Not mentioned	Cu_9Ga_4, Zn	[113]
Ga	Two Cu foil	160 °C	96 h	$CuGa_2$, Cu_9Ga_4	[111]
Ga	Two Cu foil coated with 40 nm thick Pt, Ga/Pt thickness ≤ 1	300 °C	7 h	Ga_7Pt_3	[110]
Ga	Two Cu foil coated with 40 nm thick Pt, Ga/Pt thickness ≤ 4	300 °C	7 h	Cu_9Ga_4, Cu(Ga), Ga_7Pt_3, $CuGa_2$	[110]
Ga-10 wt.%Zn	Cu-37 wt.%Zn or Cu-32 wt.%Zn	150 or 200 °C	Not mentioned	Cu_9Ga_4	[113]
Ga-45 wt.%Al	a Cu foil	700 °C	20 min	Cu_3Ga, Cu_9Ga_4	[97]
Ga-45 wt.%Ni-15 wt.%Al	a Cu foil	700 °C	20 min	Cu_3Ga	[97]

Regarding the Cu-Ga intermetallics, Lin et al. described the interaction between Ga and Cu foils at different temperatures [111]. For instance, Figure I–22 shows the intermetallics at 160 °C; they found that two intermetallics formed: $CuGa_2$ (θ) and Cu_9Ga_4 (γ_3); the image shows that there is only a small amount of phase γ_3, which is between θ and the Cu foil. In addition, they described that there is more formation of γ_3 when the temperature is closer to the temperature of the peritectic reaction: $\gamma_3 + L \rightarrow \theta$ (254 °C as seen from the phase diagram in Figure I–20).

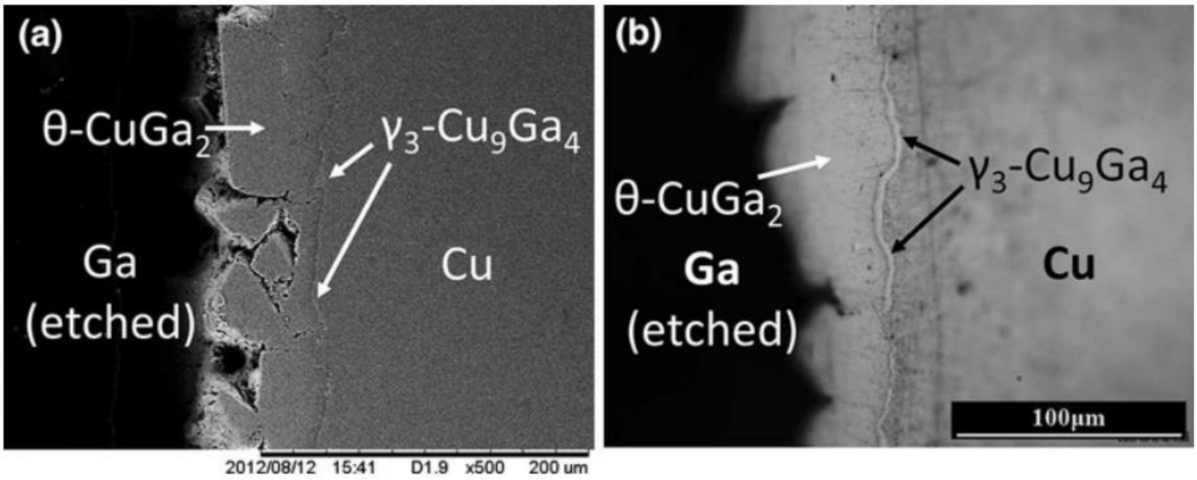

Figure I–22 Micrographs of Cu/Ga couples reacted at 160 °C for (a) 48 h and (b) 96 h [111].

Additionally, they studied the intermetallics' reaction kinetics and mechanism of growth at different temperatures. According to them, reaction controls the growth at 160 °C, volume diffusion controls the growth at temperatures between 200 and 240 °C, and grain-boundary diffusion controls the growth between 280 and 300 °C [111].

Another remark of their work is the morphology evolution of the interface between Cu and Ga at 200 °C, which Figure I–23 schematizes. According to them, liquid Ga reacts at specific points, e.g., grain boundaries, and dissolves Cu; this generates a basin structure where the θ phase then nucleates. According to them, the θ phase also forms in the uncorroded areas, but the thermal convection detaches the phase from the Cu. Eventually, the corrosion stops when the θ phase covers the entire Cu surface and the interface level [111].

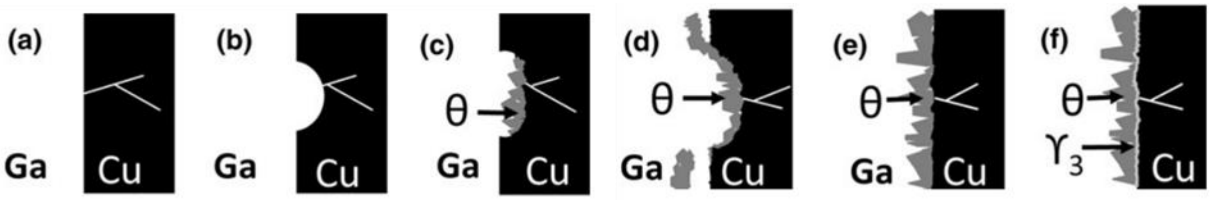

Figure I–23 Schematic diagram of the microstructural evolution of Cu/Ga interfacial reactions at 200 °C [111].

Froemel et al. found similar results; they reported the bonding of Cu/Ga by the intermetallic $CuGa_2$ that then transitioned into Cu_9Ga_4 at 90 °C, which enhanced the shear strength of the bond. Indeed they propose that, depending on the temperature, the $CuGa_2$ phase will eventually be fully converted into Cu_9Ga_4 if there is enough copper in the interface [70].

However, at room temperature, Liu et al. reported that $CuGa_2$ is the only intermetallic compound that forms between liquid Ga and pure Cu at 30 °C for as long as 96 h [77]. They also reported that the formation of the intermetallic is faster in some "preferred dissolution sites". They mention grain boundaries as a possible preferential site but do not include any evidence to support this.

Liu et al. also presented the morphology of the $CuGa_2$ intermetallic, Figure I–24. Furthermore, they characterized the intermetallic hardness as around 2.5 GPa, compared with Cu, which has a hardness of 1.7 GPa. Compared with other intermetallic compounds in solder joints, $CuGa_2$ is softer and more compliant [77].

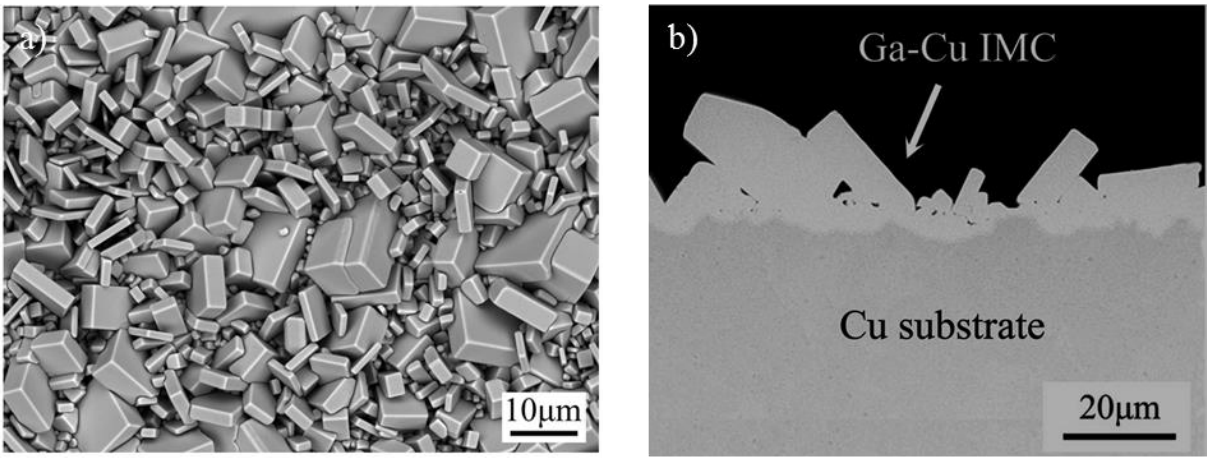

Figure I–24 Morphology of the $CuGa_2$ intermetallic compound formed after 40 h of contact of Ga and Cu at 30 °C [77].

In the case of mechanical alloying of Cu-powders with Ga at room temperature, $CuGa_2$ is the only intermetallic compound that appears. In this case, the melting of Ga is unnecessary to form $CuGa_2$ since the reaction occurs in the solid state [114].

Alternatively, Deng et al. quantified the corrosion development on T2 Cu foils in contact with liquid Ga [92]. Nevertheless, their surface preparation allowed the formation of oxides on the liquid metal and the metallic foil, which may have influenced the corrosion development. Still, they estimated the corrosion rate to be 30-60 µm per month at 60 °C, presumably belonging to a slightly high corrosion resistance grade. Besides, they reported that the corrosion area presented rugged and rough characteristics but no apparent cracks or defects. At room temperature in an HCl solution, a $CuGa_2$ intermetallic layer of approximately 3−5 μm forms when a Cu foil is in contact with liquid EGaIn for 10 min [102].

Similarly, Geddis et al. studied the contact between a Cu-15 wt.%Zn brass in contact with Galinstan at different temperatures. The behaviour is similar to that of Cu in contact with Ga-based alloys, forming a $CuGa_2$ intermetallic layer. The intermetallic layers had In and Sn in small amounts. Moreover, they reported the dezincification of the brass by the dissolution of the Zn into the Galinstan drop [74].

Tang et al. deduced that in the case of Cu powder that enters contact with the EGaIn, the Cu first dissolves into the liquid metal; then, it crystallizes with Ga to form the $CuGa_2$ phase. Although other intermetallics between Cu and In are thermodynamically possible, they did not observe any trace in the chemical analysis of Cu powder in contact with EGaIn [115].

Another interesting example is the case of the mechanochemically synthesized solid solution Cu⟨In⟩ that reacts with the EGaIn to form the $CuGa_2$ intermetallic and coarse In [105].

I.3. Relevant literature around the LME of Cu-Zn by EGaIn

To the author's knowledge, there are no studies on the liquid metal embrittlement of Cu-Zn alpha brasses in contact with the EGaIn. However, there are studies on LME on similar systems; Table I–5 presents some. The most relevant are further discussed hereunder.

Table I–5 Works on LME in some similar systems.

Solid metal	**Liquid metal**	**Reference**
Cu-30 wt.%Zn and Cu-40 wt.%Zn	Ga	[47]
Single crystal beta-brass	Ga	[116]
Binary and ternary beta-brass alloys	Ga, EGaIn, Ga-1.6%Hg, In, and Hg-70%In	[29]
Cu-30 wt.%Zn	Hg	[32]
Cu	Hg	[10]
Cu	Li	[117]
Cu	Bi	[16]
Zn	Ga, In, In-Bi eutectic, and Sn-Bi eutectic	[118]
Zn	Hg	[25]
Zn	Ga, Hg, In, Sn, Bi and Cd	[119]

The studied system closest to ours is the Cu-30%Zn/Ga, reported by Fernandes and Jones [47]. They performed tensile tests on brass with grain sizes ranging between 24 and 148 µm under different testing conditions: strain rates between $3.33 \times 10^{-4}\ s^{-1}$ and $3.33 \times 10^{-2}\ s^{-1}$ and temperatures between 20 and 200 °C. They reported no evidence of LME under any conditions tested and that all specimens presented a ductile fracture with signs of microvoid coalescence.

Fernandes and Jones further repeated the tensile tests on notched brass specimens and observed a diminution in the plastic deformation accompanying fracture and the fracture stress. On those specimens, they observed a brittle intergranular cracking (Figure I–25), confirming the brass embrittlement by Ga.

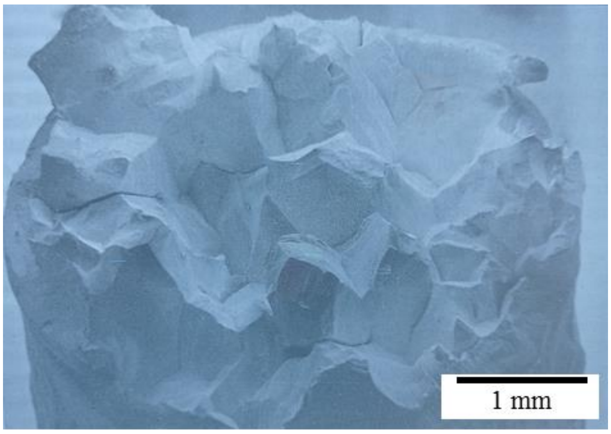

Figure I–25 Fracture surface of the notched Cu-30%Zn brass specimen tested in gallium [47].

Fernandes and Jones explain the differences between the notched and unnotched specimens by stating that in Cu-30%Zn brass, the dislocation climb relieves the localized stress; therefore, the stress does not increase sufficiently to cause crack initiation. In this sense, the notch acts as a stress concentration site that increases the localized stress to a level that promotes brittle cracking over plastic deformation [47].

In the same article, Fernandes and Jones studied the behaviour of the Cu-40%Zn brass in contact with liquid Ga. We recall that this alloy is a biphasic alpha-beta brass, and the β phase presents a BCC structure. Fernandes and Jones used unnotched tensile specimens under the same strain rate, temperature and grain size conditions to study this alloy. They reported that when there was LME, Cu-40%Zn cracked by brittle cleavage. They do not report which of the two phases presented this fracture type. Moreover, they characterized the temperatures of the ductility trough and found that increasing the strain rate expands the range of temperatures where LME occurs. Similarly, increasing grain size expands the ductility trough and increases embrittlement severity [47].

They explain the differences in the alloys' mechanical behaviour in contact with liquid Ga with the differences in their slip behaviour, which also explains the effect of the temperature and the strain rate. On one side, the Cu-40%Zn brass deforms predominantly by planar glide, which promotes higher stress at dislocation pile-ups and facilitates crack initiation. On the other side, they propose that the wavy slip behaviour in the case of the Cu-30%Zn brass relieves the stress at dislocation pile-ups and inhibits crack initiation [47]. Worth noting that they compared a monophasic alloy with a biphasic alloy, and they are not considering the different contributions to the LME of the two phases in the alpha-beta brasses.

In a different study, Lukowski et al. tested monocrystal beta brass specimens in contact with Ga using tensile tests at the relatively low strain rate of 5×10^{-6} s^{-1}. They found LME with cracks propagating discontinuously in a series of jumps linked to a non-uniform interaction between Ga and the beta brass [116]. Figure I–26 shows these discontinuities.

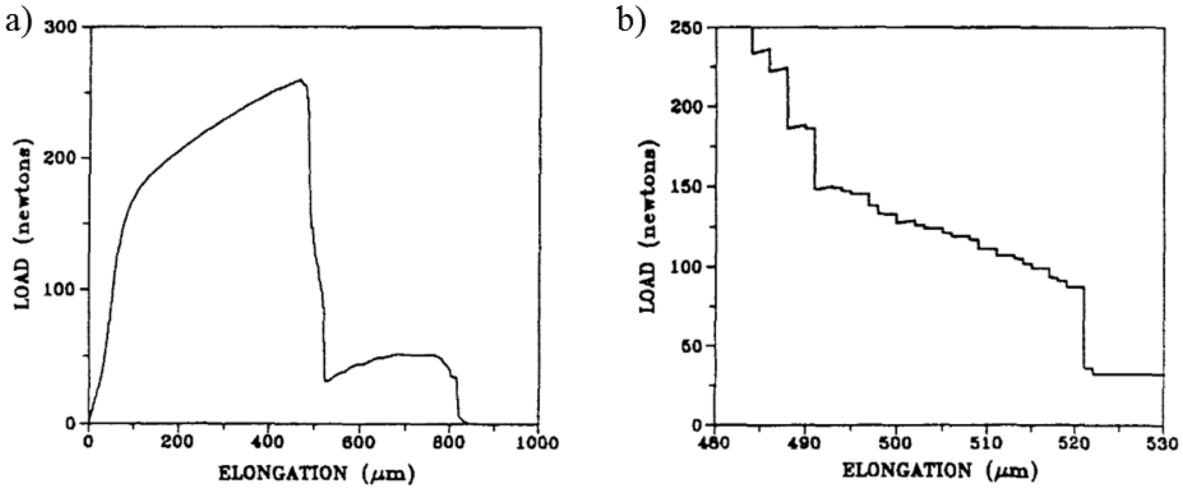

Figure I–26 a) Load vs crosshead displacement for the beta brass tensile specimen embrittled by Ga. b) Expanded load-displacement curve for a portion of the test exhibiting discontinuous cracking [116].

The authors explain this behaviour by proposing that each crack advance is associated with a time interval dependent on the diffusion-controlled reactions between the brass and Ga at the crack tip [116].

In a parallel study, the authors did tensile tests on notched monocrystal beta brass specimens in contact with Ga [120]. In this study, they limited the quantity of Ga to reduce the liquid metal available during crack propagation. They observed a fracture that changes in its fracture mode at some point due to the starvation of Ga. Figure I–27 shows the correspondent fracture surface, where there is a cleavage-like brittle zone followed by a transition zone and, finally, a ductile zone.

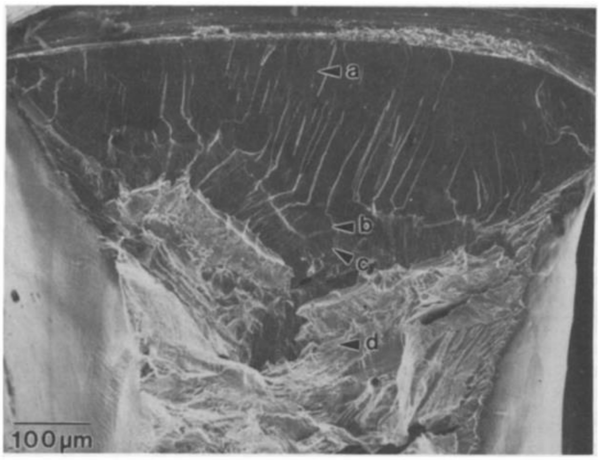

Figure I–27 A transgranular LME fracture surface of beta brass embrittled by gallium. (a) near the notch, (b) at the crack tip, (c) in the transition zone, and (d) in the ductile overload region [120].

Through auger electron spectroscopy, the authors found the presence of Ga in the brittle fracture but not in the transition zone or the ductile fracture. According to them, the absence of Ga beyond the brittle crack suggests there is no need for diffusion or penetration of the liquid metal ahead of the crack for it to propagate. In addition, they state that a Ga coverage of the order of a monolayer is sufficient to sustain the LME crack. They also reported that the Zn concentration is inversely related to the thickness of the Ga layer, which they did not observe for the Cu concentration. This relation could be linked to the diffusion of copper from the brass into Ga to form intermetallic phases [120].

It is worth noticing that the work of Au-Yeung et al. is the only one that mentions the possibility of an effect of the intermetallic on the LME of a Cu-based alloy by Ga, although there is no further discussion about it. On the other hand, there is no mention of the $CuGa_2$ intermetallic in none of the other studies on LME of Cu-based alloys by Ga-based alloys.

Regarding the beta brass, Shea and Stoloff studied the effect of Mn and Ni additions on the embrittlement of bet brass by different liquid metals using sheet-type tensile specimens. Mn and Nickel are two alloying elements that produce solid solution strengthening in beta brass; both decrease the ductility of the alloys, Mn being the one that does it more significantly. They found that adding Mn increases the severity of the embrittlement of beta brass by Ga and its transition temperature, while nickel additions have the opposite effect. The fracture was transgranular in all cases [29].

On the other hand, additions of In to liquid Ga up to 16.5 % and of Hg up to 1.6 % slightly increased the embrittlement severity without affecting the transition temperature. When testing single crystal specimens in contact with Ga and Ga-16.5%In, they found the same behaviour as the polycrystalline samples [29].

Shea and Stoloff related the effect of Mn and Nickel on the degree of embrittlement with the slip behaviour of the alloys; Figure I–28 shows this slip behaviour. According to them, Mn enhances planar slip, while Nickel enhances wavy glide. In this sense, Mn restricts cross slip, resulting in stress concentration and subsequent crack nucleation, increasing susceptibility to embrittlement [29].

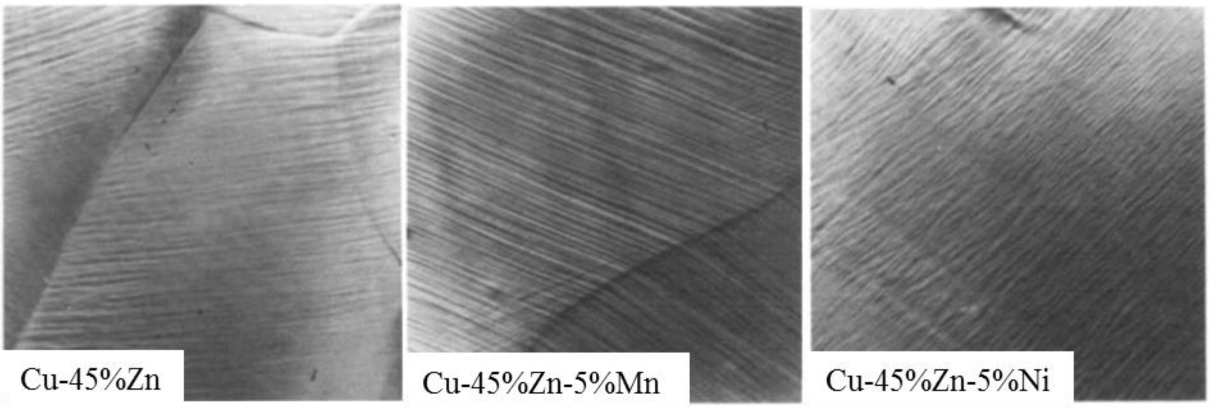

Figure I–28 Slip traces in polycrystalline beta-brasses, deformed 12 % in tension at 25 °C [29].

In the same article, Shea and Stoloff studied the embrittlement of the same alloys by In and In-30%Hg. When there was embrittlement of the alloys by these liquid metals, the fracture presented a profuse intergranular penetration to considerable distances from the fracture. They found that adding Mn to the beta brass slightly increased the embrittlement severity but not the transition temperature [29].

They also performed tests where the beta brass specimens were in contact with the liquid metal for 48 h, and then the liquid metal was removed just before performing the test. In those cases, the liquid metal had no effect on the specimens' mechanical properties, which indicates that in these cases, stress is a necessary condition for intergranular penetration [29].

The single crystals of the same alloys tested in contact with In and In-30%Hg presented a higher ductility than those tested in contact with Ga. Below 50 °C, the specimens fracture with the separation plane close to either {321}, {320}, or {100}; the last for the case of orientations near <100> [29].

Zn is highly soluble in In and Hg, which could indicate that this induces or enhances liquid penetration along grain boundaries. However, Zn is also soluble in Ga, but the embrittlement by Ga is transgranular. In this sense, solubility does not control the embrittlement mode alone [29].

In contrast, the Cu-30%Zn brass in contact with pure Hg presents an intergranular failure mode when there is LME. Furthermore, there is a direct relationship between the transition temperature and the logarithm of the grain size [32]; Tl, Zn, and Ga additions to Hg decrease the degree of embrittlement [15]; the fracture stress is independent of the exposure time [121]; and the susceptibility to embrittlement increases with pre-strain [15]. In addition, there is a reduction in the crack propagation rate above 50 °C, which was associated with the formation of intermetallics that would impede Hg from flowing to the crack tip. However, Cu solubility into Hg is very low at that temperature, and Zn does not form stable compounds [15].

On the other hand, Hg also embrittles Cu, and the fracture stress is inversely dependent on the square root of the grain size [15]. In addition, alloying copper to form a solid solution increases its tendency to be embrittled by Hg, which is related to an SFE decrease in the alloys. Figure I–29 shows this tendency. Kamdar explains this by stating that in the case of materials with low SFE, the dislocations that pile up on obstacles cannot cross-slip readily; this enables stress concentrations that enhance the nucleation of cracks [15].

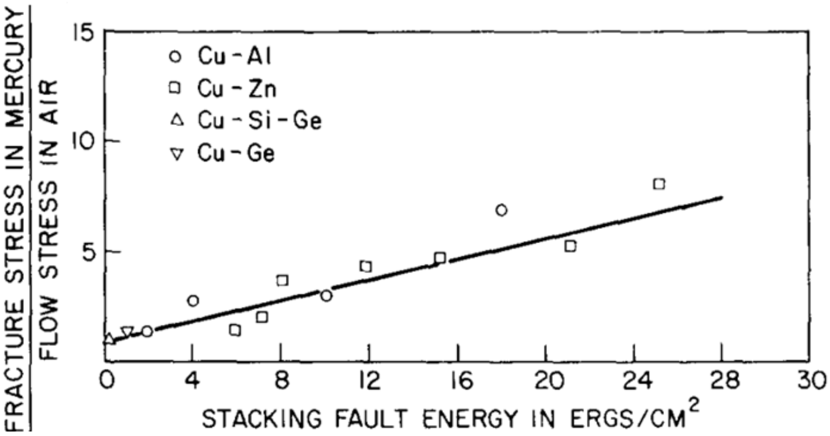

Figure I–29 Embrittlement of copper-base alloys as a function of their stacking fault energy [15].

Nonetheless, this system presents embrittlement even if the liquid metal is retired from the surface. An incubation period of 5×10^4 s is necessary [10]. In the taxonomy used in this work, this phenomenon would correspond to LMIE instead of LME.

Cu/Ga was enlisted as not susceptible to LME in a table in 1974 [122]. Nonetheless, it was indicated in the table that there was no published information on the tests. Previously, Westwood stated that Hg and Bi embrittled Cu but that Ga did not and explained it by recalling that their electronegativities values are close for the embrittled couples and different for the non-embrittled couples [27]. However, there have not been any further studies on this couple, so the possibility that Cu/Ga can present LME under certain conditions is still open.

I.4. Conclusions

Based on the previous information, Figure I–30 schematizes the possible chemical compounds for Cu-Zn/EGaIn at room temperature. The image has a division to illustrate two cases: the system without surface treatment and with an HCl treatment.

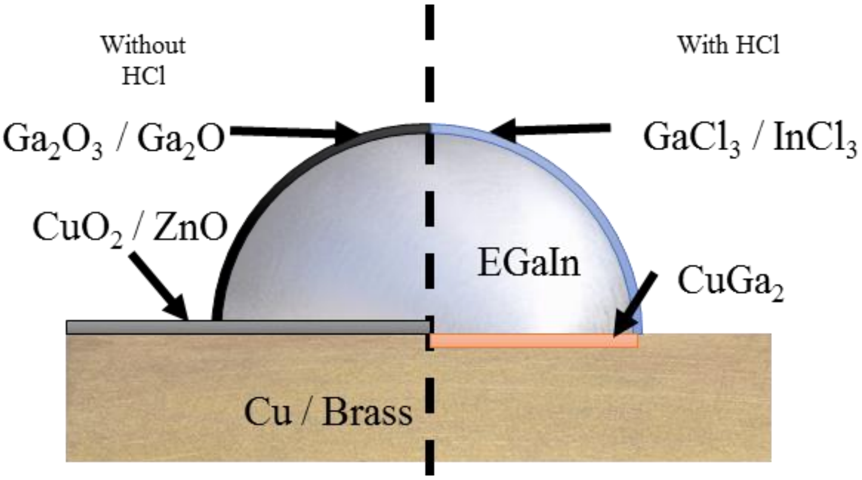

Figure I–30 Possible chemical compounds involved in the system alpha brass/EGaIn.

Without surface treatment, the liquid metal presents Ga_2O_3 and Ga_2O [86]; however, there is no In oxide since Ga is more reactive with oxygen that In [72], [87], [89]. Besides, pure copper presents CuO_2, while alpha brass presents CuO_2 and ZnO [67].

With an HCl surface treatment, the liquid metal may present chlorides on its surface [87], [90]. Also, since there is no oxide on the solid surface, there will be contact between the liquid and the solid, which allows the formation of the $CuGa_2$ intermetallic [72], [102]; in addition, there is no formation of the Cu_9Ga_4 intermetallic since the room temperature is far enough from the peritectic temperature [111].

Considering the tendencies of similar systems, some aspects of the behaviour of the alpha brasses in contact with the EGaIn can be inferred.

As for the Cu-30%Zn alloy embrittled by Ga, our system should present intergranular brittle cracking when there is LME [47]. Also, there should be a high dependence on the embrittlement with the stress state since the Cu-30%Zn/Ga presented embrittlement when testing notched tensile specimens, contrary to unnotched specimens [47]. Moreover, the embrittlement of the alpha brass by EGaIn may be similar to the embrittlement by Ga, although the In addition may increase the embrittlement's severity if our system follows the same tendency as beta brass [29].

As for the Cu/Hg and the Cu-40%Zn/Ga systems, larger grain sizes may increase the LME sensitivity [5], [47]. As for Cu-40%Zn/Ga, higher strain rates may increase the LME severity [21].

Similarly to the cases of Fe/Zn [4], En19 steel/Sn [38], and Cu/Sb [39], the intermetallic may play a role in the LME sensitivity of our system. Remarkably, the LME studies of Cu-Zn alloys in contact with Ga-based liquid alloys do not report any effect of the intermetallic in the LME sensitivity. Moreover, the passivating Ga-oxides should prevent any oxygen effect in the interface between the liquid EGaIn and the solid alpha brass once they have good contact.

The alpha brasses with higher Zn content are expected to present a higher LME sensitivity, as observed for the different Cu-base alloys, including Cu-Zn, which presented higher embrittlement by Hg at higher degrees of alloying [15]. Nonetheless, these systems have spontaneous liquid metal penetration, so our case may not follow the same tendency. However, the Zn alloying diminishes the stacking fault energy [60], and the diminution of the stacking fault energy relates to enhancing the LME of FCC alloys, such as Al [5].

I.5. References

[1] V. V. Popovich and I. G. Dmukhovskaya, “The embrittlement of metals and alloys being deformed in contact with low-melting alloys (a review of foreign literature),” *Sov. Mater. Sci.*, vol. 23, no. 6, pp. 535–544, 1988.

[2] M. H. Kamdar, “The occurrence of liquid-metal embrittlement,” *Phys. Status Solidi*, vol. 4, no. 1, pp. 225–233, 1971.

[3] T. Auger, J.-B. Vogt, and I. Proriol Serre, “Liquid Metal Embrittlement,” in *Mechanics - Microstructure - Corrosion Coupling*, vol. 25, Elsevier, 2019, pp. 507–534.

[4] M. H. Razmpoosh, C. DiGiovanni, Y. N. Zhou, and E. Biro, “Pathway to understand liquid metal embrittlement (LME) in Fe-Zn couple: From fundamentals toward application,” *Prog. Mater. Sci.*, vol. 121, p. 100798, Aug. 2021.

[5] M. G. Nicholas and C. F. Old, “Review Liquid metal embrittlement,” *J. Mater. Sci.*, vol. 14, pp. 1–18, 1979.

[6] D. G. Kolman, “A review of recent advances in the understanding of liquid metal

embrittlement," *Corrosion,* vol. 75, no. 1, pp. 42–57, 2019.

[7] K.-F. Nilsson and A. Hojna, "Overview of Mechanisms & Models for Liquid Metal Embrittlement and Future Directions," *Eur 29437 En,* pp. 1–26, 2018.

[8] S. P. Lynch, "Environmentally assisted cracking: Overview of evidence for an adsorption-induced localised-slip process," *Acta Metall.*, vol. 36, no. 10, pp. 2639–2661, Oct. 1988.

[9] V. Laporte, "Pénétration intergranulaire fragilisante du cuivre par le bismuth liquide : identification de la cinétique et du mécanisme de type diffusionnel entre 300 et 600 °C," Ecole Nationale Supérieure des Mines de Saint-Etienne; Université Jean Monnet - Saint-Etienne, 2005.

[10] K. Ina and H. Koizumi, "Penetration of liquid metals into solid metals and liquid metal embrittlement," *Mater. Sci. Eng. A,* vol. 387–389, no. 1-2 SPEC. ISS., pp. 390–394, 2004.

[11] B. Joseph, M. Picat, and F. Barbier, "Liquid metal embrittlement: A state-of-the-art appraisal," *EPJ Appl. Phys.*, vol. 5, no. 1, pp. 19–31, 1999.

[12] J. E. Norkett, M. D. Dickey, and V. M. Miller, "A Review of Liquid Metal Embrittlement: Cracking Open the Disparate Mechanisms," *Metall. Mater. Trans. A*, vol. 52, no. 6, pp. 2158–2172, Jun. 2021.

[13] A. Hojna and F. Di Gabriele, "On the kinetics of LME for the ferritic–martensitic steel T91 immersed in liquid PbBi eutectic," *J. Nucl. Mater.*, vol. 413, no. 1, pp. 21–29, Jun. 2011.

[14] J. Vogt, A. Verleene, I. Serre, F. Balbaud-Célérier, L. Martinelli, and A. Terlain, "Understanding the liquid metal assisted damage sources in the T91 martensitic steel for safer use of ADS," *Eng. Fail. Anal.*, vol. 14, no. 6, pp. 1185–1193, Sep. 2007.

[15] M. H. Kamdar, "Embrittlement by liquid metals," *Prog. Mater. Sci.*, vol. 15, no. 4, pp. 289–374, Jan. 1973.

[16] B. Joseph, F. Barbier, and M. Aucouturier, "Embrittlement of copper by liquid bismuth," *Scr. Mater.*, vol. 40, no. 8, pp. 893–897, 1999.

[17] T. Auger *et al.*, "Liquid metal embrittlement and deformation induced martensite: The

case of 316 L austenitic steel LME by liquid eutectic gallium-indium," *Corros. Sci.*, vol. 192, p. 109850, Nov. 2021.

[18] E. E. Glickman, *Multiscale Phenomena in Plasticity: From Experiments to Phenomenology, Modelling and Materials Engineering*. Dordrecht: Springer Netherlands, 2000.

[19] H. Lee *et al.*, "Microstructural evolution of liquid metal embrittlement in resistance-spot-welded galvanized TWinning-Induced Plasticity (TWIP) steel sheets," *Mater. Charact.*, vol. 147, pp. 233–241, Jan. 2019.

[20] J.-H. Kang, S.-H. Hong, J. Kim, and S.-J. Kim, "Zn-induced liquid metal embrittlement of galvanized high-Mn steel: Strain-rate dependency," *Mater. Sci. Eng. A*, vol. 793, p. 139996, Aug. 2020.

[21] P. J. . Fernandes and D. R. . Jones, "Specificity in liquid metal induced embrittlement," *Eng. Fail. Anal.*, vol. 3, no. 4, pp. 299–302, Dec. 1996.

[22] M. H. Kamdar, "Fracture in liquid metal environments," in *Fracture 84,* Elsevier, 1984, pp. 3851–3875.

[23] C. F. Old, "Liquid metal embrittlement of nuclear materials," *J. Nucl. Mater.*, vol. 92, no. 1, pp. 2–25, Aug. 1980.

[24] J. P. Hilditch, J. R. Hurley, P. Skeldon, and D. R. Tice, "The liquid metal embrittlement of iron and ferritic steels in sodium," *Corros. Sci.*, vol. 37, no. 3, pp. 445–454, Mar. 1995.

[25] A. R. C. Westwood and M. H. Kamdar, "Concerning liquid metal embrittlement, particularly of zinc monocrystals by mercury," *Philos. Mag.*, vol. 8, no. 89, pp. 787–804, May 1963.

[26] C. M. Preece and A. R. C. Westwood, "Temperature-Sensitive Embrittlement of FCC Metals by Liquid Metal Solutions," *Trans. ASM*, vol. 62, no. 2, pp. 418–425, 1969.

[27] A. R. C. Westwood, C. M. Preece, and M. H. Kamdar, "Adsorption-induced brittle fracture in liquid-metal environments," in *Engineering Fundamentals and Environmental Effects*, vol. 53, no. 9, Elsevier, 1971, pp. 589–644.

[28] I. Proriol Serre, J. B. Vogt, and N. Nuns, "ToF-SIMS investigation of absorption of lead and bismuth in T91 steel deformed in liquid lead bismuth eutectic," *Appl. Surf. Sci.*, vol.

471, pp. 36–42, 2019.

[29] M. M. Shea and N. S. Stoloff, “Embrittlement of beta-brass alloys by liquid metals and aqueous ammonia,” *Mater. Sci. Eng.*, vol. 12, no. 5–6, pp. 245–253, 1973.

[30] B. Long, Z. Tong, F. Gröschel, and Y. Dai, “Liquid Pb–Bi embrittlement effects on the T91 steel after different heat treatments,” *J. Nucl. Mater.*, vol. 377, no. 1, pp. 219–224, Jun. 2008.

[31] L. Vitos, J.-O. Nilsson, and B. Johansson, “Alloying effects on the stacking fault energy in austenitic stainless steels from first-principles theory,” *Acta Mater.*, vol. 54, no. 14, pp. 3821–3826, Aug. 2006.

[32] H. Nichols and W. Rostoker, “Ductile-brittle transition in alpha brass,” *Acta Metall.*, vol. 8, no. 12, pp. 848–850, 1960.

[33] I. G. Dmukhovskaya and V. V. Popovich, “Role of grain size in liquid-metal embrittlement of iron,” *Sov. Mater. Sci.*, vol. 16, no. 4, pp. 334–337, 1981.

[34] H. R. Tipler and D. McLean, “Influence of Interface Energy on Creep Rupture,” *Met. Sci. J.*, vol. 4, no. 1, pp. 103–107, 1970.

[35] E. É. Glikman, Y. V. Goryunov, V. M. Demin, and K. Y. Sarychev, “Kinetics and mechanism of copper fracture due to deformation in surface-active paths,” *Sov. Phys. J.*, vol. 19, no. 5, pp. 547–554, May 1976.

[36] S. P. Lynch, “Metal-induced embrittlement of materials,” *Mater. Charact.*, vol. 28, no. 3, pp. 279–289, 1992.

[37] P. Gordon and H. H. An, “The mechanisms of crack initiation and crack propagation in metal-induced embrittlement of metals,” *Metall. Trans. A*, vol. 13, no. 3, pp. 457–472, 1982.

[38] R. E. Clegg and D. R. H. Jones, “Liquid metal embrittlement of tensile specimens of En19 steel by tin,” *Eng. Fail. Anal.*, vol. 10, no. 1, pp. 119–130, 2003.

[39] E. E. Glikman and Y. V. Goryunov, “Mechanism of embrittlement by liquid metals and other manifestations of the Rebinder effect in metal systems,” *Sov. Mater. Sci.*, vol. 14, no. 4, pp. 355–364, 1979.

[40] A. Legris, G. Nicaise, J.-B. Vogt, J. Foct, D. Gorse, and D. Vançon, “Embrittlement of

a martensitic steel by liquid lead," *Scr. Mater.*, vol. 43, no. 11, pp. 997–1001, Nov. 2000.

[41] T. Auger, I. Serre, G. Lorang, Z. Hamouche, D. Gorse, and J.-B. Vogt, "Role of oxidation on LME of T91 steel studied by small punch test," *J. Nucl. Mater.*, vol. 376, no. 3, pp. 336–340, Jun. 2008.

[42] M. H. Kamdar, "Liquid Metal Embrittlement," *Treatise Mater. Sci. Technol.*, vol. 25, pp. 361–459, 1983.

[43] P. Gordon, "Metal-Induced embrittlement of metals-an evaluation of embrittler transport mechanisms," *Metall. Trans. A*, vol. 9, no. 2, pp. 267–273, 1978.

[44] S. P. Lynch, "Failures of structures and components by metal-induced embrittlement," in *Stress Corrosion Cracking*, Elsevier, 2011, pp. 714–748.

[45] I. Proriol Serre and J.-B. Vogt, "Mechanical behavior in liquid lead of Al2O3 coated 15-15Ti steel and an Alumina-Forming Austenitic steel designed to mitigate their corrosion," *Eng. Fail. Anal.*, vol. 139, p. 106443, 2022.

[46] E. É. Glikman, Y. V. Goryunov, V. M. Demin, and K. Y. Sarychev, "Kinetics and mechanism of copper fracture during deformation in surface-active baths," *Sov. Phys. J.*, vol. 19, no. 7, pp. 839–843, Jul. 1976.

[47] P. J. L. Fernandes and D. R. H. Jones, "The effects of microstructure on crack initiation in liquid-metal environments," *Eng. Fail. Anal.*, vol. 4, no. 3, pp. 195–204, 1997.

[48] C. Ye, J.-B. Vogt, and I. Proriol Serre, "Liquid metal embrittlement of the T91 steel in lead bismuth eutectic: The role of loading rate and of the oxygen content in the liquid metal," *Mater. Sci. Eng. A*, vol. 608, pp. 242–248, Jul. 2014.

[49] E. E. Glickman, "Grain Boundary Grooving Accelerated by Local Plasticity as a Possible Mechanism of Liquid Metal Embrittlement," *Interface Sci.*, vol. 11, no. 4, pp. 451–459, 2003.

[50] A. Hojná, F. Di Gabriele, J. Klecka, and J. Burda, "Behaviour of the steel T91 under uniaxial and multiaxial slow loading in contact with liquid lead," *J. Nucl. Mater.*, vol. 466, pp. 292–301, 2015.

[51] P. A. Rebinder and E. D. Shchukin, "Surface phenomena in solids during the course of their deformation and failure," *Sov. Phys. Uspekhi*, vol. 15, no. 5, pp. 533–554, May

1973.

[52] W. M. Robertson, “Propagation of a Crack Filled with Liquid Metal,” *Trans. Metall. Soc. AIME*, vol. 236, no. 10, pp. 1478–1482, 1966.

[53] E. E. Glickman, “Dissolution Condensation Mechanism of Stress Corrosion Cracking in Liquid Metals: Driving Force and Crack Kinetics,” *Metall. Mater. Trans. A*, vol. 42, no. 2, pp. 250–266, Feb. 2011.

[54] N. S. Stoloff and T. L. Johnston, “Crack propagation in a liquid metal environment,” *Acta Metall.*, vol. 11, no. 4, pp. 251–256, 1963.

[55] V. V. Popovich and I. G. Dmukhovskaya, “Rebinder effect in the fracture of Armco iron in liquid metals,” *Sov. Mater. Sci.*, vol. 14, no. 4, pp. 365–370, 1979.

[56] D. E. Tyler and W. T. Black, “Introduction to Copper and Copper Alloys,” in *Properties and Selection: Nonferrous Alloys and Special-Purpose Materials*, ASM International, 1990, pp. 216–240.

[57] P. Poupeau, “Diagrammes d’équilibre d’alliages binaires,” *Techniques de l’ingénieur - M 70p1*. pp. 1–111, 1987.

[58] W. Ozgowicz, E. Kalinowska-Ozgowicz, and B. Grzegorczyk, “The microstructure and mechanical properties of the alloy CuZn30 after recrystallizion annealing,” *J.Amme*, vol. 40, no. 1, pp. 15–24, 2010.

[59] R. Le Hazif, P. Dorizzi Et, and J. . Poirier, “Glissement {110} 〈110〉 dans les metaux de structure cubique a faces centrees,” *Acta Metall.*, vol. 21, no. 7, pp. 903–911, Jul. 1973.

[60] G. Gottstein, M. Goerdeler, and G. V. S. S. Prasad, “Mechanical Properties: Plastic Behavior,” in *Encyclopedia of Condensed Matter Physics*, Elsevier, 2005, pp. 298–305.

[61] A. Rohatgi, K. S. Vecchio, and G. T. Gray, “The influence of stacking fault energy on the mechanical behavior of Cu and Cu-al alloys: Deformation twinning, work hardening, and dynamic recovery,” *Metall. Mater. Trans. A Phys. Metall. Mater. Sci.*, vol. 32, no. 1, pp. 135–145, 2001.

[62] E. El-Danaf, S. R. Kalidindi, and R. D. Doherty, “Influence of grain size and stacking-fault energy on deformation twinning in fcc metals,” *Metall. Mater. Trans. A Phys.*

Metall. Mater. Sci., vol. 30, no. 5, pp. 1223–1233, 1999.

[63] Y. H. Zhao, X. Z. Liao, Y. T. Zhu, Z. Horita, and T. G. Langdon, “Influence of stacking fault energy on nanostructure formation under high pressure torsion,” *Mater. Sci. Eng. A*, vol. 410–411, pp. 188–193, 2005.

[64] R. D. Bert Verlinden, Julian Driver, Indradev Samajdar, *Thermo-Mechanical Processing of Metallic Materials*, 1st ed. Elsevier Ltd, 2007.

[65] J. Li, J. W. Mayer, and E. G. Colgan, “Oxidation and protection in copper and copper alloy thin films,” *J. Appl. Phys.*, vol. 70, no. 5, pp. 2820–2827, Sep. 1991.

[66] P. Qiu and C. Leygraf, “Initial oxidation of brass induced by humidified air,” *Appl. Surf. Sci.*, vol. 258, no. 3, pp. 1235–1241, Nov. 2011.

[67] S. Maroie, R. Caudano, and J. Verbist, “The oxidation of the α and β phases of brass studied by XPS and nuclear reaction spectroscopy,” *Surf. Sci.*, vol. 100, no. 1, pp. 1–13, Oct. 1980.

[68] N. Habbache, N. Alane, S. Djerad, and L. Tifouti, “Leaching of copper oxide with different acid solutions,” *Chem. Eng. J.*, vol. 152, no. 2–3, pp. 503–508, 2009.

[69] J. Colombeau, T. Auger, D. Johnson, and L. Wang, “Cu Grain Boundary Embrittlement by Liquid Hg: A Comparison between Experiment and ab-initio Modeling,” *MRS Proc.*, vol. 1515, pp. mrsf12-1515-ii12-05, Oct. 2013.

[70] J. Froemel, M. Baum, M. Wiemer, and T. Gessner, “Low-Temperature Wafer Bonding Using Solid-Liquid Inter-Diffusion Mechanism,” *J. Microelectromechanical Syst.*, vol. 24, no. 6, pp. 1973–1980, Dec. 2015.

[71] S. Liu, K. Sweatman, S. McDonald, and K. Nogita, “Ga-based alloys in microelectronic interconnects: A review,” *Materials (Basel).*, vol. 11, no. 8, pp. 1–20, 2018.

[72] M. D. Dickey, R. C. Chiechi, R. J. Larsen, E. A. Weiss, D. A. Weitz, and G. M. Whitesides, “Eutectic gallium-indium (EGaIn): A liquid metal alloy for the formation of stable structures in microchannels at room temperature,” *Adv. Funct. Mater.*, vol. 18, no. 7, pp. 1097–1104, 2008.

[73] K. Ling, H. K. Kim, M. Yoo, and S. Lim, “Frequency-switchable metamaterial absorber injecting eutectic gallium-indium (EGaIn) liquid metal alloy,” *Sensors (Switzerland)*,

vol. 15, no. 11, pp. 28154–28165, 2015.

[74] P. Geddis, L. Wu, A. McDonald, S. Chen, and B. Clements, "Effect of static liquid Galinstan on common metals and non-metals at temperatures up to 200 °C," *Can. J. Chem.*, vol. 98, no. 12, pp. 787–798, Dec. 2020.

[75] Q. Xu, N. Oudalov, Q. Guo, H. M. Jaeger, and E. Brown, "Effect of oxidation on the mechanical properties of liquid gallium and eutectic gallium-indium," *Phys. Fluids*, vol. 24, no. 6, p. 063101, Jun. 2012.

[76] H. Song, T. Kim, S. Kang, H. Jin, K. Lee, and H. J. Yoon, "Ga- Based Liquid Metal Micro/Nanoparticles: Recent Advances and Applications," *Small*, vol. 16, no. 12, p. 1903391, Mar. 2020.

[77] S. Liu *et al.*, "Properties of CuGa2 Formed Between Liquid Ga and Cu Substrates at Room Temperature," *J. Electron. Mater.*, vol. 49, no. 1, pp. 128–139, 2020.

[78] S. J. French, D. J. Saunders, and G. W. Ingle, "The system gallium-indium," *J. Phys. Chem.*, vol. 42, no. 1, pp. 265–274, Feb. 1938.

[79] T. . Anderson and I. Ansara, "The Ga-In (Gallium-Indium) System," *J. Phase Equilibria*, vol. 12, no. 1, pp. 64–72, Feb. 1991.

[80] D. Zrnic and D. S. Swatik, "On the resistivity and surface tension of the eutectic alloy of gallium and indium," *J. Less Common Met.*, vol. 18, no. 1, pp. 67–68, May 1969.

[81] T. Liu, P. Sen, and C. J. Kim, "Characterization of liquid-metal Galinstan® for droplet applications," *Proc. IEEE Int. Conf. Micro Electro Mech. Syst.*, pp. 560–563, 2010.

[82] Y. Plevachuk, V. Sklyarchuk, G. Gerbeth, S. Eckert, and R. Novakovic, "Surface tension and density of liquid Bi–Pb, Bi–Sn and Bi–Pb–Sn eutectic alloys," *Surf. Sci.*, vol. 605, no. 11–12, pp. 1034–1042, Jun. 2011.

[83] M. C. Wilkinson, "Surface properties of mercury," *Chem. Rev.*, vol. 72, no. 6, pp. 575–625, Dec. 1972.

[84] R. C. Chiechi, E. A. Weiss, M. D. Dickey, and G. M. Whitesides, "Eutectic gallium-indium (EGaIn): A moldable liquid metal for electrical characterization of self-assembled monolayers," *Angew. Chemie - Int. Ed.*, vol. 47, no. 1, pp. 142–144, 2008.

[85] M. J. Regan *et al.*, "X-ray study of the oxidation of liquid-gallium surfaces," *Phys. Rev.*

B, vol. 55, no. 16, pp. 10786–10790, Apr. 1997.

[86] F. Scharmann *et al.*, “Viscosity effect on GaInSn studied by XPS,” *Surf. Interface Anal.*, vol. 36, no. 8, pp. 981–985, Aug. 2004.

[87] K. Doudrick *et al.*, “Different Shades of Oxide: From Nanoscale Wetting Mechanisms to Contact Printing of Gallium-Based Liquid Metals,” *Langmuir*, vol. 30, no. 23, pp. 6867–6877, Jun. 2014.

[88] M. F. Dumke, T. A. Tombrello, R. A. Weller, R. M. Housley, and E. H. Cirlin, “Sputtering of the gallium-indium eutectic alloy in the liquid phase,” *Surf. Sci.*, vol. 124, no. 2–3, pp. 407–422, Jan. 1983.

[89] H. Tostmann, O. Shpyrko, P. S. Pershan, E. Dimasi, B. Ocko, and M. Deutsch, “Surface Structure of Liquid Metals and the Effect of Capillary Waves: X-ray Studies on Liquid Indium,” *Phys. Rev. B*, vol. 59, no. 2, p. 9, Jun. 2004.

[90] D. Kim *et al.*, “Recovery of nonwetting characteristics by surface modification of gallium-based liquid metal droplets using hydrochloric acid vapor,” *ACS Appl. Mater. Interfaces*, vol. 5, no. 1, pp. 179–185, 2013.

[91] J. Tang, X. Zhao, J. Li, Y. Zhou, and J. Liu, “Liquid Metal Phagocytosis: Intermetallic Wetting Induced Particle Internalization,” *Adv. Sci.*, vol. 4, no. 5, p. 1700024, May 2017.

[92] Y. G. Deng and J. Liu, “Corrosion development between liquid gallium and four typical metal substrates used in chip cooling device,” *Appl. Phys. A Mater. Sci. Process.*, vol. 95, no. 3, pp. 907–915, 2009.

[93] P. R. Luebbers and O. K. Chopra, “Compatibility of ITER candidate materials with static gallium,” in *Proceedings of 16th International Symposium on Fusion Engineering*, vol. 1, pp. 232–235.

[94] Ž. Marinković and V. Simić, “Comparative analysis of interdiffusion in some thin film metal couples at room temperature,” *Thin Solid Films*, vol. 217, no. 1–2, pp. 26–30, Sep. 1992.

[95] J. Fromel, Y.-C. Lin, M. Wiemer, T. Gessner, and M. Esashi, “Low temperature metal interdiffusion bonding for micro devices,” in *2012 3rd IEEE International Workshop on Low Temperature Bonding for 3D Integration*, 2012, vol. 217, no. 1–2, pp. 163–163.

[96] H. Kolb, R. Sottong, T. Dasgupta, E. Mueller, and J. de Boor, “Evaluation of Detachable Ga-Based Solder Contacts for Thermoelectric Materials,” *J. Electron. Mater.*, vol. 46, no. 8, pp. 5057–5063, Aug. 2017.

[97] S. Sommadossi, H. E. Troiani, and A. Fernández Guillermet, “Diffusion soldering using a Gallium metallic paste as solder alloy: study of the phase formation systematics,” *J. Mater. Sci.*, vol. 42, no. 23, pp. 9707–9712, Sep. 2007.

[98] E. M. Okamoto, H. and Schlesinger, M.E. and Mueller, *Alloy Phase Diagrams*. ASM International, 2016.

[99] Z. Bahari, E. Dichi, B. Legendre, and J. Dugué, “The equilibrium phase diagram of the copper-indium system: A new investigation,” *Thermochim. Acta*, vol. 401, no. 2, pp. 131–138, 2003.

[100] M. Purwins *et al.*, “Phase relations in the ternary Cu–Ga–In system,” *Thin Solid Films*, vol. 515, no. 15, pp. 5895–5898, May 2007.

[101] C. P. Muzzillo, C. E. Campbell, and T. J. Anderson, “Cu–Ga–In thermodynamics: experimental study, modeling, and implications for photovoltaics,” *J. Mater. Sci.*, vol. 51, no. 7, pp. 3362–3379, Apr. 2016.

[102] Y. Cui *et al.*, “Metallic Bond-Enabled Wetting Behavior at the Liquid Ga/CuGa2 Interfaces,” *ACS Appl. Mater. Interfaces*, vol. 10, no. 11, pp. 9203–9210, 2018.

[103] B. Yuan *et al.*, “Liquid Metal Machine Triggered Violin- Like Wire Oscillator,” *Adv. Sci.*, vol. 3, no. 10, p. 1600212, Oct. 2016.

[104] A. I. Ancharov, T. F. Grigoryeva, A. P. Barinova, and V. V. Boldyrev, “Interaction between copper and gallium,” *Russ. Metall.*, vol. 2008, no. 6, pp. 475–479, Dec. 2008.

[105] A. I. Ancharov, T. F. Grigorieva, S. V. Tsybulya, and V. V. Boldyrev, “Chemical interaction of Cu-In, Cu-Sn, and Cu-Bi solid solutions with liquid Ga-In and Ga-Sn eutectics,” *Inorg. Mater.*, vol. 42, no. 10, pp. 1058–1064, Oct. 2006.

[106] A. I. Ancharov, T. F. Grigoriyeva, S. V. Tsybulya, and V. V. Boldyrev, “Interaction of copper-based solid solutions with liquid gallium eutectics,” *Russ. Metall.*, vol. 2006, no. 2, pp. 143–146, 2006.

[107] T. F. Grigor’eva, A. I. Ancharov, A. P. Barinova, S. V. Tsybulya, and N. Z. Lyakhov,

"Structural transformations in mechanochemical synthesis of solid solutions in the Cu-Ga system," *Russ. J. Appl. Chem.*, vol. 82, no. 5, pp. 779–782, May 2009.

[108] T. F. Grigor'Eva, S. A. Kovaleva, A. P. Barinova, P. A. Vityaz', and N. Z. Lyakhov, "Study of the interaction of mechanochemically produced cu-in solid solutions with liquid gallium and of the structure of metallic cements on their basis," *Phys. Met. Metallogr.*, vol. 111, no. 1, pp. 45–52, 2011.

[109] O. I. Tikhomirova, M. V. Pikunov, L. P. Ruzinov, and I. D. Marchukova, "Interaction of liquid gallium with copper," *Sov. Mater. Sci.*, vol. 5, no. 6, pp. 586–590, 1972.

[110] S. Lin, H. Chang, C. Cho, Y. Liu, and Y. Kuo, "Formation of solid-solution Cu-to-Cu joints using Ga solder and Pt under bump metallurgy for three-dimensional integrated circuits," *Electron. Mater. Lett.*, vol. 11, no. 4, pp. 687–694, Jul. 2015.

[111] S. Lin, C. Cho, and H. Chang, "Interfacial Reactions in Cu/Ga and Cu/Ga/Cu Couples," *J. Electron. Mater.*, vol. 43, no. 1, pp. 204–211, Jan. 2014.

[112] C.-H. Chen, B.-H. Lee, H.-C. Chen, C.-M. Wang, and A. T. Wu, "Interfacial Reactions of Low-Melting Sn-Bi-Ga Solder Alloy on Cu Substrate," *J. Electron. Mater.*, vol. 45, no. 1, pp. 197–202, Jan. 2016.

[113] A. A. Mikheev *et al.*, "Kinetics and products of interaction of zinc-containing gallium pastes–solders," *Weld. Int.*, vol. 36, no. 5, pp. 314–315, May 2022.

[114] S.-J. Hong and C. Suryanarayana, "Mechanism of low-temperature θ-CuGa2 phase formation in Cu-Ga alloys by mechanical alloying," *J. Appl. Phys.*, vol. 96, no. 11, pp. 6120–6126, Dec. 2004.

[115] J. Tang, X. Zhao, J. Li, R. Guo, Y. Zhou, and J. Liu, "Gallium-Based Liquid Metal Amalgams: Transitional-State Metallic Mixtures (TransM2ixes) with Enhanced and Tunable Electrical, Thermal, and Mechanical Properties," *ACS Appl. Mater. Interfaces*, vol. 9, no. 41, pp. 35977–35987, 2017.

[116] J. T. Lukowski, D. B. Kasul, L. A. Heldt, and C. L. White, "Discontinuous crack propagation in Ga induced liquid metal embrittlement of β-brass," *Scr. Metall. Mater.*, vol. 24, no. 10, pp. 1959–1964, 1990.

[117] C. F. Old and P. Trevena, "Reaction in copper-lithium system and its implications for liquid-metal embrittlement," *Met. Sci.*, vol. 15, no. 7, pp. 281–286, Jul. 1981.

[118] N. Tsutsui and H. Koizumi, “Intergranular/transgranular fracture in the liquid metal embrittlement of polycrystalline zinc,” *Procedia Struct. Integr.*, vol. 13, pp. 849–854, 2018.

[119] C. F. Old and P. Trevena, “Embrittlement of zinc by liquid metals,” *Met. Sci.*, vol. 13, no. 8, pp. 487–495, Aug. 1979.

[120] P. H. Au-Yeung, J. T. Lukowski, L. A. Heldt, and C. L. White, “An auger spectrometric study of the crack tip surface chemistry for liquid metal embrittlement: Beta brass embrittled by gallium,” *Scr. Metall. Mater.*, vol. 24, no. 1, pp. 95–100, 1990.

[121] H. Ichinose, “A Simple Evaluation of Grain Boundary Diffusion in Liquid Metal Embrittlement,” *Trans. Japan Inst. Met.*, vol. 7, no. 1, pp. 56–58, 1966.

[122] F. A. Shunk and W. R. Warke, “Specificity as an aspect of liquid metal embrittlement,” *Scr. Metall.*, vol. 8, no. 5, pp. 519–526, May 1974.

II. The interface between alpha brasses and the EGaIn

This chapter shows the study on the interface between the alpha brasses with different Zn content and the liquid eutectic Ga-In (EGaIn). First, there is a short description of the concept of wetting, followed by the results on the measurement of the wetting of the alpha brasses with different Zn contents by the liquid EGaIn. Finally, the chapter shows the characterization of the intermetallic that forms whenever the alpha brasses and the EGaIn enter into contact.

II.1. Wetting of Cu and Cu-Zn alloys by the EGaIn

As exposed in the previous chapter, an essential aspect of liquid metal embrittlement (LME) is the contact between liquid metal and solid metal. Indeed, good contact is considered a necessary condition for LME to occur, hence the necessity of its assessment.

To quantify the contact quality between a liquid and a solid, a numerical value named Young contact angle describes how well a liquid wets a surface.

II.1.1. Wetting and the Young contact angle

Let us consider a system in equilibrium composed of a solid, a liquid, and a vapour. The liquid experiences adhesive forces that favour its spreading on the solid. At the same time, cohesive forces within the liquid resist the spreading of the drop [1].

Figure II–1 represents the system in equilibrium and shows three interfacial tensions. The three phases intersect in a line referred to as the triple line. In the triple line, the solid-liquid and the liquid-vapour interfacial tensions form an angle. This angle is called the Young contact angle or simply the contact angle.

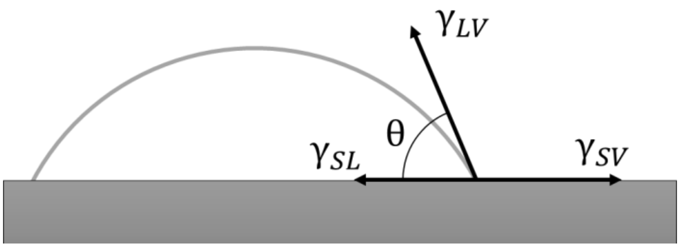

Figure II–1 Representation of the equilibrium between three distinct phases: solid (S), liquid (L), and vapour (V).

Equation (10) describes the relationship between interfacial tensions and the Young contact angle.

$$\gamma_{SV} = \gamma_{SL} + \gamma_{LV} cos\theta_{eq} \tag{10}$$

where γ_{SV}, γ_{SL}, and γ_{LV} correspond to the interfacial tensions between solid/vapour, solid/liquid, and liquid/vapour, respectively. This equation is valid only in equilibrium; hence the angle θ_{eq} refers to a Young contact angle at equilibrium.

Equation (10) has the practical limitation that the values of the interfacial tensions on the solid surfaces are impossible to be measured directly [2]. Still, the Young contact angle allows the characterization of the wetting capacity of a liquid over a solid, mainly since its value directly indicates how much the liquid spreads on the solid. According to the contact angle values, the wetting capacity can be categorized into four regimes, Figure II–2 schematizes these regimes.

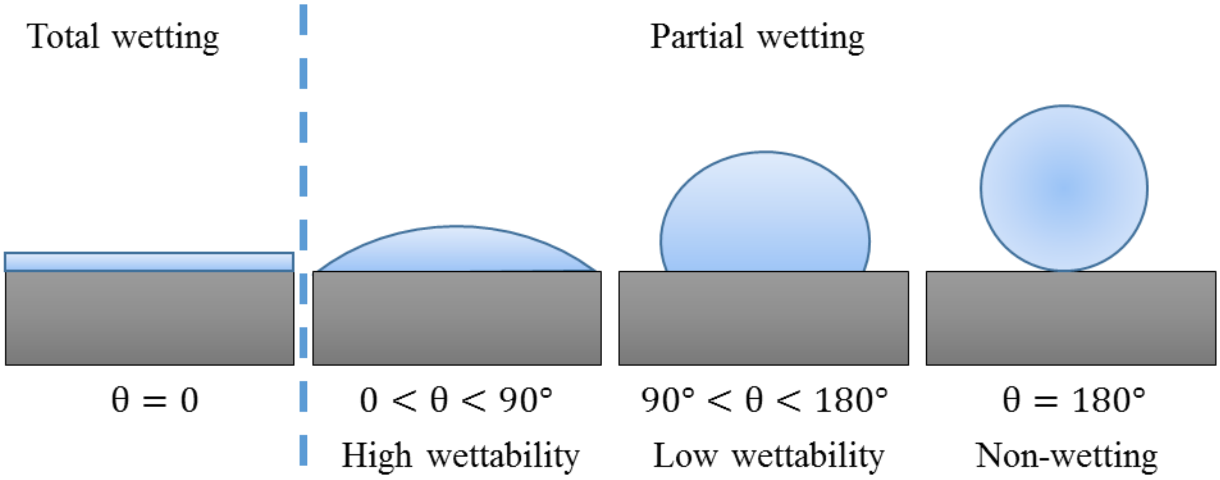

Figure II–2 Different wetting regimes according to the contact angle value.

Therefore, measuring the contact angle is often necessary to evaluate the contact quality between a liquid and a solid.

II.1.1.1. Young contact angle measurements

Due to its simplicity, the sessile drop technique is the most widely used method to measure the Young contact angle. This method works by placing a drop of liquid over a solid surface and measuring the contact angle using a camera and a light source. The camera must be placed horizontally with the solid/liquid and the light source. The last is a critical element since the drop should not reflect any straight light, the picture's background must be homogeneous, and the baseline of the drop must be easily identified [1]. Figure II–3 schematizes the typical arrangement for the sessile drop method.

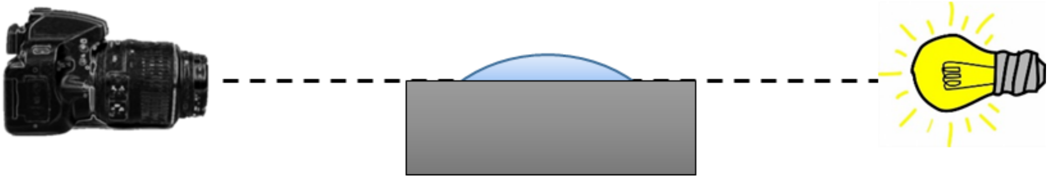

Figure II–3 Typical arrangement for the static sessile drop method.

With the image taken, the contact angle is measured using a goniometer or by using an image analyzing software such as ImageJ or MatLab [1], [3]–[5]. Nowadays, several built-in instruments work with the same principle in a standardized manner, including their image-analyzing software. The software often calculates the contact angle by fitting a function to the shape of the drop that is commonly a polynomial-type function; however, this type of function does not have a physical sense, unlike the use of a circle best-fit [5]–[7].

Another common technique, the Wilhelmy method, involves a balance of the forces involved when a simple solid (rod, plate, or other) is dipped into the liquid [8]. This method requires reliable force measurements to calculate a "synthetic" contact angle and has the advantage of diminishing errors due to measurement subjectivity [9].

There are other more complex techniques based on the study of the dynamics of the drop, e.g., dispensing a drop and analyzing its shape from the departure from the needle until it achieves equilibrium [3], [10], [11]. Other alternative static methods exist but have not been significantly used [12], [13].

Due to its simplicity and practicality, the sessile drop method is used in this work.

II.1.1.2. Contact angle hysteresis

The previous formulation of the contact angle considers an equilibrium corresponding to an ideal, smooth, homogeneous, rigid, and isotropic surface [2]. In reality, there is often a range of possible angles; this variation is known as the contact angle hysteresis and is related to the pin of the triple line.

When a drop is in motion, e.g., when posing the drop at the beginning of the sessile technique, the contact angle will vary or not in function of the rate of the triple line. When the liquid-vapour interface moves, the contact angle will not change if the triple line moves freely at the same rate. In contrast, if the triple line pins to a defect and does not move, the contact angle will change, exhibiting contact angle hysteresis [14].

The possible pinning defects are often related to roughness and chemical heterogeneity [15], [16]. Other physical defects such as holes, pores, and scratches also prevent the movement of the triple line. Likewise, oxygen can generate variations in the contact angle due to the creation of oxide skins on the liquid and the solid metal [15].

When the liquid is spreading, there is an advancing contact angle (θ_a); in the opposite case, when the liquid moves inwards or retreats, there is a receding angle (θ_r). By definition, the hysteresis is the difference between these angles, and it is always true that $\theta_a \geq \theta_{eq} \geq \theta_r$ [15].

II.1.1.3. Reactive wetting

During wetting, the interaction between the phases could lead to reactions that modify the wetting behaviour of the liquid. If this is the case, there can be a formation of a continuous layer of the reaction product between the liquid and the solid, the triple line can coincide with the end of the product layer, or the product layer could be found further from the liquid [17]. Figure II–4(a) and (b) schematize both possibilities.

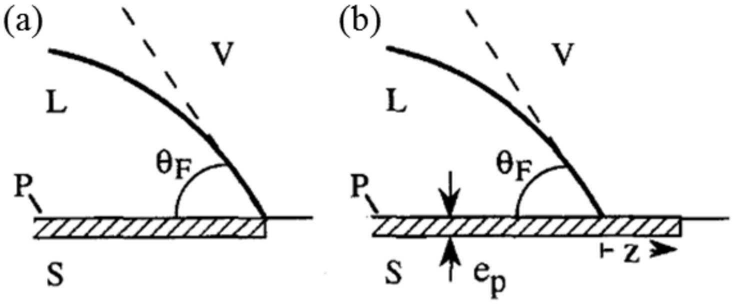

Figure II–4 Possible states of the triple line in reactive wetting [17].

In the first case, it is possible to write a variation of the Young contact angle formula (above written in Eq. (10) by including the corresponding surface tension of the interface between the product and the liquid (γ_{PL}), resulting in Eq. (11):

$$\gamma_{SV} = \gamma_{PL} + \gamma_{LV} cos\theta_{eq} \tag{11}$$

Similarly, Eq. (12) describes the second state by including the product-vapour surface tension (γ_{PV}):

$$\gamma_{PV} = \gamma_{PL} + \gamma_{LV} cos\theta_{eq} \tag{12}$$

Some works report that in reactive wetting, there is no sign of a long-lasting time dependence on the contact angle since the equilibrium contact angle is reached rapidly (in less than 30 seconds) [18]–[20]. In other studies, there are comparisons of systems where the equilibrium occurs almost instantaneously and others that take thousands of seconds or days to reach equilibrium [6], [17].

II.1.1.4. Measurements of contact angle on liquid metals

Few works couple the Young contact angle with the occurrence of LME [21]–[23]. Beyond LME, some other studies present the wetting properties of liquid metals over solid metals [10], [15], [16], [24]–[26], including some works which include some or more elements that attain our current study, i.e., Cu, Zn, Ga and In [6], [19], [20], [27]. Table II–1 lists some relevant results.

Table II–1 Contact angles of Ga-based liquid over different solids and conditions.

Liquid	**Solid**	**Contact angle (°)**	**Temperature (°C)**	**Observations**	**Reference**
Ga	Cu	134	37	In 1M NaOH	[19]
		69		In 1M HCl	
	$CuGa_2$	16		In 1M NaOH	
		14		In 1M HCl	
EGaIn	Si	162	Room temperature	Sputtered with In 10min	[6]
	In foil	140		-	
	Si foil	135		-	
Galinstan	Si	160		Sputtered with In 10min	
	In foil	145		-	
	Si foil	145		-	
EGaIn	Cu	51	Room temperature	In 1M HCl	[27]
	Cu	42		In 0.1M NaCl and 2.0 V	
	Cu	36		In 1M NaOH	
Ga	Glass	148	50	In 0.01M HCl	[20]
		169		In 0.1M HCl	
		180		In 1M HCl	

In the study of Cui et al., there are measurements of the contact angle of Ga droplets on Cu and $CuGa_2$ substrates [19], shown in Figure II–5. They performed the experiments at room temperature and immersed the system in HCl or NaOH during the sessile drop test. Still, they found that Ga wetting behaviour is better on $CuGa_2$ and speculated that the metallic bond induces the wetting force between Ga and $CuGa_2$. However, they did not explain how they obtained a coarse layer of $CuGa_2$ to test the wetting; if they did it by simple reaction without any further surface treatment, the roughness of the intermetallic could have played a role in the contact angle measured. Nevertheless, another study also reported the affinity of the liquid metal to the reaction product in the system Cu/Ga [28].

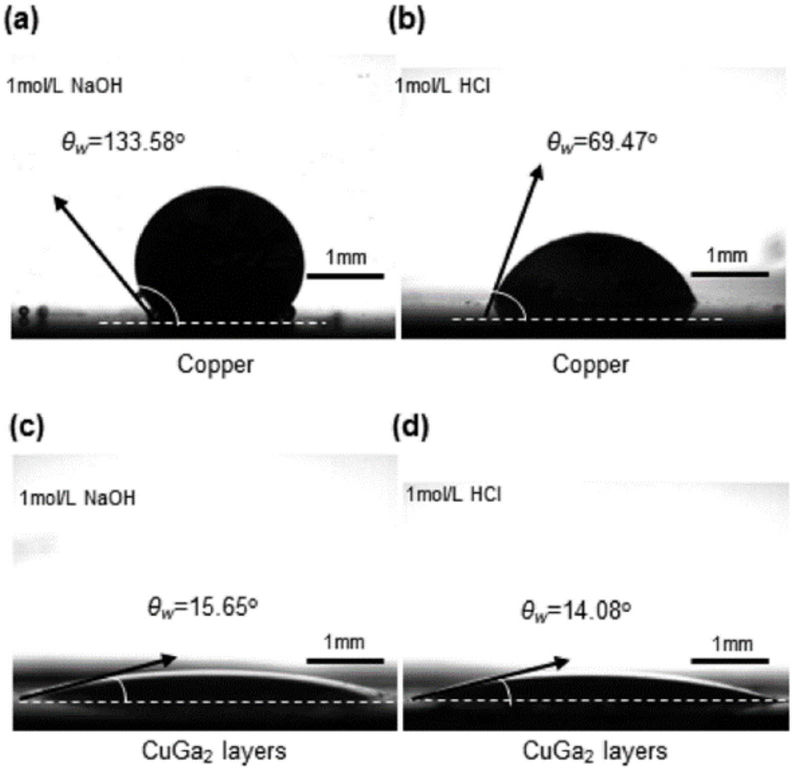

Figure II–5 Static contact angles of the Ga droplets under different excitations at 37 °C. (a) Copper substrate in NaOH solution. (b) Copper substrate in HCl solution. (c) $CuGa_2$ *substrate in NaOH solution. (d)* $CuGa_2$ *substrate in HCl solution* [19].

Some general tendencies exist regarding the wetting behaviour of liquid metals. For example, in millimetre-size drops, the spreading time is less than 1s if there is no reaction with the substrate [17]. Also, liquid metals wet metallic and semi-metallic solids with contact angles lower than 60°, while they wet oxides with contact angles higher than 100° [14].

Additionally, several authors have studied the effect of the oxide on the wetting capacity of Ga-base alloys. For instance, Xu et al. observed that when they dissolved the oxide film with HCl acid, the contact angle between EGaIn/glass and Ga/glass increased, implying that bulk EGaIn or Ga does not wet the glass [20]. Figure II–6 illustrates this behaviour.

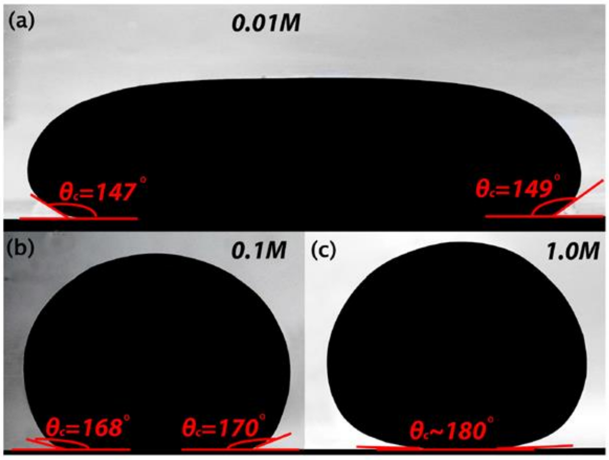

Figure II–6 Measurement of the contact angle θc for droplets of Ga on a glass surface submerged at different HCl concentrations [20].

Also, they pressed down the drops with a spoon and observed that the drops returned to the spherical shape after removing the external force only at HCl concentrations > 0.2 M; below that concentration, the drop did not bounce back, and hence the contact angle varied significantly in repeated measurements [20].

Similarly, Kim et al. proposed an HCl vapour treatment to promote the non-wetting capacity of Ga-based alloys over glasses (section I.2.2.1 details the treatment) [29]. Figure II–7 shows the effects of this HCl vapour treatment in Galinstan on different substrates.

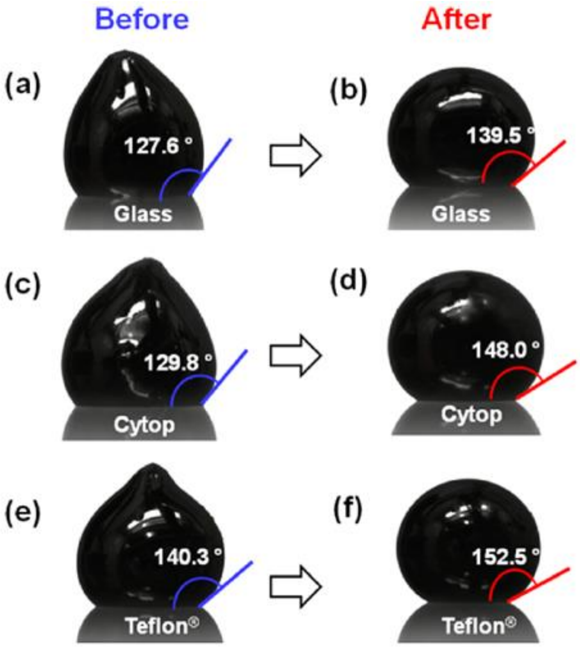

Figure II–7 Contact angle of Galinstan droplets on (a, b) a bare glass slide, (c, d) Cytop-coated glass slide, and (e, f) Teflon-coated glass slide, before (panels a, c, and e) and after (panels b, d, and f) the HCl vapour treatment [29].

II.1.2. Wetting of Cu-Zn alloys by the EGaIn

To measure the contact angle between the liquid EGaIn and the different solids, a Krüss DSA100 drop analyzer was used. Experiments were carried out in different conditions to study two main aspects of the wetting between the EGaIn and the solids: the effect of the oxidized surface and the effect of the Zn content in the solid. All experiments were carried out at room temperature.

The EGaIn used in this work was prepared using 99,99 wt.% pure Ga supplied by Mining & Chemical Products and 99,99 wt.% pure In supplied by Alfa Aesar. For this, a hot plate was used to heat water in a beaker to approximately 80 °C. Then, the bottle containing Ga was introduced in the beaker for it to heat enough so Ga melts. Liquid Ga was then poured into a ceramic crucible. The corresponding quantity of In was added at room temperature into the crucible to form the EGaIn composition (24.5 wt.%In). Finally, the ensemble was mixed until obtaining a homogeneous liquid EGaIn.

A plastic syringe without a needle was used to extract the liquid from the crucible for its use. A RAININ micropipette with a capacity of 2-20 µL was used to depose drops of the EGaIn in a controlled manner.

Three commercial metals and alloys were used in this study, oxygen-free high thermal conductivity (OFHC) Cu, Cu-15 wt.%Zn, and Cu-30 wt.%Zn, which were supplied in sheet form by Goodfellow, Wieland, and Alfa Aesar, respectively. In addition, the Cu-20 wt.%Zn and Cu-25 wt.%Zn were also studied; these were produced in the Institut de Chimie et des Matériaux Paris-Est (ICMPE) by using an induction furnace to melt 99.99 wt.% purity Cu and 99.95 wt.% purity Zn in a glassy carbon crucible to produce cylinders, which were then cross-rolled.

The solid samples tested in these experiments were metallographically prepared using SiC abrasive paper and diamond paste of 6, 3, and 1 µm. A Bruker Contour GT-K 3D Optical Microscope was used to consider a possible effect of the roughness of the sample on the wetting behaviour. The roughness was measured by calculating the average of the absolute values of the profile heights (Ra) [30]. This value was consistently below 20 nm for all of the samples.

The open-source image processing package FIJI and the Contact Angle plugin were used to measure the contact angle [5], [31]. To use this plugin, the image of the drop taken by the drop analyzer is open in FIJI. Manually, two points were chosen to define the baseline, and then several points of the interface liquid-vapour were selected. Finally, the plugin calculates the ellipse best fit and gives the values for the left and right contact angles.

Like in Figure II–7, a protuberance is present in some of the EGaIn drops, which is a consequence of the oxidation of the liquid EGaIn surface. Only the interface zones free of protuberance were considered for the measurement in these cases.

II.1.2.1. Contact angle in oxidized surfaces

The previous section indicated that oxides could significantly influence or impede the contact between liquid and solid metals. Therefore, experiments with different surface oxidation states were carried out to study the effects of the Cu and Zn oxides on the wettability of Cu and Cu-Zn alloys by the EGaIn.

A DS3210 automatized dosing unit, and the Krüss drop analyzer were used for these tests. The unit operates with a plastic syringe and a stainless steel needle of 0.5 mm in diameter. This syringe is filled manually with the liquid EGaIn before the test.

The oxide layer from the solids was diluted using a 1 M HCl solution following the works exposed in section I.2.1.2. [32], [33]. A cotton swab soaked in the HCl solution was rubbed on the solid samples to perform this deoxidization. The solution was then removed with a clean cotton swab, and the liquid metal drop was placed *t* seconds later. The values for *t* are 10, 100, 1000, and 10000 seconds. These times were respected with a margin of ±10 s. In addition, drops were also placed without any chemical treatment of the solid.

The solid samples subjected to these tests were Cu and the brasses with 15 and 30 wt.%Zn; the results from these materials are shown in Figure II–8, Figure II–9, and Figure II–10, respectively.

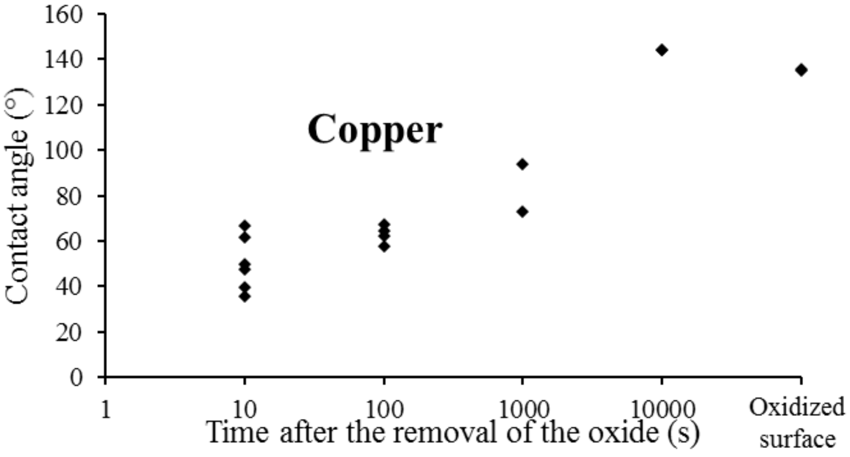

Figure II–8 Evolution of the contact angle with time after the deoxidization of Cu in contact with the liquid EGaIn.

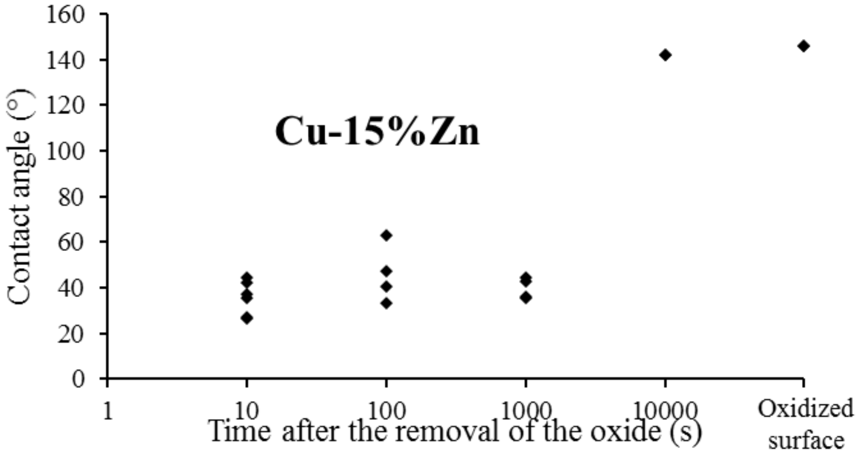

Figure II–9 Evolution of the contact angle with time after the deoxidization of Cu-15%Zn in contact with the liquid EGaIn.

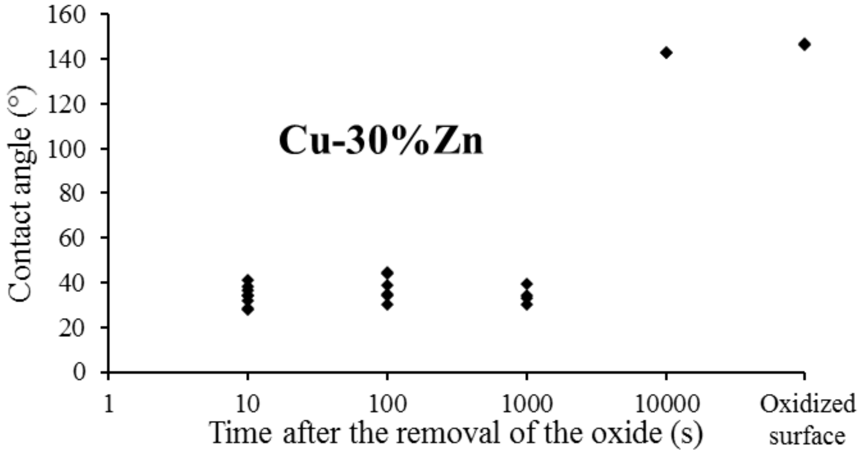

Figure II–10 Evolution of the contact angle with time after the deoxidization of Cu-30%Zn in contact with the liquid EGaIn.

There are general tendencies present in the three materials. If the oxide layer is present in the solid, there is no good contact between the EGaIn and any of the solids. Cu presents contact angles around 135°, and the 15%Zn and 30%Zn brasses present contact angles around 146 and 147°, respectively.

Whenever the oxide layer is not present, the contact angle significantly decreases. Indeed, there is high wettability of the deoxidized samples in contact with the EGaIn. Moreover, there is a long window after the oxide removal for the oxide layer to regrowth and impede the contact. This time window for the three solid materials is between 1000 and 10000 seconds (between 16.7 and 166.7 minutes). After this time, the solids present low wettability in contact with the EGaIn. The contact angle is similar to that of the solid samples that did not undergo the deoxidization procedure.

Furthermore, in some drops, the EGaIn oxide impedes it from taking the geometry with the lowest surface energy due to its viscoelasticity and instead, a protuberance is formed when the needle deposes the liquid metal. This behaviour appeared consistently in conditions with low wettability, i.e., whenever the oxide from the solid impedes a good contact. Figure II–11 illustrates this condition with examples of EGaIn drops on a Cu-30%Zn sample. The form of the drop in Figure II–11c is similar to that reported by Chiechi et al. and Kim et al. (Figure I–18 and Figure II–7) [29], [34].

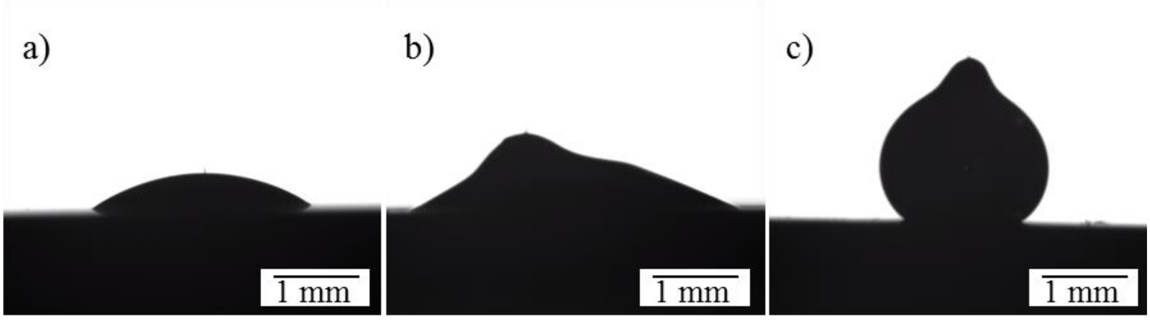

Figure II–11 Drops of EGaIn on Cu-30%Zn samples: a) without protuberance on a deoxidized surface, b) with a protuberance on a deoxidized surface, and c) with a protuberance on an oxidized surface.

Independently of the apparition of a protuberance, the contact angles under the same condition were similar. A drop of the HCl solution was applied to the sample to deoxidize the liquid metal to corroborate if the protuberance elimination could modify the wetting behaviour. Then, the HCl was retired using paper, and the contact angle was measured. Figure II–12 shows this process and the values of the contact angles in both conditions, which are similar. This similarity indicates that the oxidized surface of the EGaIn does not impede its good wetting over the solid samples.

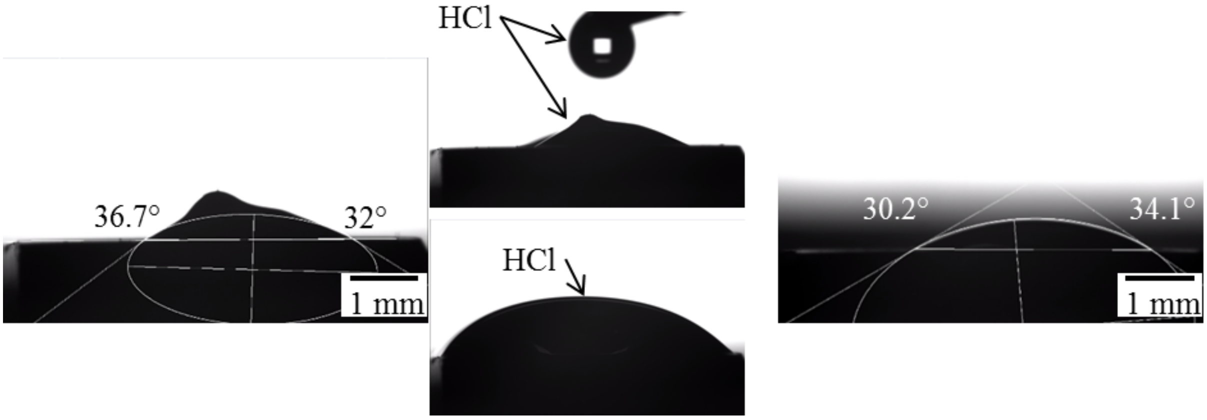

Figure II–12 Evolution of a drop of EGaIn on a deoxidized surface after treatment with HCl.

Similarly, a drop of the HCl solution was applied to a sample with low wettability to deoxidize the liquid and solid metal surfaces. Figure II–13 schematizes this process and shows that the contact angle changes after the drop is in contact with the HCl, and there is a transition to a regime of high wettability.

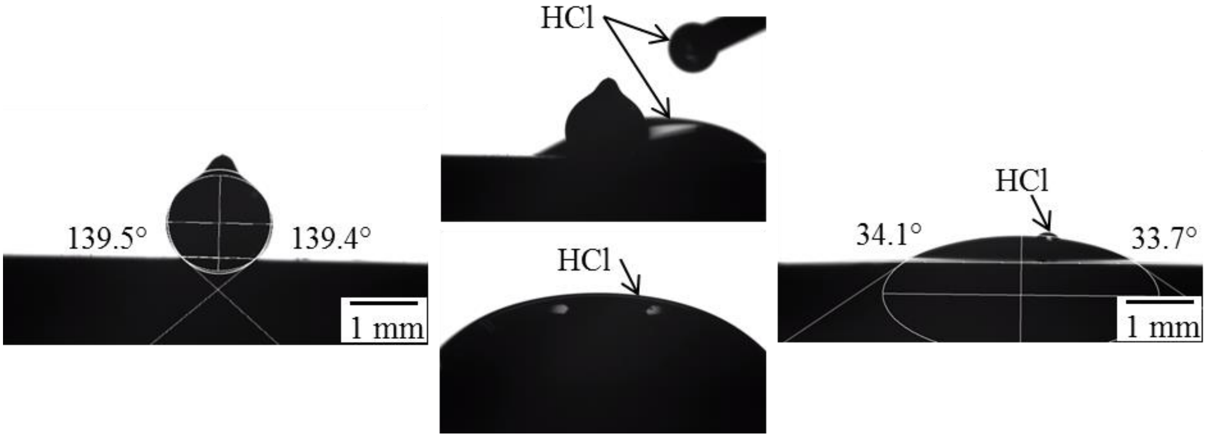

Figure II–13 Evolution of a drop of EGaIn on an oxidized surface after treatment with HCl.

The values of the contact angles are similar to the other experiments when there is no oxide layer in the solid, which indicates that following this methodology, the same wetting conditions occur. However, with this methodology, traces of HCl may hinder a good measurement of the contact angles.

Another consequence of the oxide layer formed in the solid was the impossibility of measuring the contact angle hysteresis by tilting the sample. The EGaIn drop did not move whenever the substrate was tilted, and the contact angle remained practically the same.

In addition, back in Figure II–8, Figure II–9, and Figure II–10, it can be observed that there is a dispersion of the contact angle in some of the conditions. This dispersion is unrelated to a specific solid composition or the time after the deoxidization. This dispersion can be related to the oxide present on the surface of the EGaIn, which is responsible for the protuberances, which could have impeded the triple line from moving freely.

The subsequent experiments were done with HCl-treated EGaIn, to avoid this dispersion. There is no use in repeating the previous experiments with deoxidized EGaIn since residual HCl in the liquid metal could modify the oxide layer on the solid. Moreover, it was shown in Figure II–8 that the oxide on the liquid surface does not modify the wetting regime, which was the main focus of the previous experiments.

With the knowledge of the conditions that allow a high wetting condition between the Cu-based solids and the liquid EGaIn, the next step is to characterize the variation of this contact condition with the composition of the alloy.

II.1.2.2. Evolution of the contact angle with the Zn content

To evaluate the variation of the contact angle with the Zn content, liquid metal drops were placed into solids with different compositions. The solids were deoxidized using a cotton swab soaked with a 1M HCl solution like in the previously described experiments. Additionally, the EGaIn was deoxidized before taking it with a micropipette. This deoxidization was done by immersing it into the same HCl solution in a beaker and then removing it with paper.

Instead of the automatized dosing unit, a RAININ micropipette with a capacity of 2-20 µL was used to place the drop on the solid sample just before introducing the solid into the Krüss DSA100 drop analyzer to avoid oxidation of the EGaIn.

The time between the deoxidizations and the drop placement was always below 5 minutes, which is far less than the lower limit for the regrowth of the oxide layer. At least 12 contact angles were measured for each of the compositions. Figure II–14 summarizes the resulting contact angles.

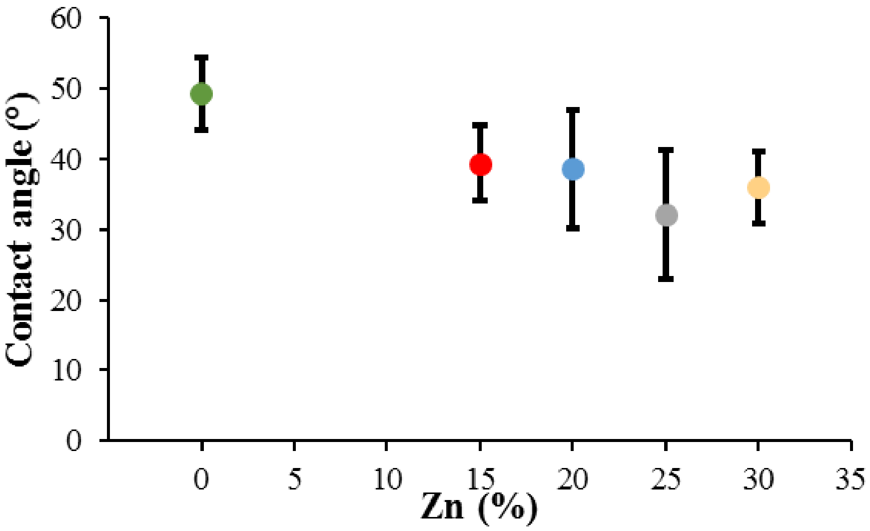

Figure II–14 Evolution of the contact angle with Zn content of Cu-Zn alloys in contact with liquid EGaIn.

These results show good wetting conditions in all the compositions since the contact angle is always below 60°. Also, the dispersion in the contact angle values is similar for all compositions. This dispersion could be related to the contact angle hysteresis caused by the reaction between the solid and the liquid or by the liquid metal oxide layer. Since both phenomena may not change significantly with the composition of the solid, in this range of compositions, the contact angle hysteresis does not change significantly with the composition.

With the deoxidization of the liquid metal, none of the drops presented protuberances, and the dispersion was lower than in the previous experiments. However, it was still impossible to measure the contact angle hysteresis by tilting the platform since there is an immediate reformation of the oxide layer in the liquid that impedes the movement of the drop.

Moreover, there is a slight tendency to have a lower contact angle as the Zn content increases, which means that in these alloys, Zn enhances the wetting capacity of the EGaIn.

II.2. The intermetallic between Cu and Cu-Zn alloys and EGaIn

An essential consequence of the good contact conditions of Cu and alpha brasses with the EGaIn is the formation of an intermetallic compound, which is expected in this system, as concluded in section I.4..

The first observation of the intermetallic was done in samples that were mechanically tested; the next chapter addresses these tests in detail. The observations were done using a Hitachi SU5000 scanning electron microscope (SEM). Figure II–15 shows some micrographs of the intermetallic formed on the surface of a Cu-30%Zn sample in contact with the EGaIn. The liquid metal was cleaned in an ultrasonic bath using a 1.1 M solution of HNO_3 to observe these samples. The appearance of the intermetallic is similar to that of the $CuGa_2$ compound reported in the literature [35].

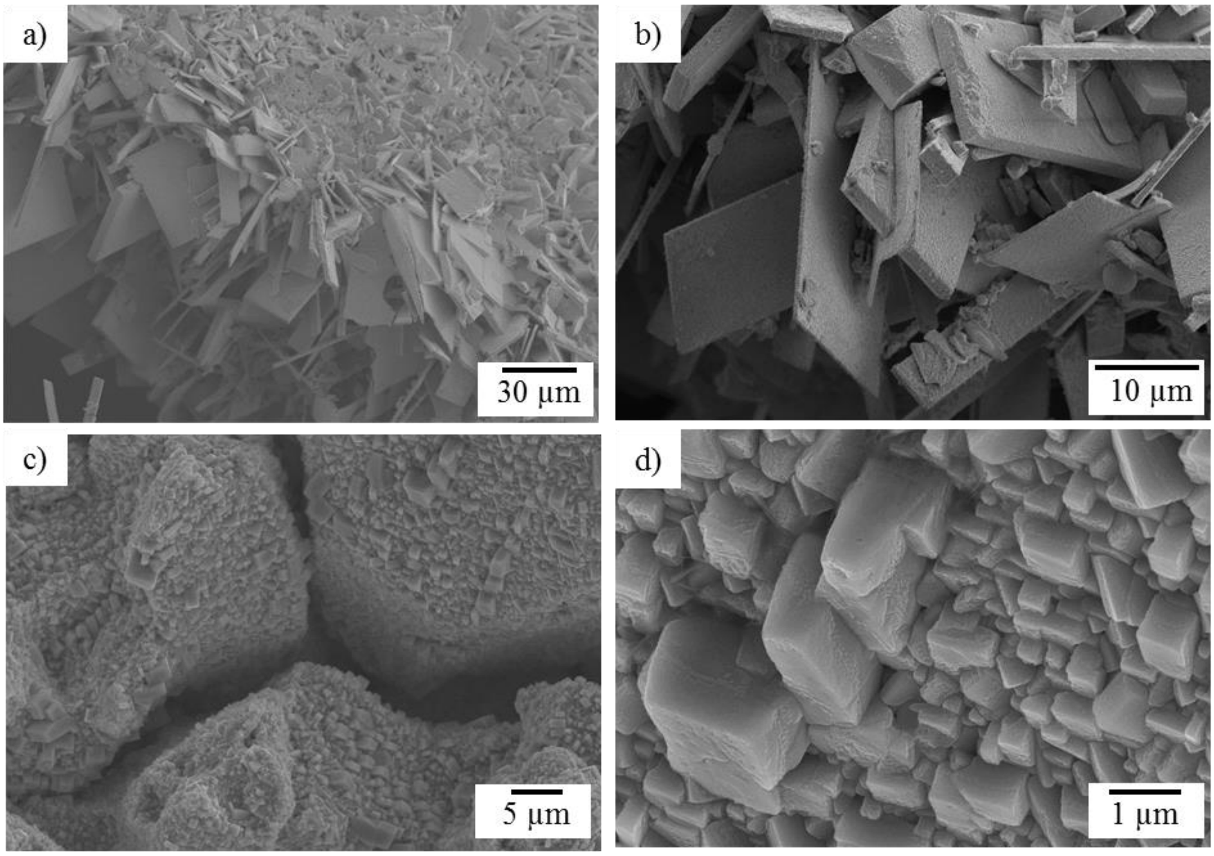

Figure II–15 Intermetallic formed between EGaIn and Cu-30%Zn samples. b) Is a zoom of a), and d) is a zoom of c).

It must be noted that whenever the liquid metal is not removed correctly, e.g., when the cleaning time is less than necessary, there is a significant quantity of liquid metal on the solid. For instance, Figure II–16 shows one case where the liquid metal was not completely removed. This micrograph was taken with a backscattered electron detector, which implies that the contrast depends on the atomic number of the elements present; in this case, the brightest zones correspond to the EGaIn while the rest corresponds to the intermetallic.

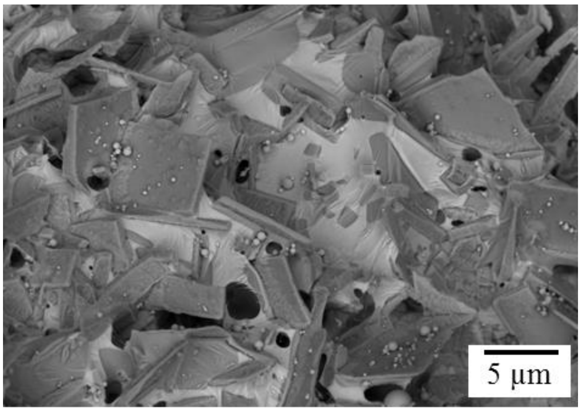

Figure II–16 Backscatter electron image on a Cu-30%Zn sample that was in contact with the EGaIn and did not undergo proper removal of the liquid metal before observation.

Since the intermetallic makes observation of the samples' fracture difficult, a cleaning method was developed. The method consists in submerging the samples in a 1 M solution of NaOH in an ultrasonic bath for 15 minutes. An energy dispersive x-ray spectroscopy (EDS) was carried out in the SEM to detect the presence of Ga in the samples after this cleaning method.

The EDS technique works under the principle that each element has a unique set of peaks on its electromagnetic emission spectrum. While the electron beam impacts the sample in the SEM, there are emissions of characteristic X-rays. A detector collects these X-rays, and the present elements are identified by matching the position of the peaks in an energy vs intensity graph with the predicted positions by Moseley's law [36].

Figure II–17 shows the SEM images and the EDS analysis of one simple before and after using the cleaning method. The absence of the Ga peaks in the EDS spectrogram indicates that the cleaning method does retire the intermetallic from the sample's surface.

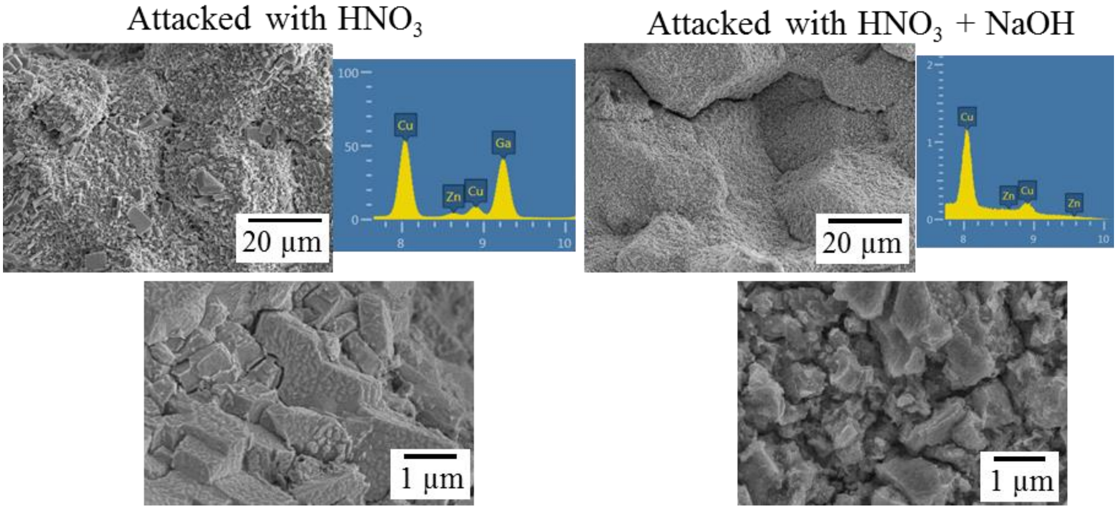
Attacked with HNO_3

Attacked with HNO_3 + NaOH

Figure II–17 Comparison of surfaces a)before and b)after the removal of the intermetallic.

Without the intermetallic, the sample's surface can be observed directly, which allows the interpretation of the fracture mode in the case of the fractured samples. However, we must consider the abrasion left when the NaOH removed the intermetallic. The liquid metal must be cleaned just after the test so the formation of the intermetallic is limited and hence the damage is reduced.

Cu-30%Zn samples were in contact with liquid EGaIn, and then the liquid metal was retired using HNO_3 after different times of contact to study the evolution of the intermetallic formation with time. These samples were cut transversally, mounted in resin, and prepared metallographically for observation. Figure II–18 shows the Cu-30%Zn samples with different contact times with the EGaIn.

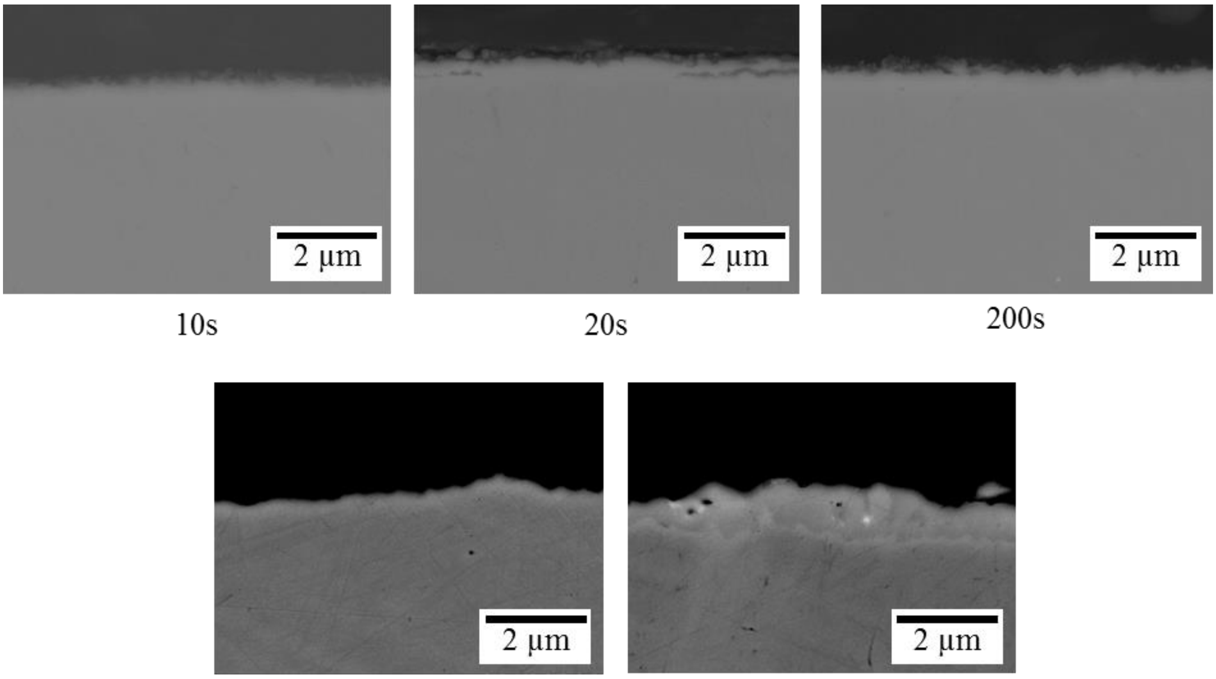

10s 20s 200s

2000s 20000s

Figure II–18 Transversal cut of the intermetallic formation at different times.

Only after 20000 s, a significant amount of intermetallic in these samples is observable via the SEM. At this time, the image resembles other images reported on the formation of the $CuGa_2$ intermetallic [35], [37].

EDS analysis indicated Ga presence on the surface of all the samples, which indicates that the intermetallic formed even in the samples that were in contact only for 10 seconds with the liquid EGaIn. The intermetallic size is too small to be measured by EDS since the volume of the interaction between the electrons and the sample is too big compared with the intermetallic layer size.

A coarser intermetallic layer was created by putting Cu-30%Zn samples in contact with liquid EGaIn for two months. Figure II–19 presents the EDS results, which show that Cu and Ga compose the intermetallic. The atomic ratio between Cu and Ga is 1:2 and matches the $CuGa_2$ compound, which is the intermetallic reported in the literature on similar systems at room temperature [35], [37].

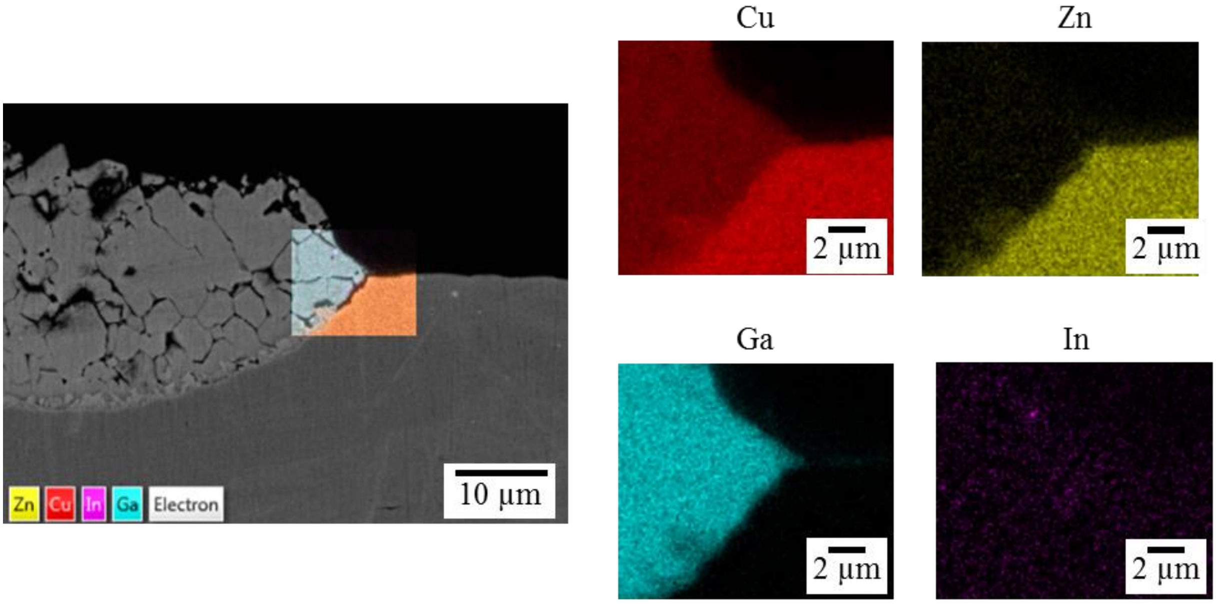

Figure II–19 SEM image and EDS analysis of a transversal cut of a Cu-30%Zn sample that was in contact with liquid EGaIn for two months.

The $CuGa_2$ intermetallic should also be the compound present at shorter contact times since no other Cu-Ga intermetallics form at room temperature, and there are no other reported phases composed of Ga and Zn or In [38]–[41].

The Time-of-Flight Secondary Ion Mass Spectrometry (ToF-SIMS) technique was employed to analyze the presence of the elements in terms of depth from the surface. The analyses were carried out using a ToF.SIMS 5 (ION-TOF GmbH Germany) instrument equipped with a Bi^+ liquid metal ion gun. This technique consists of sputtering the surface of a sample with a Cs^+ ion beam and then analyzing the free ions in the gas phase at different depths using pulsed Bi^+ primary ions. These ions are then accelerated into a flight path towards a detector that measures the ions' flight time. This time of flight is related to each ion's mass; hence they can be identified by their mass with a mass resolution higher than any other surface analysis technique [42].

For our analysis, a Cs^+ (2 kV) source was used to sputter a square area of 300x300 µm into different solid samples and then analyzed by Bi^+ ions (25 kV). The obtained data consist of intensity vs time of sputtering graph. It is important to note that due to the nature of the ToF-

SIMS technique, the intensities of the curves are not related linearly with the concentration of the elements, and they are not proportional between them.

Moreover, the analysis depth was approximated by supposing a direct constant relation between the sputtering time and depth. This relation was calculated by taking the total sputtering time and dividing it by the total sputtered depth for each of the samples. The total depth of the sputtering was measured using a Bruker Contour GT-K 3D Optical Microscope. This assumption is idealistic since the ablation speed depends on the composition of the material. However, the approximation allows us to have a qualitative vision of the profile of each element.

Figure II–20 schematized the main results on a Cu-%30Zn sample that was treated with HCl to retire the oxides, then a drop of liquid EGaIn was placed for 20 s, and after this time, the liquid metal was retired using the 1.1 M HNO_3 solution.

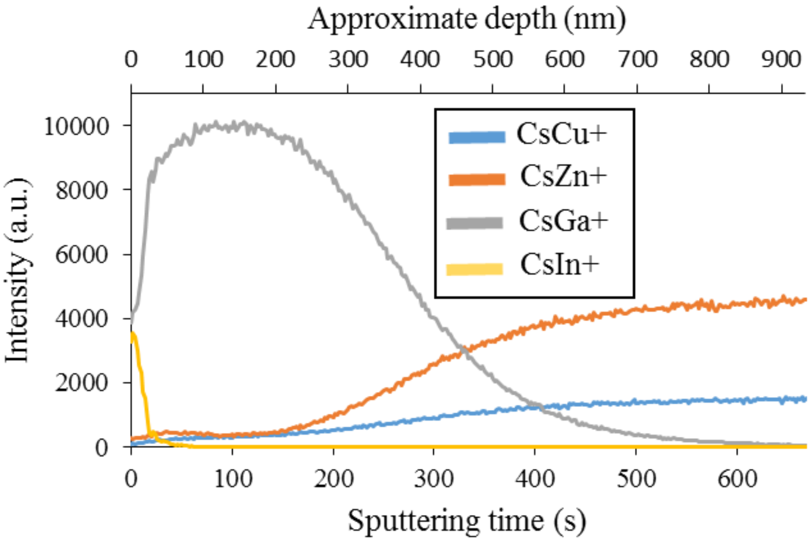

Figure II–20 ToF-SIMS profiles of a Cu-30%Zn sample cleaned with HCl, put in contact with liquid EGaIn and then cleaned with HNO_3.

On the sample's surface, there is In that disappears at some nanometres from the surface. Moreover, Ga extends to several hundreds of nm from the surface before disappearing. The diminution in Ga concentration is much less abrupt than for In.

Also, there is little presence of Cu and Zn at the surface, increasing with the depth until a plateau around the same depth at which Ga disappears. These tendencies indicate that in this sample, there was an intermetallic compound that presents a depth of some hundreds of nanometres, which matches with the fact that, by EDS-SEM, it was not possible to observe it at short contact times.

Furthermore, the ToF-SIMS showed no presence of Cl or N (not included in the figure) that could result from the chemical cleanings with HCl and HNO_3.

Another ToF-SIMS analysis was done on a similar sample, but this one underwent chemical cleaning with both 1.1 M HNO_3 and 1 M NaOH solutions. Figure II–21 shows its correspondent analysis, which shows no traces of Ga and suggests that the NaOH cleaning effectively removes the intermetallic from the samples. Furthermore, this chemical cleaning leaves significant traces of O and OH resulting from the reaction between $CuGa_2$ and NaOH.

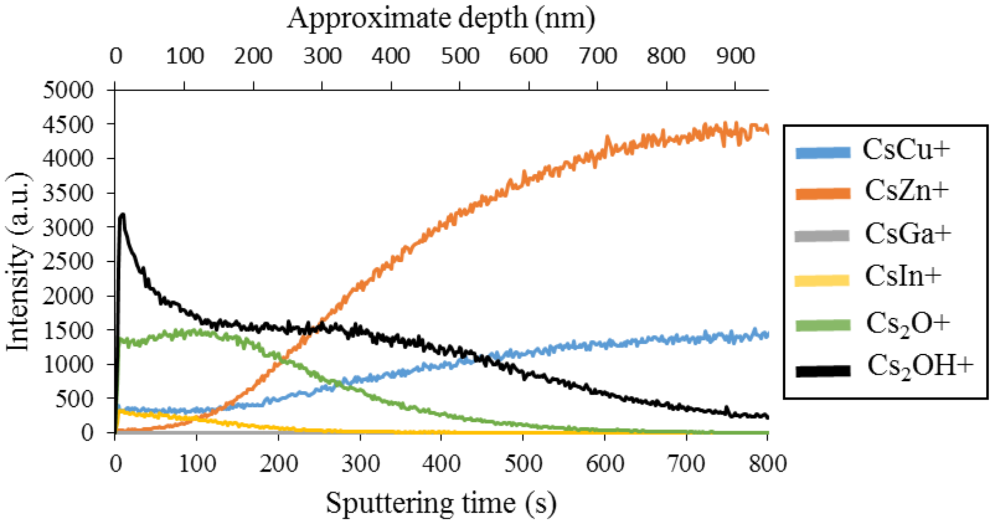

Figure II–21 ToF-SIMS profiles of a Cu-30%Zn sample cleaned with HCl, put in contact with liquid EGaIn, cleaned with HNO_3, and then with NaOH.

Analogous results were found on Cu samples after an HNO_3 and an HNO_3 + NaOH treatment. Figure II–22 and Figure II–23 present these results, respectively.

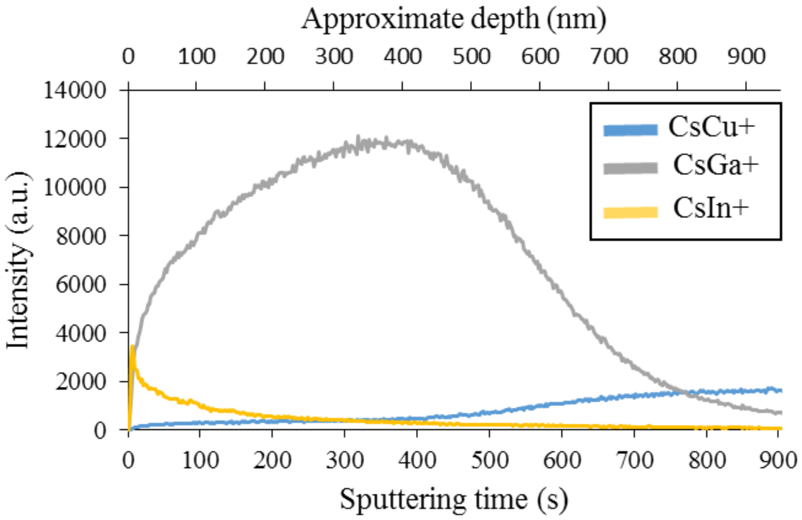

Figure II–22 ToF-SIMS profiles of a Cu sample cleaned with HCl, put in contact with liquid EGaIn and then cleaned with HNO_3.

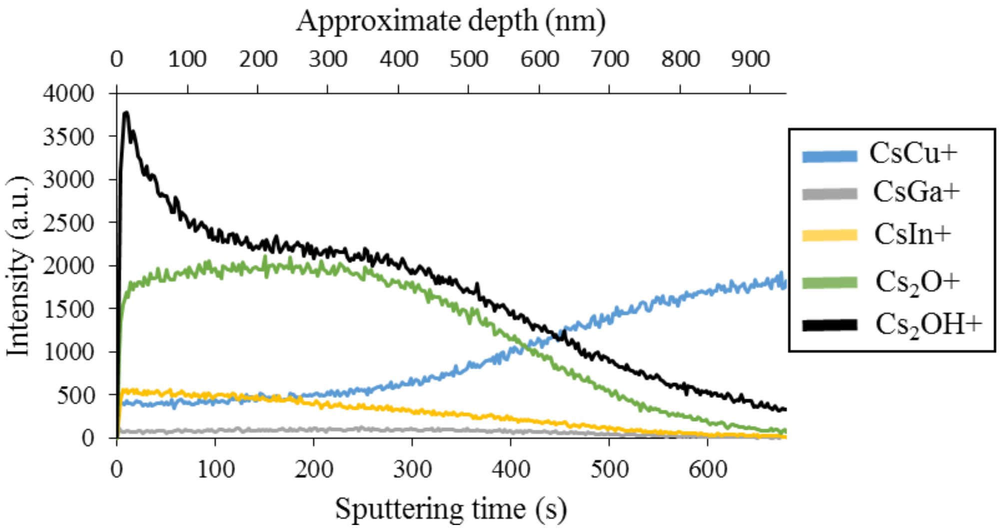

Figure II–23 ToF-SIMS profiles of a Cu sample cleaned with HCl, put in contact with liquid EGaIn, cleaned with HNO_3*, and then with NaOH.*

With the solid phase's characterization, studying the liquid metal to have a complete vision of the interactions is interesting. A suitable technique for this matter is the Inductively Coupled Plasma-Optical Emission Spectroscopy (ICP-OES) technique, used to analyze the liquid EGaIn after contact with the Cu or Cu-30%Zn samples. This technique works with the principle that the electrons in the atoms can move to an excited state whenever they absorb enough energy, and then they transition back to a lower energy level which generates an emission of light. This emission is proportional to the number of atoms that make the transition, and the wavelength is specific to the element. For this, the ICP-OES uses argon plasma as a source of energy that excites the atoms and then measures the intensity of emitted light for each wavelength to calculate the concentration of specific elements based on a calibration graph [43]. For this work, an ICP-OES Agilent 5110 was used.

To prepare the samples, 600 mg of liquid EGaIn was placed on a Cu-30%Zn 10x10 mm specimen that was metallographically prepared and then cleaned using HCl just before placing the liquid metal. This preparation was done following the same methodology used for the wetting experiments. After 1 hour of contact, 200 mg of the liquid EGaIn was retired using a RAININ micropipette with a capacity of 2-20 µL, and it was placed directly in test tubes for its analysis. The same was done with a Cu sample for the same contact time and another Cu-30%Zn sample for a contact time of 2 days. Table II–2 summarizes the results from the three samples.

Table II–2 Results from the ICP-OES analysis.

Solid	**Contact time**	**Cu (mg/kg)**	**Zn (mg/kg)**
Cu	1 hour	48.2	0.22
Cu-30 wt.%Zn	1 hour	49.3	37.9
Cu-30 wt.%Zn	2 days	60.2	646

In agreement with the literature [35], [37], [44], Cu was dissolved into the liquid metal for all three conditions. The quantity of dissolved Cu is the same for the pure Cu specimen as for the Cu-30%Zn specimen. Moreover, the quantity of dissolved Cu is slightly higher when the contact time is 2 days instead of 1 hour. Zn dissolves in the liquid metal similarly to Cu for a contact time of 1 hour. Unlike the case of the dissolved Cu, the quantity of dissolved Zn increases considerably when the contact time is 2 days.

These differences can be because once Cu dissolves into the EGaIn, it reacts with Ga to form the $CuGa_2$ intermetallic. This reaction happens continuously; hence the concentration of dissolved Cu does not increase beyond the solubility limit of Cu in the EGaIn (which is unknown). On the other hand, Zn does not react with the liquid, so it is dissolved continuously with time.

II.3. Conclusions

To conclude, the contact conditions of the EGaIn with Cu and the alpha brasses are under the regime of high wettability. This regime is favoured with the Zn content into the solid, although the EGaIn does not wet pure Zn.

Nevertheless, the solid must undergo a deoxidization process to eliminate the Cu and Zn oxides to obtain this regime of high wettability. Whenever these oxides are present, the EGaIn presents a low wetting regime with contact angles of around 140°. The deoxidization of the solid can be done with a 1 M HCl solution and the efficacy of this deoxidization on maintaining the good wetting for at least 1000 s (16 minutes).

On the other hand, the liquid EGaIn also presents an oxide on its surface. Although it does not impede contact with the solids, it prevents the liquid from taking the form with the least surface energy possible. This behaviour is evidenced by the protuberances apparition on the liquid metal whenever there were bad wetting conditions with the solid and, in some cases, when there were good wetting conditions with the solid. The same 1 M HCl solution can remove this oxide layer.

When the EGaIn enters contact with Cu or the alpha brasses, there is $CuGa_2$ formation. This intermetallic forms rapidly to hundreds of nm in just tens of seconds. For this formation, the Cu dissolves into the EGaIn, and there is a subsequent reaction between dissolved Cu and Ga. Zn also dissolves into the EGaIn but does not participate in any reaction.

It is possible to perform a cleaning using a 1.1 M HNO_3 solution to eliminate the residual liquid metal from the solid and then a second cleaning using a 1 M NaOH solution to eliminate the $CuGa_2$.

Figure II–24 presents a graphic summary of the main results of this chapter.

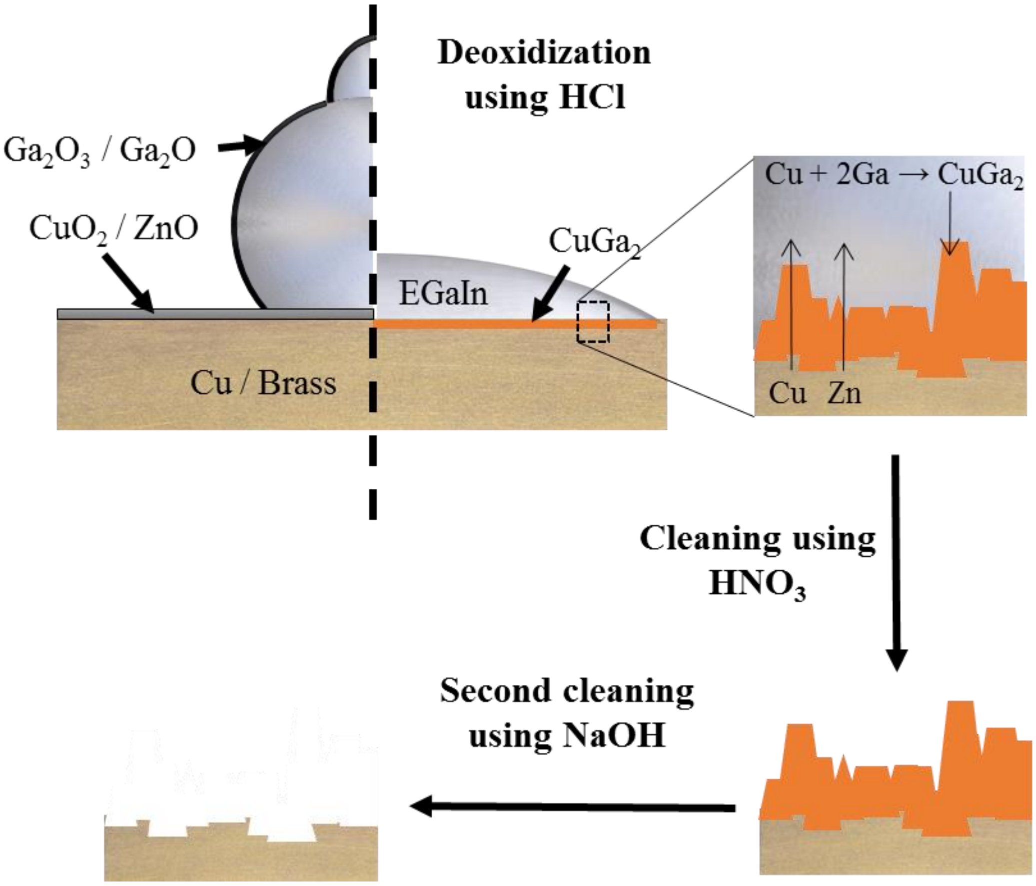

Figure II–24 Summary of the main results on the interface of EGaIn in contact with Cu and Cu-Zn.

II.4. References

[1] G. Lamour *et al.*, “Contact angle measurements using a simplified experimental setup,” *J. Chem. Educ.*, vol. 87, no. 12, pp. 1403–1407, 2010.

[2] J. D. Bernardin, I. Mudawar, C. B. Walsh, and E. I. Franses, “Contact angle temperature dependence for water droplets on practical aluminum surfaces,” *Int. J. Heat Mass*

Transf., vol. 40, no. 5, pp. 1017–1033, 1997.

[3] J. Diawara, “Mouillabilité de surfaces hétérogènes (fer/oxyde) par un alliage de zinc liquide,” Ecole Centrale Paris, 2011.

[4] M. Diallo, “Wetting on heterogeneous metal-oxides regular patterned surfaces by a non-reactive liquid metal,” Université Paris-Saclay, 2019.

[5] M. Brugnara, “Contact Angle,” 2004. [Online]. Available: https://imagej.net/ij/plugins/contact-angle.html. [Accessed: 01-Dec-2020].

[6] R. K. Kramer, J. W. Boley, H. A. Stone, J. C. Weaver, and R. J. Wood, “Effect of microtextured surface topography on the wetting behavior of eutectic gallium-indium alloys,” *Langmuir*, vol. 30, no. 2, pp. 533–539, 2014.

[7] G. Bhutani, K. Muralidhar, and S. Khandekar, “Determination of Apparent Contact Angle and Shape of a Static Pendant Drop on a Physically Textured Inclined Surface,” *Interfacial Phenom. Heat Transf.*, vol. 1, no. 1, pp. 29–49, 2013.

[8] C. Vergelati, A. Perwuelz, L. Vovelle, M. A. Romero, and Y. Holl, “Poly(ethylene terephthalate) surface dynamics in air and water studied by tensiometry and molecular modelling,” *Polymer (Guildf).*, vol. 35, no. 2, pp. 262–270, 1994.

[9] L. M. Lander, L. M. Siewierski, W. J. Britain, and E. A. Vogler, “A Systematic Comparison of Contact Angle Methods,” *Langmuir*, vol. 9, no. 8, pp. 2237–2239, 1993.

[10] J. Fukai *et al.*, “Wetting effects on the spreading of a liquid droplet colliding with a flat surface: Experiment and modeling,” *Phys. Fluids*, vol. 7, no. 2, pp. 236–247, 1995.

[11] D. Richard and D. Quéré, “Bouncing water drops,” *Europhys. Lett.*, vol. 50, no. 6, pp. 769–775, Jun. 2000.

[12] D. G. Stroppa, J. S. Unfried, T. Hermenegildo, and A. J. Ramirez, “Measuring contact angles on sessile drop test samples,” *Weld. J. (Miami, Fla)*, vol. 89, no. 3, pp. 47–49, 2010.

[13] A. Awasthi, Y. J. Bhatt, and S. P. Garg, “Measurement of contact angle in systems involving liquid metals,” *Meas. Sci. Technol.*, vol. 7, no. 5, pp. 753–757, 1996.

[14] V. de Jonghe and D. Chatain, “Experimental study of wetting hysteresis on surfaces with controlled geometrical and/or chemical defects,” *Acta Metall. Mater.*, vol. 43, no. 4, pp.

1505–1515, 1995.

[15] N. Eustathopoulos, N. Sobczak, A. Passerone, and K. Nogi, “Measurement of contact angle and work of adhesion at high temperature,” *J. Mater. Sci.*, vol. 40, no. 9–10, pp. 2271–2280, 2005.

[16] V. De Jonghe, D. Chatain, I. Rivollet, and N. Eustathopoulos, “Contact angle hysteresis due to roughness in four metal/sapphire systems,” *J. Chim. Phys.*, vol. 87, pp. 1623–1645, 1990.

[17] K. Landry, C. Rado, R. Voitovich, and N. Eustathopoulos, “Mechanisms of reactive wetting: The question of triple line configuration,” *Acta Mater.*, vol. 45, no. 7, pp. 3079–3085, 1997.

[18] P. Kritsalis, B. Drevet, N. Valignat, and N. Eustathopoulos, “Wetting transitions in reactive metal/oxide systems,” *Scr. Metall. Mater.*, vol. 30, no. 9, pp. 1127–1132, 1994.

[19] Y. Cui *et al.*, “Metallic Bond-Enabled Wetting Behavior at the Liquid Ga/CuGa2 Interfaces,” *ACS Appl. Mater. Interfaces*, vol. 10, no. 11, pp. 9203–9210, 2018.

[20] Q. Xu, N. Oudalov, Q. Guo, H. M. Jaeger, and E. Brown, “Effect of oxidation on the mechanical properties of liquid gallium and eutectic gallium-indium,” *Phys. Fluids*, vol. 24, no. 6, p. 063101, Jun. 2012.

[21] S. G. Keller and A. P. Gordon, “Experimental study of liquid metal embrittlement for the aluminum 7075-mercury couple,” *Eng. Fract. Mech.*, vol. 84, pp. 146–160, 2012.

[22] Z. Hamouche, “Etude de la fragilisation des aciers T91 et 316L par l’eutectique plomb-bismuth liquide,” Paris Est, 2008.

[23] C. F. Old, “The liquid metal embrittlement of zinc and aluminum,” in *The Physical Metallurgy of Fracture*, vol. 2 A, Elsevier, 1978, pp. 331–340.

[24] C. Lesueur, D. Chatain, C. Bergman, P. Gas, and F. Baque, “Analysis of the stability of native oxide films at liquid lead/ metal interfaces,” *J. Phys. IV Fr.*, vol. 12, no. 8, pp. 155–162, 2002.

[25] J. Lee, K. Seo, N. Hirai, N. Takahira, and T. Tanaka, “Intrinsic contact angle and contact interaction between liquid silver and solid graphite,” *Met. Mater. Int.*, vol. 13, no. 2, pp. 83–86, 2007.

[26] B. C. Allen and W. D. Kingery, “Surface Tension and Contact Angles in Some Liquid Metal-Solid Ceramic Systems at Elevated Temperatures,” *Trans. Am. Inst. Min. Metall. Eng.*, vol. 215, no. 1, pp. 30–37, 1959.

[27] J. Tang, X. Zhao, J. Li, Y. Zhou, and J. Liu, “Liquid Metal Phagocytosis: Intermetallic Wetting Induced Particle Internalization,” *Adv. Sci.*, vol. 4, no. 5, p. 1700024, May 2017.

[28] Y. G. Deng and J. Liu, “Corrosion development between liquid gallium and four typical metal substrates used in chip cooling device,” *Appl. Phys. A Mater. Sci. Process.*, vol. 95, no. 3, pp. 907–915, 2009.

[29] D. Kim *et al.*, “Recovery of nonwetting characteristics by surface modification of gallium-based liquid metal droplets using hydrochloric acid vapor,” *ACS Appl. Mater. Interfaces*, vol. 5, no. 1, pp. 179–185, 2013.

[30] D. Whitehouse, *Surfaces and Their Measurement*. Gulf Professional Publishing, 2002.

[31] J. Schindelin *et al.*, “Fiji: an open-source platform for biological-image analysis,” *Nat. Methods*, vol. 9, no. 7, pp. 676–682, Jul. 2012.

[32] N. Habbache, N. Alane, S. Djerad, and L. Tifouti, “Leaching of copper oxide with different acid solutions,” *Chem. Eng. J.*, vol. 152, no. 2–3, pp. 503–508, 2009.

[33] J. Colombeau, T. Auger, D. Johnson, and L. Wang, “Cu Grain Boundary Embrittlement by Liquid Hg: A Comparison between Experiment and ab-initio Modeling,” *MRS Proc.*, vol. 1515, pp. mrsf12-1515-ii12-05, Oct. 2013.

[34] R. C. Chiechi, E. A. Weiss, M. D. Dickey, and G. M. Whitesides, “Eutectic gallium-indium (EGaIn): A moldable liquid metal for electrical characterization of self-assembled monolayers,” *Angew. Chemie - Int. Ed.*, vol. 47, no. 1, pp. 142–144, 2008.

[35] S. Liu *et al.*, “Properties of CuGa2 Formed Between Liquid Ga and Cu Substrates at Room Temperature,” *J. Electron. Mater.*, vol. 49, no. 1, pp. 128–139, 2020.

[36] J. I. Goldstein *et al.*, *Scanning Electron Microscopy and X-ray Microanalysis*. Boston, MA: Springer US, 2003.

[37] S. Lin, C. Cho, and H. Chang, “Interfacial Reactions in Cu/Ga and Cu/Ga/Cu Couples,” *J. Electron. Mater.*, vol. 43, no. 1, pp. 204–211, Jan. 2014.

[38] J. Froemel, M. Baum, M. Wiemer, and T. Gessner, “Low-Temperature Wafer Bonding

Using Solid-Liquid Inter-Diffusion Mechanism," *J. Microelectromechanical Syst.*, vol. 24, no. 6, pp. 1973–1980, Dec. 2015.

[39] S. Liu, K. Sweatman, S. McDonald, and K. Nogita, "Ga-based alloys in microelectronic interconnects: A review," *Materials (Basel).*, vol. 11, no. 8, pp. 1–20, 2018.

[40] C. P. Muzzillo, C. E. Campbell, and T. J. Anderson, "Cu–Ga–In thermodynamics: experimental study, modeling, and implications for photovoltaics," *J. Mater. Sci.*, vol. 51, no. 7, pp. 3362–3379, Apr. 2016.

[41] M. Purwins *et al.*, "Phase relations in the ternary Cu–Ga–In system," *Thin Solid Films*, vol. 515, no. 15, pp. 5895–5898, May 2007.

[42] A. Benninghoven, "Chemical Analysis of Inorganic and Organic Surfaces and Thin Films by Static Time-of-Flight Secondary Ion Mass Spectrometry (TOF-SIMS)," *Angew. Chemie Int. Ed. English*, vol. 33, no. 10, pp. 1023–1043, Jun. 1994.

[43] J. W. Olesik, "Elemental analysis using ICP-OES and ICP/MS," *Anal. Chem.*, vol. 63, no. 1, pp. 12A-21A, Jan. 1991.

[44] J. Tang, X. Zhao, J. Li, R. Guo, Y. Zhou, and J. Liu, "Gallium-Based Liquid Metal Amalgams: Transitional-State Metallic Mixtures (TransM2ixes) with Enhanced and Tunable Electrical, Thermal, and Mechanical Properties," *ACS Appl. Mater. Interfaces*, vol. 9, no. 41, pp. 35977–35987, 2017.

III. Sensitivity to LME of Cu and Cu-Zn in contact with the EGaIn in different mechanical conditions

There are two prerequisites for Liquid Metal Embrittlement to occur: contact between the liquid metal and the solid metal and plastic deformation at the macroscopic and the microscopic scales. The previous chapter studied the contact between the liquid eutectic Ga-In (EGaIn) with Cu and alpha brass. This chapter analyses the effect of the mechanical conditions on the liquid metal embrittlement (LME) sensitivity of Cu and alpha brasses while in contact with the liquid EGaIn. Two mechanical tests were used: the small punch test and the bending test. The last sections of the chapter present these tests' finite element modelling (FEM) to quantify the effect of the mechanical parameters on the conditions where there is LME sensitivity.

III.1. The small punch test

The small punch test (SPT) consists of a punching rod with a hemispherical tip or a ball that applies a force onto a disc or square specimen fixed between two dies. The punching rod moves at a constant displacement velocity, and the correspondent force is measured along with the displacement [1], [2]. The punching rod is usually placed on the upper side of the assembly, but in our study, the punching rod is placed on the lower side to use the upper die as a repository for the liquid metal. With this configuration, the sample’s face under tension stress is in contact with the liquid metal. Figure III–1 illustrates the assembly and the specimen used for this test.

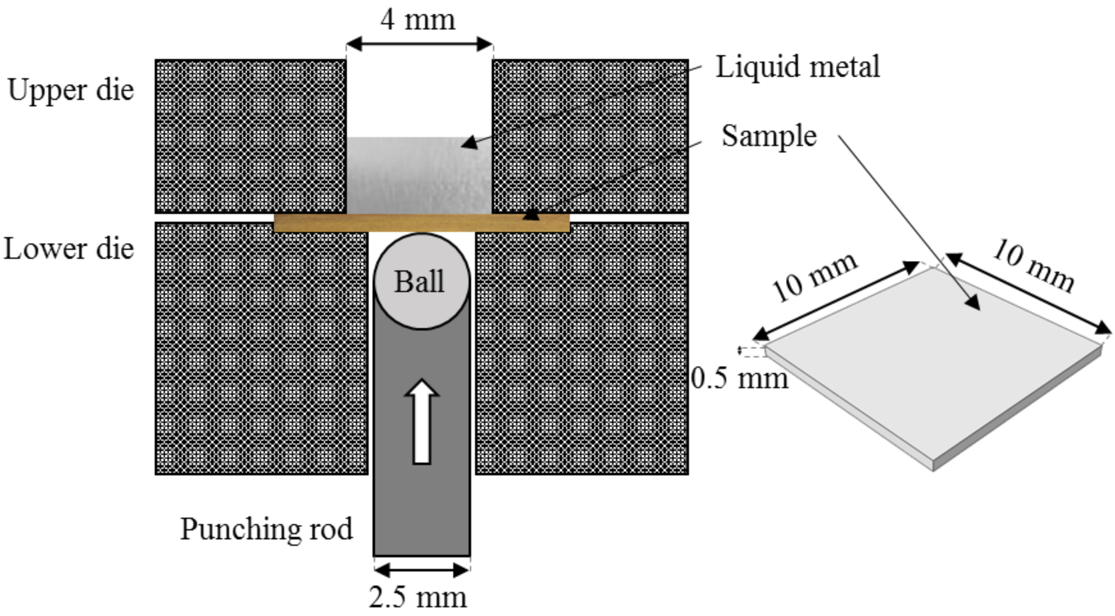

Figure III–1 Schema of the small punch test and the sample.

For the SPT, there are "standard" and "miniaturized" specimen dimensions. The thickness of the standard specimens is 0.5 mm, and they can be circular with a diameter of 8 mm or square with dimensions of 10 x 10 mm; while the thickness of the miniaturized specimens is 0.25 mm, and the diameter of the circular geometry is of 3 mm [1]–[3].

The SPT is particularly convenient when there is a limitation on the material's availability and when the material is difficult to handle [2]. For example, some researchers used this technique to investigate irradiated materials [4]–[6].

In the case of the study of liquid metal embrittlement, handling the liquid metal is often onerous, and the availability of both the liquid and the solid may be limited. Also, since the apparition of liquid metal embrittlement (LME) depends strongly on several parameters, there is a need to perform several tests varying these parameters to characterize the phenomenon comprehensively. Moreover, since the LME is a phenomenon that occurs essentially on the surface, the SPT is more suitable than other tests, such as the tensile tests. Despite this, only a few works on LME use this technique [7]–[12].

Moreover, there are several studies on using this technique to extrapolate several mechanical properties of the materials, such as the preserved structural strength, yield strength, ultimate tensile strength, and fracture toughness [13]–[17].

In all the applications presented, especially the last one, correctly analysing the data obtained with the SPT is critical to this technique.

III.1.1. Interpretation and treatment of the curves

The raw data obtained from the SPT consist of a force-displacement curve. The force is often obtained from load cells incorporated in the mechanical testing machine, while the displacement measurement varies from set-up to set-up. Some studies use a rod to follow the movement of the surface of the sample [15], [16], others use a free-standing extensometer attached to the dies [18], [19], and another more complex set-up incorporates the use of digital image correlation [20].

The force-displacement curves usually present a characteristic profile that consists of separated stages. Depending on the definition, the total number of these stages in the force-displacement curves is between 4 and 6 [11], [18], [20]–[24]. In this thesis, the force-displacement curve is considered as having the following five stages: (I) elastic bending, (II) transition between elastic and plastic bending, (III) plastic hardening, (IV) softening due to material damage initiation, and (V) crack growth [21], [23]. Figure III–2 illustrates these stages. In contrast, some researchers suggest that the material damage initiation appears in the early stages of the SPT [18].

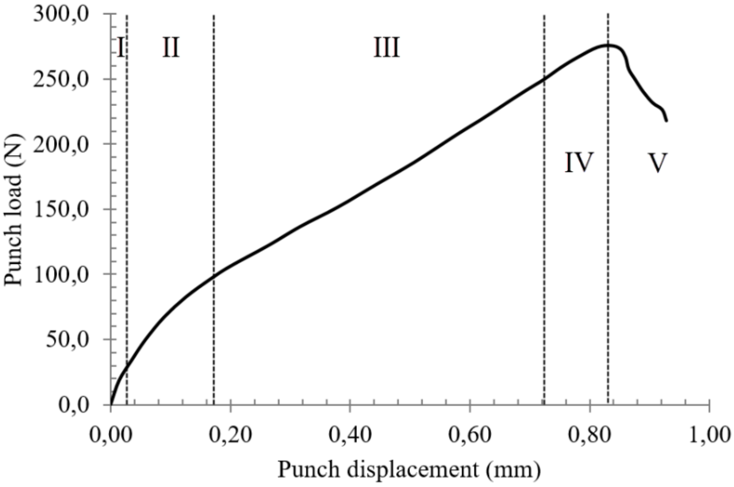

Figure III–2 Main zones in the SPT force-displacement curves [23].

Several methods are available to estimate the mechanical properties using the SPT curves. For instance, Eq. (13) derives the yield strength (σ_{ys}) from the force at which the SPT curve changes from stage I to stage II (P_y).

$$\sigma_{ys} = \alpha_1 \frac{P_y}{t^2} + \alpha_2 \tag{13}$$

where α_1 and α_2 are test constants, and t is the initial thickness of the specimen.

There are various methods to calculate P_y, each of which gives a different value and uses different test constants. The calculation of these values is exemplified graphically in Figure III–3.

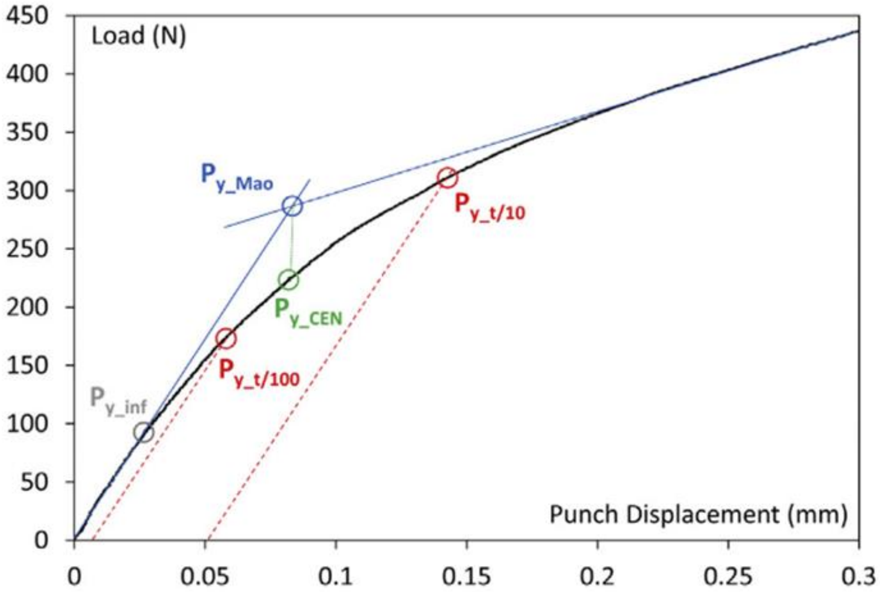

Figure III–3 Different methodologies for determining P_y [25].

P_{y_inf} is the value of the force at the first point of inflexion [26]. In contrast, $P_{y\_t/100}$ and $P_{y\_t/10}$ are computed by taking the slope of the line on stage I, then shifting it to a displacement of $t/100$ or $t/10$, and subsequently finding the points of intersection between the shifted line and the force-displacement curve [27]. P_{y_MAO} corresponds to the interception between the line that best fits stage I and the one that best fits stage II [28]. P_{y_CEN} value is calculated similarly to P_{y_MAO}, but instead of taking the force value in the lines' interception, P_{y_CEN} corresponds to the point in the experimental force-displacement curve with the same displacement value as P_{y_MAO} [1], [25].

To the author's knowledge, the only available work on the use of SPT for the characterization of Cu-alloys is the one published by Ghodke et al., which used the methodology proposed by

Mao et al. and found a relatively good correlation (R=0.9417) when using the constants α_1=0.3586 and α_2=0 [29]. The same methodology and constant values are used in this work.

On the other hand, slight dimension variations can significantly alter the obtained results since the sample's dimensions are small compared to other standard mechanical tests. These alterations are more critical for the specimens' thickness which can be dissimilar due to small fluctuations during the preparation of the samples, which are often difficult to machine. The thickness variation influences the force-displacement curve, which motivates several studies on this influence [30], [31]. The multiplication of the force by the factor f, defined in Eq. (14), accounts for the effect of the specimens' thickness on the curves and allows comparing the behaviour of samples with different thicknesses [25], [32].

$$f = \frac{t_{real}^2}{0.5^2} \tag{14}$$

Finally, the small punch fracture energy was computed by calculating the area under the force-displacement curve [15], [33]. This area was calculated up to the maximum force (Wm) and the last registered value in the force-displacement curve (W_f).

III.1.2. Notched specimens

Some studies estimate the fracture toughness of a material using the SPT using empirical correlations based on the specimen's minimum thickness at the fracture point. However, the absence of a pre-crack in the SPT standard specimen makes these results doubtful [34].

Researchers developed alternative specimens to overcome the lack of pre-crack and better estimate the fracture toughness using the SPT. These specimens present a notch that works as a pre-crack. This pre-crack enhances the measurement of the material's fracture toughness by acting as a stress concentrator providing a triaxiality state closer to the standard fracture tests [35]–[38].

There are four notched specimen geometries reported in the literature: central notch [38], lateral notch [39], circular notch [40], and longitudinal notch [41]. Figure III–4 schematizes these geometries.

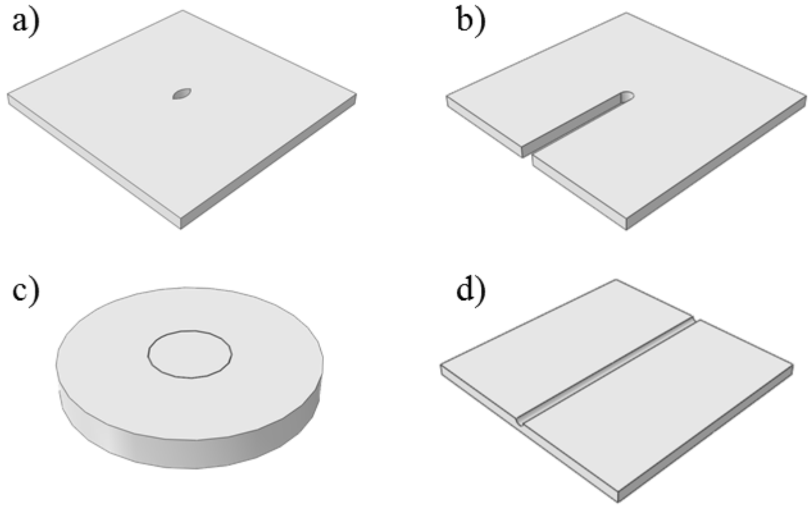

Figure III–4 The different notched SPT geometries: a) central notch [38], *b) lateral notch* [39], *c) circular notch* [40], *and d) longitudinal notch* [41].

Even though introducing a notch in solid samples enhances the sensitivity of tensile tests to LME [42]–[45], none of these SPT notched geometries have been used to study the LME. Hamdane et al. reported the only alternative SPT sample for the study of the LME, which consisted of indented SPT samples to study the role of liquid Na on the crack initiation and propagation of the T91 steel [46].

III.2. Study on the sensitivity to LME of Cu and Cu-30%Zn in contact with the EGaIn by the Small Punch Test

Since the SPT is a practical test suitable for studying the LME phenomenon, this technique was chosen to study the LME sensitivity of pure Cu and Cu-30 wt.%Zn in contact with the eutectic Ga-In (EGaIn). Moreover, alternative notched specimen geometries were used in this work to study the LME. The suitability of this kind of specimen compared with the standard SPT specimens to study LME is also discussed.

III.2.1. Methodology of the SPT

Two solid metals were studied using the SPT: oxygen-free high thermal conductivity (OFHC) Cu and Cu-30 wt.%Zn alpha brass. Both were supplied in sheet form with a 0.7 and 0.64 mm thickness, respectively. Table III–1 and Figure III–5 show their metallurgical conditions and microstructures, respectively.

Table III–1 Metallurgical condition of the solid metals studied by SPT.

Composition	**Thickness (mm)**	**Manufacturer**	**Hardness (HV)**	**Grain size (µm)**
Cu (OFHC)	0.7	Goodfellow	84 ± 4	8 ± 2
Cu -30 wt.%Zn	0.64	Alfa Aesar	133 ± 8	16 ± 2

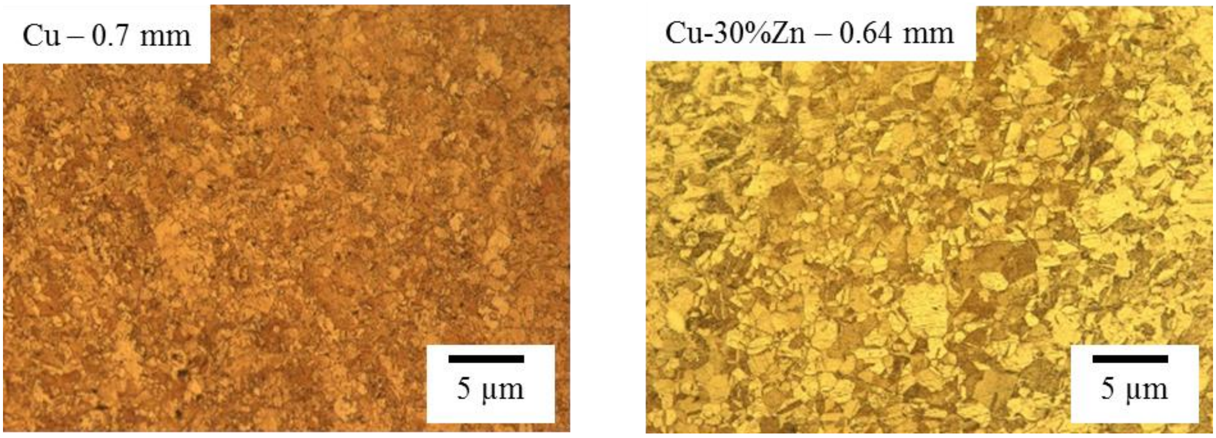

Figure III–5 Microstructures of the materials tested with the SPT.

The samples were prepared through automatic polishing using a Struers Tegramin-30 machine, gradually decreasing the granulometry of the abrasive solution down to 1 µm. This preparation was done to avoid potential roughness effects during the test and to reduce the thickness of the samples to 500 ± 20 µm, which is the necessary thickness for the SPT. The thickness reduction was performed alternating between both faces to limit the introduction of plastic strain in the samples.

For the mounting into the assembly, the specimen was placed between the dies, and then the assembly was tightened using four screws to restrain the pieces’ movement during the manipulation. A 100C6 (AISI 52100) steel ball is placed on the pushing rod tip, and both are introduced into the lower die of the assembly. Then, the entire assembly is placed in a 5567A Instron Universal Testing Machine to carry out the test. A 20 N preload was applied, ensuring the assembly's contact with the sample from the beginning of the test.

For the tests in contact with the liquid EGaIn, the oxide from the solid specimens was dissolved using a 1 M HCl solution following the same methodology as for the wetting experiments exposed in section II.1.2.. After the oxide dissolution, the assembly was mounted, and drops of EGaIn were added through the upper die just before doing the test, using a RAININ micropipette with a capacity of 2-20 µL. The time between the solid samples' deoxidization and the liquid metal placement was always below 5 minutes. According to the previous chapter results (section II.1.2.), 5 minutes is below the time necessary for enough oxide to reform and impede good contact between the solid and the EGaIn. Furthermore, the liquid EGaIn was also deoxidized just before placing the drops of EGaIn into the assembly. The deoxidization of the EGaIn was also done using the 1 M HCl with the methodology detailed in the previous chapter (section II.1.2.).

Also, in the case of these tests, the samples were unmounted as soon as possible after the end of the test, then the liquid EGaIn was removed using a 1.1 M HNO_3 solution in an ultrasonic bath for 10 minutes, and the intermetallic was equally removed using a 1 M NaOH solution in an ultrasonic bath for 15 minutes.

The SPT were carried out at different displacement rates of the cross-head of the tensile machine: 5, 0.5, 0.05, and 0.005 mm/min and always at room temperature, with no control of the temperature.

Three different geometries were used in this study: the standard SPT specimens [1], specimens with a blind longitudinal notch [37], and specimens with a lateral notch [39]. The blind longitudinal notches were machined by wire electrical discharge machining (WEDM) or with a Buehler ISOCUT wafering blade, while the lateral notches were machined using a 30A15 disc in a Struers Accutom-100. Figure III–6 shows the geometries and dimensions of the specimens.

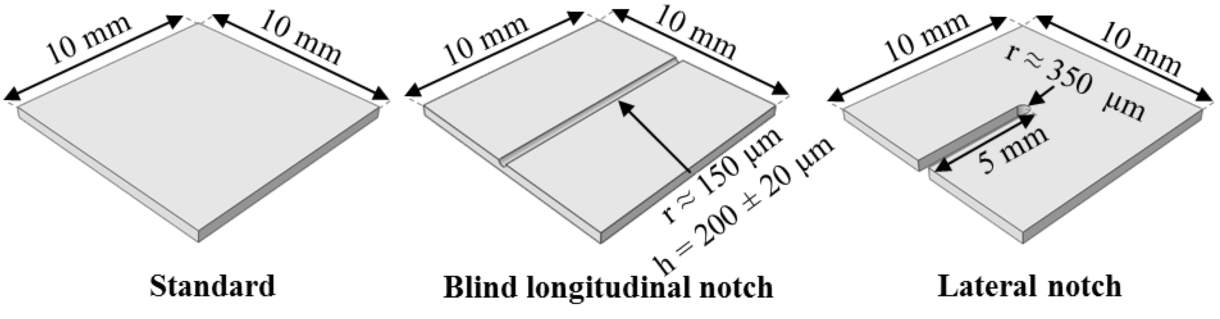

Standard **Blind longitudinal notch** **Lateral notch**

Figure III–6 Dimensions of the specimens used for the SPT.

The notch tip radii obtained by the cutting techniques used in this work are similar to that reported in other works. For example, Alegre et al. used the WEDM to machine a lateral notch in a 15.5pH stainless steel and reported a top-notch radius of 200-250 µm [36].

Before analysing the force-displacement curve, the displacement was calibrated by considering the set-up deformation during the SPT. For this, a test was done on an over-dimensioned steel sample (thickness of 2.54 mm) with a high hardness value of 674 ± 3 HV. Figure III–7 shows the correspondent force-displacement curve.

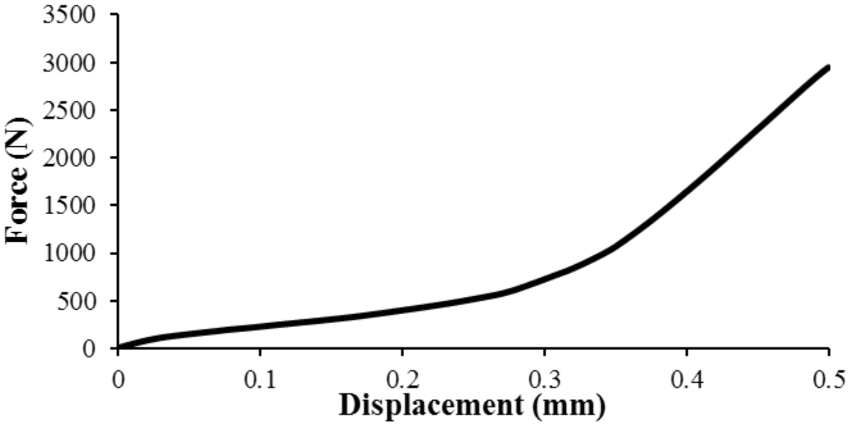

Figure III–7 Force-cross head displacement curve used to calibrate the displacement of the SPT puncher.

This test aims to obtain a force-displacement curve characterizing the assembly and punch deformations during the SPT. Each SPT curve was calibrated by subtracting the corresponding displacement at the corresponding force.

With the calibrated curves, the P_y, W_m, and W_f values were calculated using the corresponding methods explained in section III.1.1.. To account for the effect of the thickness variation, the force of all of the curves was multiplied by the factor in Eq. (14). The thickness of each sample was measured in its centre using a digital micrometre.

After the tests, some samples were observed with the scanning electron microscope (SEM) Hitachi SU5000 to perform the fractographic analysis.

III.2.2. Mechanical behaviour of Cu and Cu-30%Zn in contact with the EGaIn using standard SPT specimens

In the first place, Cu and Cu-30%Zn specimens were tested in air at different displacement rates. Figure III–8 and Figure III–9 show some representative force-displacement curves for Cu and Cu-30%Zn, respectively.

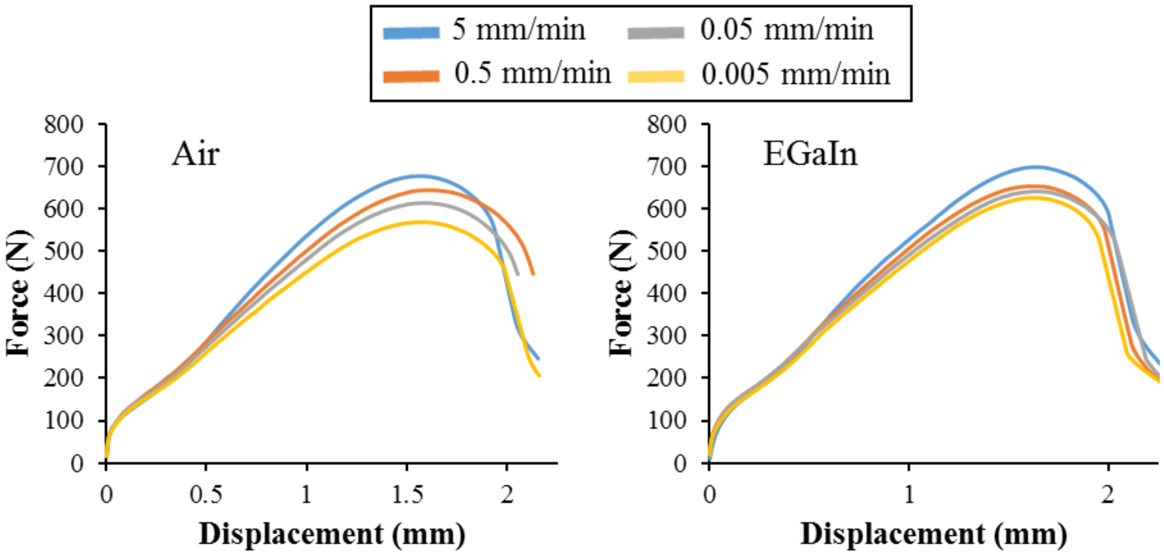

Figure III–8 Force-displacement SPT curves for pure Cu tested in air and in contact with the EGaIn at different displacement rates.

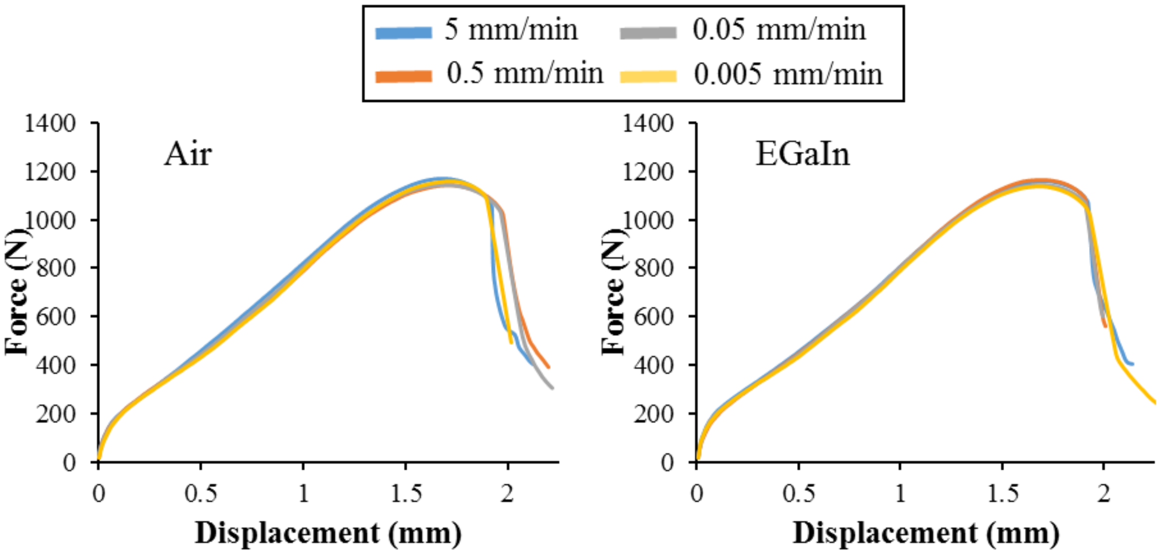

Figure III–9 Force-displacement SPT curves for Cu-30%Zn tested in air and in contact with the EGaIn at different displacement rates.

Observing the different zones of the classical force-displacement SPT curves on both materials is possible. Moreover, the force in the Cu-30%Zn curves is higher than that of Cu, which matches the fact that Zn acts as a solid solution strengthener and that the brass presents higher hardness values.

In the case of Cu, the samples behaved differently depending on the displacement rate applied during the tests. These differences appear in zone III (see Figure III–2) of the force-displacement curves, corresponding to the sample's plastic deformation. These variations suggest a strain rate dependence on the hardening of this material. This effect is absent for the Cu-30%Zn samples, as their curves are virtually identical at all the displacement rates tested.

The same compositions were tested in contact with the EGaIn using the same conditions. Figure III–8 shows some of the tested curves for Cu, and Figure III–9 shows the corresponding curves for Cu-30%Zn.

For the Cu samples, the force during the strain hardening stage slightly increases with the displacement rate, while for the alpha brass, the curves are practically identical. The force-displacement curves of the samples tested in contact with the EGaIn present the same behaviour as those tested in air. Table III–2 summarizes the values of σ_y, W_m and W_f calculated at the different conditions, which support the similitude in the mechanical behaviour.

Table III–2 Mechanical properties estimated by SPT of Cu and Cu-30%Zn tested in air and tested in contact with the EGaIn.

Material	**Speed (mm/min)**	**Environment**	**$\sigma_{Y\text{-}Mao}$ (MPa)**	**W_m (J)**	**W_f (J)**
Cu	5	Air	115	0.64	0.96
		EGaIn	129	0.71	1.07
	0.5	Air	136	0.64	0.96
		EGaIn	137	0.68	1.01
	0.05	Air	137	0.62	0.88
		EGaIn	134	0.67	0.98
	0.005	Air	130	0.57	0.84
		EGaIn	126	0.64	0.95
Cu-30%Zn	5	Air	209	1.19	1.57
		EGaIn	243	1.18	1.58
	0.5	Air	216	1.18	1.59
		EGaIn	227	1.18	1.49
	0.05	Air	221	1.15	1.60
		EGaIn	231	1.15	1.48
	0.005	Air	242	1.17	1.47
		EGaIn	240	1.15	1.58

The values in the table show no significant variations between the samples tested in air and those tested in contact with the liquid EGaIn. The lack of differences denotes that the EGaIn do not seem to modify the mechanical behaviour of these solids under these conditions.

In addition, the samples were observed via SEM to identify if there was a different fracture behaviour between the samples tested in air and those tested in contact with the liquid EGaIn.

Figure III–10 and Figure III–11 show the fractographies of two Cu samples tested at a displacement rate of 5 mm/min, the first was tested in air, and the second was tested in contact with EGaIn.

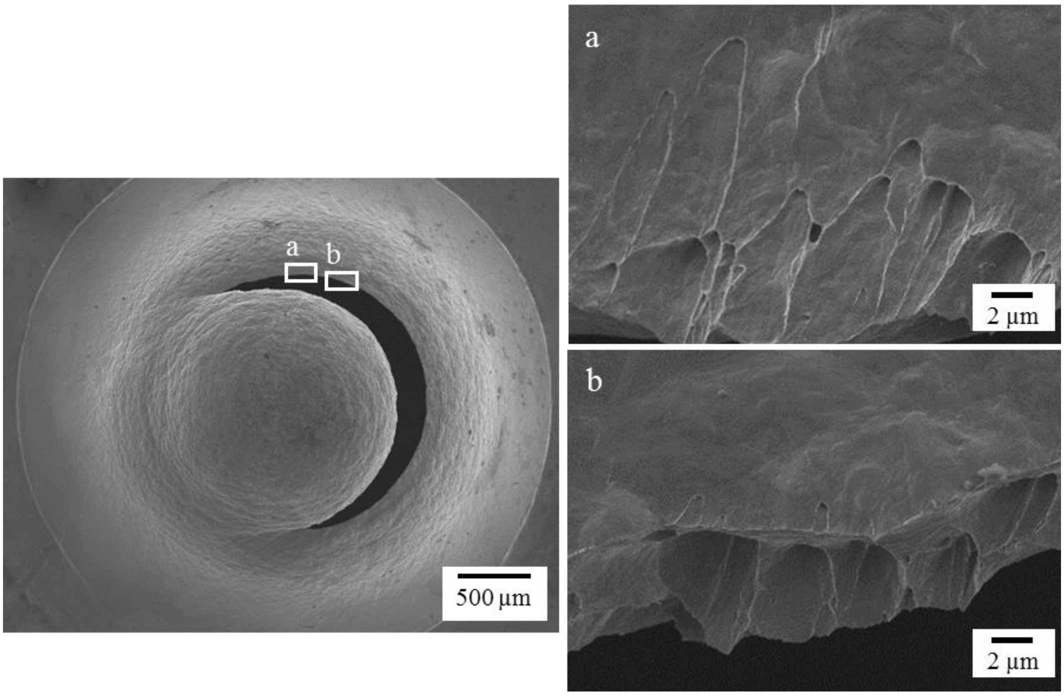

Figure III–10 Fractographies of a Cu sample tested by SPT in air at a displacement rate of 5 mm/min.

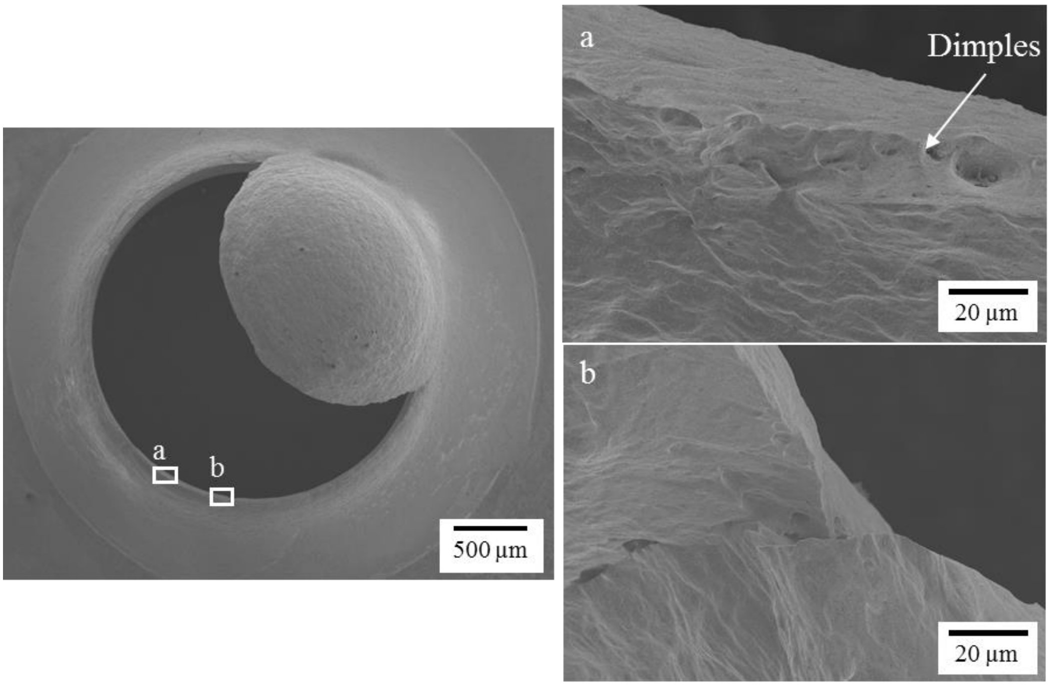

Figure III–11 Fractographies of a Cu sample tested by SPT in contact with the EGaIn at a 5 mm/min displacement rate.

Both Cu samples present a circular fracture that is typical of ductile materials [11], [36], [47]. Moreover, there are ductility dimples in the fracture surface of the samples, regardless if they were tested in air or in contact with the EGaIn. These dimples are more evident in the samples tested in air than those tested in the presence of the EGaIn since these last underwent the chemical removal of the liquid metal and the intermetallic, which corrodes the surface. The samples tested at lower displacement rates presented the same fracture behaviour.

In the case of the Cu-30%Zn samples that were tested in air, there are circular fractures, and they also present ductility dimples, which are signs of ductile behaviour. Figure III–12 exemplifies this fracture behaviour with a fractography of a sample tested at a displacement rate of 5 mm/min.

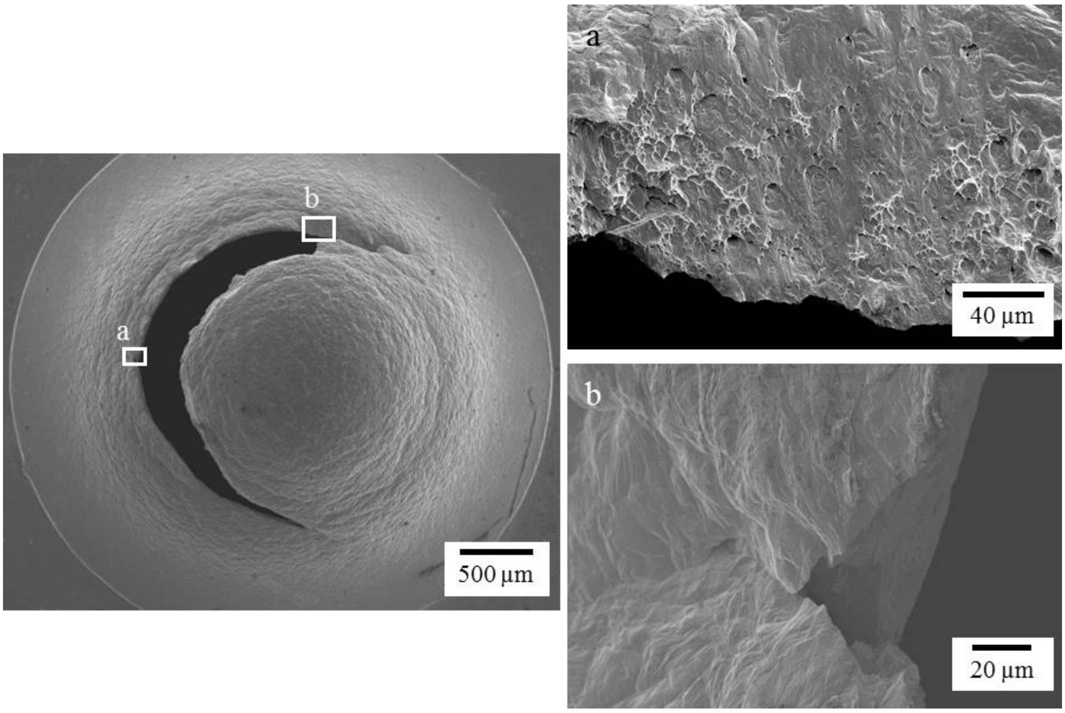

Figure III–12 Fractographies of a Cu-30%Zn sample tested by SPT in air at a 5 mm/min displacement rate.

On the other hand, the Cu-30%Zn samples tested in contact with the EGaIn present similar fractures with ductile characteristics, i.e., the circular shape of the fracture and the ductility dimples, as Figure III–13 illustrates. Furthermore, these samples present slight differences from those tested in air on the secondary fractures propagating radially from the circular fracture (Figure III–12b and Figure III–13b). The secondary fractures in these samples look more profound than those of the samples tested in air, and the plastic deformation seems less important, but the nature of these fractures is unclear.

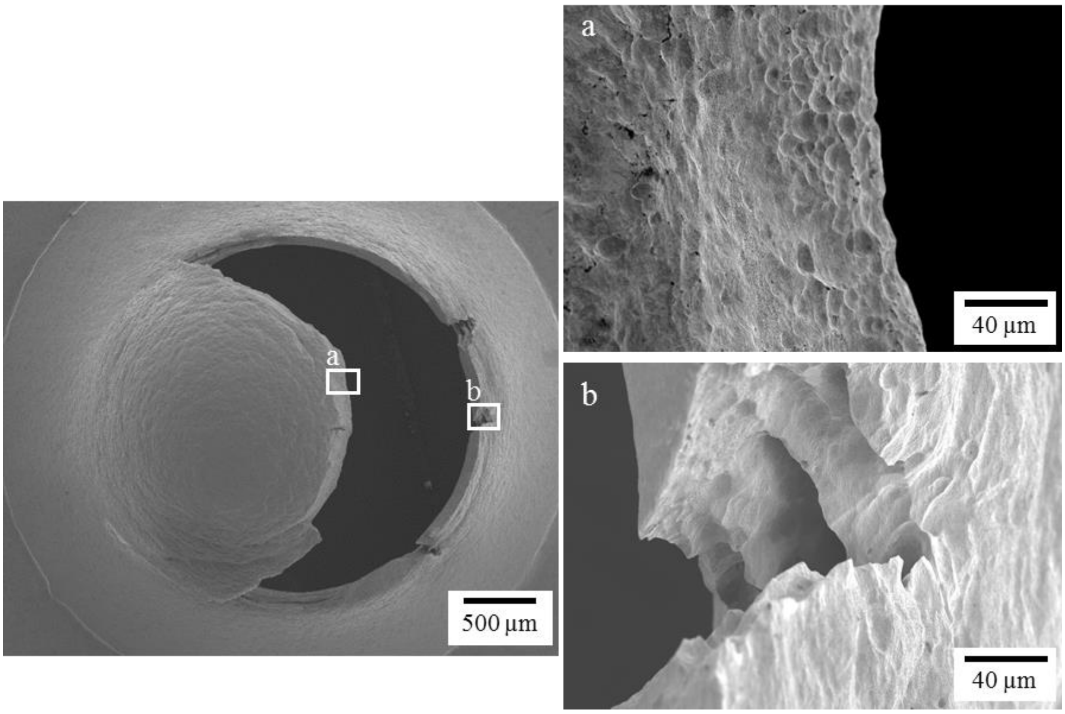

Figure III–13 Fractographies of a Cu-30%Zn sample tested by SPT in contact with the EGaIn at a 5 mm/min displacement rate.

The fact that the differences are found only in the secondary fractures could explain why there are no apparent differences in the force-displacement curves since these fractures would appear in the material after the propagation of the circular fracture and hence, at the very end of the force-displacement curves.

For this reason, using alternative geometries that present a more extended fracture propagation path seems to be a possible method to enhance the effect of the EGaIn on the Cu-30%Zn samples. Indeed, by using notched SPT specimens, the fracture propagation changes significantly.

III.2.3. Mechanical behaviour of Cu and Cu-30%Zn in contact with the EGaIn using notched SPT specimens

The notched specimens were tested according to the methodology explained before. The machining of these samples is significantly more complicated than the standard SPT specimens, and there are slight dissimilarities in the dimensions of the samples, independently of the production method used. In addition, there are variations in the positioning of the specimens in the SPT setup. All these are critical sources of irregularities that must be considered for interpreting the results.

Figure III–14 presents the force-displacement curves of the Cu specimens with a lateral notch. The form of these curves differs from those obtained with the standard specimens, and they are similar to that reported in works that used similar specimen geometries [34], [36], [39].

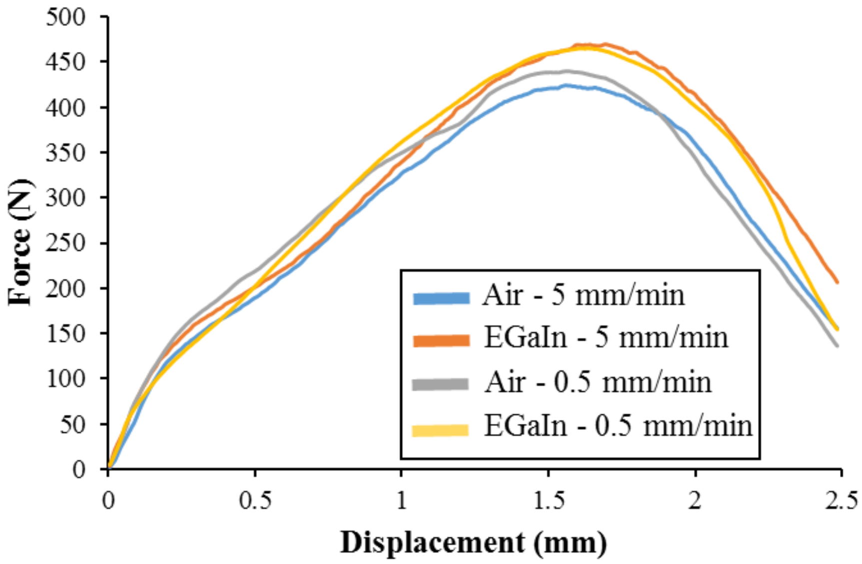

Figure III–14 Force-displacement SPT curves for Cu specimens with a lateral notch tested in air and tested in contact with the EGaIn at different displacement rates.

On the other hand, there is an evident dispersion of the results caused by the sources of variations exposed early. This dispersion is similar to that observed when testing specimens with different notch lengths [36], suggesting that the curves’ scattering is principally due to variation in the notch position regarding the setup during the tests.

There is no evident effect of the EGaIn on the mechanical properties of pure Cu tested by SPT with a lateral notch. The curves are similar regardless of the medium or the displacement rate. There was a similar behaviour at slower displacement rates (0.05 and 0.005 mm/min).

Some samples were observed with the SEM to detect differences between the samples tested in air and those tested in contact with liquid EGaIn. Figure III–15 and Figure III–16 show the fractographies of the Cu specimens with a lateral notch tested in air and in contact with the EGaIn, respectively.

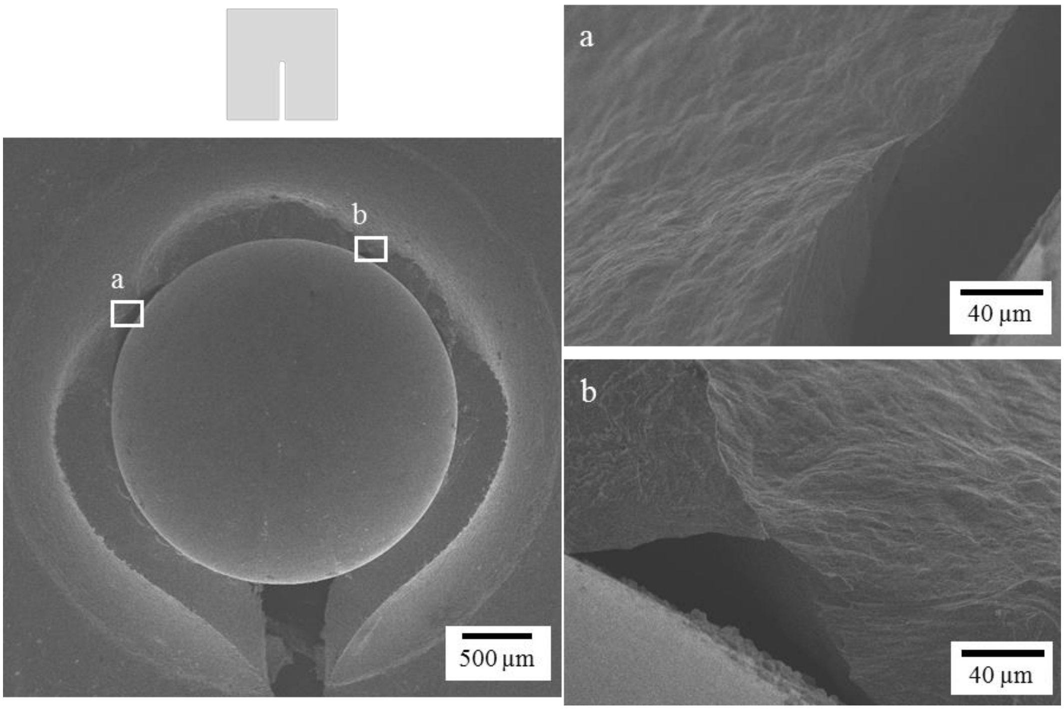

Figure III–15 Fractographies of a Cu SPT specimen with a lateral notch tested in air at a 5 mm/min displacement rate.

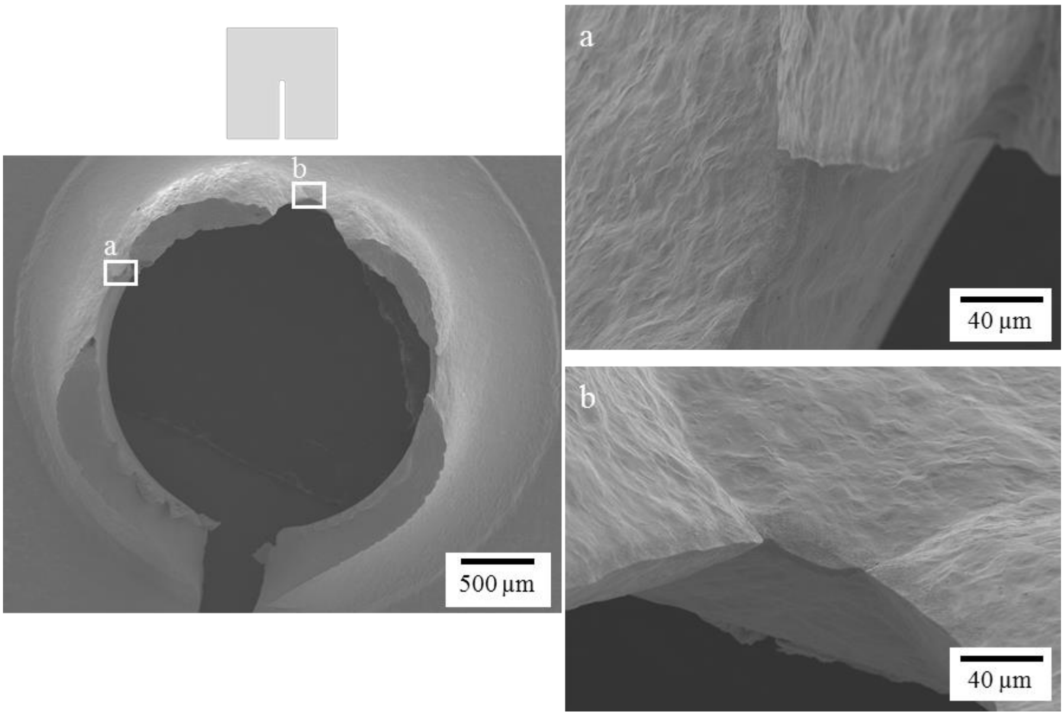

Figure III–16 Fractographies of a Cu SPT specimen with a lateral notch tested in contact with the EGaIn at a 5 mm/min displacement rate.

In these samples, there are no signs of ductility dimples; instead, all the specimens present rupture by necking, i.e., a reduction of the area transversal to the stress until the material breaks. This type of fracture implies a high plastic deformation of the Cu during its fracture and that the Cu samples presented a ductile behaviour in the conditions tested. There was no evidence of fracture modification by the EGaIn. The form and localization of the fractures are similar to other ductile materials tested with a similar specimen geometry [36].

On the other hand, Figure III–17 shows the correspondent force-displacement curves of the Cu-30%Zn specimens with a lateral notch. In them, there is a considerable dispersion of the measurements.

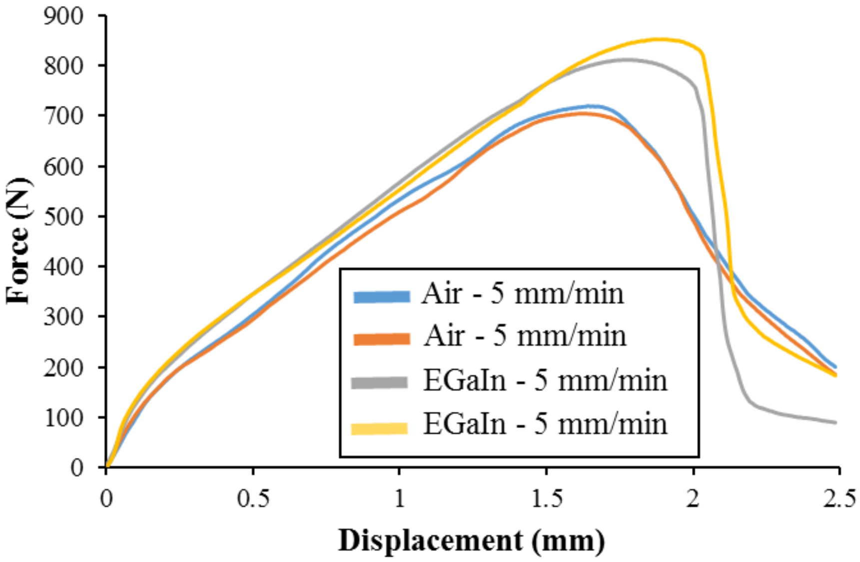

Figure III–17 Force-displacement SPT curves for Cu-30%Zn specimens with a lateral notch tested in air and in contact with the EGaIn at 5 mm/min.

There are differences in the fracture propagation stage between the samples tested in air and those tested in contact with the EGaIn. In the case of the samples tested in air, there is a constant force reduction, while for the samples tested in contact with the EGaIn, there is a more abrupt decrease of the force.

These differences are present after the point of maximum force, which is the crack initiation point in these specimens [36]. The lack of effect before the maximum force indicates that the EGaIn affects the fracture propagation of Cu-30%Zn under these conditions.

SEM images of the samples were taken to corroborate this effect. Figure III–18 shows the fractographies of a Cu-30%Zn sample tested in air, while Figure III–19 shows the fractographies of its counterpart tested in contact with the EGaIn.

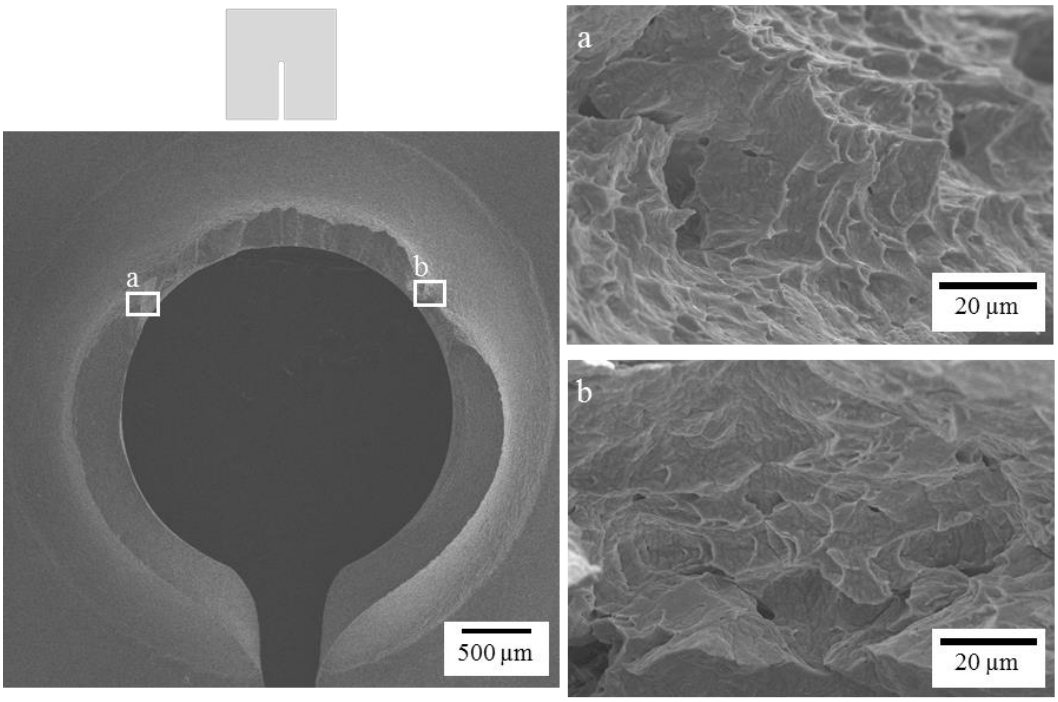

Figure III–18 Fractographies of a Cu-30%Zn SPT specimen with a lateral notch tested in air at a 5 mm/min displacement rate.

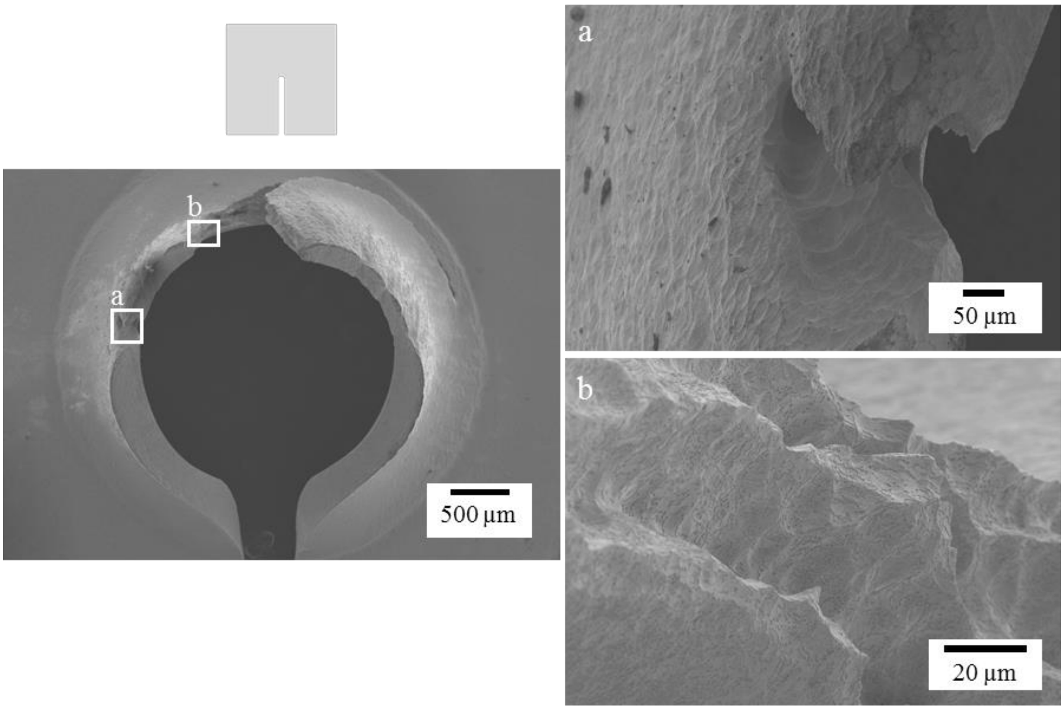

Figure III–19 Fractographies of a Cu-30%Zn SPT specimen with a lateral notch tested in contact with the EGaIn at a 5 mm/min displacement rate.

In the sample tested in air, there are clear signs of ductility in the multiple fractures formed at the bottom of the notch. Unlike Cu samples, these alpha brass samples present ductility dimples on the whole surface of the fractures. Moreover, the fractures' shape and localisation are similar to the case of Cu.

On the other hand, the sample tested in contact with the EGaIn presents some critical differences. The fracture in this sample is significantly more extensive, and no signs of significant plasticity exist. Figure III–20 shows a lateral view of this sample, where the fracture extension is visible.

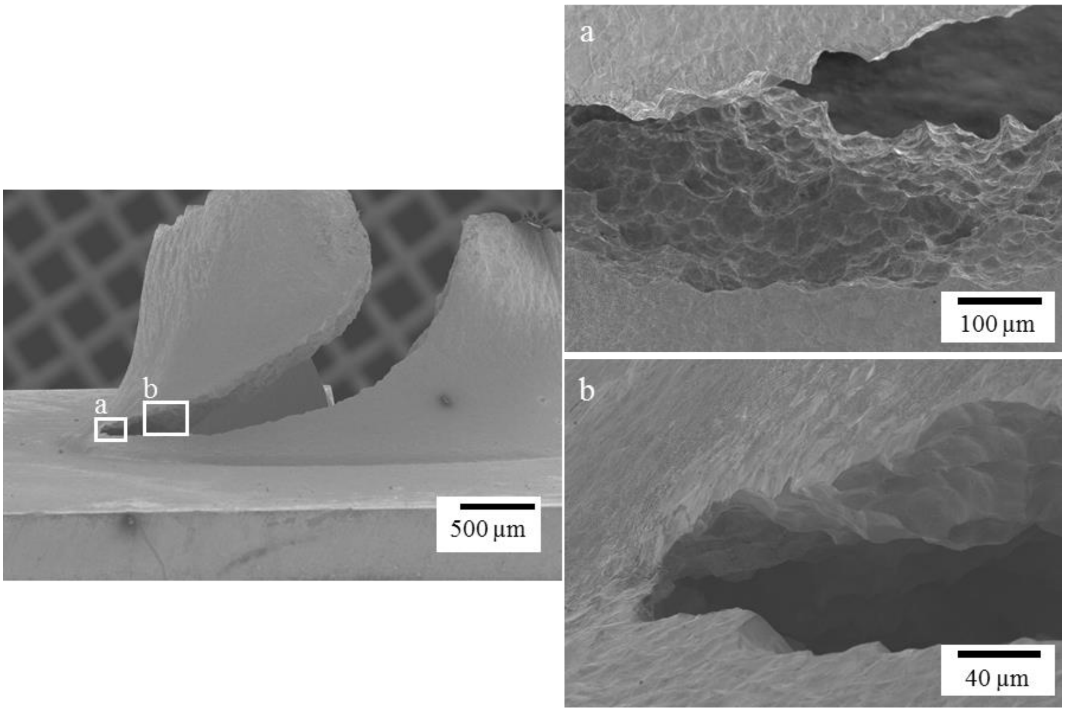

Figure III–20 Fractographies of a Cu-30%Zn SPT specimen with a lateral notch tested in contact with the EGaIn at a displacement rate of 5 mm/min (continuation).

The fracture propagates deep in the sample until it reaches the zone restrained by the dies. Moreover, there is a fracture with brittle nature. This nature seems more evident at the end of the fracture than at the beginning. These results confirm that the liquid EGaIn embrittles Cu-30%Zn under the specific conditions of this test.

Conversely, the samples tested at a slower displacement rate (0.5 mm/min) do not present any effect of the liquid EGaIn on their mechanical behaviour, as observed in their correspondent force-displacement curves in Figure III–21. The curves do not present any differences caused by the presence of the EGaIn.

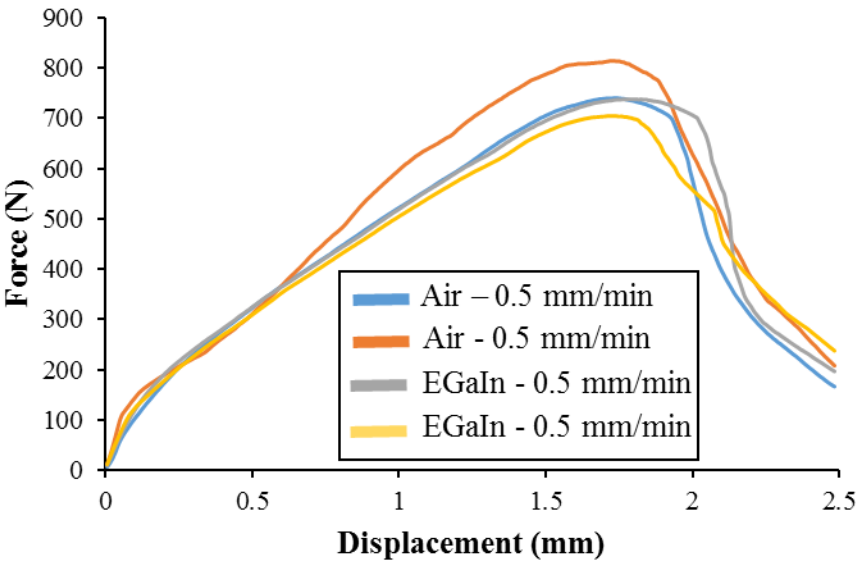

Figure III–21 Force-displacement SPT curves for Cu-30%Zn specimens with a lateral notch tested in air and in contact with the EGaIn at 0.5 mm/min.

To confirm that there was no effect of the EGaIn on the samples' fracture, fractographies of these samples were taken. The samples presented a ductile behaviour, and none showed signs of embrittlement, and there were no significant differences between the samples tested in air and those tested in contact with the EGaIn.

Additionally, to study the effect of varying the metallurgical conditions of the solids on their sensitivity to LME by the EGaIn, additional materials with the same composition as the initially studied materials but with a different metallurgical state were also tested employing the SPT using the lateral notched specimens. Table III–3 summarizes the metallurgical conditions of both of them.

Table III–3 Metallurgical conditions of the supplementary metals studied by SPT.

Composition	Thickness (mm)	Manufacturer	Hardness (HV)	Grain size (µm)
Cu - OFHC	0.5	Goodfellow	132 ± 2	Not measured
Cu -30 wt.%Zn	0.64	Alfa Aesar/annealed	82 ± 2	20 ± 3

The objective was to observe if a higher hardness could increase the sensitivity of LME in the case of pure Cu and if a lower hardness could decrease the sensitivity of LME in the case of Cu-30 wt.%Zn. For this, an additional sheet of OFHC Cu with a higher hardness was acquired from the supplier that provided the previous OFHC Cu sheet. This sheet presented a highly deformed microstructure, making the measurement of its grain size unfeasible by optical microscopy. For the case of Cu-30%Zn, annealing of 400 °C for 2 h was applied.

The Cu samples with a higher hardness presented the same mechanical behaviour as the previously tested Cu samples. As seen from the curves in Figure III–22, the only difference is that the force-displacement curves present a higher force than the Cu with less hardness (Figure III–14), which was expectable. Moreover, there are no significant differences between the Cu samples tested in air and those tested in contact with the liquid EGaIn, which was corroborated by SEM observation.

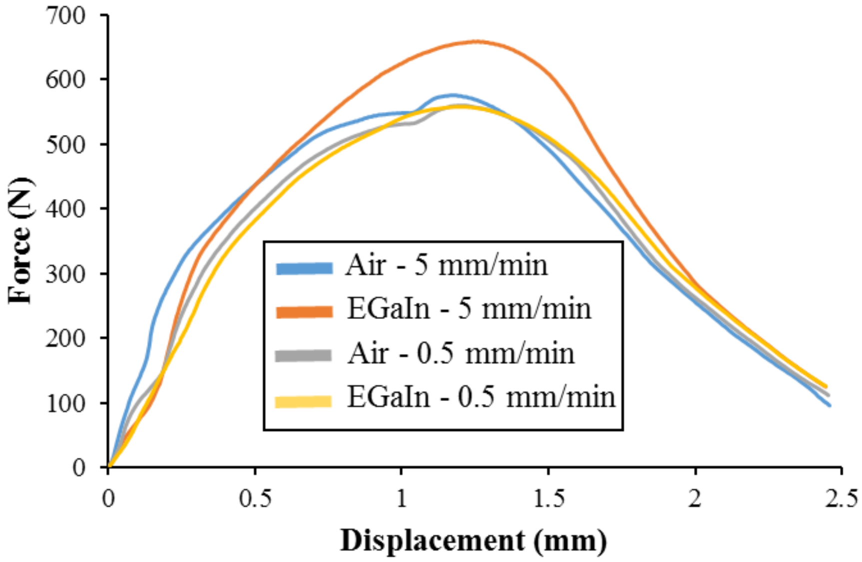

Figure III–22 Force-displacement SPT curves for Cu with higher hardness specimens with a lateral notch tested in air and in contact with the EGaIn.

Similarly, the annealed Cu-30%Zn samples presented the same tendency as those without heat treatment. Figure III–23 this tendency with the correspondent force-displacement curves. The curves of the samples tested in contact with the liquid EGaIn present slight differences in the stage of fracture propagation compared to the curves of the samples tested in air. These differences appear only for the samples tested at a 5 mm/min displacement rate. There are no differences in the force-displacement curves for the samples tested at slower displacement rates.

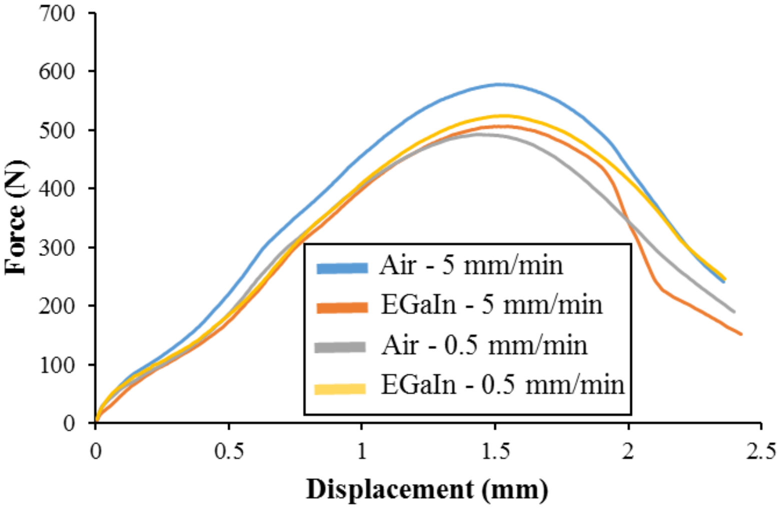

Figure III–23 Force-displacement SPT curves for annealed Cu-30%Zn specimens with a lateral notch tested in air and in contact with the EGaIn.

These differences indicate that there was embrittlement of the samples tested in contact with the liquid EGaIn when testing at a displacement rate of 5 mm/min but not on those tested at 0.5 mm/min. Figure III–24 and Figure III–25 corroborate this embrittlement by fractographic analyses. The first sample shows signs of embrittlement, while the second presents ductility dimples and no signs of embrittlement.

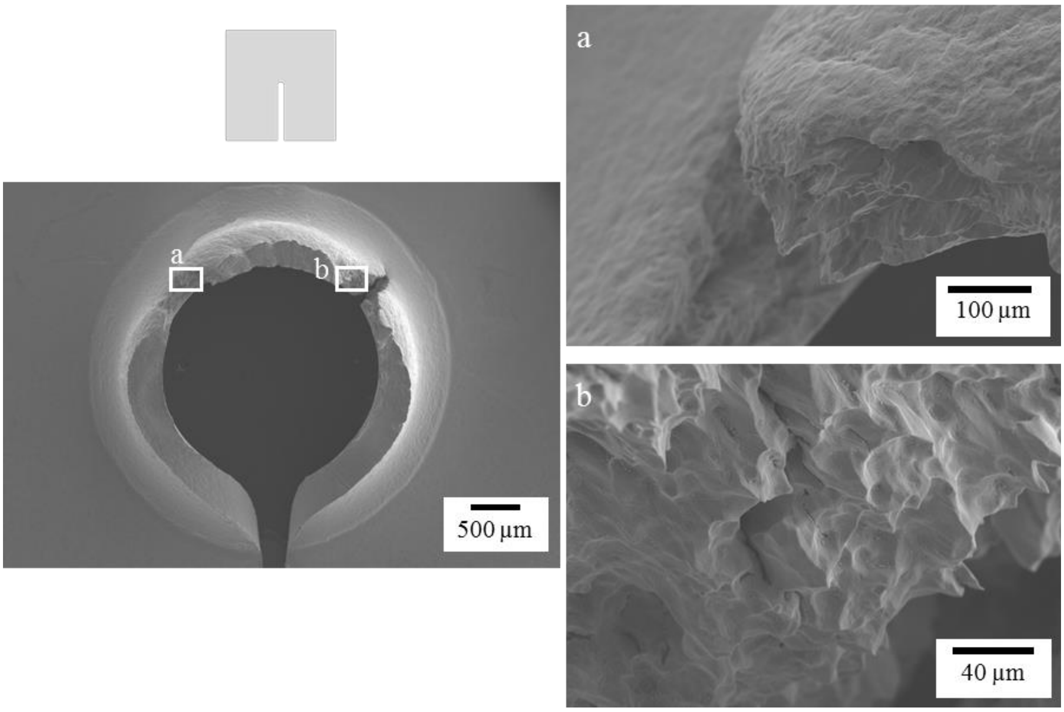

Figure III–24 Fractographies of annealed Cu-30%Zn SPT specimen with a lateral notch tested in contact with the EGaIn at a 5 mm/min displacement rate.

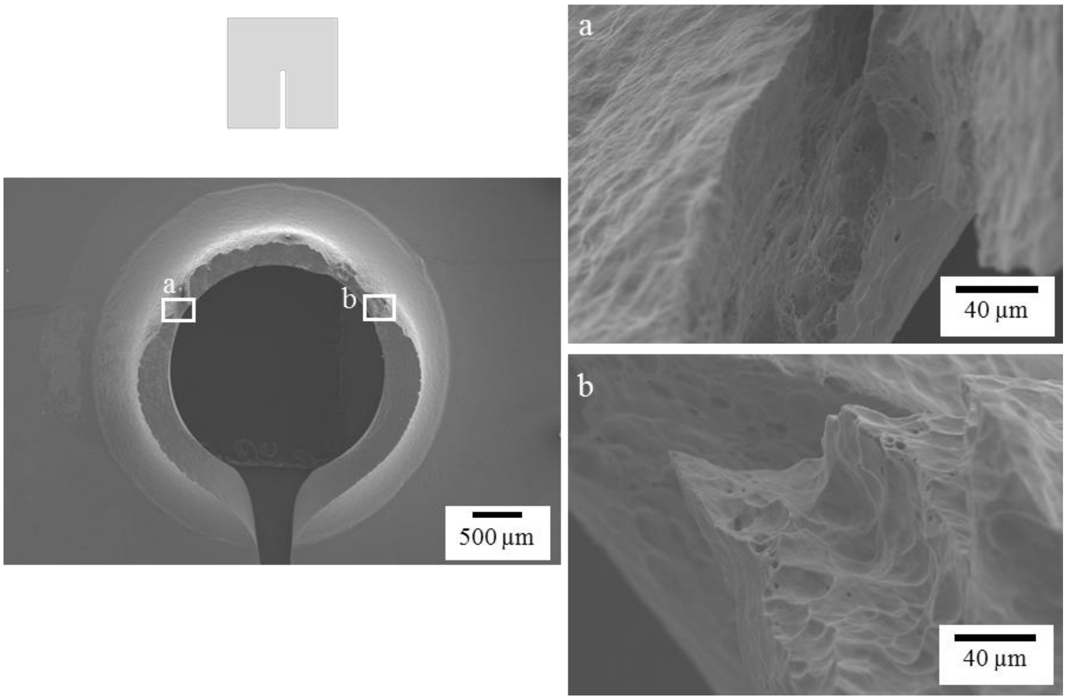

Figure III–25 Fractographies of annealed Cu-30%Zn SPT specimen with a lateral notch tested in contact with the EGaIn at a 0.5 mm/min displacement rate.

In addition to the laterally notched geometry, the longitudinally notched geometry was also used as an alternative to the standard SPT to study the EGaIn effect on the brass's fracture propagation. The longitudinal notch was done using a wafering blade or WEDM. Figure III–26 presents representative force-displacement curves for a 5 mm/min displacement rate for both notching methods.

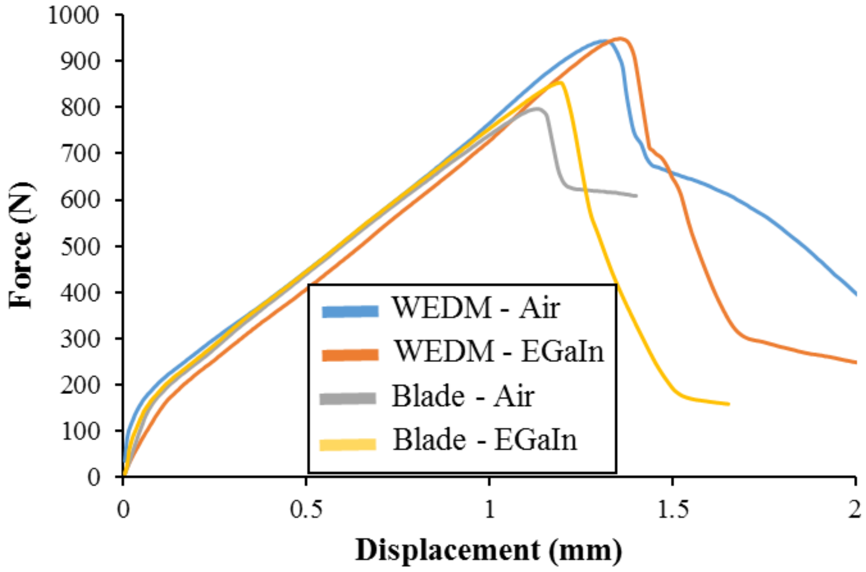

Figure III–26 Force-displacement SPT curves for Cu-30%Zn specimens with a longitudinal notch tested in air and in contact with the EGaIn at 5 mm/min.

The form of the curves is almost identical in air and in contact with the EGaIn. The curves present a behaviour similar to the classical SPT; at the end, there is a sudden decrease in force whenever the fracture starts. After this point, there are differences between the samples in air and those in contact with the EGaIn. In the curves of the samples tested in air, after the sudden decrease of the force, the force continues decreasing but at a slower rate. For the samples tested in contact with the EGaIn, the correspondent curves present the same decrease in the force, but at the end, the force falls abruptly again. These variations indicate differences during fracture propagation, possibly due to the LME.

SEM images were taken to compare the cracking and fracture behaviour in air (Figure III–27) and in contact with the liquid EGaIn (Figure III–28) to corroborate the embrittlement of the samples. The images show ductility dimples in the whole fracture surface of the sample tested in air. On the contrary, the sample tested in contact with the EGaIn only presents a partial ductile behaviour. More specifically, at the beginning of the fracture, ductility dimples evidence that there is ductile behaviour, but in a later stage, the fracture becomes brittle in one of the extremities of the sample, and the fracture propagates significantly more than in the sample tested in air.

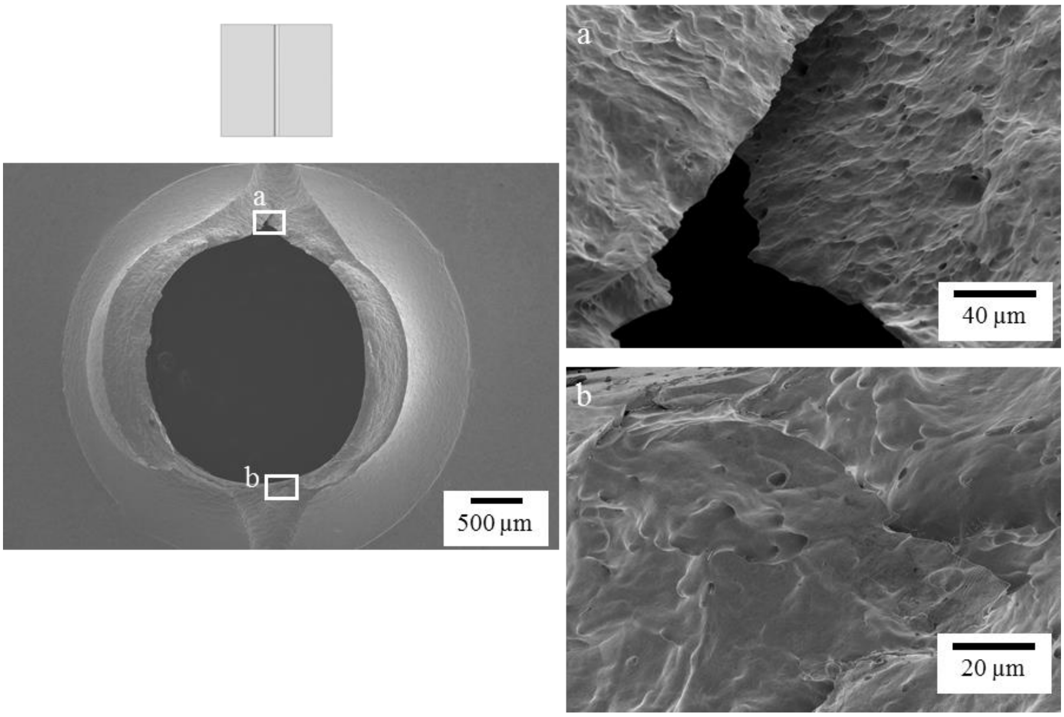

Figure III–27 Fractographies of Cu-30%Zn SPT specimen with a longitudinal notch tested in air at a 5 mm/min displacement rate.

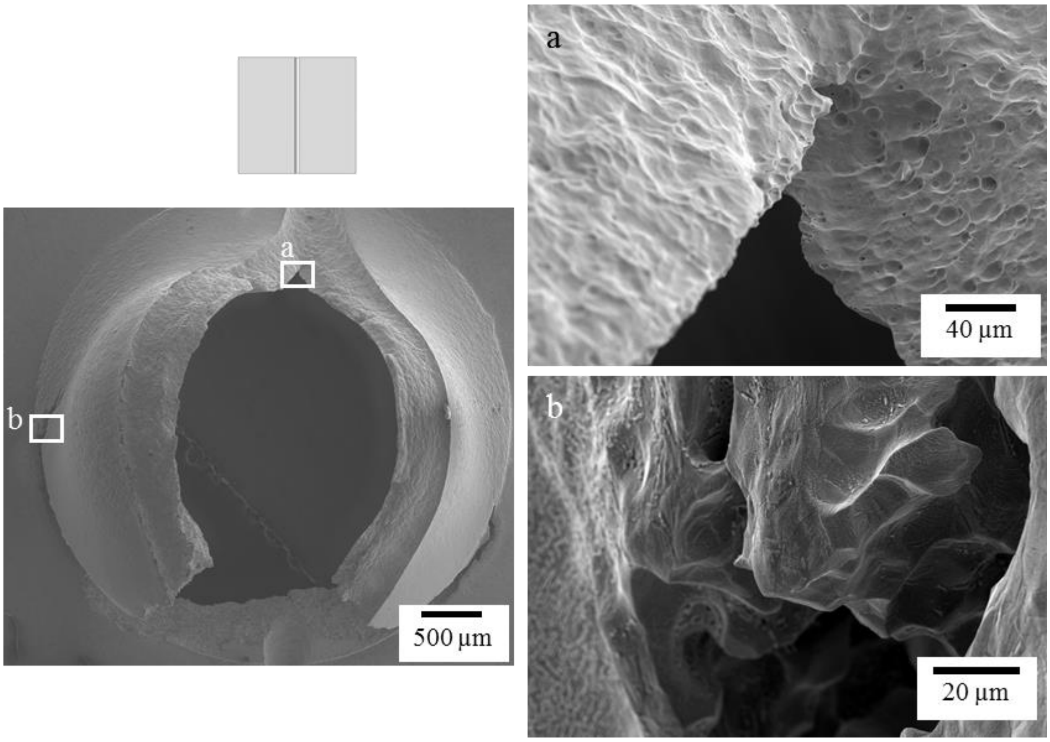

Figure III–28 Fractographies of Cu-30%Zn SPT specimen with a longitudinal notch tested in contact with the EGaIn at a 5 mm/min displacement rate.

On the other hand, when repeating the experiments with the same specimen geometry but at slower displacement rates, there are no apparent differences between the samples tested in air and in contact with the EGaIn. Figure III–29 shows the correspondent force-displacement curves. These curves are similar to that of the samples tested in air at a displacement rate of 5 mm/min, i.e., there is a sudden decrease of the force that stops at a certain point, after which the force decreases steadily.

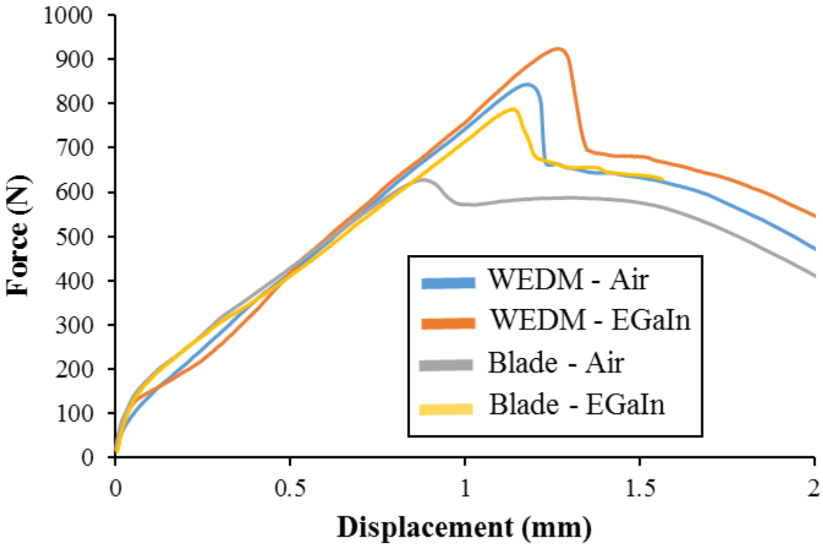

Figure III–29 Force-displacement SPT curves for Cu-30%Zn specimens with a longitudinal notch tested in air and in contact with the EGaIn at 0.5 mm/min.

SEM images of the samples corroborated that the samples behaved the same in air and in contact with the EGaIn. Figure III–30 shows one of the samples tested in contact with the EGaIn. In this sample, ductility dimples cover the fracture surface entirely, with no signs of embrittlement.

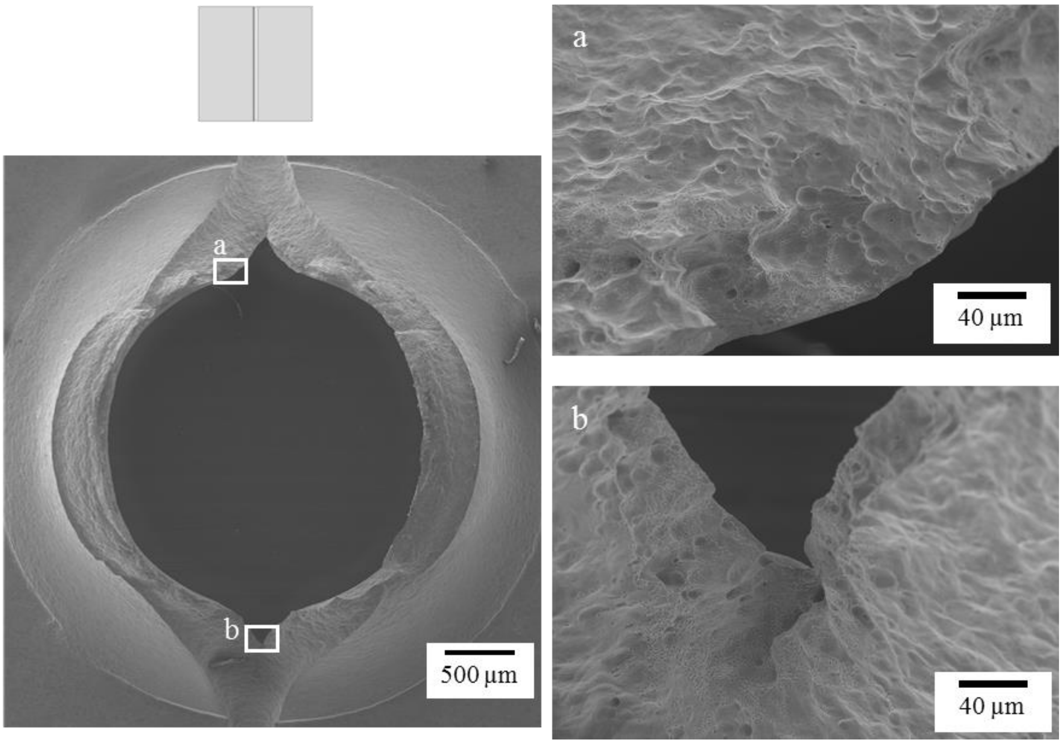

Figure III–30 Fractographies of Cu-30%Zn SPT specimen with a longitudinal notch tested in contact with the EGaIn at a 0.5 mm/min displacement rate.

Figure III–31 evidence that similar behaviour is observed at lower displacement rates when testing the samples notched using the WEDM. The fractographic analysis showed that in all of these samples, there was a continuous ductile fracture, similar to Figure III–30.

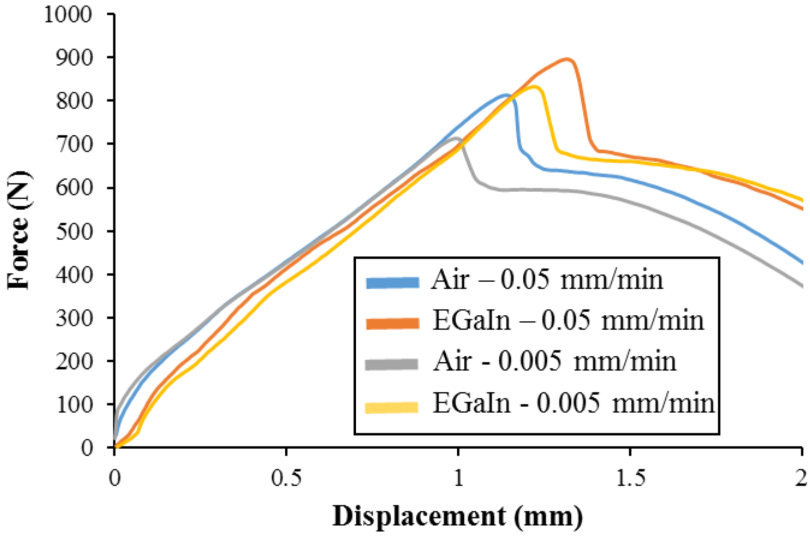

Figure III–31 Force-displacement SPT curves for Cu-30%Zn specimens with a longitudinal notch (WEDM) tested in air and in contact with the EGaIn at 0.05 and 0.005 mm/min.

These results confirmed that the longitudinally notched Cu-30%Zn samples presented a modification of its fracture propagation when in contact with the EGaIn only at high displacement rates.

III.3. Discussion on the effect of the EGaIn on the mechanical behaviour of Cu and Cu-30%Zn during the Small Punch Test

In the case of the Cu samples, there were no signs of LME by the EGaIn when using the SPT. For all the displacement rates tested, there were no significant differences in the force-displacement curves between the samples tested in air and those tested in contact with the liquid EGaIn.

The fractographies of these standard SPT samples show that the Cu failed by necking and by microvoid coalescence showing a circular fracture in all cases, which is a sign of a ductile behaviour not affected by the presence of the liquid EGaIn. In the case of the notched specimens, the necking was sharper than for the standard samples, and there were no ductility dimples at any of the displacement rates tested, both when tested in air and in contact with the liquid EGaIn. There was no effect of the hardness on the LME sensitivity of Cu.

In the case of the Cu-30 wt.%Zn, the force-displacement curves of the standard SPT samples did not present significant differences between the samples tested in air and those tested in contact with the liquid EGaIn. Moreover, their fractographies present a circular fracture, similar to the Cu samples, which indicates a ductile behaviour confirmed by the presence of ductility dimples in the surface of this circular fracture in all cases. This fracture behaviour was the same regardless of the displacement rate or the environment. Additionally, there are secondary fractures that appear perpendicular to the circular fracture. In the case of the samples tested in air, these secondary fractures present an explicit ductile behaviour with some necking and ductility dimples. However, there are some signs of brittleness for the samples tested in contact with the liquid EGaIn, but the fracture's nature is unclear.

The differences in the secondary fractures but not the principal circular fracture could be due to the EGaIn effect on the Cu-30%Zn mechanical behaviour during fracture propagation. If this is true, using another specimen that favours a long crack propagation stage would allow observing the effect of the EGaIn.

The Cu-30%Zn SPT specimens with a lateral notch present differences in their mechanical behaviour when tested in air and in contact with the liquid EGaIn at a 5 mm/min displacement rate. These changes are present in the force-displacement curves after the point of maximum force, where the samples tested in contact with the EGaIn present a more sudden decrease of the force, contrary to the samples tested in air which present a decrease of the force that is less pronounced. Before the point of maximum force, the curves do not present significant differences when tested in air and in contact with the liquid EGaIn, which indicates that the effect of the liquid EGaIn is present only during the stage of fracture propagation and that it does not seem to affect the yield strength, the plastic deformation, or the fracture initiation.

The fractographies of these samples showed that in the samples tested in contact with the EGaIn, the fracture propagates significantly more than in the samples tested in air. The samples tested in air have a ductile behaviour, with ductility dimples across their surface. On the contrary, the fracture of the samples tested in contact with the liquid EGaIn presents a brittle behaviour that is more pronounced at the end of the fracture.

On the other hand, the EGaIn effect on the fracture propagation of the Cu-30%Zn was only present when testing at a displacement rate of 5 mm/min. At lower displacement rates, there were no significant differences in the force-displacement curves or fracture behaviour, which indicates that higher strain rates favour the LME of Cu-30%Zn by the EGaIn.

The use of longitudinal notched geometries had a similar outcome. The samples tested at lower displacement rates did not present any effect of the EGaIn on their mechanical behaviour, while the samples tested at a displacement rate of 5 mm/min presented differences when tested in contact with the liquid EGaIn in comparison with those tested in air. In the case of the samples tested in air, the force-displacement curve presented a sudden decrease in the force that stopped, and then the force continued to decrease more gradually. For the samples tested in contact with the EGaIn, the force decreased continuously without changing significantly the rate of force decreasing.

The differences in the force-displacement curves that appear after the point of maximum force indicate that the EGaIn modified the fracture propagation of the samples. The fractographic analysis confirmed this effect, showing that the samples tested in contact with the EGaIn present a ductile fracture that propagates along the notch direction, as expected, and then bifurcates in brittle fractures at the bottom of the specimens. Moreover, the samples tested in air present fractures with ductility dimples and no signs of embrittlement.

No differences in the LME sensitivity appeared on Cu-30%Zn with lower hardness, which may be surprising given the influence of hardness reported by different authors [11], [48], [49].

Further investigation is needed to conclude if a more critical variation in the hardness could change the LME sensitivity of these materials.

The SPT is suitable for studying the LME phenomenon [11]. However, for the study of the LME of Cu-30%Zn in contact with the EGaIn, the standard SPT specimen was not sensitive to LME. In contrast, because of the liquid metal's effect on the crack's propagation and not on the initiation, the notched SPT specimens demonstrated to be more suitable for studying the LME sensitivity in this system.

The longitudinal notch geometry is more suitable for studying the LME in this system since the effect of the LME is present more evidently in the force-displacement curves without the need to perform fractographic studies. However, the production of this kind of sample is more complicated than the lateral notched geometries, which are still suitable for studying the LME. The lateral notched presents slight differences when tested in contact with the liquid EGaIn, so a fractographic study is needed to confirm the LME in these samples.

An alternative mechanical test is necessary to observe better the EGaIn effect on the fracture propagation of the Cu-30%Zn samples. This test should present a wide crack propagation with a crack initiation that starts on the material's surface, so the presence of liquid metal can influence it. A mechanical test that fulfils these requirements is the bending test.

III.4. The bending test

The bending test consists of the bending of a rectangular prism specimen supported at two points located at a distance L from the centre of the specimen, as Figure III–32 schematizes. The 3-point bending test has a third support in the centre of the opposite face of the specimen. The 4-point bending test has two supports allocated in the opposite face at a distance of L/2 from the centre.

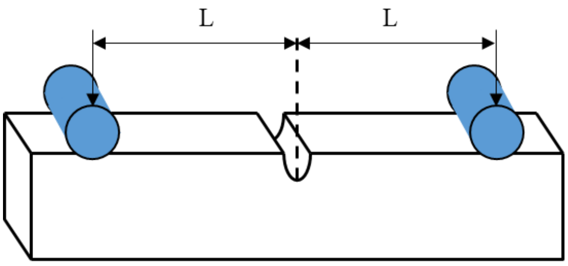

Figure III–32 Schema of a specimen for the bending test.

The test involves applying a compressive force to the supports that bend the specimen. This test generates a stress state where one of the faces presents tensile stress while the opposite face is under compressive stress. The stress magnitude is higher at the centre of the specimen's length, and, in the elastic regime of the material, this magnitude decreases linearly away from the centre. Figure III–33 illustrates these stress distributions in the elastic regime for the 4-point and 3-point bending tests.

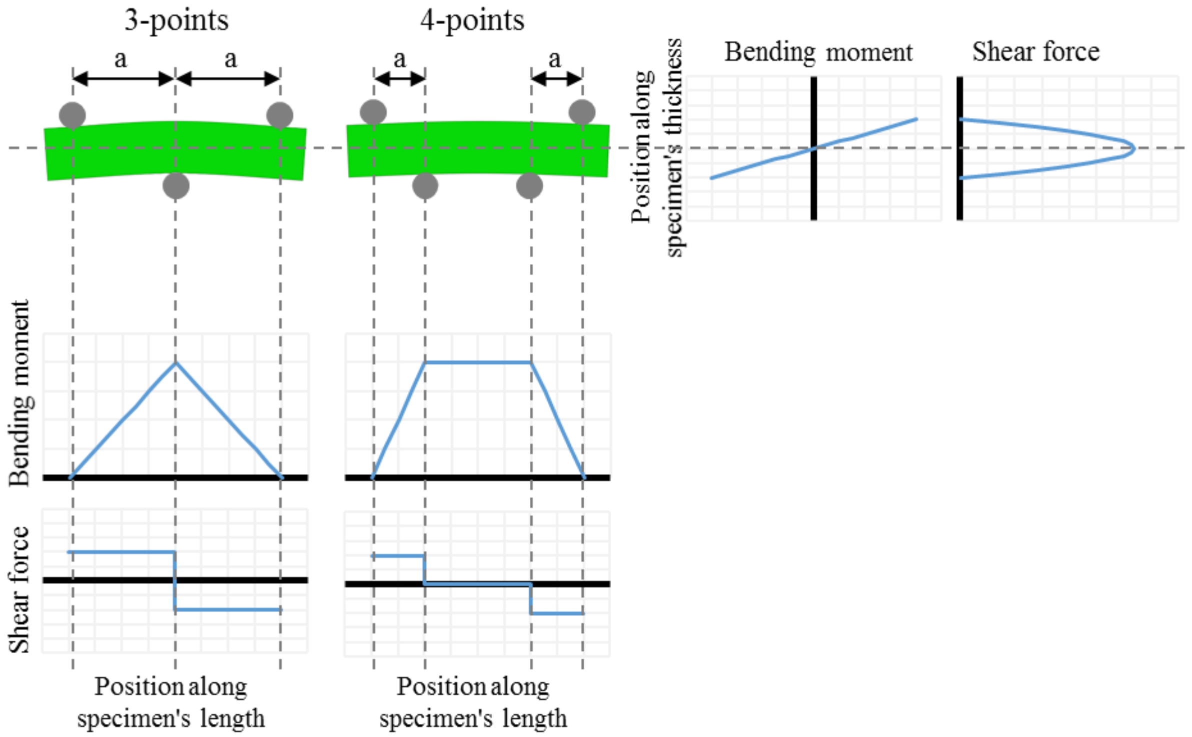

Figure III–33 Distribution of the bending and shearing stresses in the elastic regime during the bending test.

In the elastic regime, Eq. (15) express the relation between the magnitude of the stress in the longitudinal direction (σ_{xx}) and the applied load (F).

$$\sigma_{xx} = \frac{F \cdot a \cdot y}{2 \cdot I} \tag{15}$$

where a is the distance between the supports, y is the vertical distance from the centre of the sample, and I is the area moment of inertia for the cross-section.

This equation shows that at the same load magnitude, the longitudinal stress is higher in the 3-point bending test than in the 4-point bending test since the distance between the supports (a) is higher in the 3-point bending test.

Another difference between the two setups is that in the 3-point bending test, the maximum bending moment is located in the middle of the specimen, while in the 4-point bending test, the maximum bending moment covers all the zone between the central supports. This stress distribution makes the 4-point bending test less sensitive to misalignments of the supports. Also, in the 3-point bending test, there is a constant shear force along the beam's length that changes its direction at the middle point of the specimen, while for the 4-point bending test, the shear force is zero between the supports. The case presented is a simplified vision of the stress distribution in the bending tests.

Using a bending test to study the LME presents the advantage that the zone of the higher stress is on the outermost material surface, precisely at the notch of the specimen. This condition makes it possible to guarantee that the zone of failure initiation is in contact with the liquid metal during the test. In contrast, in the tensile tests, the core of the sample presents the same magnitude of stress, and the failure can start from the core and not necessarily from the surface. This condition can be modified by introducing a notch in the tensile test sample, but the stress concentration is not as high as for the bending tests. For these reasons, similar studies used bending tests to test in contact with liquid metals [50], [51].

III.5. Study of the sensitivity to LME of Cu and alpha brasses in contact with the EGaIn using the bending test

III.5.1. Methodology used in this work

The samples were manufactured by wire electrical discharge machining (WEDM) with the dimensions in Figure III–34, including the notch. The dimensions were chosen to perform miniaturized tests that allow for screening several testing conditions using little material. The sample height corresponds to the thickness of the initial sheet used for machining the samples, and the rest of the dimensions correspond to the typical relations for a bending test sample. The notch depths were measured by optical profilometry on several samples. The radius of the notch was measured by optical microscopy, with a value of approximately 0.15 mm.

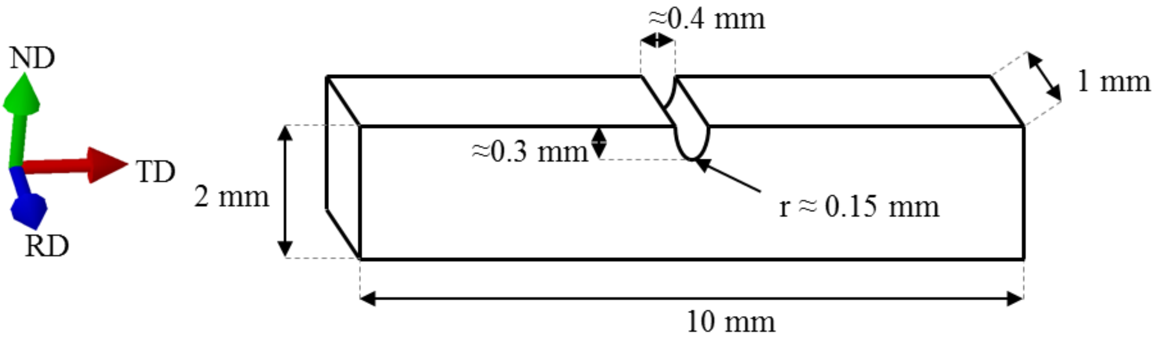

Figure III–34 Dimensions of the bending test sample.

A 5567A Instron Universal Testing Machine was used in compression mode along with the different setups in Figure III–35 to perform the bending tests. The 4-point setup was the first used in this study due to its low sensitivity to misalignments; the other setups were further used to increase the stress applied to the notch. The supports consist of 316 (UNS S31600) steel pins with a diameter of 1 mm. Four displacement rates were used: 5, 0.5, 0.05, and 0.005 mm/min. The tests stopped when the force decreased considerably. For some conditions, there was no such force decrease, and after certain displacement, the extremes of these samples touched the dies of the setups, which produced a sudden increase in the force; in these cases, the test was manually stopped.

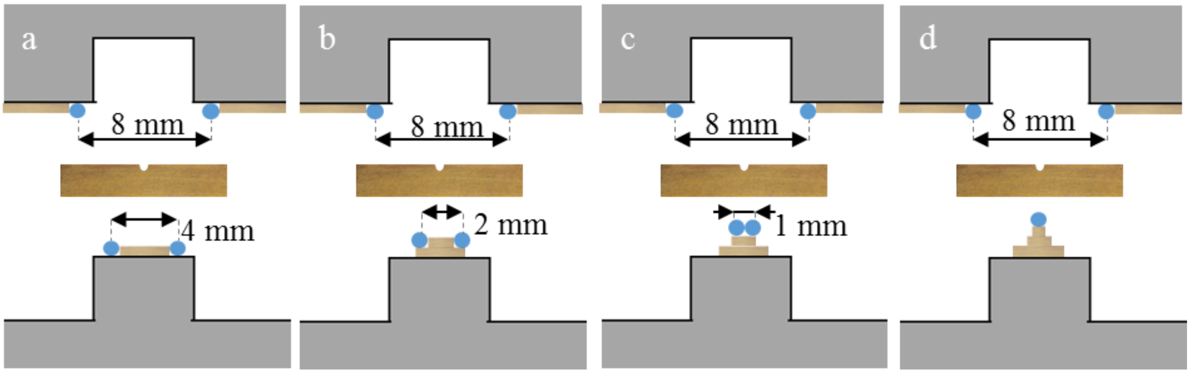

Figure III–35 Setups for the bending tests: a) 4-point, b) 2 mm, c) 1 mm, and d) 3-point.

For the test in contact in the presence of the EGaIn, good contact between the solid metal and the liquid metal was assured by removing the oxides from both of them just before the test, following a similar methodology described in the previous chapter (section II.1.2.). First, drops of EGaIn were submerged in a 1M HCl solution and stirred for a few seconds; then, the acid was removed. Likewise, a cotton swab was soaked with the same 1M HCl solution, and it was used to apply the acid on the top surface of the solid, taking special attention to rubbing the totality of the notch, then the acid was removed using a dry cotton swap.

Immediately after the oxide removal, a clean EGaIn drop with a volume of $\approx 1 \mu L$ was deposited on the notch with a RAININ micropipette. Before each test, it was confirmed with the naked eye that the EGaIn enters the notch. To exemplify, Figure III–36 depicts two situations of the contact of the liquid EGaIn on Cu-30 wt.%Zn samples: the situation on the left corresponds to a sample that undergoes the oxide-removing process, and the situation on the right side corresponds to a sample that did not undergo this process. Only in the first sample the EGaIn enters the notch; in the other sample, the drop suspends over the notch.

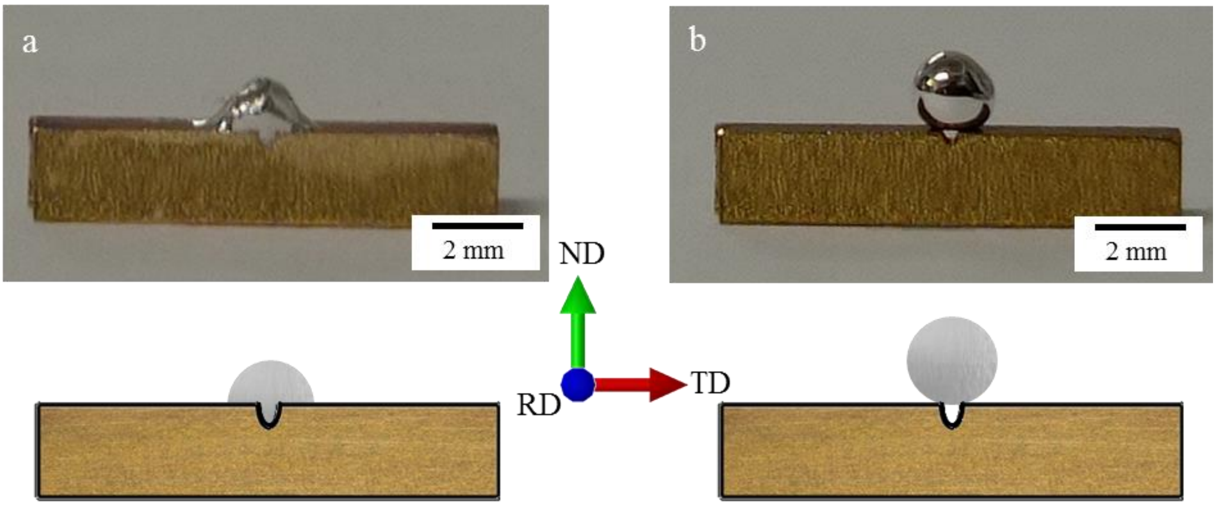

Figure III–36 Cu-30%Zn bending test samples in contact with the EGaIn a) with deoxidization and b) without deoxidization.

III.5.2. Effect of the bending test setup in the mechanical behaviour of Cu-30%Zn in contact with the EGaIn.

The first bending tests were carried out on a Cu-30%Zn alloy with a grain size of 39 ± 7 µm and a hardness of 142 ± 4 HV, which Alfa Aesar supplied in a sheet form with a thickness of 2 mm. This alloy was tested using the different setups in Figure III–35 in contact with the EGaIn at a 5 mm/min displacement rate.

As shown in their corresponding force-displacement curves in Figure III–37, the force in the curves is lower when testing the alloy with the setups with a smaller distance between the lower supports. These differences come from the relation between the stress magnitude and the distance between the supports, expressed previously in Eq. (15).

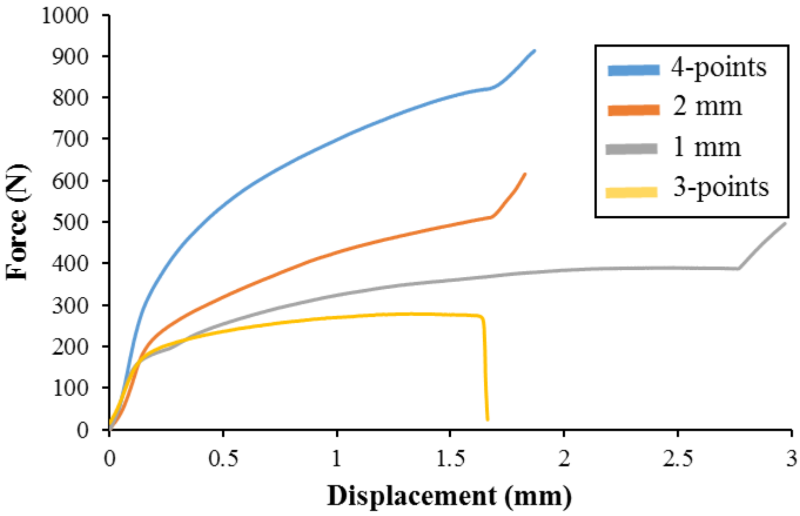

Figure III–37 Force-displacement curves of Cu-30%Zn specimens notched by WEDM and tested in contact with EGaIn at 5 mm/min with the different bending setups.

Moreover, there was a sudden decrease in the force only in the curves of the Cu-30%Zn samples tested using the 3-point setup. On the curves corresponding to the other setups, 4-point, 2 mm, and 1 mm, the force did not decrease at any moment. At the end of these curves, a sudden force increase corresponds to the specimens touching the setup.

Furthermore, the supports indented the sample during the tests. Moreover, this effect was less critical for the specimens with a lower distance between the lower supports, and the specimens tested using the 3-point setup did not present a significant indentation. Figure III–38 exemplifies these indentations. On the tests where there were indentations, significant plastic deformation occurred far from the centre, limiting the plastic deformation applied to the notch.

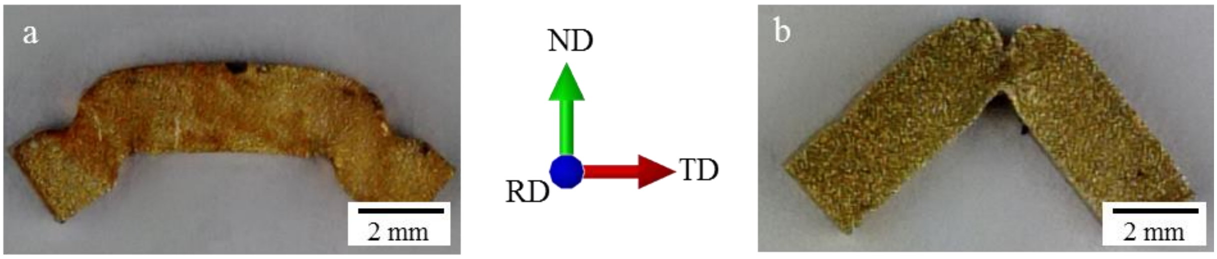

Figure III–38 Cu-30%Zn samples tested at a displacement rate of 5 mm/min in air using the a) 4-point and b) 3-point bending tests.

Only the 3-point bending test samples presented a fracture at the bottom of the notch. In the later section III.11., an analysis using the finite element method (FEM) compares the degree of plastic deformation and the stress states achieved by each bending test setup.

These results showed that the 3-point is the most suitable bending setup to study the sensitivity to LME. Hence, this setup is used for further tests in contact with the EGaIn and air.

III.5.3. Study on the LME sensitivity of the Cu-30%Zn in contact with the EGaIn by the 3-point bending test

The Cu-30%Zn samples were tested at different displacement rates in air and in contact with the liquid EGaIn. Figure III–39 shows the force-displacement curves of some samples tested at 5 and 0.5 mm/min in air and in contact with the liquid EGaIn; the curves indicate differences in the mechanical response between these samples.

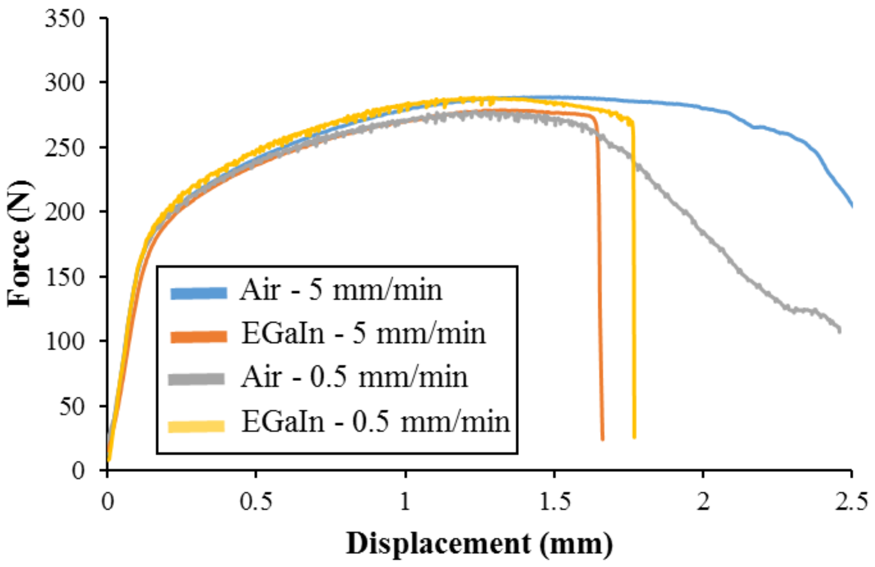

Figure III–39 Force-displacement curves of 3-point bending tests at 5 and 0.5 mm/min for Cu-30%Zn samples tested in air and in contact with the EGaIn.

The samples tested at air present a gradual decrease in the force after reaching the point of maximum force. On the contrary, the samples tested in contact with the liquid EGaIn show a sudden decrease in the force after reaching the point of maximum force.

Before reaching the point of maximum force, there are no significant differences in the mechanical behaviour of the Cu-30%Zn samples tested in air and in contact with the EGaIn. The fracture initiation in these samples should correspond to the point of maximum force or right before this point. Thus, the sudden decrease of the force that appears after the point of maximum force indicates that the EGaIn does not affect the mechanical behaviour of the solid before the point of fracture propagation.

There are slight differences in the force of curves between the samples due to misalignments of the central support. These differences appeared even between the samples tested under the same conditions. However, these force variations are not sufficiently significant enough to override the effect of the EGaIn on the mechanical properties of the Cu-30%Zn samples.

The Cu-30%Zn samples at slower displacement rates presented a similar mechanical behaviour, i.e., the samples at air present a gradual decrease of the force after the point of maximum force while the samples tested in contact with the EGaIn present a sudden decrease of the force after this point. Figure III–40 shows the correspondent force-displacement curves.

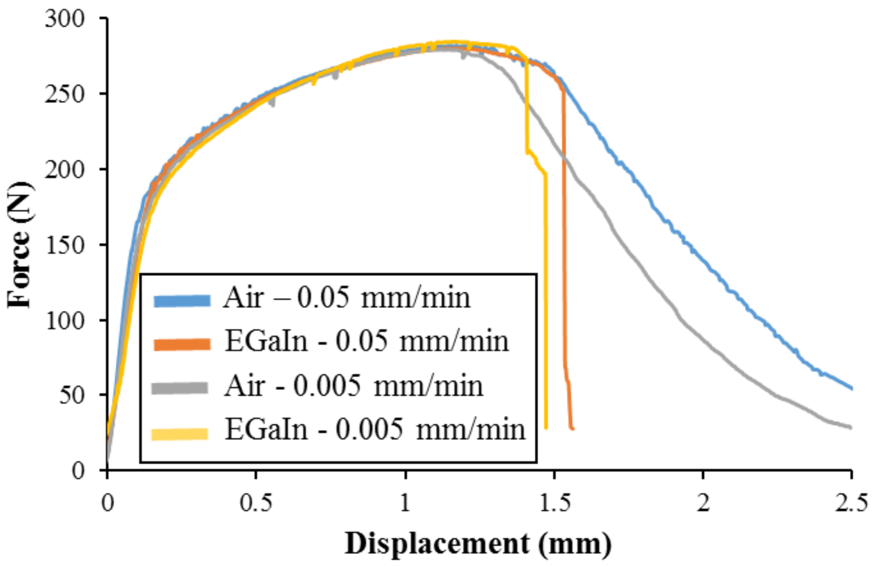

Figure III–40 Force-displacement curves of 3-point bending tests at 0.05 and 0.005 mm/min for Cu-30%Zn samples tested in air and in contact with the EGaIn.

Moreover, in the samples tested in air and those tested in contact with the EGaIn, the displacement to maximum force decreases when the displacement rate decreases. This difference is evident on a test with an even slower displacement rate (Figure III–41). For easier comparison, Table III–4 shows the displacement to maximum force (L_m) for some samples tested at the different displacement rates.

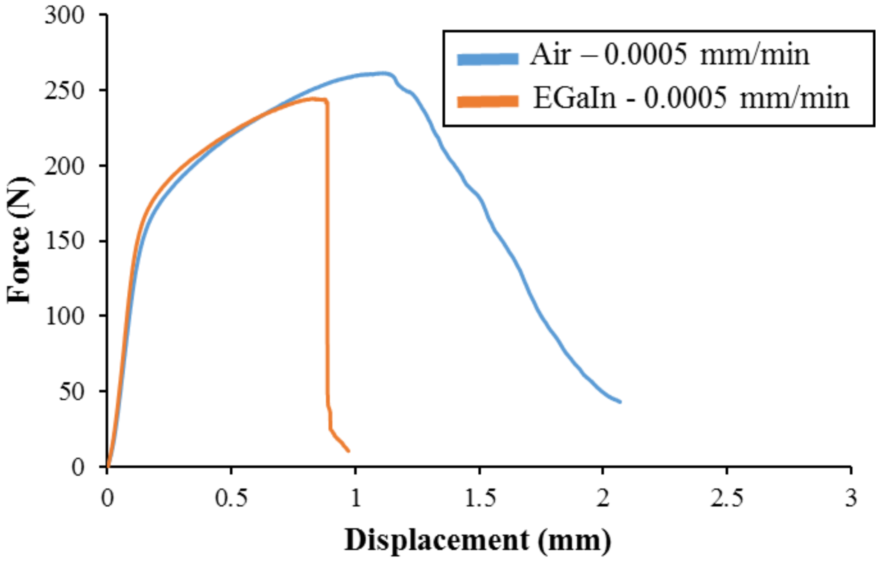

Figure III–41 Force-displacement curves of 3-point bending tests at 0.0005 mm/min for Cu-30%Zn samples tested in air and in contact with the EGaIn.

Table III–4 Maximum force and the correspondent displacement for Cu-30%Zn samples tested at different displacement rates.

Displacement rate (mm/min)	**Environment**	**Maximum Force (N)**	**L_m (mm)**	**ΔL_m (mm)**
5	Air	282 ± 9	1.41 ± 0.13	0.02
	EGaIn	277 ± 8	1.43 ± 0.14	
0.5	Air	279 ± 2	1.26 ± 0.04	0.04
	EGaIn	275 ± 10	1.30 ± 0.11	
0.05	Air	280 ± 5	1.20 ± 0.08	-0.04
	EGaIn	274 ± 7	1.16 ± 0.02	
0.005	Air	285 ± 8	1.10 ± 0.01	-0.08
	EGaIn	272 ± 13	1.02 ± 0.13	
0.0005	Air	262	1.11	-0.29
	EGaIn	242 ± 20	0.82 ± 0.11	

The samples tested in contact with the liquid EGaIn tend to present a lower displacement to fracture when the displacement rate is slower. This behaviour alone could indicate that the effect of the EGaIn on the mechanical behaviour of the brass is more critical at slower displacement rates. However, since the Cu-30%Zn samples presented the same tendency in air at all displacement rates, the effect of the EGaIn should be compared differently. The area under the curve was calculated to measure the energy related to the sample's deformation to better compare the EGaIn effect on the brass mechanical response. Two different criteria were used for this calculation. One calculates the area under the curve at a displacement corresponding to the fracture propagation when a force value of 200 N is reached. The 200 N is used as a criterion to compare the energy at fracture better since not all samples reached the sample force value at the end of the curve. In addition, the area under the curve is calculated at a displacement corresponding to the maximum force value. Table III–5 shows the difference between the areas of the samples tested in air and those tested in contact with the EGaIn; the average of two samples tested in air and two samples tested in the presence of liquid EGaIn were used for the computations.

Table III–5 Difference of the energy associated with the deformation between the samples tested in air and those tested in contact with the liquid EGaIn.

Displacement rate (mm/min)	ΔEnergy at 200 N (mJ)	ΔEnergy at maximum force (mJ)
5	-225	-11
0.5	-56	-8
0.05	-52	7
0.005	-36	4
0.0005	-77	-39

The table shows that the change in the area at 200 N is more significant at a displacement rate of 5 mm/min. At the other displacement rates, the change in the area under the curves decreases with the displacement rate. However, the difference at the lower displacement rate does not follow this tendency, presenting a higher difference in the change of the area under the curve. Additionally, when comparing the area under the curve at maximum force, it can be corroborated that there is no significant change in the mechanical behaviour up to the point of maximum force between the samples tested in air and those tested in contact with the liquid EGaIn. Again, the samples tested at the lowest displacement rate contraries this tendency.

As shown earlier, all force-displacement curves of the samples tested in contact with the liquid EGaIn present a sudden decrease in force. This sudden decrease indicates that in these conditions, the necessary energy for fracture propagation is lower than for the samples tested in air. If this is the case, the Cu-30%Zn presents LME in contact with the EGaIn under these conditions, and the samples' fractures should present a brittle behaviour.

In the first instance, the fractures of some Cu-30%Zn samples were observed macroscopically. Figure III–42 shows that, even at this scale, the fracture of the Cu-30%Zn samples tested in air and those tested in contact with EGaIn presented differences.

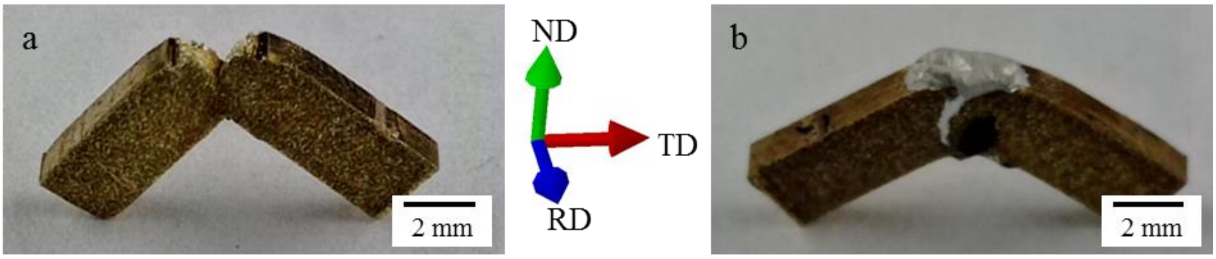

Figure III–42 Fractured specimens of Cu-30%Zn samples tested using the 3-point setup at a displacement rate of 5 mm/min: a) in air and b) in contact with the EGaIn (right).

The sample tested in air presents a fracture that started at the notch's bottom. The sample tested in contact with the liquid EGaIn also presents a fracture that initiates in the notch but propagates differently. In this case, the fracture forms an arc that departs diagonally from the notch filled with the liquid EGaIn. This fracture reaches the bottom of the sample, so the sample completely separates into two pieces.

Furthermore, some samples were observed using SEM to identify the nature of these fractures. Figure III–43 shows the fracture surface of a sample tested in air at a 5 mm/min displacement rate. This sample did not break completely, so the fracture can only be observed partially. Anyhow, the fracture surface presents ductility dimples, which evidenced the ductile nature of the material when fractured in air.

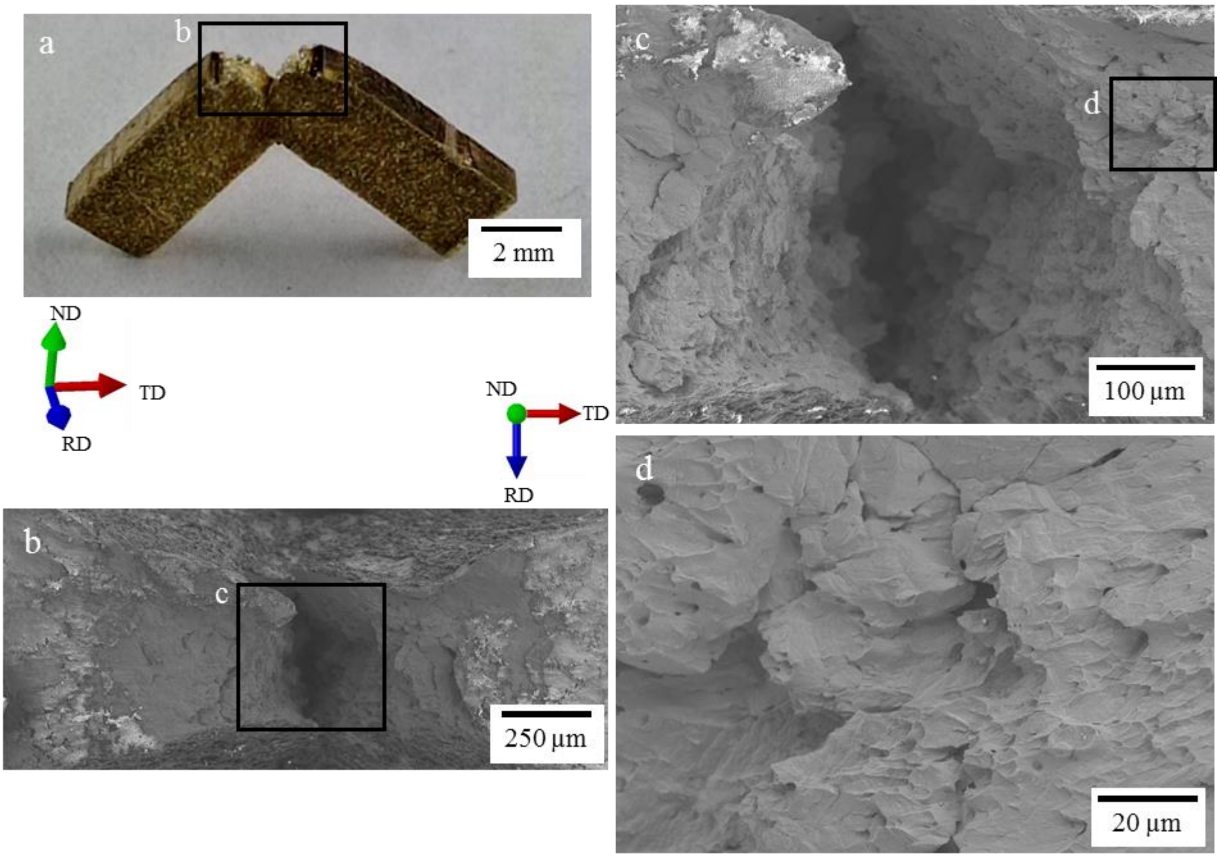

Figure III–43 Fractographies of a Cu-30%Zn sample tested using the 3-point bending test at a displacement rate of 5 mm/min in air.

The samples tested in contact with the EGaIn were chemically treated similarly to the SPT specimens to observe better their fracture surface, i.e., the liquid metal and the intermetallic were removed using 1.1 M HNO_3 and 1 M NaOH solutions. Section II.3. details this process. Figure III–44 shows the fracture of a sample tested in contact with the EGaIn at a displacement rate of 5 mm/min.

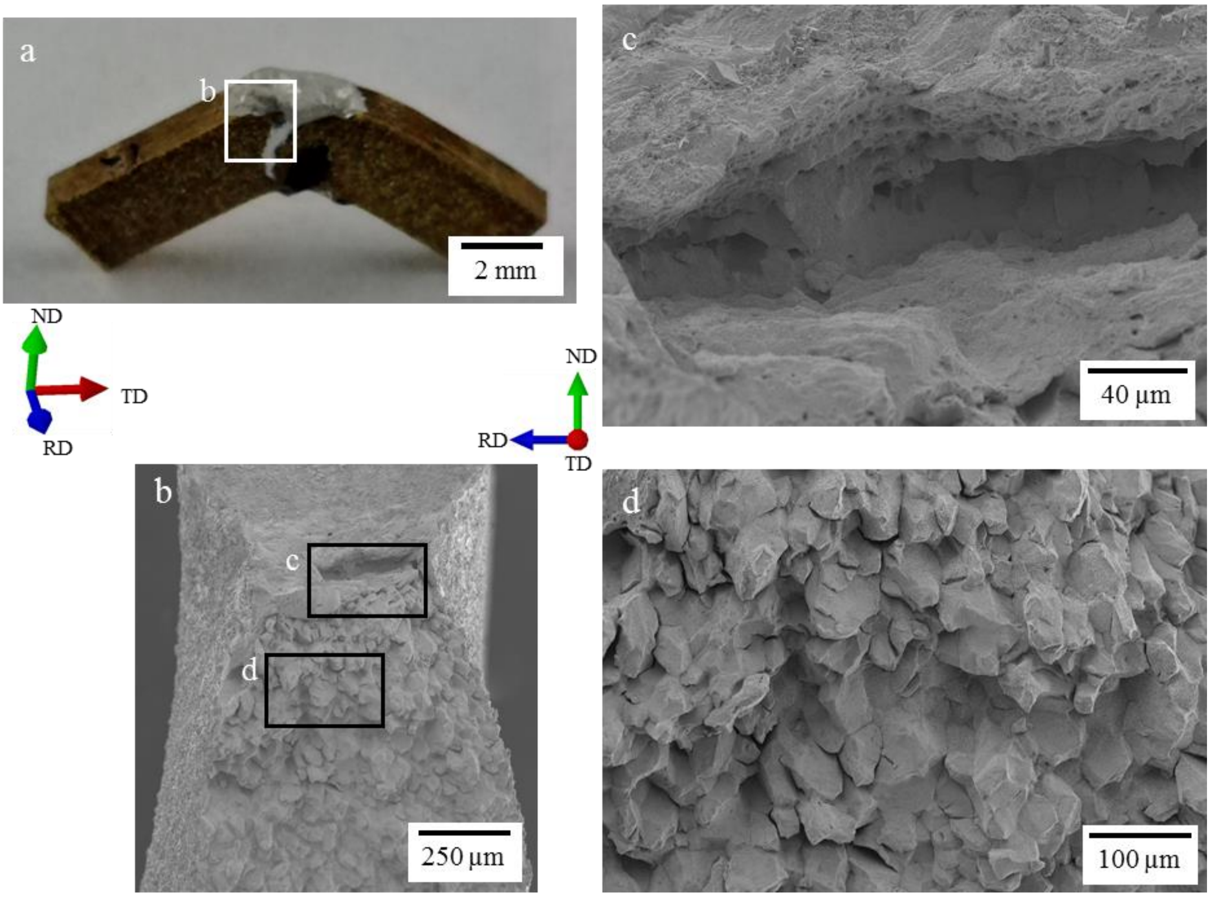

Figure III–44 Fractographies of a Cu-30%Zn sample tested using the 3-point bending test at a displacement rate of 5 mm/min in contact with the EGaIn and then chemically cleaned.

The fracture presents two different zones. In the zone next to the notch (Figure III–44c), there are ductility dimples that corrode due to the chemical cleaning treatment. Then, there is a zone with a brittle fracture that appears intergranular (Figure III–44d).

Figure III–45 presents another sample tested under the same testing conditions to illustrate further the existence of the two different fracture zones, which appeared consistently in all the samples tested in contact with the EGaIn, regardless of the displacement rate. Figure III–45b shows the crack initiation zone with several dimples. Figure III–45c presents the same zone but rotated to observe better the transition zone between the ductile fracture surface with dimples and the intergranular brittle fracture (Figure III–45d).

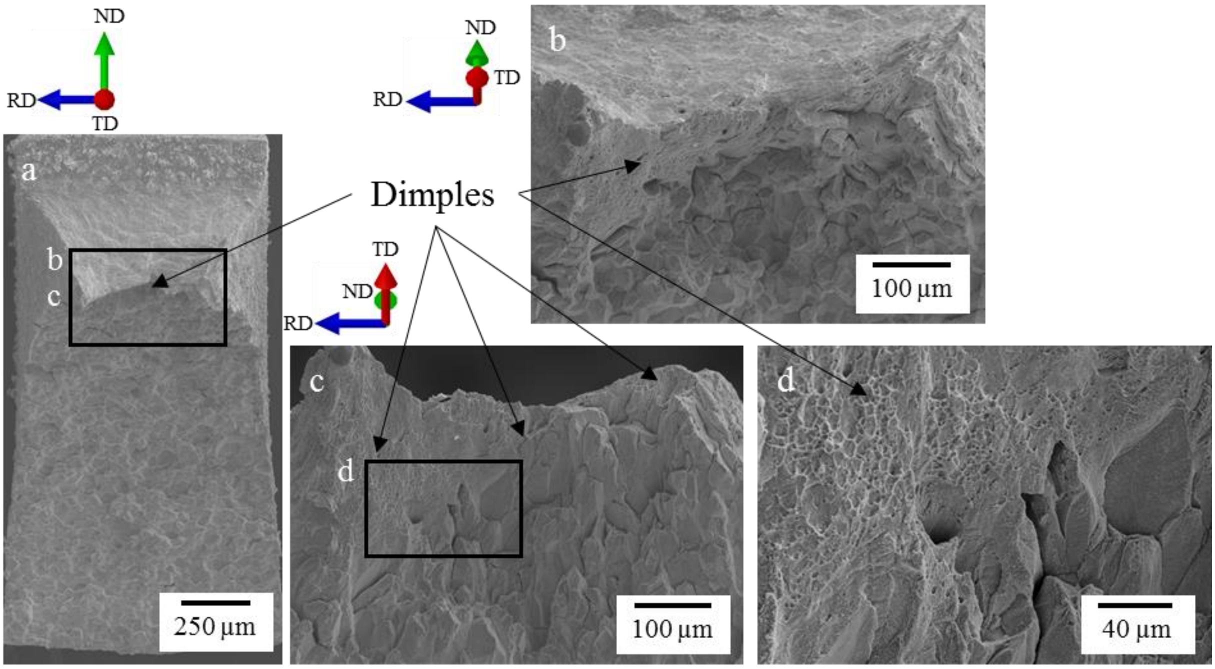

Figure III–45 Fractographies of a Cu-30%Zn sample tested using the 3-point bending test at a displacement rate of 5 mm/min in contact with the EGaIn.

For confirmation that the first zone of the fracture is a ductile fracture, a transversal cut was made on a third sample tested under the same conditions, and an Electron Backscatter Diffraction (EBSD) analysis was performed. Figure III–46 shows this analysis.

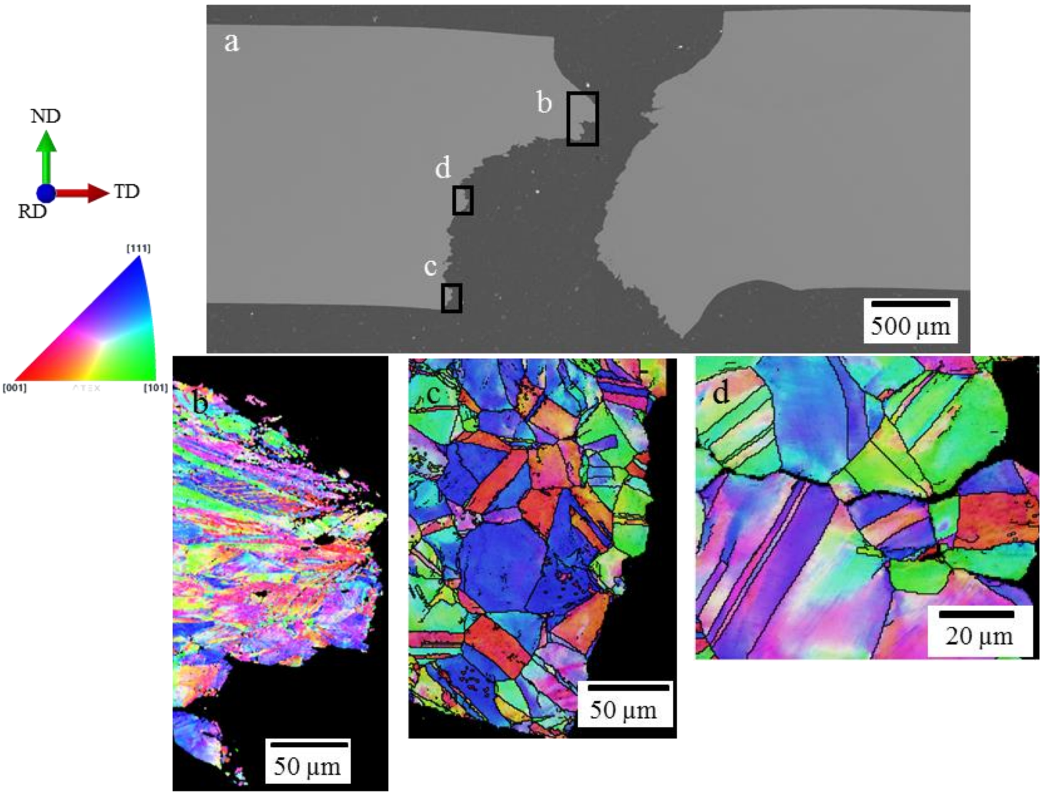

Figure III–46 EBSD analysis of the fracture of a Cu-30%Zn sample tested using the 3-point bending test at a displacement rate of 5 mm/min in contact with the EGaIn.

The EBSD analysis shows significantly more deformation in the first stages of the fracture, which matches the observation of a ductile fracture. At later stages of the fracture, only a slight deformation is present in the grains adjacent to the fracture. In this stage, the nature of the fracture is effectively intergranular.

In the analysis of the samples tested in air at lower displacement rates, the samples tested at lower displacement rates presented a complete rupture, which allowed the direct observation of the fracture; e.g., Figure III–47 shows the sample tested at a displacement rate of 0.005 mm/min. Nevertheless, the ductile behaviour is the same as for the samples tested in air at the other displacement rates tested.

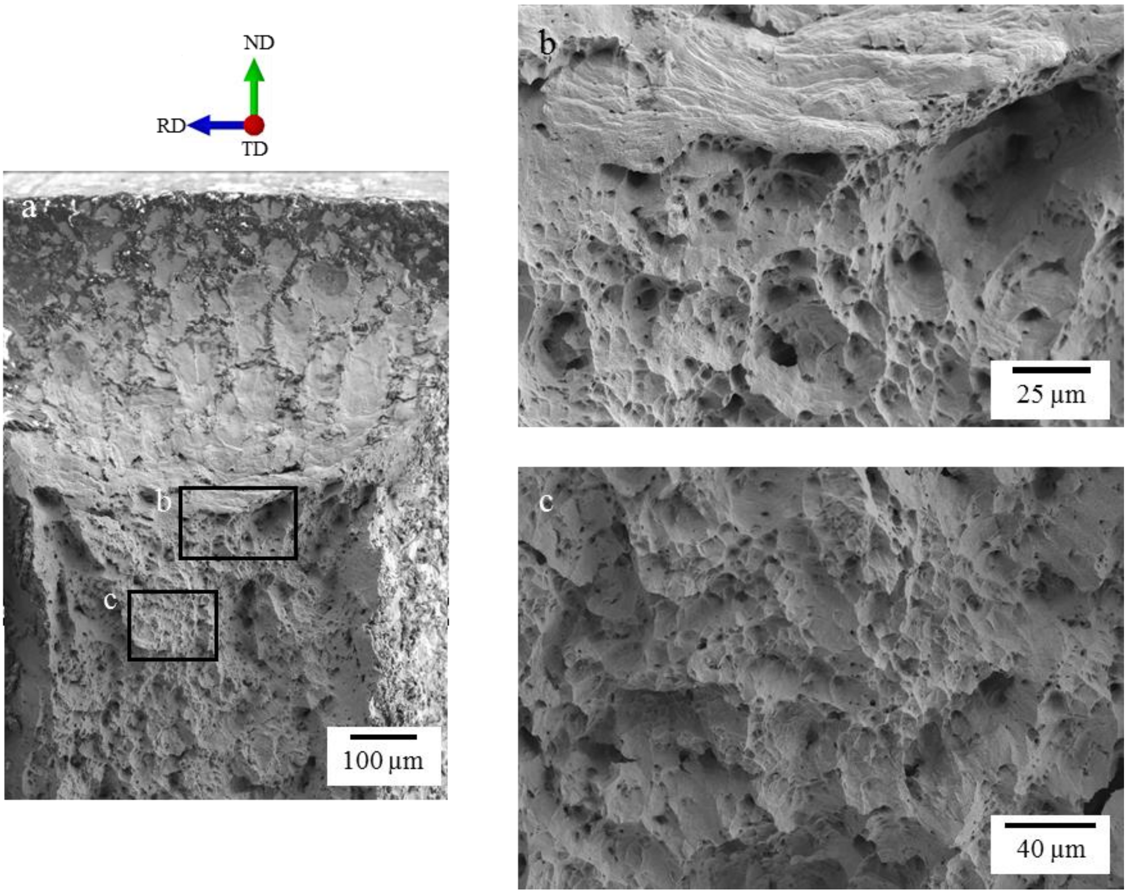

Figure III–47 Fractographies of a Cu-30%Zn sample tested using the 3-point bending test at a displacement rate of 0.005 mm/min in air.

On the other hand, the samples tested in contact with the liquid EGaIn at lower displacement rates also present the same fracture behaviour as those tested at 5 mm/min. Contrary to the samples tested at 5 mm/min, the intermetallic formation is more extended in the other samples, so the observation of the fractures is more complicated. For instance, Figure III–48 shows the fractographies of a sample tested at a displacement rate of 0.005 mm/min in contact with the

EGaIn. The ductile fracture can barely be observed in these images, but a brittle intergranular fracture remains clear.

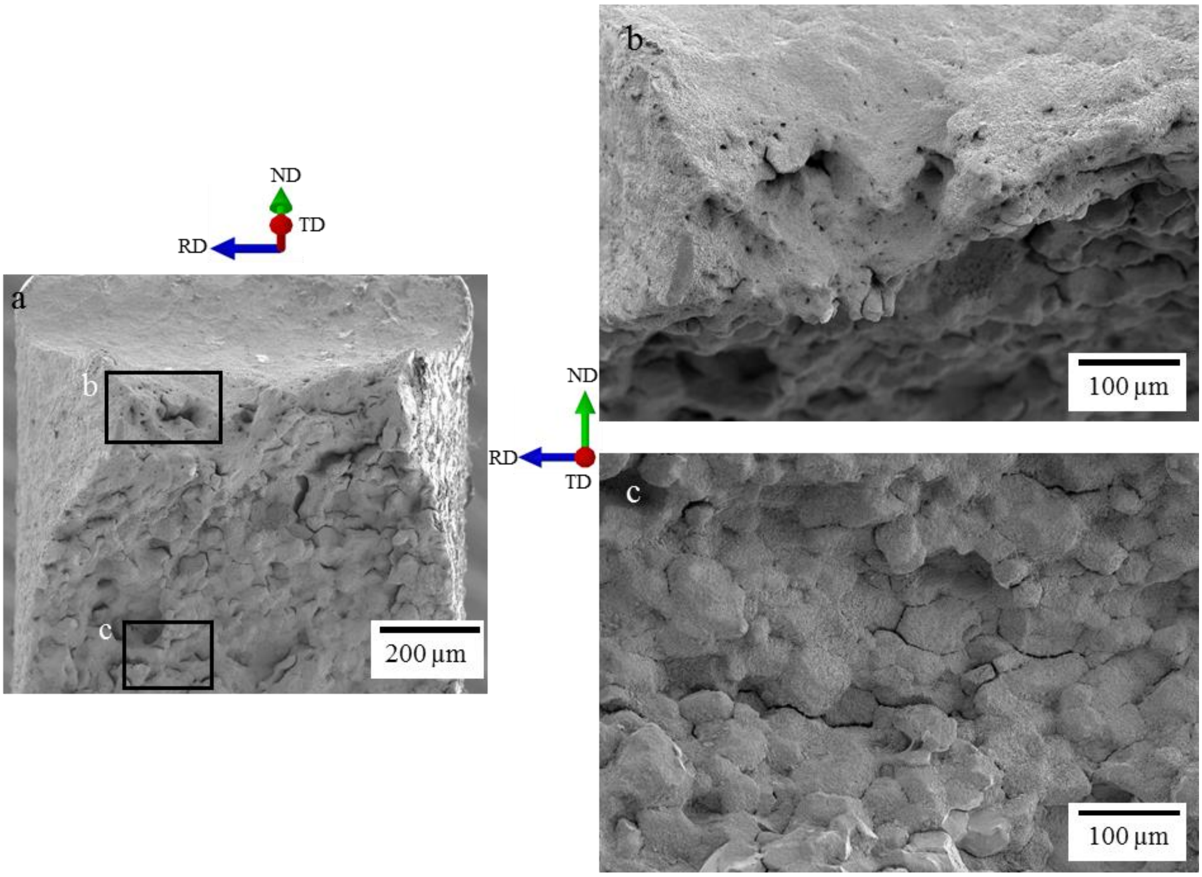

Figure III–48 Fractographies of a Cu-30%Zn sample tested using the 3-point bending test at a displacement rate of 0.005 mm/min in contact with the EGaIn.

On the other hand, the samples tested at a displacement rate of 0.005 mm/min or lower, in contact with the liquid EGaIn, had a bifurcation of the brittle fracture; Figure III–49 illustrates this on an SEM image of a Cu-30%Zn sample tested in contact with the EGaIn but not fractured completely.

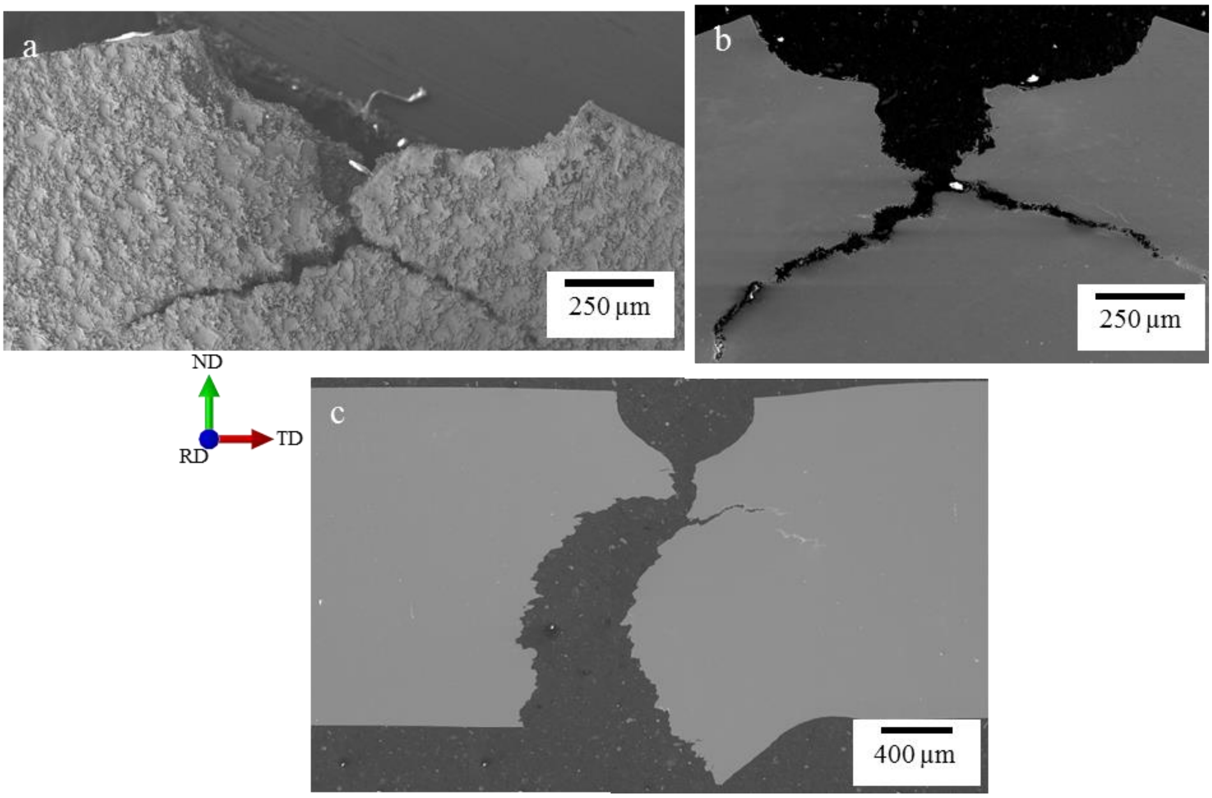

Figure III–49 SEM images of Cu-30%Zn samples tested at a displacement rate of 0.005 mm/min in contact with the EGaIn. a and b) correspond to an interrupted test, and c) corresponds to a sample tested until fracture.

In summary, the Cu-30%Zn presented LME when tested in contact with the EGaIn. Contrary to the SPT samples, the Cu30%Zn bending samples did not present any effect of the displacement rate on the LME sensitivity. In addition, the fracture initiation presents dimples, indicating a ductile fracture, while most of the fracture propagation presents a brittle intergranular fracture. Next, the effect of the Zn content is studied using the 3-point bending test on solids with less Zn content.

III.5.4. Study on the LME sensitivity of pure Cu and the Cu-15%Zn brass in contact with the EGaIn by the 3-point bending test

Since the 3-point bending test demonstrated to be most suitable to study the embrittlement by the EGaIn on the Cu-30%Zn brass, this setup was chosen to study this on pure Cu and the Cu-15 wt.%Zn brass. Alfa Aesar supplied the Cu alloy, which presented a grain size of 21 ± 3 µm and a hardness of 100 ± 3 HV, while Wieland supplied the Cu-15 wt.%Zn alloy, which presented a grain size of 20 ± 3 µm and a hardness of 75 ± 3 HV.

For testing these samples, an Adamel Lhomargy DY35 testing machine was used. Figure III–50 and Figure III–51 show some of the force-displacement curves of the bending test on Cu samples tested in air and in contact with the liquid EGaIn.

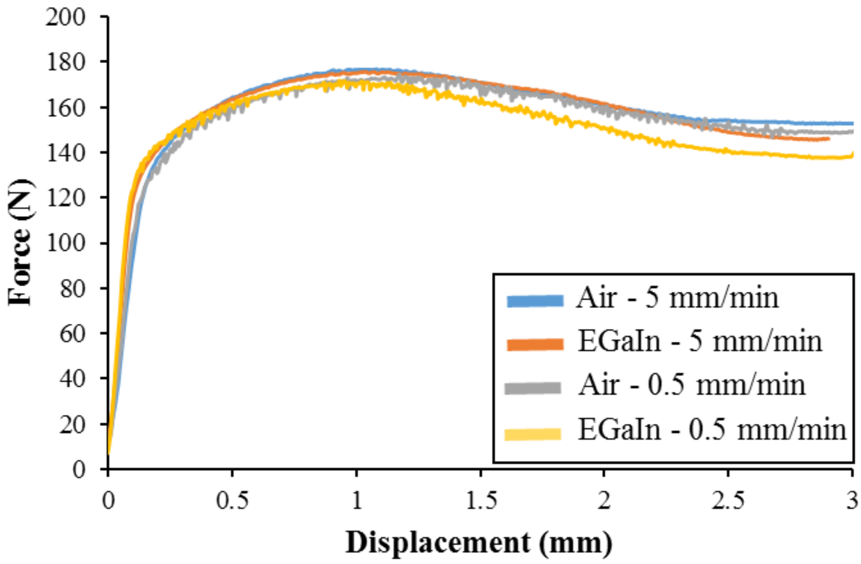

Figure III–50 Force-displacement curves of 3-point bending tests at 5 and 0.5 mm/min for Cu samples tested in air and in contact with the EGaIn.

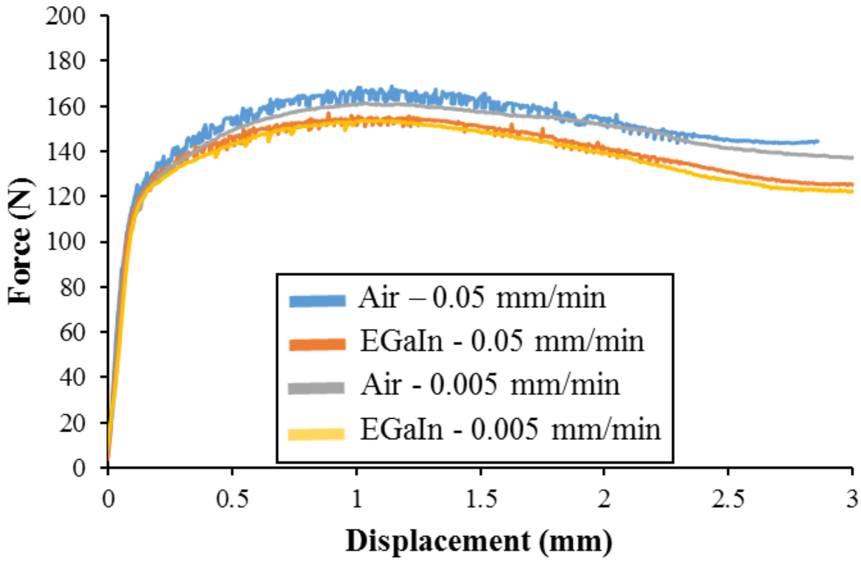

Figure III–51 Force-displacement curves of 3-point bending tests at 0.05 and 0.005 mm/min for Cu samples tested in air and in contact with the EGaIn.

Most of these curves have instabilities in measuring the force in this testing machine. This effect is more evident when testing at lower than higher displacement rates. However, the analysis of the curves can still be done.

In the force-displacement curves, it is observed that the force of the tests performed in contact with the EGaIn is slightly lower than in the tests carried out in air; this happens at all displacement rates except at 5 mm/min. Nevertheless, there is no evidence of embrittlement when in contact with the EGaIn at any displacement rate since there is no sudden force drop in any of the curves. For confirmation that there was no embrittlement effect of the EGaIn on the Cu samples, the fracture surfaces were observed by SEM. Figure III–52 shows some of these observations.

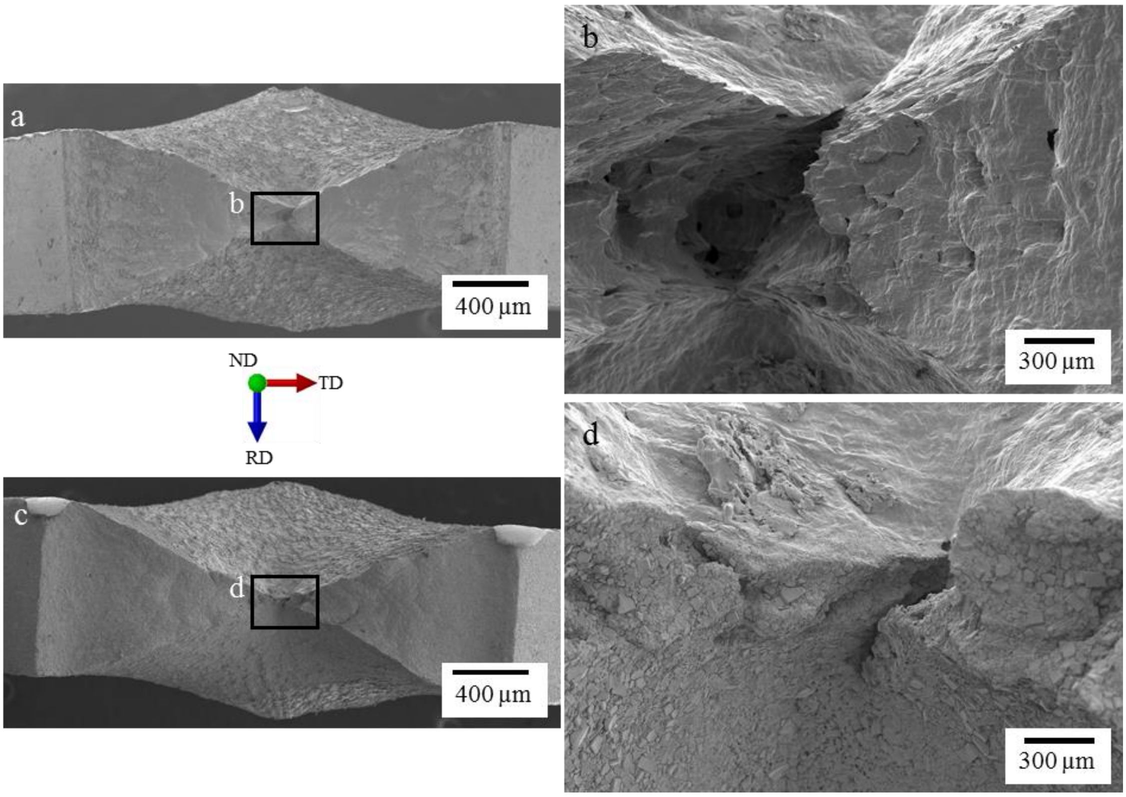

Figure III–52 Fractographies of Cu samples tested using the 3-point bending test at a displacement rate of 0.005 mm/min: a) and b) in air and c) and d) in contact with the EGaIn.

The fractographies of the Cu samples show a necking alike failure that indicates ductile behaviour. Moreover, this type of fracture is similar to that observed on the fractographies of the Cu samples tested by SPT (Figure III–15 and Figure III–16). This behaviour was observed on the samples tested in air and those tested in contact with the liquid EGaIn, which indicates that the EGaIn does not affect the mechanical behaviour of the Cu samples.

In the case of the Cu-15%Zn samples, Figure III–53 and Figure III–54 show some of the force-displacement curves of the bending tests performed at different displacement rates. There are no differences between the curves of the samples tested in air and those tested in contact with the EGaIn at any displacement rate tested.

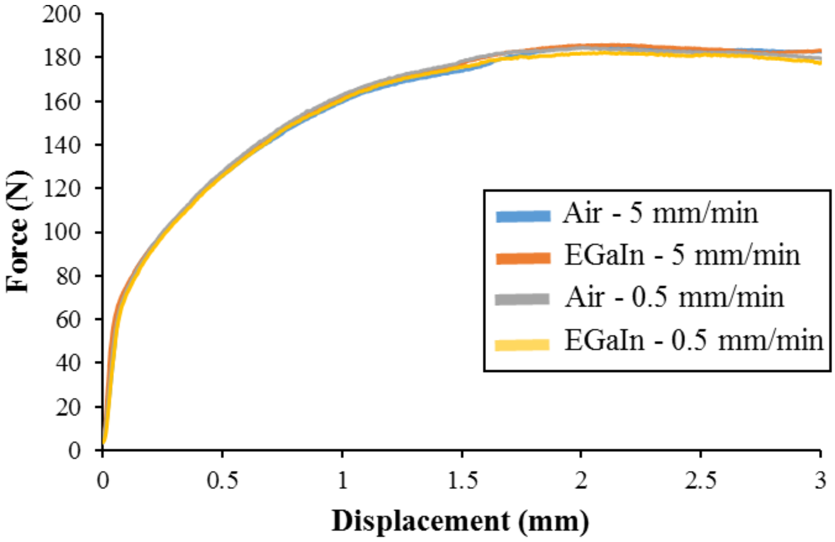

Figure III–53 Force-displacement curves of 3-point bending tests at 5 and 0.5 mm/min for Cu-15%Zn samples tested in air and in contact with the EGaIn.

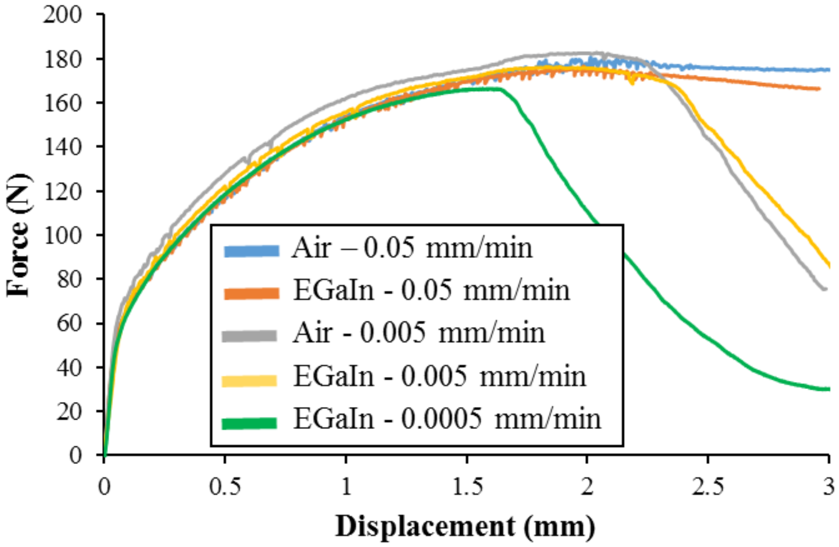

Figure III–54 Force-displacement curves of 3-points bending tests for Cu-15%Zn samples tested in air at 0.05 and 0.005 mm/min and in contact with the EGaIn at 0.05, 0.005, and 0.0005 mm/min.

In the case of the samples tested at a displacement rate of 5, 0.5, and 0.05 mm/min, the force-displacement curves do not present a force decrease; instead, the force is constant after a displacement of 2 mm until the end of the test at 3 mm. These tests could not be continued beyond a displacement of 3 mm since, at this displacement, the samples touched the supports of the setup, so further bending is impossible.

In the case of the samples tested at 0.005 mm/min, the force-displacement curves present a decrease in the force after reaching a displacement of around 2.3 mm. This point to the possibility of having a relationship between the displacement at fracture and displacement rate.

This behaviour was observed on the bending test of the Cu-30%Zn samples, in which the displacement to fracture reduced when decreasing the displacement rate (Figure III–39, Figure III–40, and Figure III–41). For this, an additional displacement rate of 0.0005 mm/min was used to test a Cu-15%Zn sample in contact with the EGaIn, which Figure III–54 also included. There is the same tendency in this curve, i.e., the fracture displacement is lower than the samples tested at higher displacement rates.

However, there are no signs of embrittlement in any of these curves since there is no sudden decrease of the force at any of the conditions tested, and the force-displacement curves are the same for the tests performed in air and in the EGaIn. For confirmation of this, the fracture surface of the samples was analyzed by SEM.

Figure III–55 shows the fractographies of two samples tested at a 5 mm/min displacement rate. For these samples, there was no significant crack propagation, which accords with the fact that the force in the force-displacement curves remained constant at the last millimetre of displacement of the test and that the force did not decrease. Moreover, there are no significant differences between the fracture behaviour of the sample tested in air and the sample tested in contact with the EGaIn.

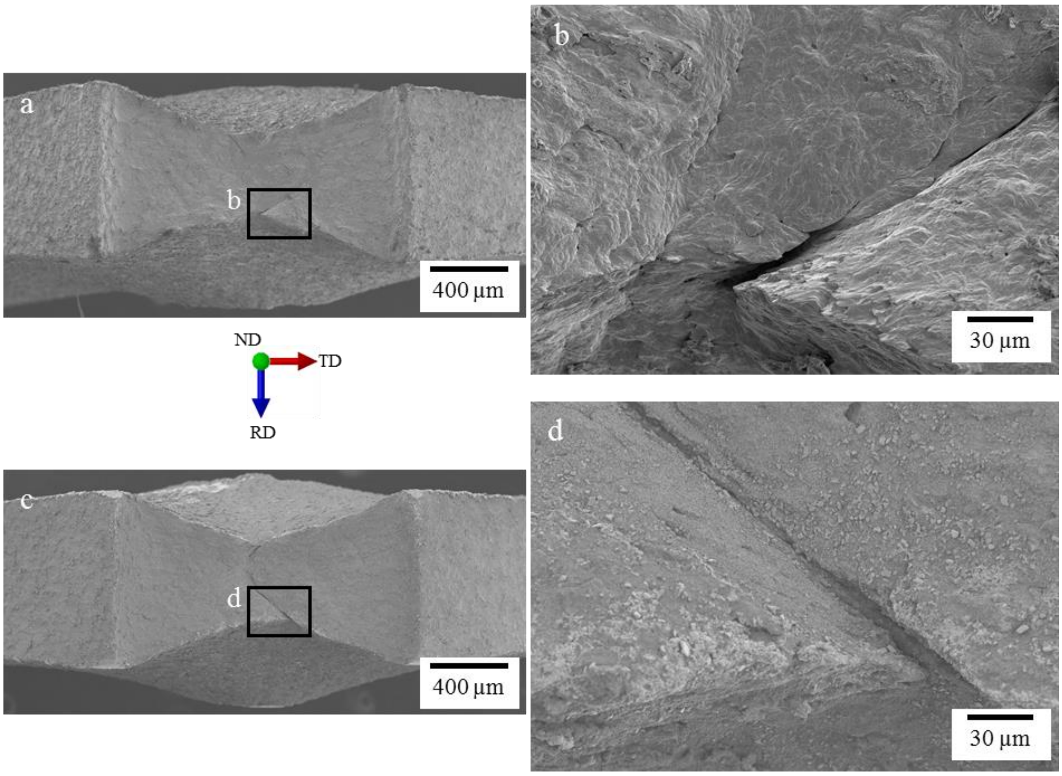

Figure III–55 Fractographies of Cu-15%Zn samples tested using the 3-point bending test at a displacement rate of 5 mm/min: a and b) in air and c and d) in contact with the EGaIn.

On the other hand, Figure III–56 and Figure III–57 present the fractures of Cu-15%Zn samples tested at 0.005 mm/min in air and in contact with the EGaIn, respectively. The fracture propagation was significant in these samples, as expected from their force-displacement curves. Furthermore, these samples presented a fractured surface similar to the Cu-30%Zn samples, i.e., the fractures do not present as much necking as for the fracture of the Cu samples, and there is the presence of ductility dimples. The sample tested in air presents a ductile behaviour. The sample tested in contact with the EGaIn presented sharp-pointed formations corresponding to the ductility dimples and indicating a ductile fracture.

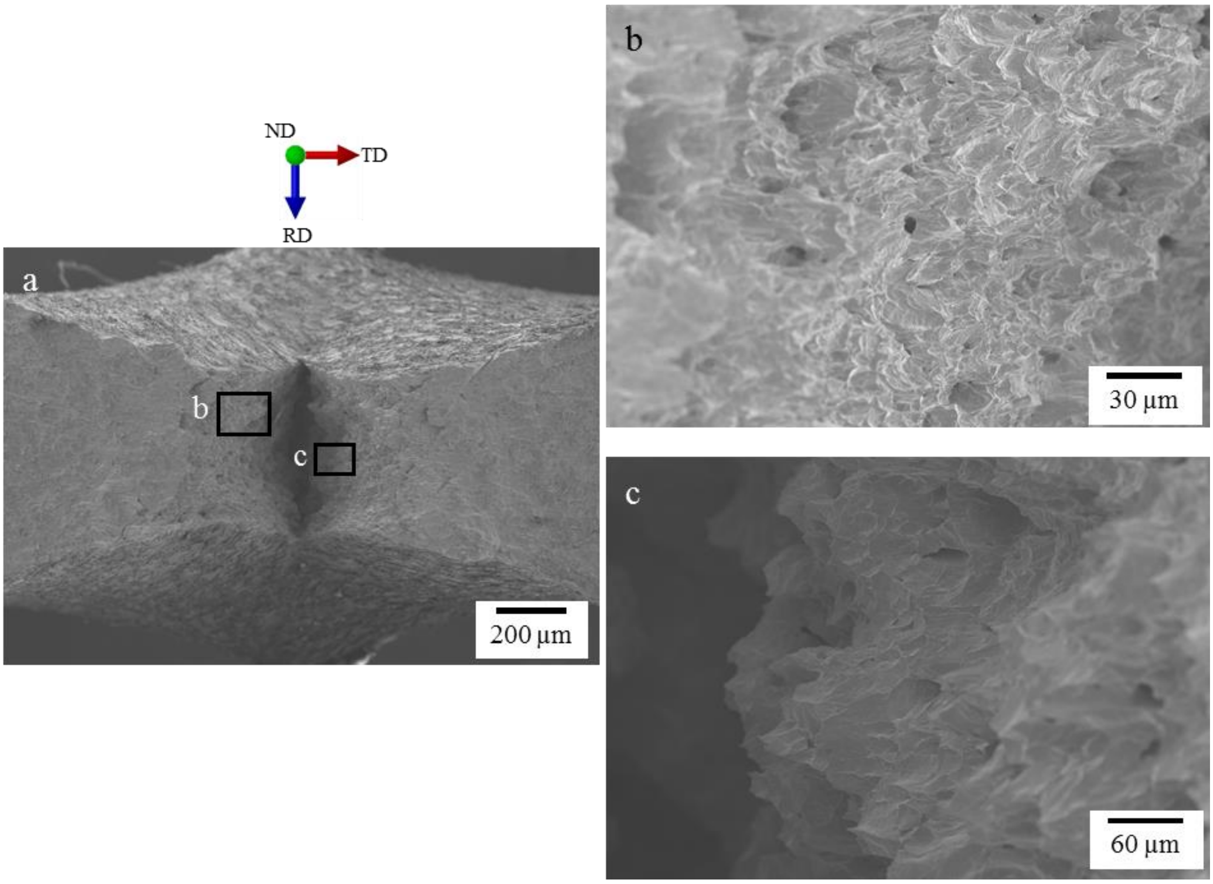

Figure III–56 Fractographies of a Cu-15%Zn sample tested using the 3-point bending test at a displacement rate of 0.005 mm/min in air.

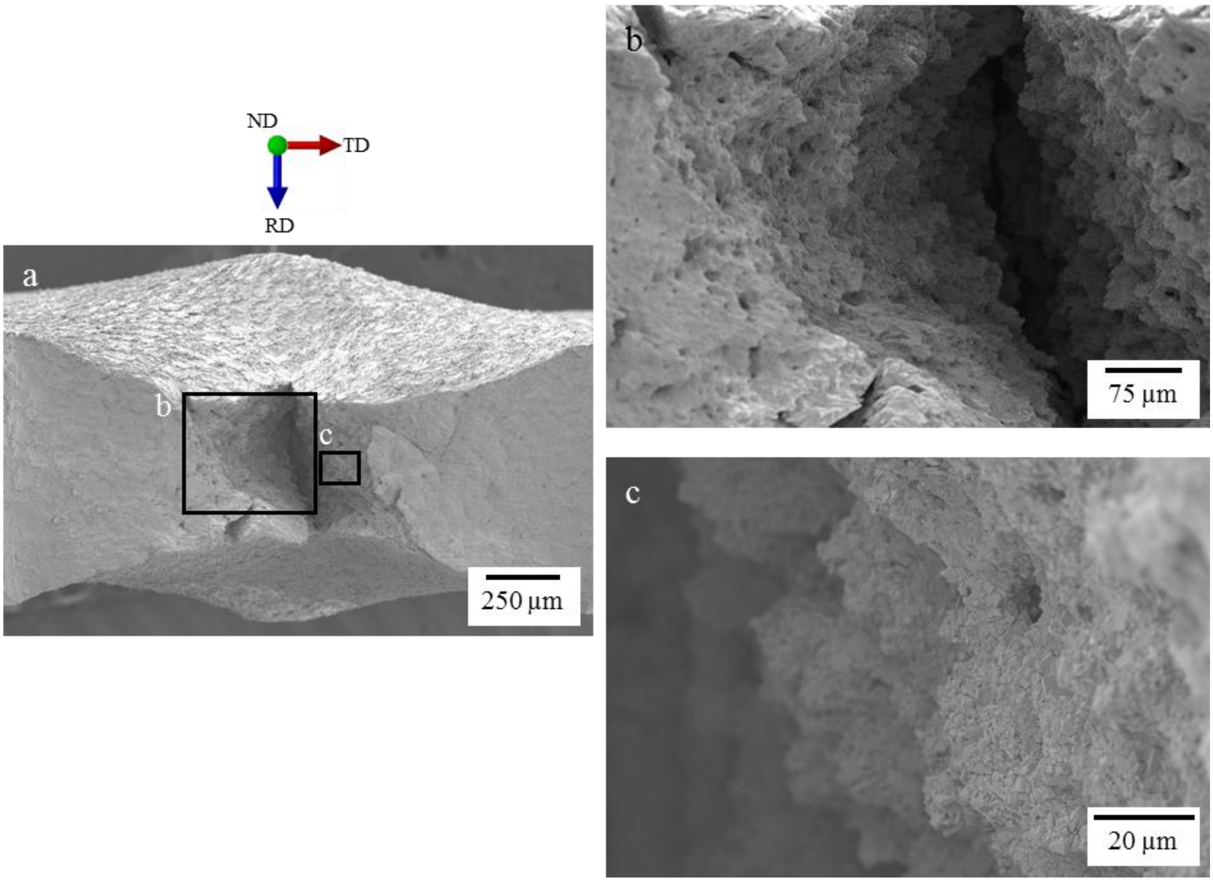

Figure III–57 Fractographies of a Cu-15%Zn sample tested using the 3-point bending test at a displacement rate of 0.005 mm/min in contact with the EGaIn.

For the case of the sample tested at a displacement rate of 0.0005 mm/min in contact with the EGaIn, the samples presented a complete fracture, which allows the direct observation of the fracture; Figure III–58 shows it. Due to the time of contact with the liquid EGaIn and the subsequent chemical treatment, the surface of the fracture presents considerable damage, but the nature of the fracture seems to be completely ductile.

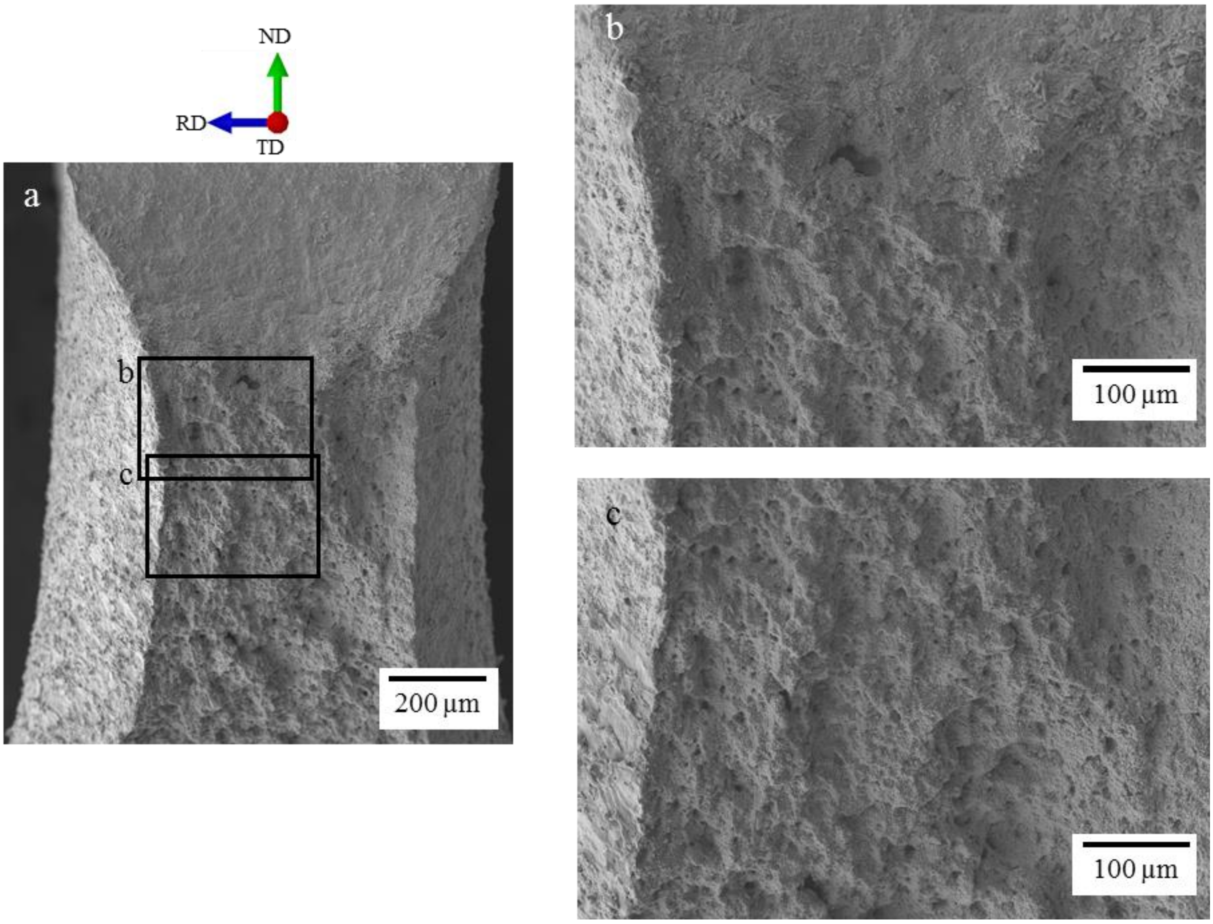

Figure III–58 Fractographies of a Cu-15%Zn sample tested using the 3-point bending test at a displacement rate of 0.0005 mm/min in contact with the EGaIn.

In the Cu-30%Zn, an initial ductile fracture was necessary to trigger the LME; this condition may apply to the Cu-15%Zn. If it is the case, at high displacement rates, where there is no ductile fracture, there could not be any LME. For this reason, only the tests at a lower displacement rate could show any embrittlement effect. However, despite the apparition of a ductile fracture at low displacement rates, there were no signs of LME of Cu-15%Zn. This lack of LME could be related to a strain rate dependence on the LME sensitivity previously observed for the Cu-30%Zn in the SPT. For recall, the laterally notched Cu-30%Zn SPT sample presented LME only at high displacement rates. Finally, another explanation for the lack of LME is that the Cu-15%Zn samples present a lower hardness than the Cu-30%Zn, which could have changed its sensitivity to LME.

Studying alloys with intermediate compositions between Cu-15%Zn and Cu-30%Zn could give us more information on the embrittlement conditions of the alpha brasses.

III.5.5. Study on the LME sensitivity of the Cu-20%Zn and Cu-25%Zn brasses in contact with the EGaIn by the 3-point bending test

The studied Cu-20 wt.%Zn and Cu-25 wt.%Zn were elaborated in the Institut de Chimie et des Matériaux Paris-Est (ICMPE) using an induction furnace to melt 99.99 wt.% purity Cu and 99.95 wt.% purity Zn in a glassy carbon crucible to produce cylinders with a diameter of 12 mm and height of 8 mm. These were then cross-rolled until achieving a thickness of 2 mm.

Due to the elaboration processes, the Cu-20 wt.%Zn and Cu-25 wt.%Zn alloys presented high hardness values, which present much dispersion due to the microstructure heterogeneity. Their hardness values were 212 ± 15 and 210 ± 11 HV, respectively. Their microstructures could not be observed due to their high level of deformation. Regarding the bending samples, the rolling directions correspond to RD and TD in Figure III–34.

First, the Cu-20%Zn was tested at displacement rates of 5 and 0.05 mm/min; Figure III–59 shows some of the correspondent force-displacement curves. The curves of the samples tested at air present a higher yielding point, and then there is a small zone of plastic deformation and strengthening followed by a steady decrease in the force, which corresponds to the fracture propagation. This behaviour is similar to the other alloys tested in air, with significantly lower deformation before a fracture initiation. Moreover, the sample tested at a displacement rate of 0.05 mm/min presented a lower yield point, which could be a consequence of the material heterogeneity, but the overall response of the sample was the same as for the sample tested at 5 mm/min.

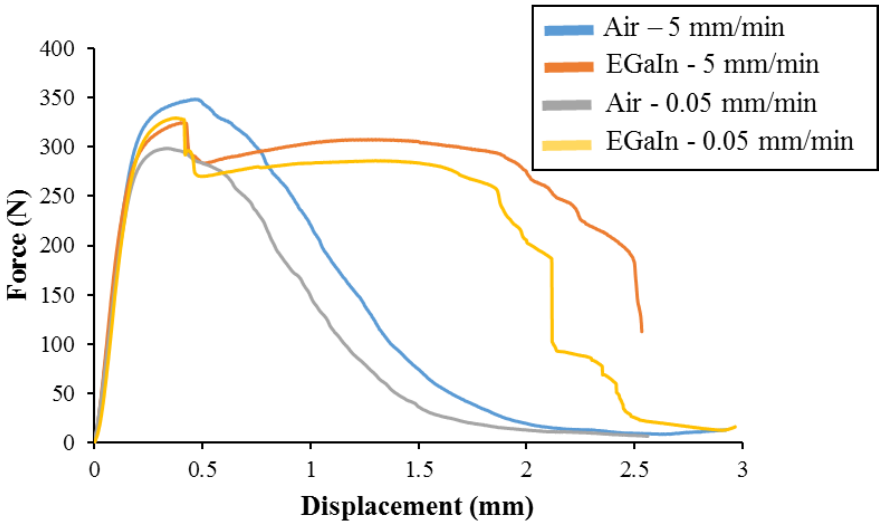

Figure III–59 Force-displacement curves of 3-point bending tests at 5 and 0.05 mm/min for Cu-20%Zn samples tested in air and in contact with the EGaIn.

Before the maximum force, the Cu-20%Zn samples tested in contact with the EGaIn behave similarly to those tested in air. After this point, a sudden decrease in the force could indicate LME. In contrast to the previous embrittled alloy, the sudden decrease in force stops after decreasing around 50N; then, the force increases and decreases steadily after reaching a high displacement value. Finally, there is a second sudden drop in the force. The sample tested at 5 mm/min reached the practical limit of deformation after this, while the sample tested at 0.05 mm/min could be further deformed. The last one presented a second stop of the sudden drop of the force and a steady decrease of the force with two more small sudden drops. This particular behaviour of these curves occurs entirely during the crack propagation stage.

The fracture surfaces were observed using the SEM to understand the curves' form better. In the first instance, Figure III–60 shows the fractographies of the Cu-20%Zn samples tested in air. There is no difference in the fracture behaviour of the samples related to the variation of the displacement rate. Like previous brasses tested in air, the surfaces of the Cu-20%Zn samples showed a ductile fracture when tested in air, evidenced by the presence of ductility dimples.

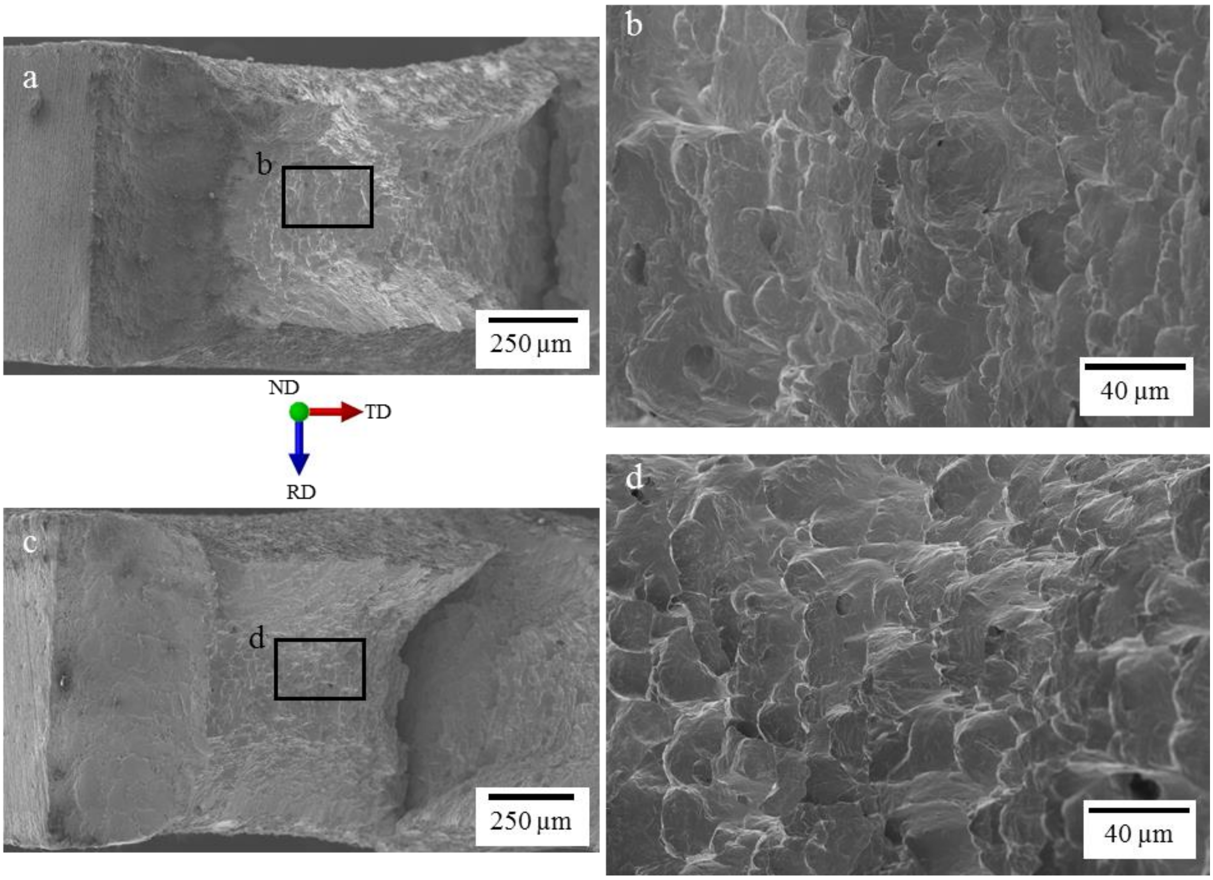

Figure III–60 Fractographies of the Cu-20%Zn samples tested using the 3-point bending test in air: at a displacement rate of a and b) 5 mm/min, and c and d) 0.05 mm/min.

On the other hand, Figure III–61 shows the fracture surfaces of a sample tested in contact with the liquid EGaIn at a displacement rate of 5 mm/min. In this sample, there are alternating zones of ductile and brittle fractures. The ductile zones present traces of ductility dimples, while the nature of the brittle fractures is not precise. The last could be an intergranular fracture, as for the other embrittled brass, but since the microstructure is severely deformed, it was impossible to determine the kind of fracture.

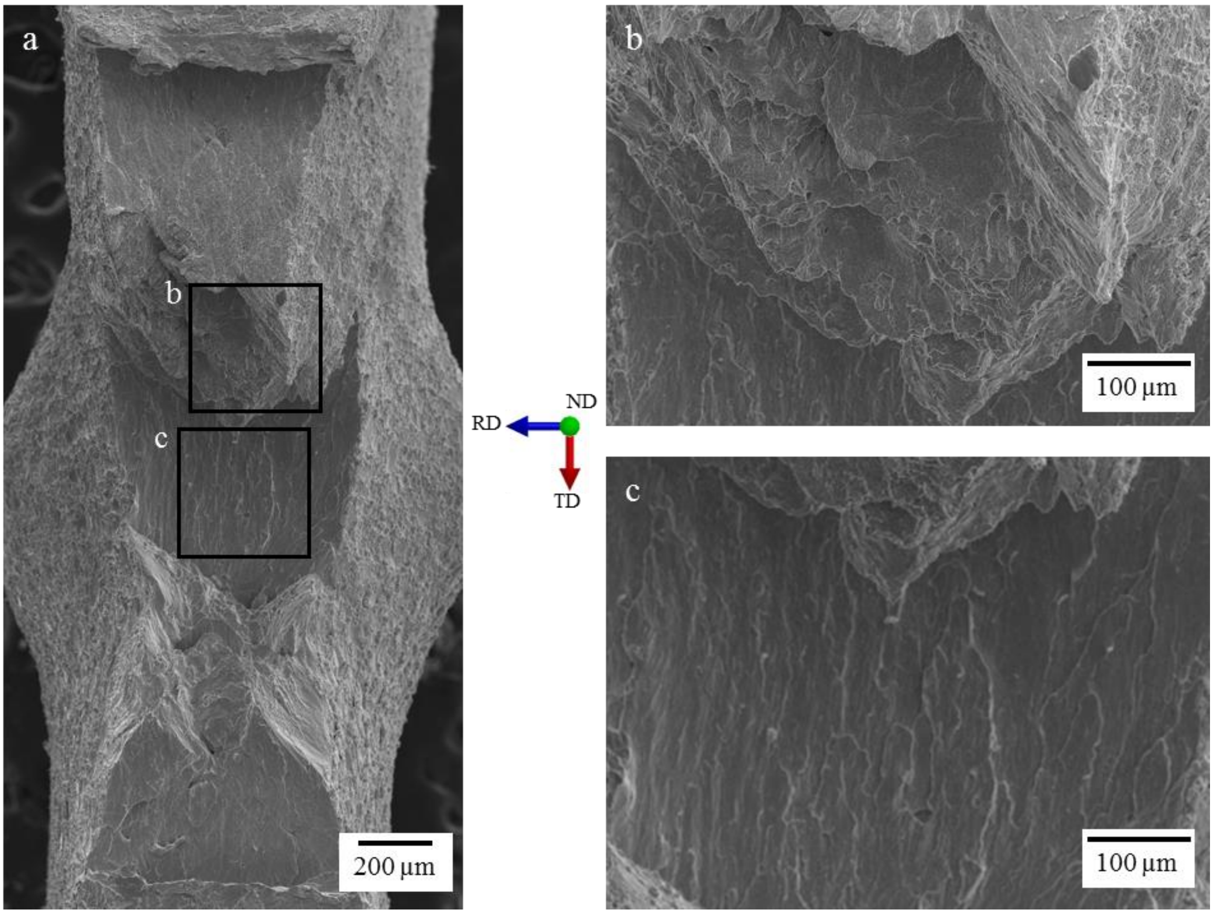

Figure III–61 Fractographies of a Cu-20%Zn sample tested using the 3-point bending test at a displacement rate of 5 mm/min in contact with the EGaIn.

The fractures that present ductile behaviour propagate in the plane perpendicular to TD, while the brittle fractures propagate perpendicular to ND. A transversal cut makes this characteristic easier to observe (Figure III–62). Similar behaviour was previously observed in the Cu-30%Zn samples when embrittled by the EGaIn (see Figure III–46).

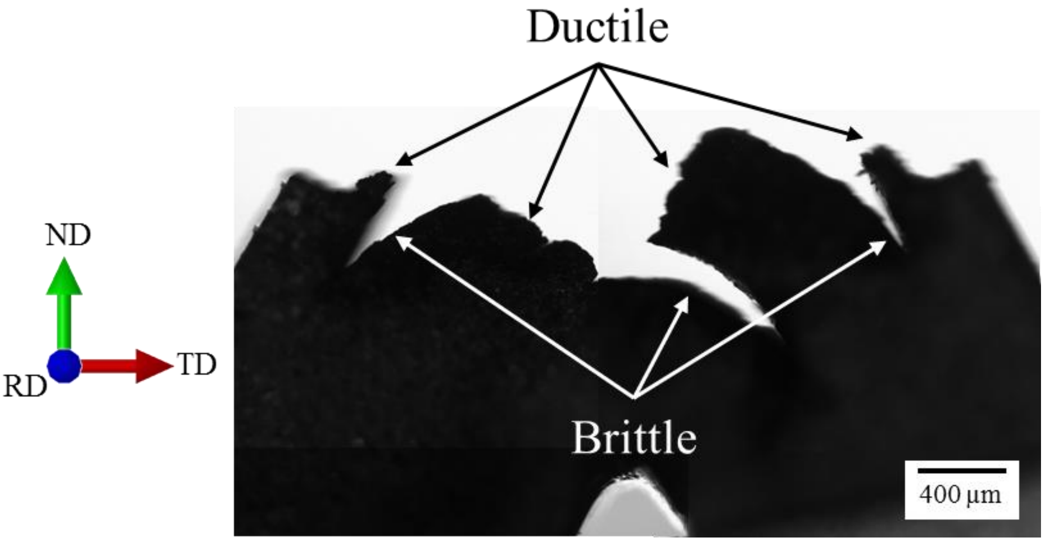

Figure III–62 Transversal cut of a Cu-20%Zn sample tested using the 3-point bending test at a displacement rate of 5 mm/min in contact with the EGaIn.

Similarly, Figure III–63 shows the fracture of the Cu-20%Zn sample tested in contact with the liquid EGaIn at a displacement rate of 0.05 mm/min. This sample presented the same fracture behaviour, with alternating zones of ductile and brittle fractures. The first fracture, which appears just after the notch, presents ductile behaviour for both samples.

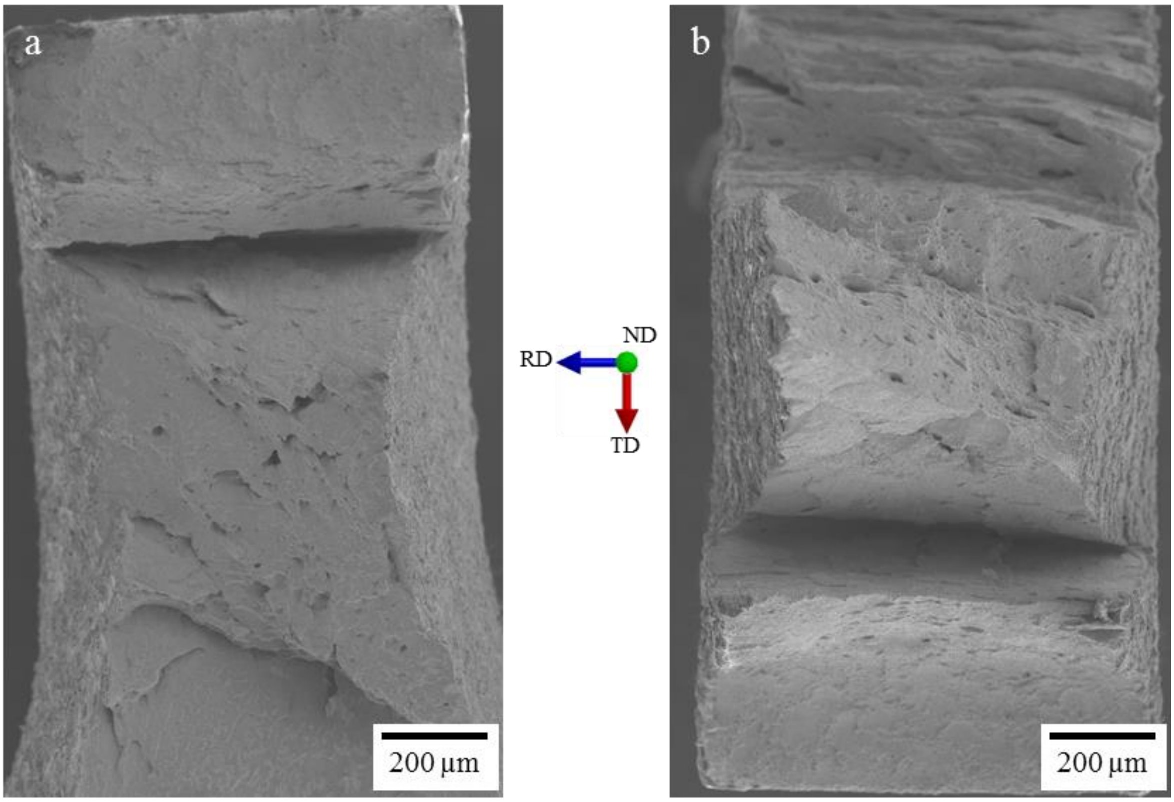

Figure III–63 Fractographies of a Cu-20%Zn sample tested using the 3-point bending test at a displacement rate of 0.05 mm/min in contact with the EGaIn.

Different factors could explain the reason for this specific fracture behaviour. On the one hand, the fracture starts as a ductile fracture for the Cu-30%Zn samples, which then becomes brittle and propagates towards the zones with the higher plastic deformation, and in this test, these zones correspond to the zones that are diagonal to the notch (section III.11. address this aspect). Furthermore, due to the elaboration process, the grains are elongated towards the rolling directions RD and TD (Figure III–34). Since the brittle fracture is presumably intergranular, the fracture propagation follows these rolling directions. Moreover, the fracture cannot propagate until the complete failure of the sample since it reaches a zone where the stress and strain are not sufficiently high for it to continue its propagation. At this moment, the sample continues its deformation until a new fracture initiates; as for the first fracture initiation, the fracture starts as ductile and becomes brittle, and the whole process repeats.

In an attempt to modify this fracture behaviour, annealing at 300 °C for 1 hour was applied to some Cu-20%Zn samples. This heat treatment significantly reduced the hardness of the alloy to 133 ± 6 HV, which is close to the hardness value of the embrittled Cu-30%Zn samples (142 ± 4 HV). The annealed Cu-20%Zn samples were tested using the 3-point bending test; Figure III–64 presents the correspondent force-displacement curves, which show that, as expected, there was a significant reduction of the yielding point and an increase in the displacement to fracture.

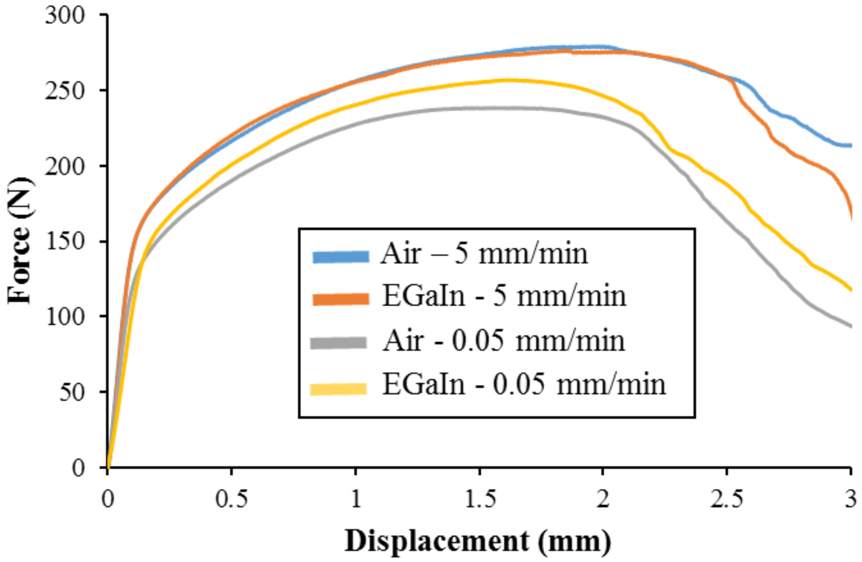

Figure III–64 Force-displacement curves of 3-point bending tests at 5 and 0.05 mm/min for annealed Cu-20%Zn samples tested in air and in contact with the EGaIn.

Moreover, from these curves, it can be observed that there are no significant differences between the mechanical behaviour of the annealed Cu-20%Zn samples tested in air in comparison with those tested in contact with the liquid EGaIn. In both cases, the decrease in the force is steady, and there is no sign of a sudden force drop. Besides, the force magnitude of the samples tested at 0.05 mm/min is slightly lower than for the samples tested at 5 mm/min, but these differences could be due to the heterogeneities of the material.

The fracture surfaces were observed by SEM, and their behaviour was similar between the samples tested in air and those tested in contact with the EGaIn, i.e., in both conditions, their fracture surface presents ductility. Figure III–65 exemplifies this fracture behaviour for the samples tested in contact with the EGaIn. This result indicates that the LME sensitivity of the Cu-20%Zn alloy depends on the metallurgical state of the sample.

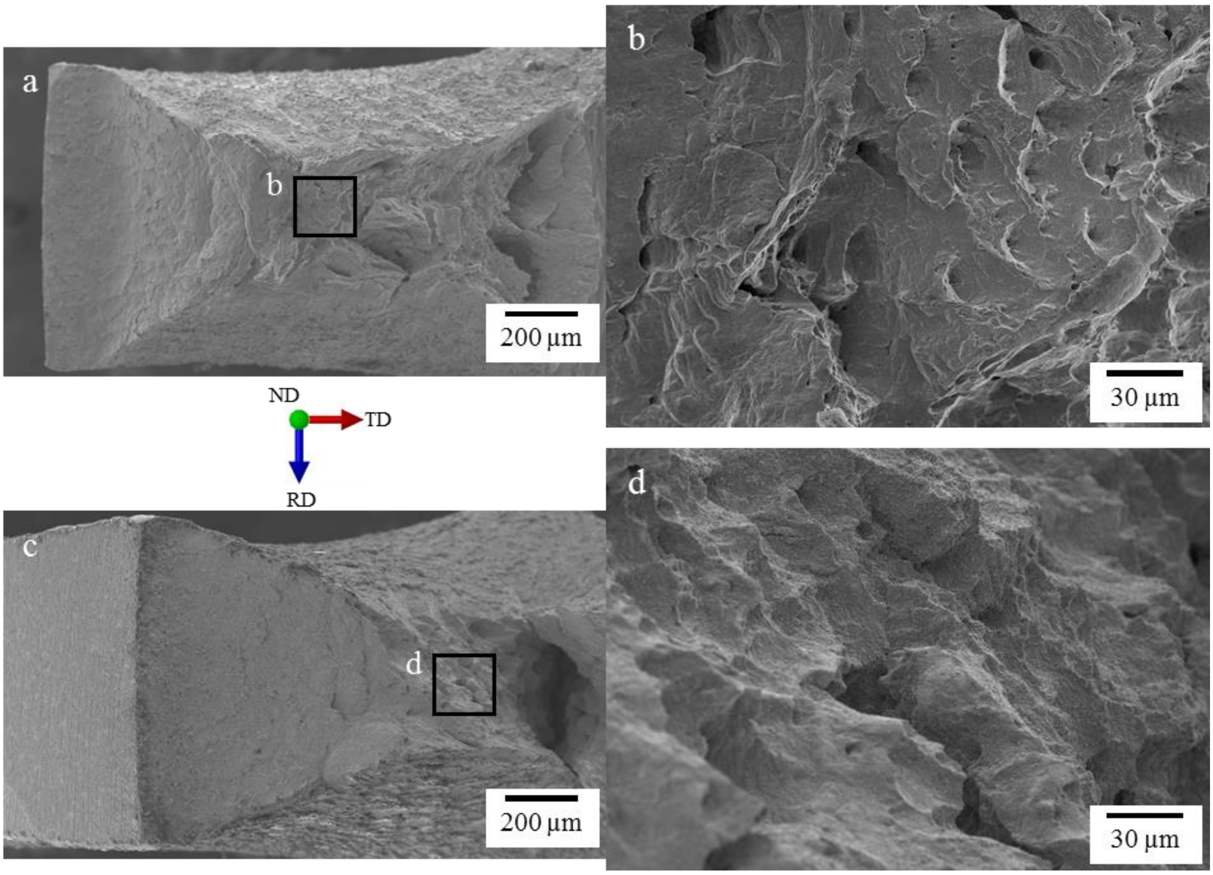

Figure III–65 Fractographies of annealed Cu-20%Zn samples tested using the 3-point bending test in contact with the EGaIn: at a displacement rate of a and b) 5 mm/min, and c and d) 0.05 mm/min.

Following the same logic, 3-point bending tests were carried out on the Cu-25%Zn alloy. First, the samples were tested in the original metallurgical state (210 ± 11 HV) using the 3-point bending test using the same displacement rates. Figure III–66 shows the corresponding force-displacement curves.

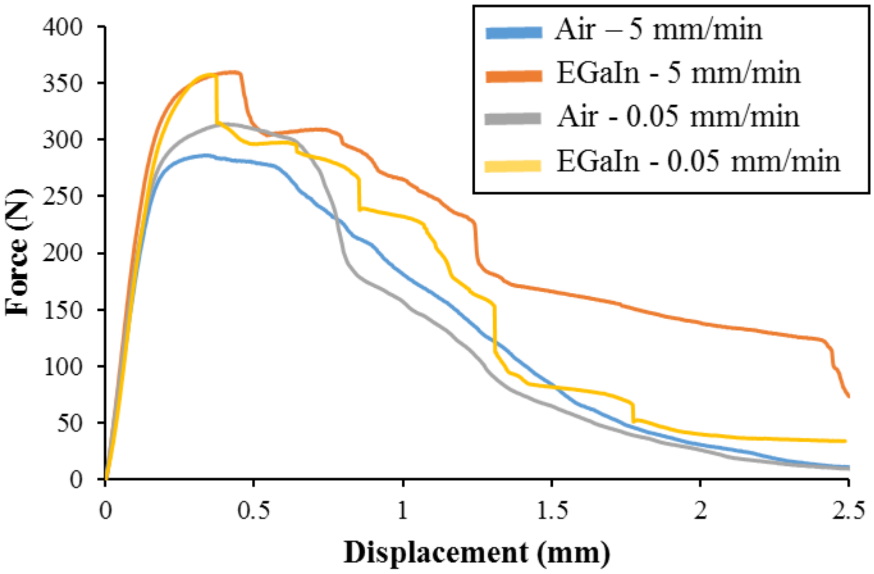

Figure III–66 Force-displacement curves of 3-point bending tests at 5 and 0.05 mm/min for Cu-25%Zn samples tested in air and in contact with the EGaIn.

The Cu-25%Zn alloy presents a similar mechanical behaviour to that of the Cu-20%Zn. In the force-displacement curves of the samples tested in air, there is a steady decrease of the force after reaching the maximum value, while the curves of the samples tested in contact with the liquid EGaIn present alternating steps of sudden decrease of the force with a steady decrease of the force.

As for the Cu-20%Zn alloy, this could indicate intermittent embrittlement of the alloy caused by the EGaIn. To corroborate this hypothesis, the fracture surfaces of these samples were observed by SEM. These analyses showed that the samples tested in air presented a ductile behaviour, while those tested in contact with the liquid EGaIn presented alternating brittle and ductile fractures. Figure III–67 and Figure III–68 present the fractographies of the Cu-25%Zn samples tested at a displacement rate of 5 and 0.05 mm/min in the presence of the liquid EGaIn. The fractographies present alternating ductile and brittle zones; the first fracture to initiate has ductile behaviour, and the ductile fractures propagate in the plane perpendicular to TD, while the brittle fractures propagate in the plane perpendicular to ND.

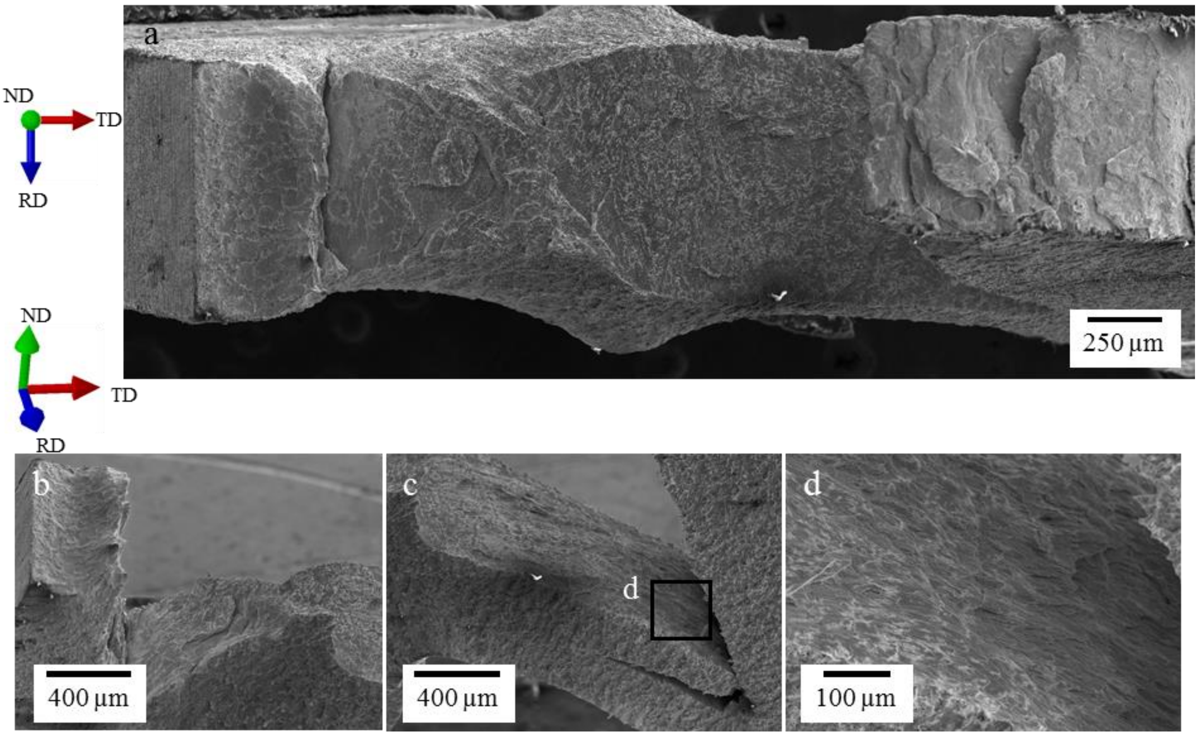

Figure III–67 Fractographies of a Cu-25%Zn sample tested using the 3-point bending test at a displacement rate of 5 mm/min in contact with the EGaIn.

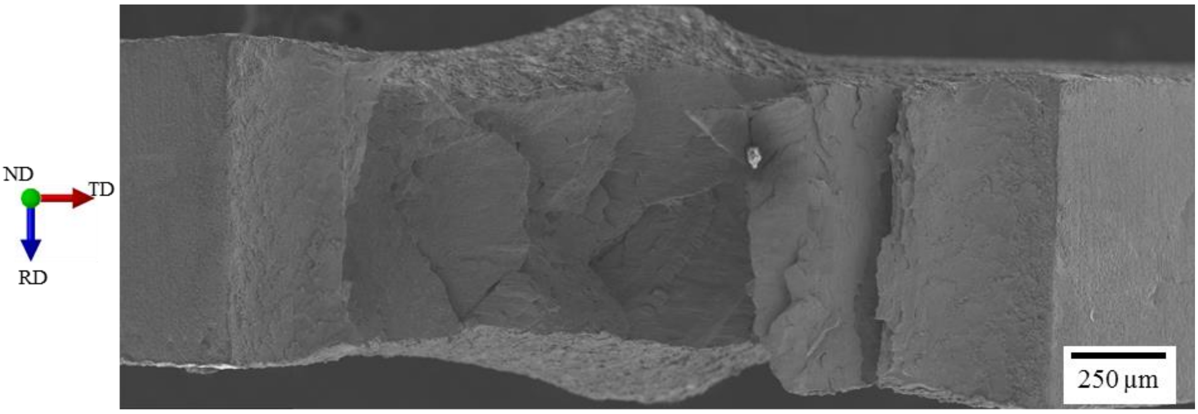

Figure III–68 Fractographies of a Cu-25%Zn sample tested using the 3-point bending test at a displacement rate of 0.05 mm/min in contact with the EGaIn.

In the same order of ideas, some Cu-25%Zn samples were annealed using the same conditions as the annealed Cu-20%Zn samples, i.e., annealing at 300 °C for 1 hour. This heat treatment reduced its hardness to 133 ± 6 HV, surprisingly the same value as the annealed Cu-20%Zn samples. Figure III–69 shows the results of the 3-point bending test of these samples. As for the Cu-20%Zn, the force-displacement curves of the annealed alloy present a higher displacement to fracture and a lower yield point.

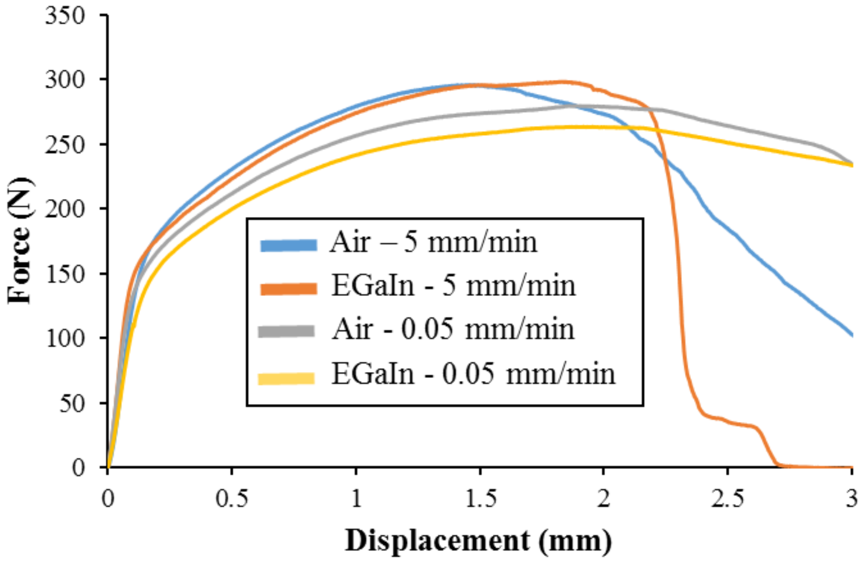

Figure III–69 Force-displacement curves of 3-point bending tests at 5 and 0.05 mm/min for annealed Cu-25%Zn samples tested in air and in contact with the EGaIn.

Conversely, in the samples tested at a displacement rate of 5 mm/min, there is a difference in decreasing the force when the sample is tested in contact with the liquid EGaIn. The sample tested in air presents a steady decrease of the force, while the sample tested in contact with the liquid EGaIn presents a sudden decrease of the force, which is a sign of the LME of the alloy. Contrariwise, this does not appear in the sample tested at 0.05 mm/min, in which case the curves of the samples tested in air and in contact with the EGaIn are similar, which indicates a lack of embrittlement.

Furthermore, these samples' fracture surfaces were observed to identify their fractures' nature. Figure III–70 and Figure III–71 show the images for the samples tested in contact with the liquid EGaIn at a displacement rate of 5 and 0.05 mm/min, respectively.

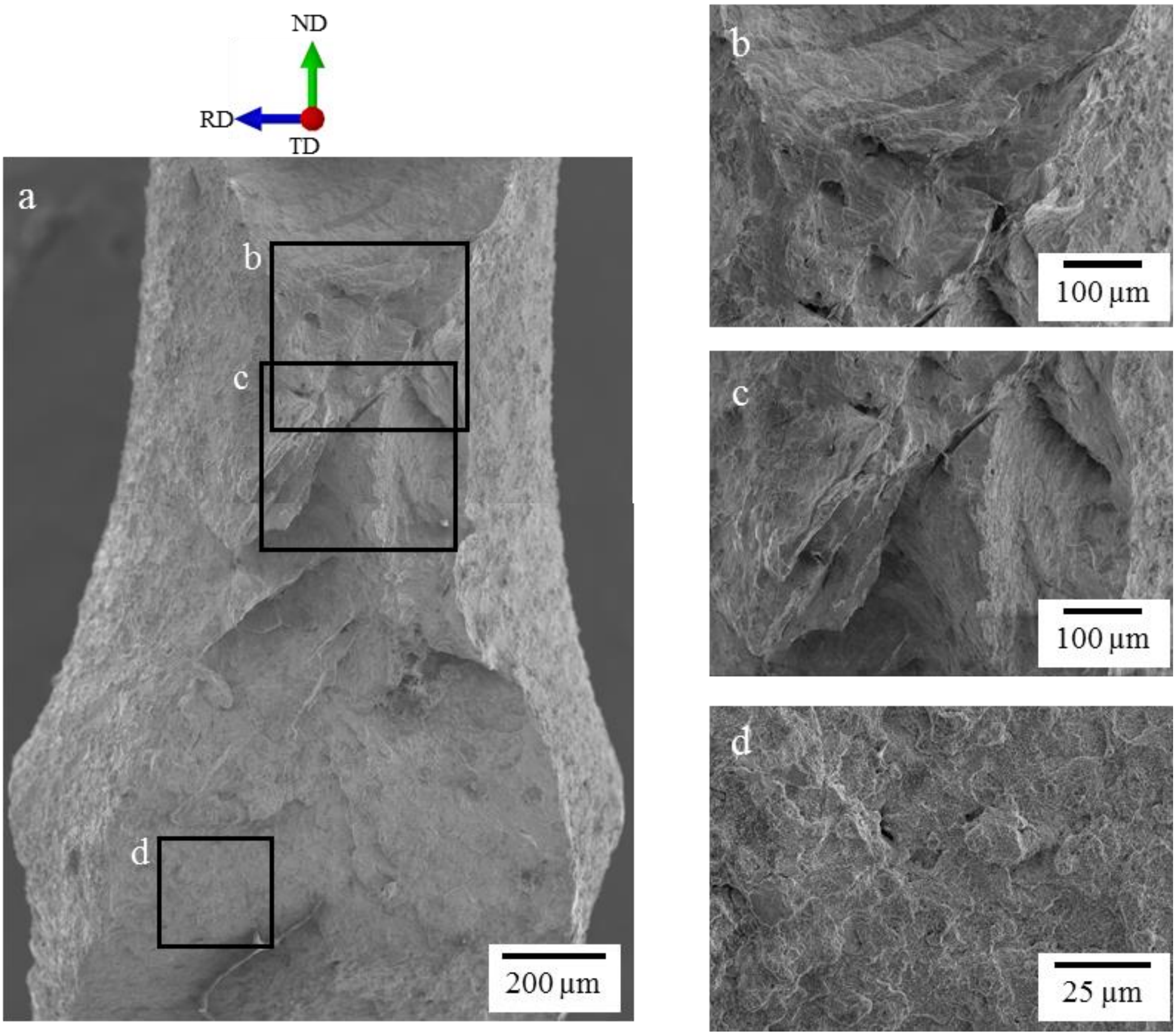

Figure III–70 Fractographies of an annealed Cu-25%Zn sample tested using the 3-point bending test at a displacement rate of 5 mm/min in contact with the EGaIn.

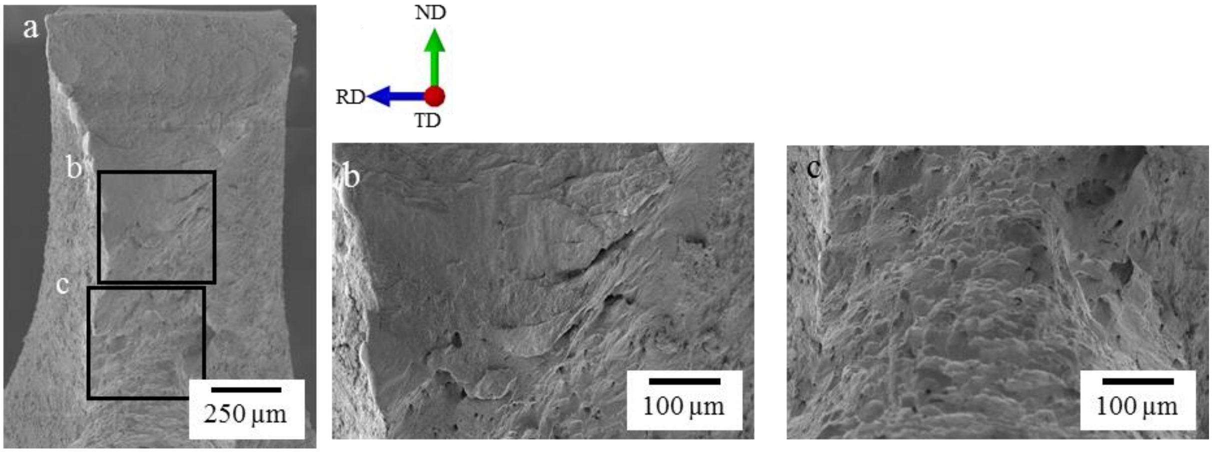

Figure III–71 Fractographies of an annealed Cu-25%Zn sample tested using the 3-point bending test at a displacement rate of 0.05 mm/min in contact with the EGaIn.

In the case of the annealed sample tested at 5 mm/min in contact with the EGaIn, the start of the fracture surface presents a ductile fracture, then there is a broad zone with a mixed behaviour that has ductile and brittle characteristics, and finally, there is a brittle zone that seems intergranular, but that is not as clear as for the Cu-30%Zn samples. On the other hand, the sample tested at 0.05 mm/min in contact with the liquid EGaIn presents a fully ductile fracture behaviour.

These results indicate that, unlike the annealed Cu-20%Zn samples, the heat treatment at 300 °C for 1 hour did not inhibit the embrittlement of the Cu-25%Zn samples when tested at a displacement rate of 5 mm/min. Also, unlike the Cu-30%Zn samples under bending, there is an apparent displacement rate effect on the LME sensitivity of the Cu-25%Zn brass, which matches the observations done on the Cu-30%Zn sample with the SPT, i.e., the sensitivity to LME increases at higher displacement rates.

Some samples were treated at 350 °C for 2 hours and tested in contact with the liquid EGaIn using the 3-point bending test to study if annealing with higher temperature and time would inhibit the LME of Cu-25%Zn. The samples presented a 102 ± 6 HV hardness after the heat treatment. Figure III–72 presents some of the force-displacement curves. There was no effect of the EGaIn on the mechanical properties of the samples since, at these displacement rates, the Cu-25%Zn samples presented the same mechanical behaviour when tested in air and in contact with the liquid EGaIn.

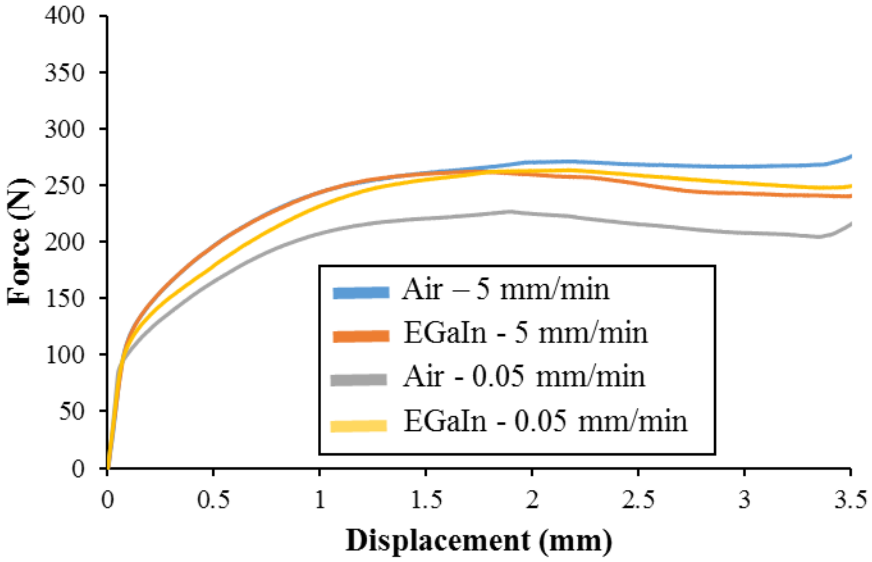

Figure III–72 Force-displacement curves of 3-point bending tests at 5 and 0.05 mm/min for Cu-25%Zn samples annealed at 350 °C and tested in air and in contact with the EGaIn.

III.6. Recapitulation of the principal results on the bending tests

In order to conclude on the results obtained by the 3-point bending test and to contrast them with those obtained with the Small Punch Test, it is convenient to recapitulate the conditions at which embrittlement occurred. Table III–6 summarizes these.

*Table III–6 Summary of the conditions at which LME occurred on materials tested by the 3-point bending test in contact with the liquid EGaIn. *Not tested*

Material	**Condition**	**Hardness (HV)**	**Displacement rate (mm/min)**				
			5	**0.5**	**0.05**	**0.005**	**0.0005**
Cu	Rolled	100 ± 3					
Cu-15 wt.%Zn	Rolled	75 ± 3					
Cu-20 wt.%Zn	Rolled	212 ± 15	**LME**	*****	**LME**	*****	*****
	Annealed at 300 °C	133 ± 6		*		*	*
Cu-25 wt.%Zn	Rolled	210 ± 11	**LME**	*****	**LME**	*****	*****
	Annealed at 300 °C	133 ± 6	**LME**	*		*	*
	Annealed at 350 °C	102 ± 6		*		*	*
Cu-30 wt.%Zn	Rolled	142 ± 4	**LME**	**LME**	**LME**	**LME**	**LME**

The alpha brass that presented the most sensitivity to be embrittled by the EGaIn was the Cu-30%Zn alloy, and the sensitivity to LME diminished on the alloys with less Zn content. Similarly, a higher hardness value of a specific alloy enhances the LME sensitivity. Also, higher displacement rates seem to promote sensitivity to embrittlement.

In the case of the Cu-30%Zn brass, the bending tests allowed the identification of the brittle fracture as an intergranular fracture. The deformed microstructure of the other embrittled alloys did not allow a clear identification of the nature of the brittle fracture.

A significant aspect of the LME of these alloys is that the liquid metal does not seem to affect the mechanical behaviour of the solid before its crack initiation. Indeed, there is no significant change in the elastic behaviour nor the plastic macroscopic behaviour; the force and displacement to failure are the same, which would traduce in the same macroscopic fracture toughness in air and in contact with the liquid EGaIn.

The effect of the EGaIn on the alpha brasses' mechanical properties appears after the fracture's initiation, which always initiates with ductile characteristics. At this moment, embrittlement modifies the solid's fracture behaviour into a brittle intergranular fracture. Once this brittle fracture initiates, it propagates very quickly.

These observations can relate to the fact that the EGaIn is not in direct contact with the solid materials since the intermetallic $CuGa_2$ forms quickly whenever the solid and the liquid enter into contact. Then, a fresh solid surface under stress occurs whenever a fracture occurs. This fresh surface enters contact with the liquid EGaIn, and embrittlement can occur. Since the brittle fracture propagation is quick once it initiates, the intermetallic cannot reform sufficiently fast; hence, the embrittlement continues.

In the case of the pure Cu samples, there were no signs of embrittlement when testing them with the 3-point bending test in contact with the liquid EGaIn. This lack of LME could be explained by the fact that this material fails by necking, which causes the absence of a fresh surface that can enter into contact with the EGaIn while it undergoes stress. Nevertheless, in the case of the alpha brasses that fail by microvoid nucleation, growth and coalescence, a fresh surface formed that entered in contact with the EGaIn, but not in all alloys the LME occurred. In particular, the Cu-25%Zn samples annealed at 350 °C presented a metallurgical state similar to that of pure Cu, and they were tested under the same conditions, but the annealed Cu-25%Zn samples did not present any signs of embrittlement. For this, the failure by necking of Cu cannot explain alone the lack of LME when in contact with the liquid EGaIn.

Moreover, as discussed in the previous chapter in section II.3., the intermetallic formation is similar in Cu and Cu-30%Zn, so the Zn content does not seem to affect the kinetics of the intermetallic formation. Hence, the intermetallic formation rate cannot explain the apparition of LME on the alloys with higher Zn content. Although the wettability is slightly higher on the alloys with higher Zn content, this difference alone cannot explain the change in the sensitivity of LME of these alloys.

Due to the need for a ductile fracture before the LME of these alloys, which occurs at high levels of plastic deformation, a practical limitation related to the displacement rate of the bending tests arises. Even if high displacement rates promote the LME of the alpha brass, slower displacement rates promote the ductile failure of the alpha brasses. In order to observe the LME, the test should be performed with a sufficiently higher displacement rate to promote embrittlement but at the same time sufficiently lower so the alpha brass can initiate a ductile fracture before the practical displacement limit of the test.

In the case of the Cu-15%Zn samples, at almost all the displacement rates tested, there was no fracture formation, which again did not allow the formation of a fresh stressed surface that could enter into contact with the EGaIn. The only displacement rate when there was a fracture is 0.005 mm/min, in which there was a ductile fracture both in air and in contact with the liquid EGaIn; even if a fresh stressed surface entered contact with the EGaIn, there was no LME. In the Cu-25%Zn samples annealed at 300 °C, the LME sensitivity increases at higher strain rates, which indicates that the reason for no LME on the Cu-15%Zn alloy could be related to the fact that a higher displacement rate would be necessary for LME to occurs. However, the fact that the Cu-20%Zn samples annealed at 300 °C did not present LME at any of the displacement rates and that this alloy presents a higher hardness value indicates that it is unlikely that there could be embrittlement of the Cu-15%Zn alloy under these conditions even if a fracture could initiate.

Another thing in common among the LME of these alloys is the path of the fracture propagation. The ductile fractures propagated in the plane perpendicular to TD, while the brittle fractures propagated in the first instance perpendicular to ND. Further, due to the change in the strain-stress state during the brittle fracture propagation, the fracture changed its direction, propagating gradually into the same plane as the propagation of the ductile fracture; Figure III–46 presented this fracture behaviour in Cu-30%Zn. The microstructure makes this change of direction too tortuous; the brittle fracture propagation can stop, as observed for the Cu-20%Zn and Cu-25%Zn alloys (Figure III–62 and Figure III–67).

III.7. Conclusions on the mechanical behaviour of Cu and alpha brasses in contact with the liquid EGaIn

According to the observations obtained with the bending tests and Small Punch Tests, we propose three situations that explain the mechanical behaviour of Cu and alpha brasses in contact with the liquid EGaIn. Figure III–73 illustrates the first, which corresponds to a situation where an alpha brass is in contact with the liquid EGaIn, and there is the intermetallic $CuGa_2$ between them. The intermetallic impedes direct contact during the mechanical solicitation of the alpha brass. So during most of the tests, the EGaIn can not influence the mechanical behaviour of the alpha brass. After the alloy undergoes a certain degree of deformation, it develops ductile damage in the volume under the surface without initiating a superficial fracture. Then, after certain strain-stress levels, a fracture initiates and reaches the sample's surface, breaking the intermetallic compound. After the intermetallic compound breaks, the liquid EGaIn can flow into the newly created fracture, entering into contact with the surface of the alpha brass under plastic strain. The viscosity of the EGaIn is relatively low (1.99×10^{-3} $kg*m^{-1}s^{-1}$), so it flows by capillarity into the crack. In this situation, the two most important conditions for the LME occurrence materialize: the contact between the solid and the liquid and the plastic strain applied to the solid. Hence, the LME occurs, and an intergranular fracture propagates into the zones with higher plastic strain.

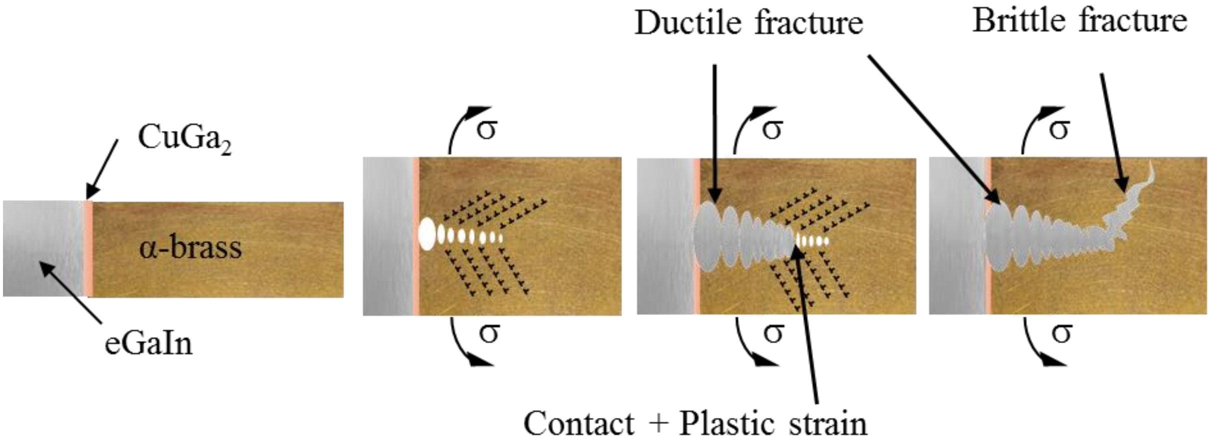

Figure III–73 Schema of the LME of the alpha brass in contact with the liquid EGaIn.

This first situation corresponds to all the conditions wherever the LME occurred. For instance, the LME of the Cu-30 wt.%Zn samples tested using the notched specimens on the Small Punch Test and the 3-point bending test correspond to this situation.

Figure III–74 illustrates a second possibility similar to the first one. In this situation, even if the liquid EGaIn enters into contact with the alpha brass under plastic strain, other parameters could play a role in the non-LME. For instance, the strain rate is an important parameter that defines the apparition of the LME on other systems, such as the case of the Cu-25 wt.%Zn samples annealed at 300 °C tested with the 3-point bending test and the case of the Cu-30 wt.%Zn samples tested using notched specimens in the SPT, both of which presented LME only at higher displacement rates.

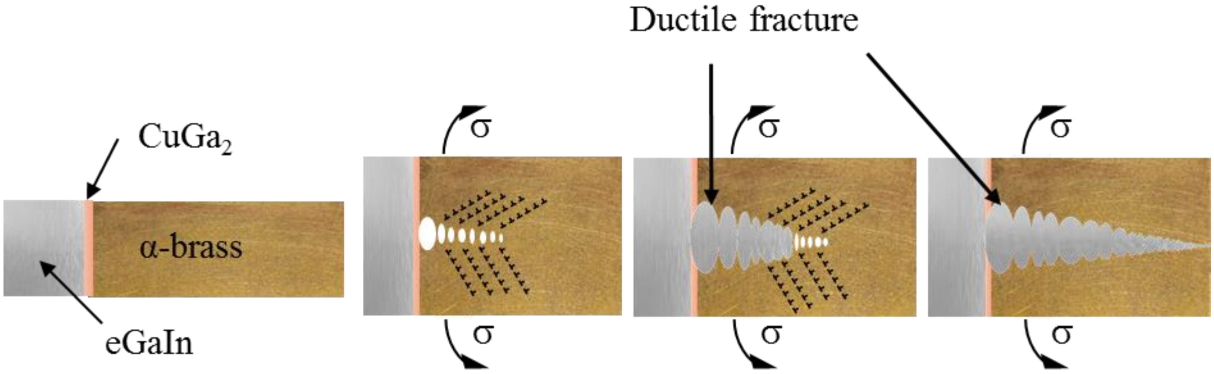

Figure III–74 Schema of the situation of non-LME of the alpha brass in contact with the liquid EGaIn.

Finally, Figure III–75 illustrates a third possible situation. Under some stress states, the ductile damage in the alpha brass extends to the totality of the solid sample’s thickness. In this case, when the fracture initiates on the surface, the ductile damage of the solid is sufficiently significant, so the totality of the fracture is ductile. This situation corresponds to the Cu-30%Zn samples tested with the standard SPT setup and explains why the LME was not present, even if the 3-point bending test showed that this alloy is susceptible to LME by the EGaIn.

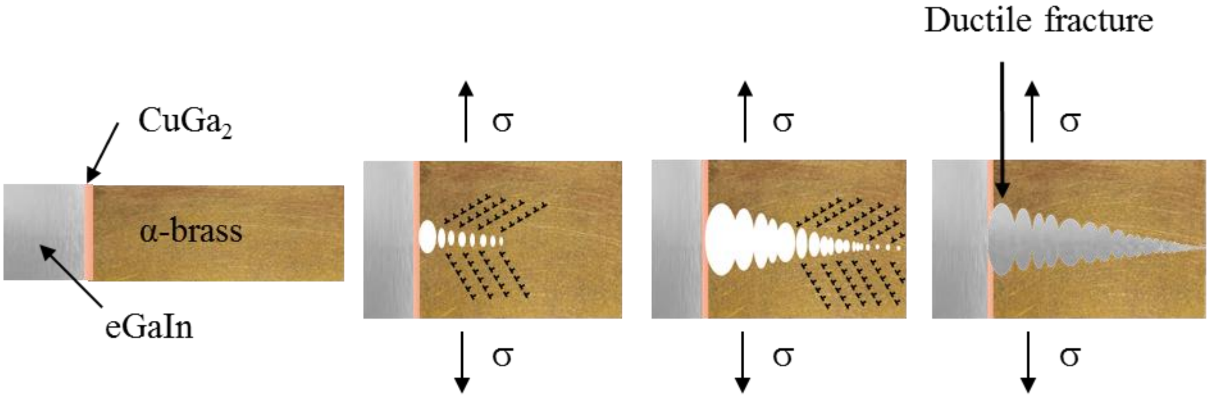

Figure III–75 Schema of the situation of non-LME of the alpha brass in contact with the liquid EGaIn.

In the bending tests, the propagation of the ductile fractures in the alpha brasses followed the samples' centre since the fractures' driving force was the nucleation, growth and coalescence of microvoids. On the other hand, since the driving force of the brittle fracture is the shearing stress or the plastic strain, the brittle fracture propagates in this direction. Moreover, since the brittle fracture is intergranular, the form and disposition of the grains can modify its propagation. Due to stress and strain distribution, the brittle fracture changes its propagation path if the microstructure allows it.

In total, three variables in this work showed to influence the LME sensitivity of the alpha brass by the liquid EGaIn: the Zn content, the strain rate, and the hardness. These three variables are closely related to two phenomena that might affect the LME occurrence: dislocation motion and twinning deformation.

Whenever the dislocation motion is limited, the material cannot accommodate significant plastic deformation, which could lead to its embrittlement. A diminution of the dislocation motion might enhance the concentration of the dislocations in the grain boundary, which matches the fracture mode observed for the alpha brasses in contact with the EGaIn. The materials with higher dislocation motion will easily accommodate these dislocations without embrittlement. Similarly, if there is twinning in the material, these twins could act as strong barriers to the dislocation motion, limiting the plastic deformation the material can withstand.

The Zn content of the alpha brasses strongly influences the dislocation motion since it is responsible for the solid solution strengthening of these alloys, i.e., Zn atoms deform the crystal lattice, which hinders the dislocation movement. Moreover, the Zn decreases the stacking fault energy (SFE) of the alpha brasses, which promotes twinning and strain hardening [52]–[54].

Regarding the strain rate, the intermetallic formation seems a compelling explanation for the diminution of the LME sensitivity at lower strain rates. Nevertheless, the kinetics of the intermetallic cannot fully explain the strain rate dependency since different alloys tested at the same strain rate showed different LME sensitivities. For instance, the Cu-30%Zn alloy presented LME even during the 3-point bending test at displacement rates of 0.0005 mm/min, a mechanical test that takes several days. Moreover, the results of section II.2. indicate that the intermetallic formation kinetics is similar for all the alloys studied in this work. It is more plausible that the effect of the strain rate is related to its effect on the dislocation motion, which is similar to the Zn-content, i.e., higher strain rates hinder the dislocation movement.

The hardness of the material directly relates to the dislocation density. When all other microstructural parameters, such as the grain boundaries, are constant, a higher hardness value indicates a higher dislocation density in the solid metal. Whenever the dislocation density increases, the quantity of deformation that the material can accommodate significantly reduces since the other dislocations restrict the dislocation motion, and the dislocation nucleation is limited. Moreover, the dislocation density is one of the two main microstructural variables influencing the deformation twinning [54]. The effect of the dislocation density may explain the particular path of brittle fracture propagation observed for the 3-point bending test since the

LME sensitivity would be higher in zones with the higher dislocation density, i.e. the zones that have undergone the higher plastic deformation. Section III.11. compares the profile of plastic strain with the brittle fracture propagation to support this hypothesis.

For a better insight into these possible conditions of LME and non-LME, the following section presents an analysis using the finite element method. With it, it would be possible to quantify and compare the strain rates and the stress states at which the LME occurred in the SPT and the 3-point bending test. Also, if the analysis incorporates a ductile damage model (such as the Gurson-Tvergaard-Needleman model), an estimation of the profile of the microvoid nucleation and growth can be carried out. This estimation could help to support or refute the depiction of these situations. Before presenting the finite element method simulations, section III.8. briefly defines the Gurson-Tvergaard-Needleman model. Then, section III.9. corresponds to the determination of the elastoplastic properties obtained experimentally. Afterwards, sections III.10. and III.11. describe the principal results obtained from the simulations of the SPT and the bending tests, respectively.

III.8. The Gurson-Tvergaard-Needleman model

It is possible to classify the fracture of metals depending on their behaviour. Figure III–76 shows the different possible fractures when a material is under tension at low temperatures. Whenever the metal is entirely brittle, its fracture occurs through cleavage or intergranular fracture. In the opposite scenario, if the metal is highly ductile, the rupture occurs by necking or shearing-off. In between, another fracture mode consists of microvoids nucleation, growth and coalescence, which can occur in the grain boundaries or inside the grains.

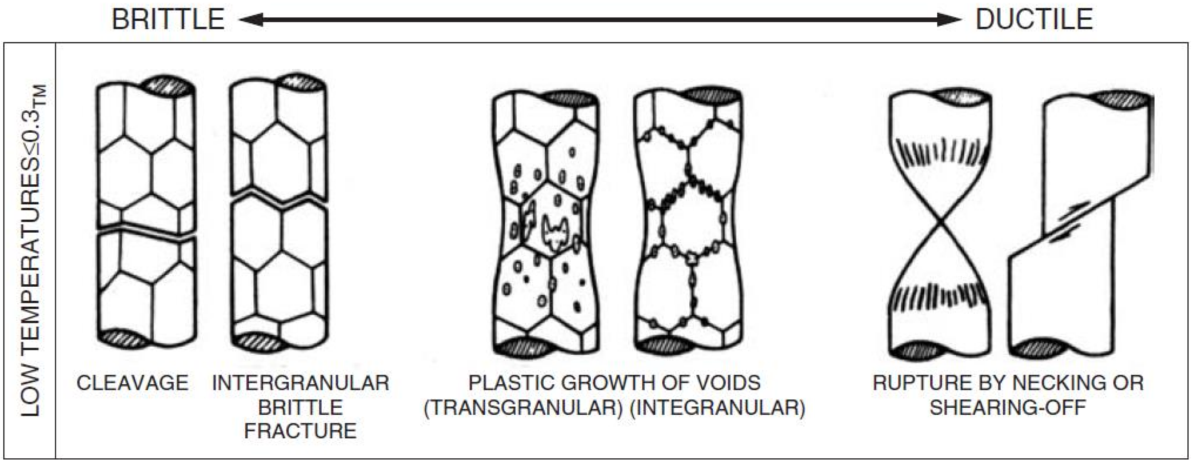

Figure III–76 Broad classes of fracture mechanisms [52].

The fractures of the Cu and Cu-30%Zn bending samples are examples of rupture by plastic growth of voids, respectively. Figure III–77 exemplifies two of these fracture surfaces. The final rupture of Cu occurred by the coalescence of micro-voids, and this material presents a high degree of necking evidenced by a contraction of the transversal area. Similarly, the Cu-30%Zn alloy presents a failure by micro-void coalescence that is more significant than for Cu, and there is very little necking.

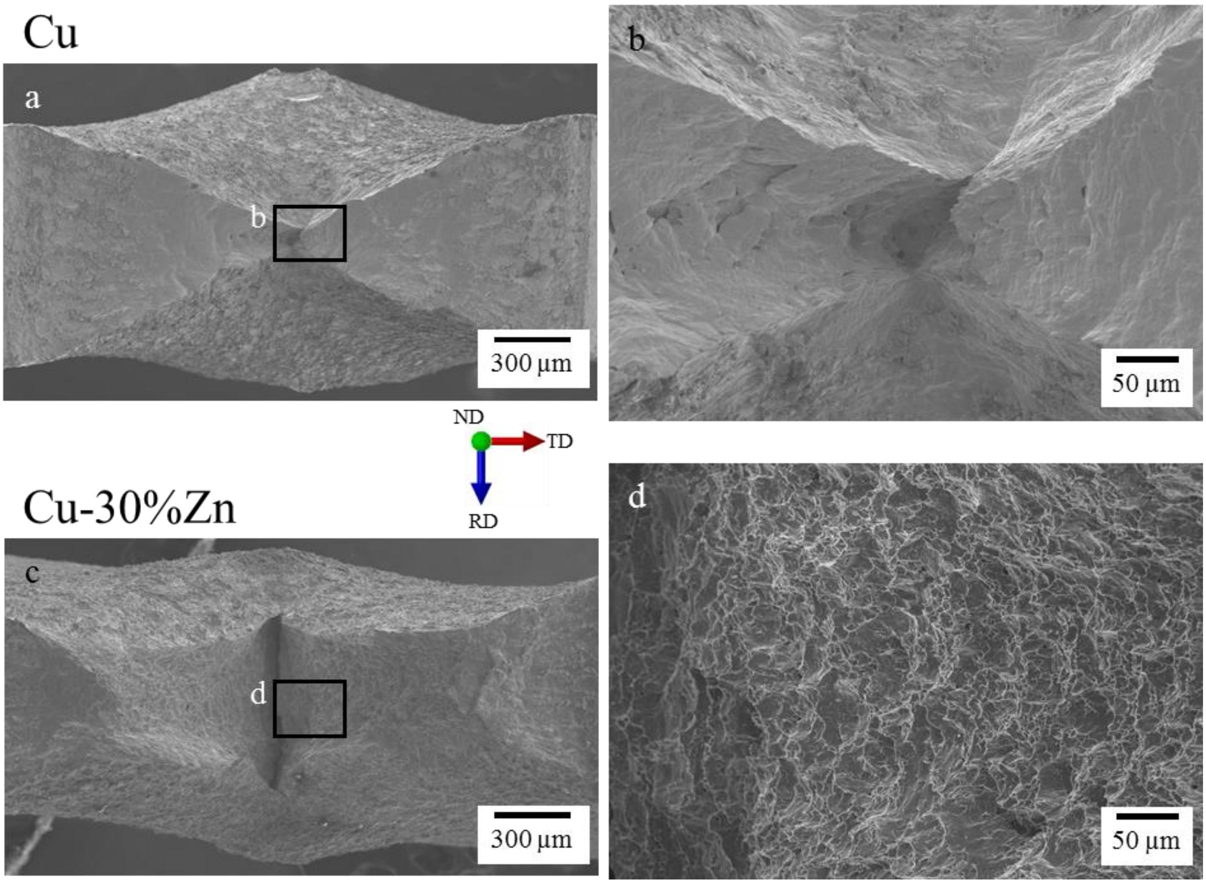

Figure III–77 Fracture behaviour of Cu and Cu-30%Zn under bending stress.

For a better description of the mechanical behaviour of these materials, the modelling should consider the phenomena of void nucleation and coalescence.

The Gurson-Tvergaard-Needleman (GTN) model [55]–[57] describes the influence of micro-voids nucleation, growth and coalescence on the mechanical response of a metallic material. For this, Eq. (16) describes the yield function in terms of the void volume fraction (*f*).

$$\Phi = \left(\frac{q}{\sigma_y(\bar{\varepsilon}_m^{pl})}\right)^2 + 2q_1 f \cosh\left(-\frac{3q_2 p}{2\sigma_y(\bar{\varepsilon}_m^{pl})}\right) - (1 + q_3 f^2) = 0 \quad (16)$$

where q is the effective Mises stress; σ_y is the yield strength as a function of equivalent plastic strain $\bar{\varepsilon}_m^{pl}$; q_1, q_2, and q_3 are material parameters; and p is the hydrostatic pressure. Furthermore, the total change in the void volume fraction ($\dot{f}$) in Eq. (17) is a sum of the growth and nucleation of the micro-voids ($\dot{f}_{growth}$ and $\dot{f}_{nucleation}$, respectively).

$$\dot{f} = \dot{f}_{growth} + \dot{f}_{nucleation} \tag{17}$$

In turn, the law of conservation of mass controls the microvoids' growth, while the nucleation of voids is a strain-controlled relationship defined in Eq. (18) with a normal distribution defined in Eq. (19)

$$\dot{f}_{nucleation} = A\dot{\bar{\varepsilon}}_m^{pl} \tag{18}$$

$$A = \frac{f_N}{s_N\sqrt{2\pi}} \exp\left[-\frac{1}{2}\left(\frac{\bar{\varepsilon}_m^{pl} - \varepsilon_N}{s_N}\right)^2\right] \tag{19}$$

where f_N is the volume fraction of the nucleated voids, s_N is the standard deviation, and ε_N is the mean value. All of these values are material dependent and define its mechanical response. For instance, Figure III–78 shows the differences in the behaviour of materials with different parameters.

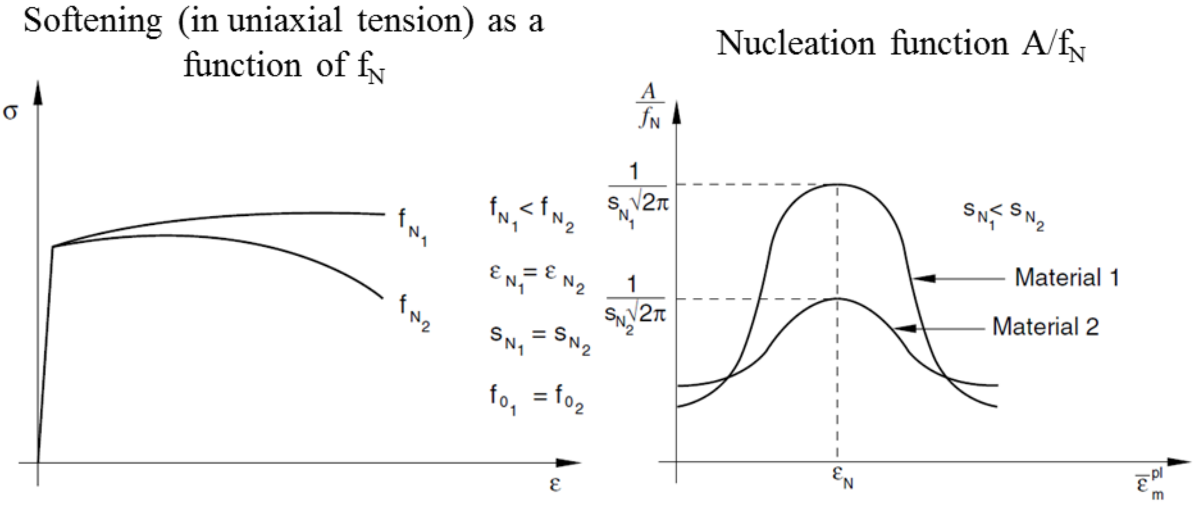

Figure III–78 Material's behaviour according to the GTN model in function of its parameters [58].

In this work, the FEM incorporates the GTN model in the simulation of the SPT and the bending tests. Various studies on mechanical tests, such as the SPT, have made use of these constitutive relationships to model material failure and damage [19], [21], [22], [34], [59].

III.9. Definition of the material behaviour for the FEM

In sections III.2. and III.5., the mechanical behaviour of Cu and alpha brasses in contact with the EGaIn was studied using two mechanical tests: SPT and bending tests. The Cu-30 wt.%Zn alloy was studied with both mechanical tests, presenting the most modification of its mechanical behaviour in contact with the EGaIn. This alloy was implemented into finite element modelling (FEM).

Tensile tests combined with digital image correlation (DIC) were carried out in flat samples to accurately obtain the material mechanical properties used in the analysis. The tests were carried out on both batches of the Cu-30%Zn alloy, i.e., the one used to extract the specimens tested by SPT and the one used to extract the bending test specimens. Table III–7 summarizes their properties and Young's modulus from the tensile tests.

Table III–7 Properties of the samples tested by the tensile tests.

Composition	**Thickness (mm)**	**Mechanical test**	**Manufacturer**	**Hardness (HV)**	**Grain size (µm)**	**Young's modulus (GPa)**
Cu -30 wt.%Zn	0.64	SPT	Alfa Aesar	133 ± 8	16 ± 2	95
Cu -30 wt.%Zn	2	Bending tests	Alfa Aesar	142 ± 4	39 ± 7	100

The true stress was calculated through Eq. (20) using the values of the force (F) obtained from the force cell, the initial cross-area of the samples (A_0), and the true strain (ε) obtained from the DIC.

$$\sigma = \frac{F}{A_0} e^{\varepsilon} \tag{20}$$

Figure III–79 presents the two materials' true stress versus true strain curves. As expected, the yielding point is higher for the sample with the higher hardness, i.e. 263 MPa for the Cu-30%Zn batch with 0.64 mm thickness and 324 MPa for the Cu-30%Zn batch with 2 mm thickness. The work hardening is similar for both materials, evidenced by the parallel slopes of both curves during the plastic regime.

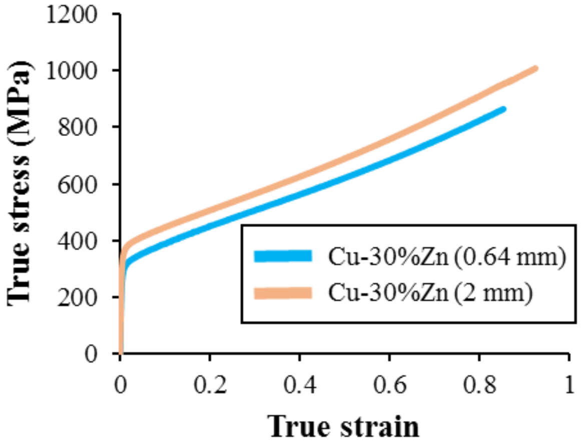

Figure III–79 True stress vs true strain curves obtained with the tensile tests.

For the stress-strain relationship description of the materials in the analysis, the true plastic strain vs the true stress data was fed into the software along with Young's modulus and Poisson's ratio, which was considered 0.33. The software used for the FEM was ABAQUS 6.13.

On the other hand, one aspect studied with the FEM is the nucleation and growth of the microvoids in the material, which are phenomena that lead to the rupture of the Cu-30%Zn alloy. To model this, the GTN model, which section III.9. describes, was implemented in the analysis.

Materials constants necessary for this model were obtained by simulating the tensile tests using initial values from the literature [58]: ε_N=0.3, S_N=0.1, and f_N=0.02. The force and displacement values were obtained from the simulations and compared with the experimental data. Then, the values of the materials constants were iteratively adjusted to fit the experimental curve. The initial relative density value was considered 1 for both materials, and the values q_1=1.5, q_2=1, and q_3=2.25 were considered.

Figure III–80 shows the assembly used for the simulations of the tensile tests. An eighth part of the specimen was modelled to save calculation time, taking advantage of the symmetry of the samples, which was imposed into the simulation using three symmetry conditions that Figure III–80a schematizes, e.g., U1=UR2=UR3=0 in the case of the face that has a symmetry in the YZ plane. A displacement in the X-axis was imposed on a sample volume corresponding to the specimen volume confined by the clamps. Figure III–80b illustrates this displacement along with the mesh used for the specimen.

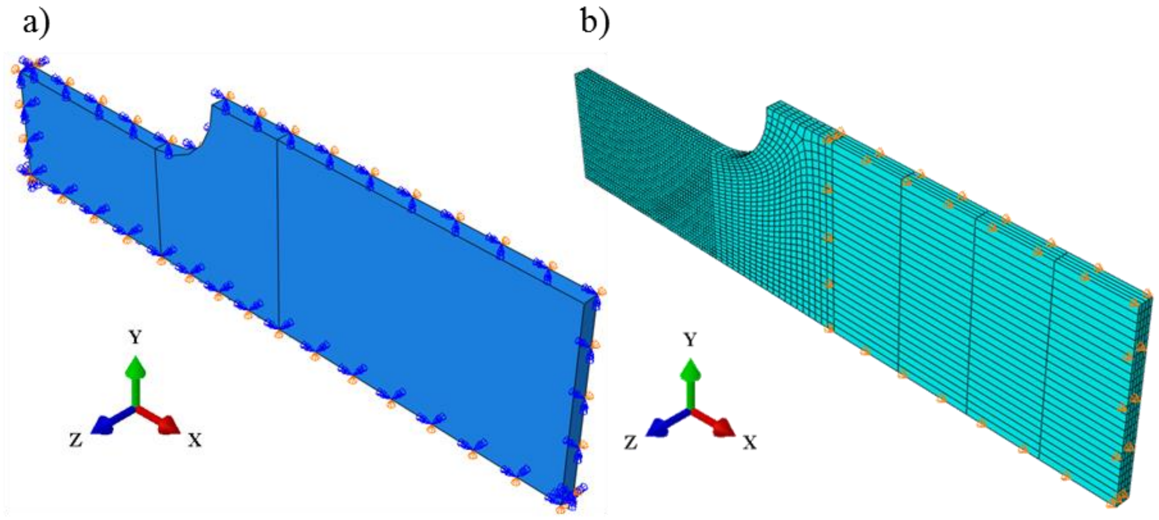

Figure III–80 Modelling of the tensile test as an eight-part specimen with a thickness of 2 mm. a) The symmetric conditions, and b) the displacement and the mesh used for this specimen.

The force was calculated by obtaining the reaction force in the YZ face of the sample and multiplying it by 4. The displacement was obtained from a point in the XZ face 1.5 mm away from the sample's centre before the test's start. This point was selected since the deformation is homogeneous in this sample zone, so the displacement can be compared more precisely with the experimental curve.

In the case of the experimental curve, the force was obtained directly from the force cell, and the displacement was calculated by supposing a homogeneous displacement and using the value of the average true strain obtained by DIC and Eq. (21)

$$\Delta L = L_0(e^{\varepsilon} - 1) \tag{21}$$

where ΔL is the displacement, L_0 is the initial length (in this case, 1.5 mm), and ε is the true strain.

Figure III–81 compares the calculated tensile tests, with and without the damage model, and the experimental test for the Cu-30%Zn alloy sample with a thickness of 2 mm.

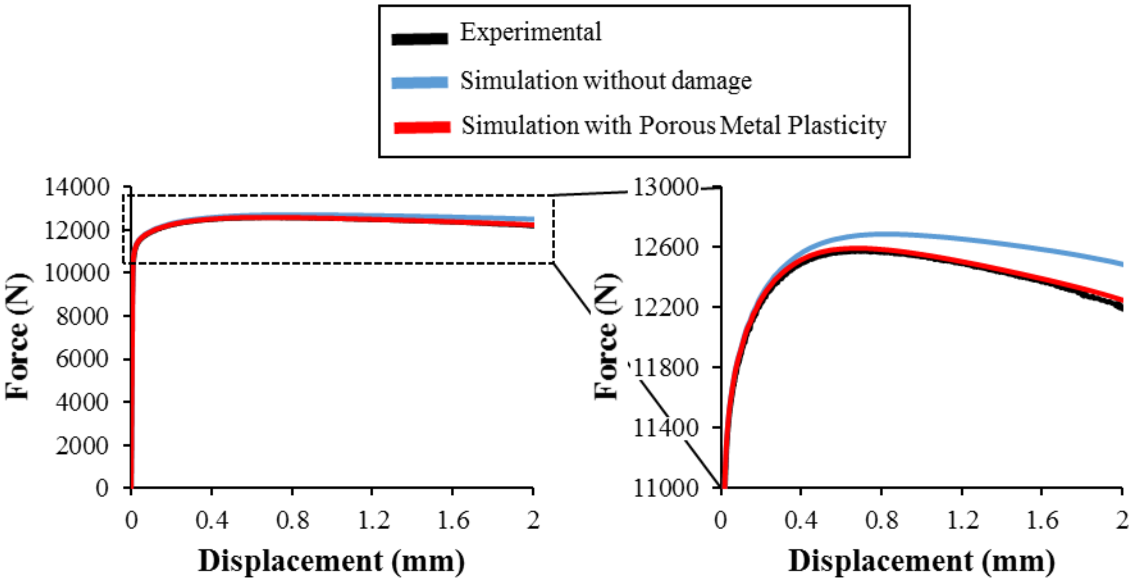

Figure III–81 Force-displacement curves of simulated tensile tests and the experimental tensile test of the Cu-30%Zn alloy with a thickness of 2 mm.

Table III–8 presents the values of the parameters of the GTN model that fit better and are further used in this work.

Table III–8 Best fitting parameters for the GTN model.

Material	ε_N	s_N	f_N
Cu -30 wt.%Zn 0.64 mm	0.5	0.1	0.025
Cu -30 wt.%Zn 2 mm	0.45	0.25	0.012

The obtained properties of both materials were implemented in the FEM of the SPT and the bending test, respectively. All simulations considered a displacement rate of 5 mm/min. The presented FEM does not consider anisotropy or strain rate effects.

III.10. Modelling of the Small Punch Test

The Small Punch Test was used to test three different specimens. Figure III–1 and Figure III–6 in section III.1. show the setup and dimensions of the SPT, respectively. The three specimen geometries used in this work with the SPT were modelled. Due to their symmetries, each of them was modelled differently. The material properties used for all of the FEM of the SPT correspond to that of the Cu-30 wt.%Zn alloy sheet with a thickness of 0.64 mm (see Table III–7 and Table III–8).

III.10.1. Standard Small Punch Test

The standard specimen was modelled as a disk, although the experimental specimen used in this work had a square geometry. The modelling of a disk-shaped specimen allows for an axisymmetric 2D simulation, which needs considerably fewer computational resources than a 3D simulation. These simulations can adequately describe the experimental tests done in this work since the square and disk geometries perform equally [2]. The similitude of the disk and square specimen behaviour was corroborated by carrying out a simplified 3D version of the simulation with coarse mesh (not shown in this work). There were no significant differences between the 2D and 3D results.

Figure III–82 shows the assembly and the mesh used for the 2D simulation. The whole assembly has an axisymmetric condition parallel to the Y-axis, represented on the left side of the assembly. The dies are modelled as rigid bodies, and their movement is restrained. The puncher is modelled as a rigid body and set to do a positive displacement along the Y-axis. A frictionless tangential behaviour was considered for all contact pairs.

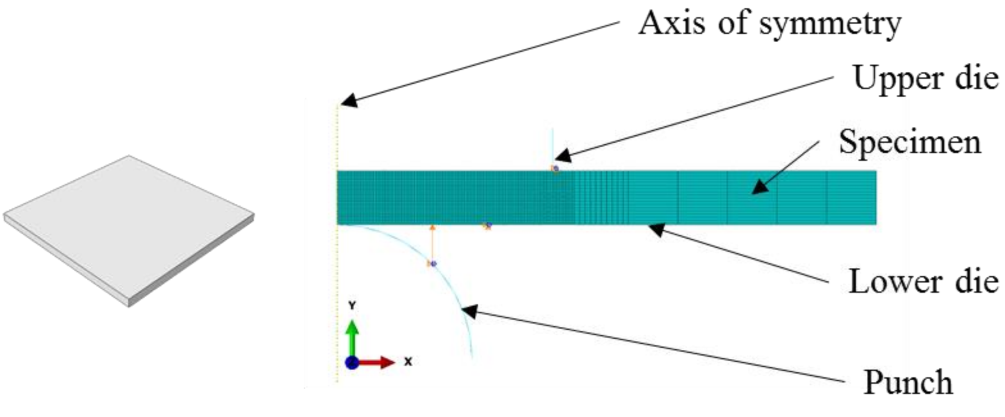

Figure III–82 Assembly used for the 2D modelling of the standard small punch test: specimen, the boundary conditions, and the mesh.

Figure III–83 contrasts the experimental and simulated force versus displacement curves. Except for the final part of the curves, there is a good agreement between the experimental and the simulation. This last part corresponds to the crack growth stage (see section III.1.1.), and the difference comes principally from the lack of implementation of a crack growth model in the simulation.

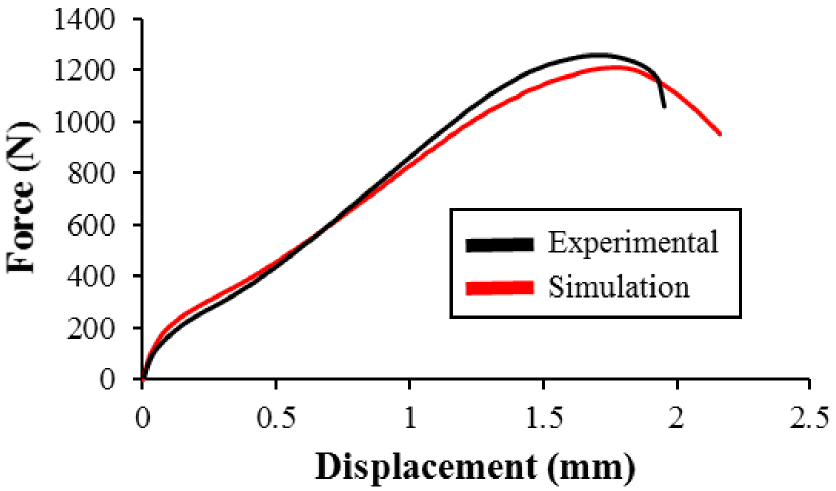

Figure III–83 Force-displacement curves for the experimental and simulated standard SPT.

Under this condition, the plotted results correspond to the state of the sample at the experimental point of the maximum force, which corresponds to the fracture initiation point [2], [13], [34]. Furthermore, for clarity, the variables' fields are shown in a half specimen by applying a sweep of 180°. Figure III–84 and Figure III–85 show two different views of the results from the same simulation.

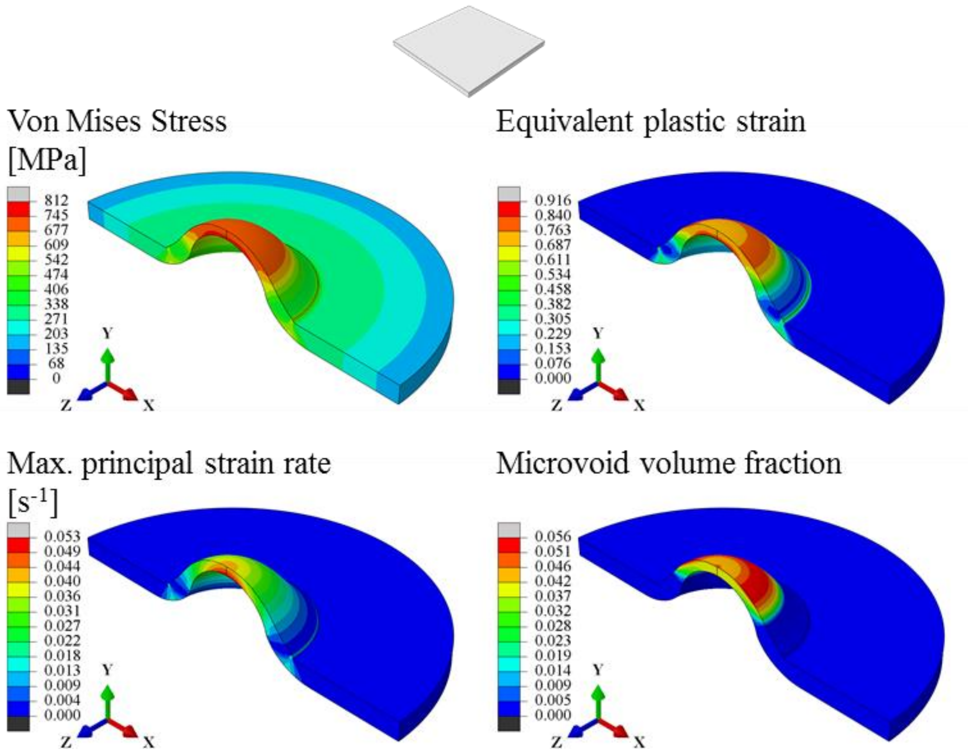

Figure III–84 Magnitude of the von Mises stress, the equivalent plastic strain, the maximum principal strain rate, and the microvoid volume fraction for a standard SPT sample.

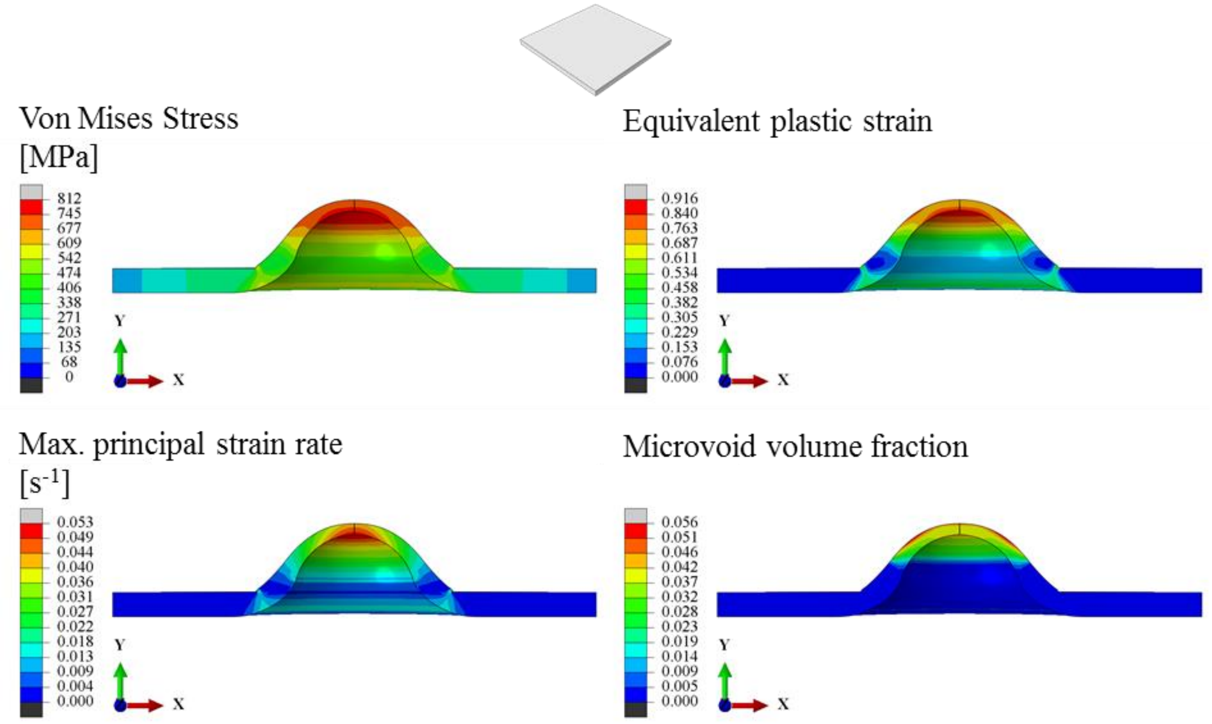

Figure III–85 Lateral view of the magnitude of the von Mises stress, the equivalent plastic strain, the maximum principal strain rate, and the microvoid volume fraction for a standard SPT sample.

The magnitude and distribution of these variables are further compared with the other mechanical tests. The stress and strain magnitude varies considerably along the specimen, including across the thickness.

In addition, from the magnitudes of the stress and strain, it would be conceivable that the specimen could fail by initiating a crack in the centre, where the magnitude of these variables is the highest. However, experimentally, ductile materials fail with a circular crack. This behaviour matches the distribution of the microvoid volume fraction calculated with the simulations.

For a further comparison with the experimental observations, Figure III–86 shows an upper view of the calculated microvoid volume fraction superposed with a micrography of a fractured sample. The profile of the maximum microvoid volume fraction matches the crack formation.

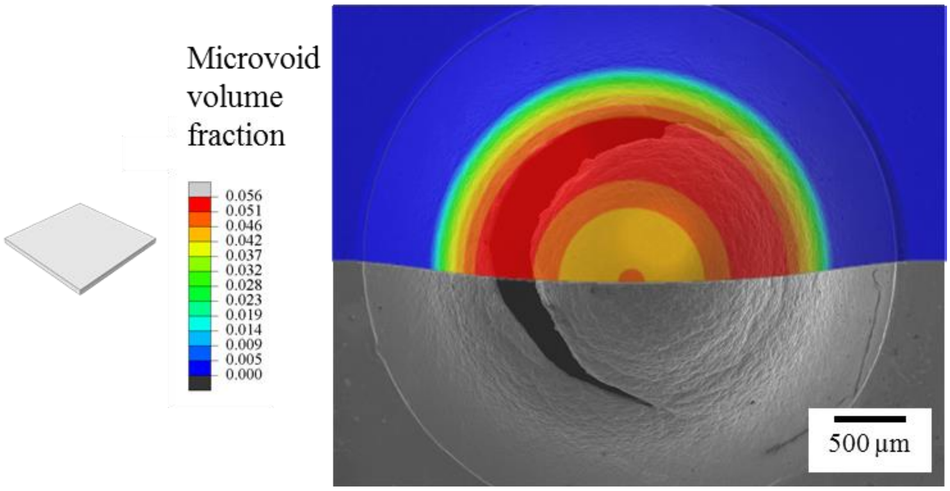

Figure III–86 Comparison of the calculated microvoid volume fraction for a standard SPT sample with an experimental fractured sample.

III.10.2. Notched Small Punch Test

The small punch test specimen with a longitudinal notch was modelled in 3D as a quarter part of the real specimen, along with the analogous part of the dies and the spherical punch. Figure III–87 illustrates this assembly and its mesh; the blue and orange arrows indicate the symmetry conditions in the correspondent faces of the sample. Symmetric boundary conditions were applied: $U_Z=UR_X=UR_Y=0$ in the XY face and $U_X=UR_Y=UR_Z=0$ in the ZY face. The dies' movement is restrained, and the puncher was set to perform a positive displacement in the Y-axis. The dies and the puncher are modelled as rigid bodies. A frictionless tangential behaviour was considered for all contact pairs.

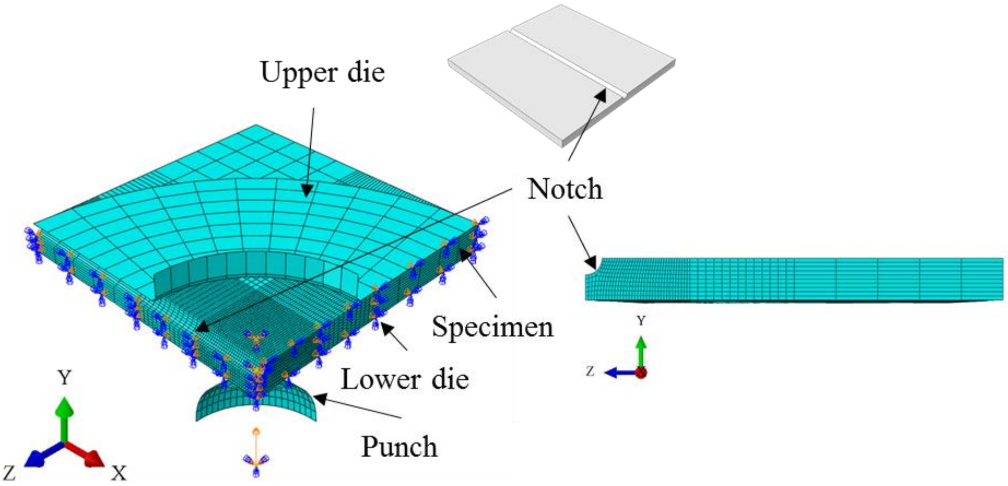

Figure III–87 Assembly used for the modelling of the small punch test on a quarter part of a longitudinally notched specimen. The representation includes the boundary conditions and the mesh.

As for the standard Small Punch Test, Figure III–88 contrasts the force-displacement curve of the simulation with one of the experimental curves. The curves match reasonably well except for the end, which corresponds to the crack growth stage. This disparity is due to the same limitation described for the standard SPT simulation, i.e., no crack initiation model is implemented in these simulations.

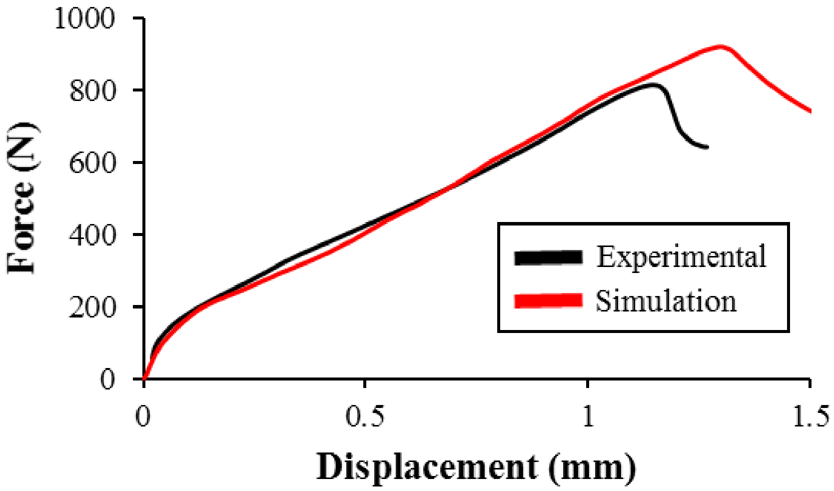

Figure III–88 Force-displacement curves for the experimental and simulated SPT on a longitudinally notched specimen.

Figure III–89 and Figure III–90 show the plot of some results obtained with the simulations. There are some differences when comparing these with the results of the standard SPT sample (Figure III–84 and Figure III–85). Contrary to the standard SPT sample, the longitudinally notched specimen presents a considerable concentration of the stress and the plastic strain in the notch. The stress and strain values vary across the sample thickness as for the standard specimen, but in the longitudinally notched specimen, the magnitude is more important in the face opposite to the punch, which is the face in contact with the EGaIn in the experimental test.

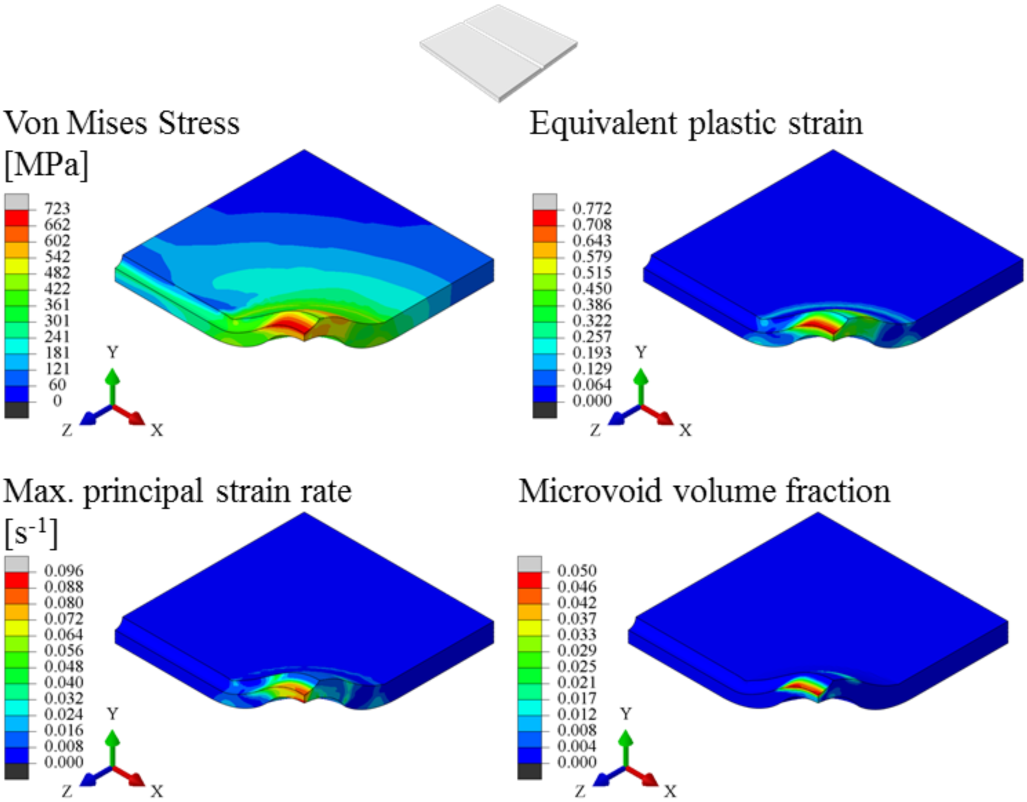

Figure III–89 Magnitude of the von Mises stress, the equivalent plastic strain, the maximum principal strain rate, and the microvoid volume fraction for a longitudinally notched SPT sample.

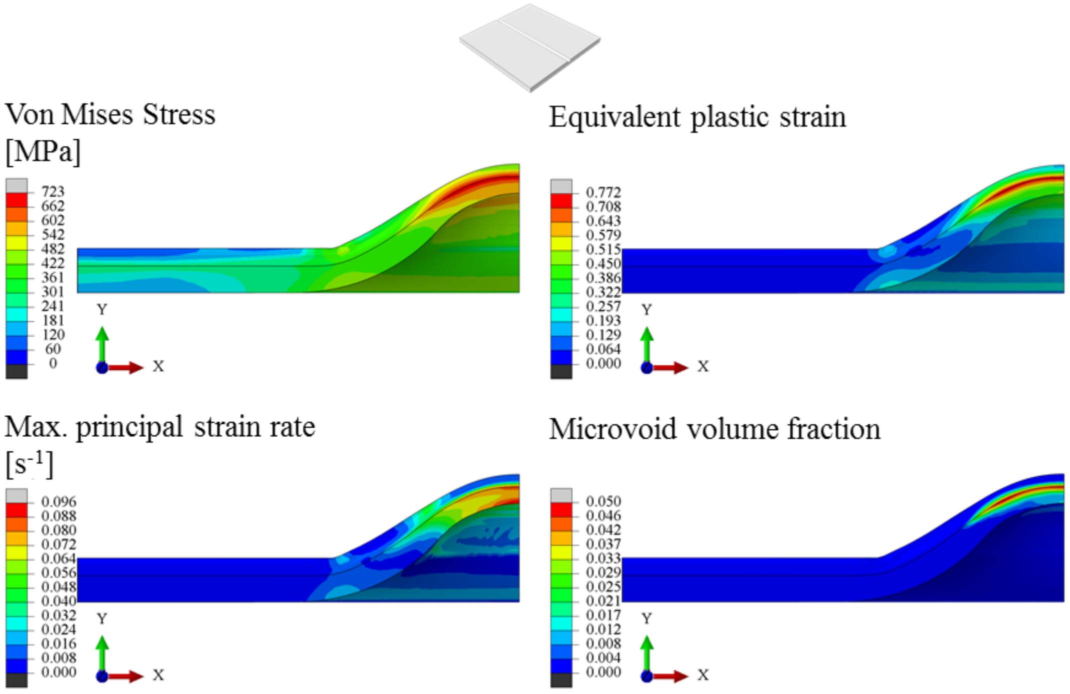

Figure III–90 Lateral view of the magnitude of the von Mises stress, the equivalent plastic strain, the maximum principal strain rate, and the microvoid volume fraction for a longitudinally notched SPT sample.

Moreover, the strain rate is higher in these specimens by a factor of 2. Finally, the nucleated microvoid concentrates into a relatively small volume in the centre of the notch instead of a significant volume. The maximum microvoid volume fraction at the point of fracture is similar in the standard specimen and the longitudinally notched specimen, 0.050 and 0.056, respectively.

On the other hand, the lateral notched specimen was modelled in 3D. Figure III–91 shows the corresponding assembly where half of the specimen was drawn. The symmetry condition $U_X=UR_Y=UR_Z=0$ was imposed in the YZ face. The dies' movement is restrained, and the puncher was set to perform a positive displacement in the Y-axis. The dies and the puncher are modelled as rigid bodies. A frictionless tangential behaviour was considered for all contact pairs.

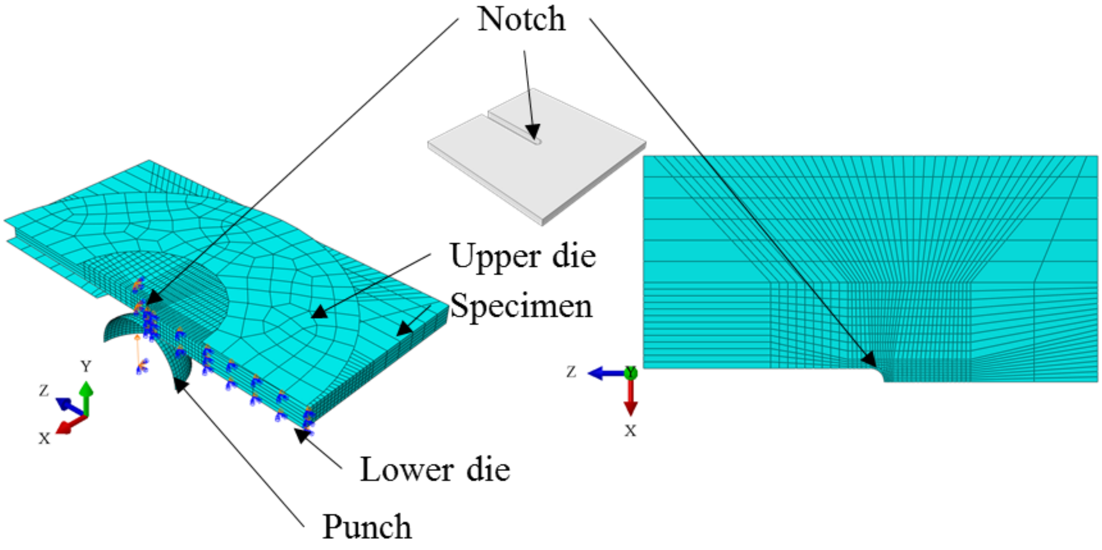

Figure III–91 Assembly used for the simulation of the small punch test on half of a laterally notched specimen; boundary conditions and mesh included.

As for the previous simulations, Figure III–92 contrasts the calculated force-displacement values with the experimental data.

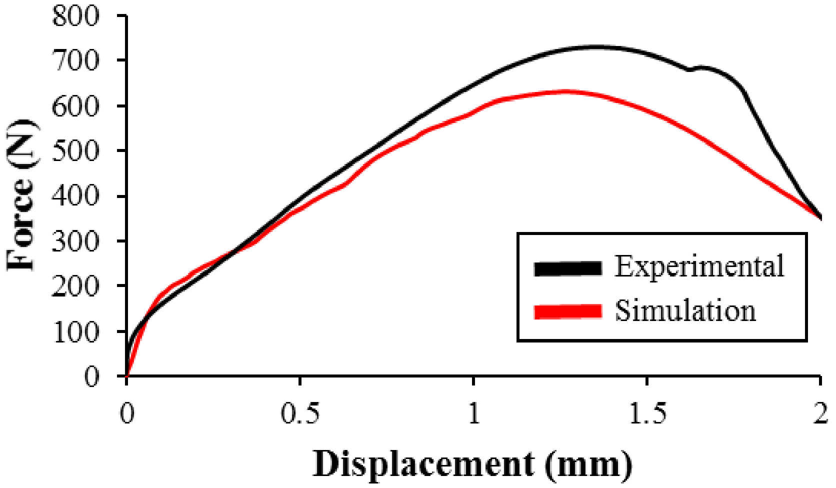

Figure III–92 Force-displacement curves for the experimental and simulated SPT on a laterally notched specimen.

Contrary to the previous simulations, the experimental force-displacement curve presents higher force values than the calculated curve. This difference could be due to a misalignment of the specimen during the experiments. However, comparing the FEM results of this sample with the other tests is helpful. Figure III–93 and Figure III–94 show these results.

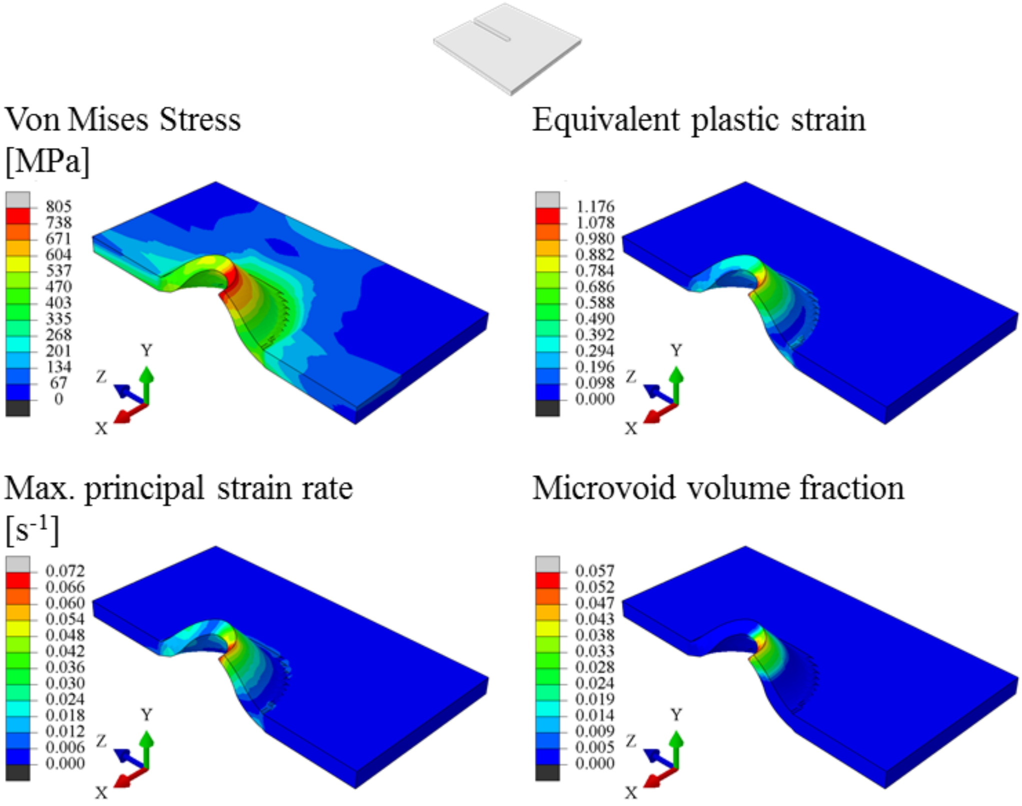

Figure III–93 Magnitude of the von Mises stress, the equivalent plastic strain, the maximum principal strain rate, and the microvoid volume fraction for a laterally notched SPT sample.

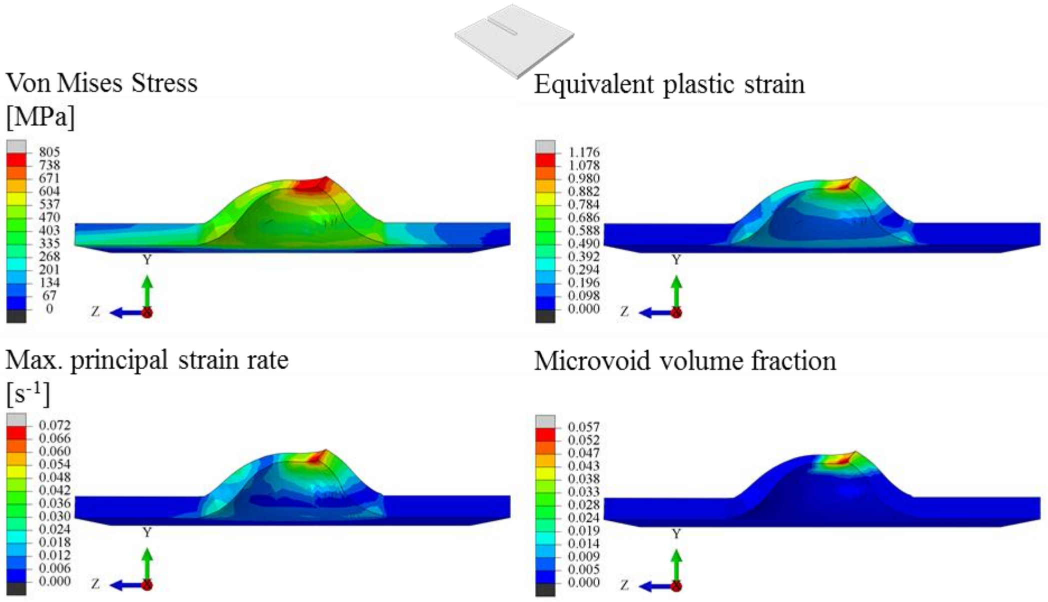

Figure III–94 Lateral view of the magnitude of the von Mises stress, the equivalent plastic strain, the maximum principal strain rate, and the microvoid volume fraction for a laterally notched SPT sample.

As for the longitudinally notched specimen, the laterally notched specimen presents a significant stress-strain concentration at the bottom of the notch. In contrast, the magnitude of stress and strain do not change considerably along the thickness. In addition, the value of the maximum microvoid volume fraction is similar to the other SPT samples.

III.11. Modelling of the bending tests

As described in section III.5., different bending test setups were used, and Figure III–35 shows their dimensions. For the FEM of the bending tests, a quarter part of the specimen was modelled, taking advantage of the two planes of symmetry of the sample. The 4-point and the 3-point bending tests were simulated. The material properties implemented in the model correspond to that of the Cu-30 wt.%Zn alloy sheet with a thickness of 2 mm, presented in Table III–7 and Table III–8.

III.11.1. FEM of the 4-point bending test

The goal of the FEM of the 4-point bending test is to detail why using this setup on miniaturized specimens is unsuitable for studying the LME of materials that need considerable plastic deformation before the apparition of this phenomenon. Figure III–95 shows the assembly and the meshing used for these simulations. There are two symmetry conditions: $U_X=UR_Y=UR_Z=0$ in the YZ face and $U_Z=UR_Y=UR_X=0$ in the XY face. The central support movement is restrained; for the other support, its movement is set to a negative displacement in the Y-axis.

Both supports were modelled as rigid bodies. A frictionless tangential behaviour was considered between the specimen and the supports.

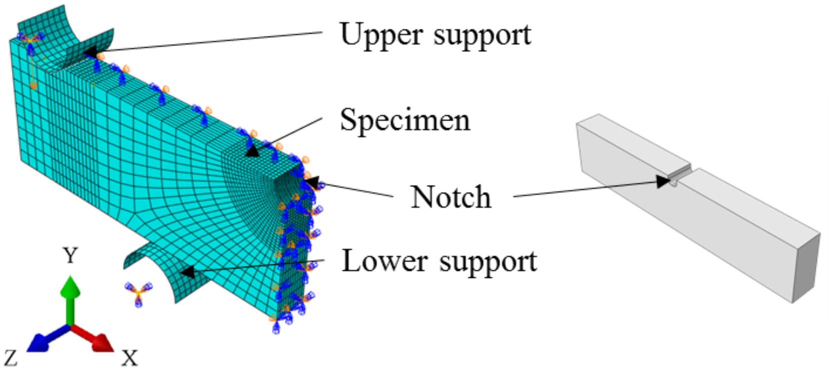

Figure III–95 Assembly used for the simulation of the 4-point bending test on a quarter part of the miniaturized specimen, boundary conditions and mesh included.

Figure III–96 compares the force versus displacement curves obtained for this simulation with an experimental test. There is a mismatch between these two curves; the experimental curve shows higher displacement values than those calculated at the same force value. The lack of an experimental displacement calibration, which was carried out for the SPT, explains this difference. Since the displacement of the experimental setup adds to the specimen displacement in the experimental curves, the displacement of the calculated curves is lower. Another mismatch source is the sample's alignment since its placement was done manually.

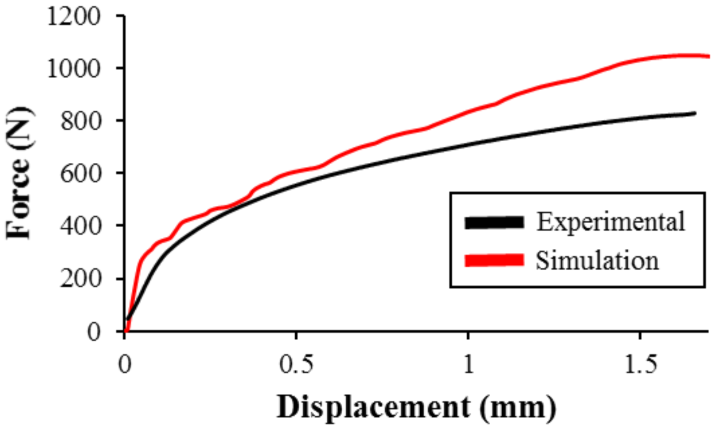

Figure III–96 Force-displacement curves for the experimental and simulated 4-point bending test on a miniaturized specimen.

Furthermore, Figure III–97 contrasts the calculated contour of the deformed samples with the experimental contour of a specimen tested with the 4-point setup to corroborate this simulation's suitability to describe the experimental 4-point bending test. From this comparison, the calculated contour matches the experimental observations and describes the deformation applied by the supports.

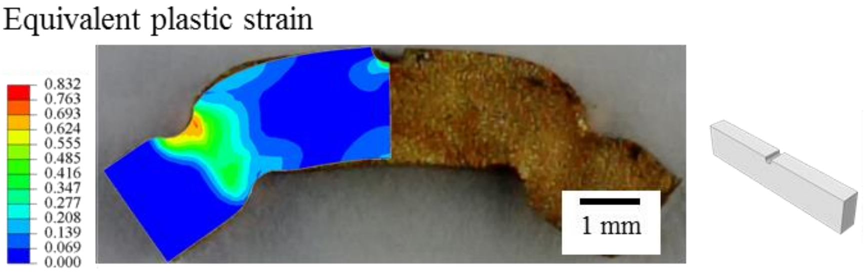
Equivalent plastic strain

Figure III–97 Simulated and experimental deformed contours of a miniaturized 4-point bending test specimen.

On the other hand, Figure III–98 shows some of the results at a displacement of 1.7 mm, corresponding to the experimental maximum displacement. These plots show considerable stress and plastic strain between the supports, which values are higher than around the notch. The notch's low stress and plastic strain values explain the lack of fracture in these tests.

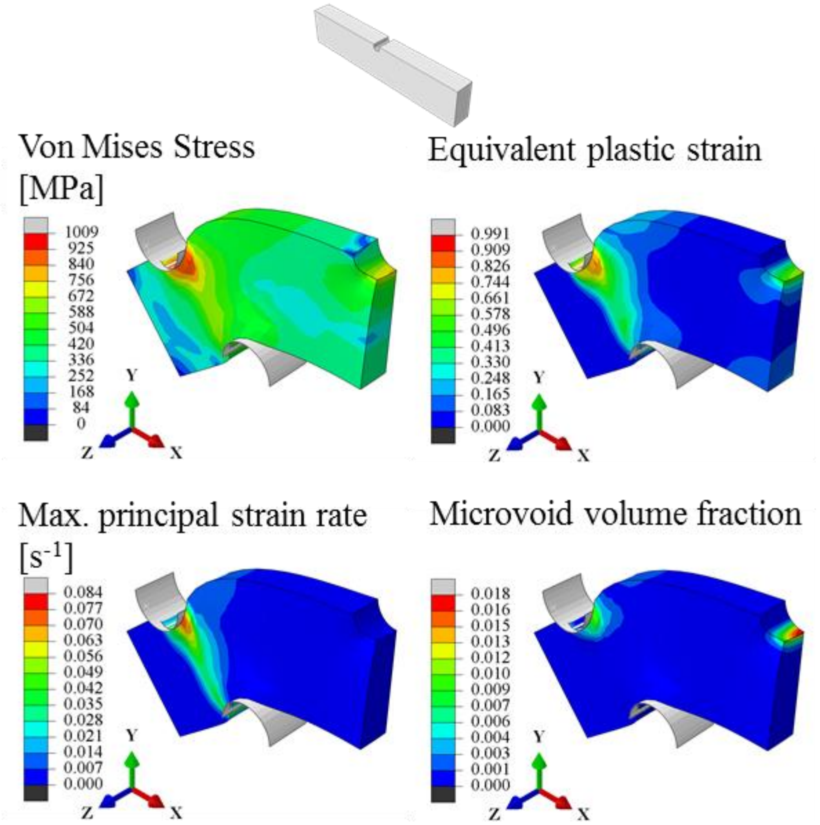
Von Mises Stress [MPa]

Equivalent plastic strain

Max. principal strain rate $[s^{-1}]$

Microvoid volume fraction

Figure III–98 Magnitude of the von Mises stress, the equivalent plastic strain, the maximum principal strain rate, and the microvoid volume fraction for a miniaturized specimen tested with the 4-point bending test at a displacement of 1.7mm.

Moreover, the strain rate near the notch is close to 0. This value indicates that there would not be an increase in the strain imposed in this zone if the test could continue. The same would happen for any material that needs a higher plastic strain and stress magnitude to initiate a fracture; hence, this test is unsuitable in those cases. On the contrary, experimentally, the 3-point bending test was suitable, and the next section shows its FEM.

III.11.2. FEM of the 3-point bending test

Figure III–99 presents the assembly used to simulate the 3-point bending test, the correspondent mesh, and the applied boundary conditions. The assembly is a replica of the one used for the 4-point bending test (Figure III–95), just with a different position of the lower support. There are two symmetry conditions: $U_X=UR_Y=UR_Z=0$ in the YZ face and $U_Z=UR_Y=UR_X=0$ in the XY face. The central support movement is restrained; for the other support, its movement is set to a negative displacement in the Y-axis. Both supports were modelled as rigid bodies. A frictionless tangential behaviour was considered between the specimen and the supports.

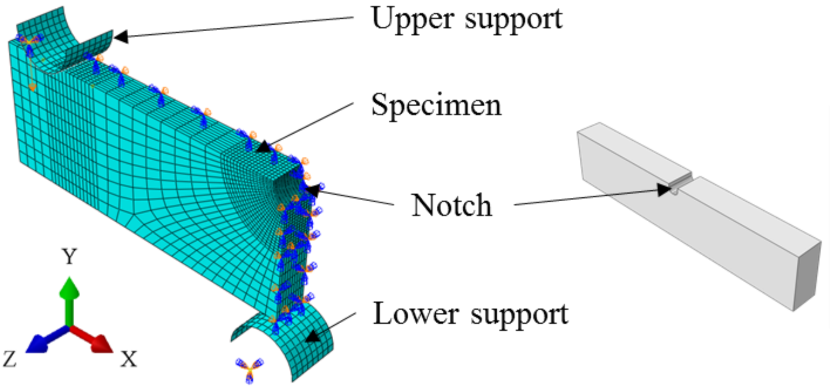

Figure III–99 Assembly used for the simulation of the 3-point bending test on a quarter part of the miniaturized specimen, boundary conditions and mesh included.

Figure III–100 shows the calculated force-displacement curve and the experimental curve corresponding to a sample tested at 5 mm/min (Figure III–39 previously presented it). Similarly to the 4-point bending test (Figure III–96), there is a mismatch between the curves, which consists of an underestimation of the displacement in the calculated curve. This mismatch is evident in the elastic zone of the curve. The mismatch cause is the setup displacement involved in the experimental curve, which the simulation does not consider. Furthermore, the simulation differs from the experimental observations at the end of the curve since the fracture initiation and propagation are not modelled in the simulation. Anyhow, the curve describes the specimen's behaviour during the test.

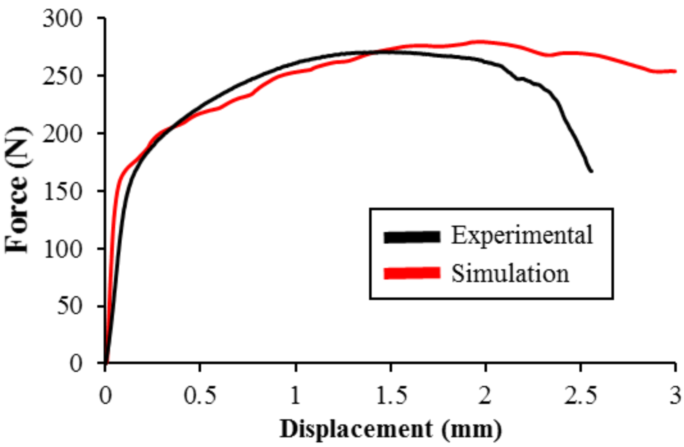

Figure III–100 Force-displacement curves for the experimental and simulated 3-point bending test on a miniaturized specimen.

Considering this and following the same methodology as for the other mechanical test, Figure III–101 shows the main results of the simulations at a point of fracture initiation, corresponding to a displacement of 1.5 mm.

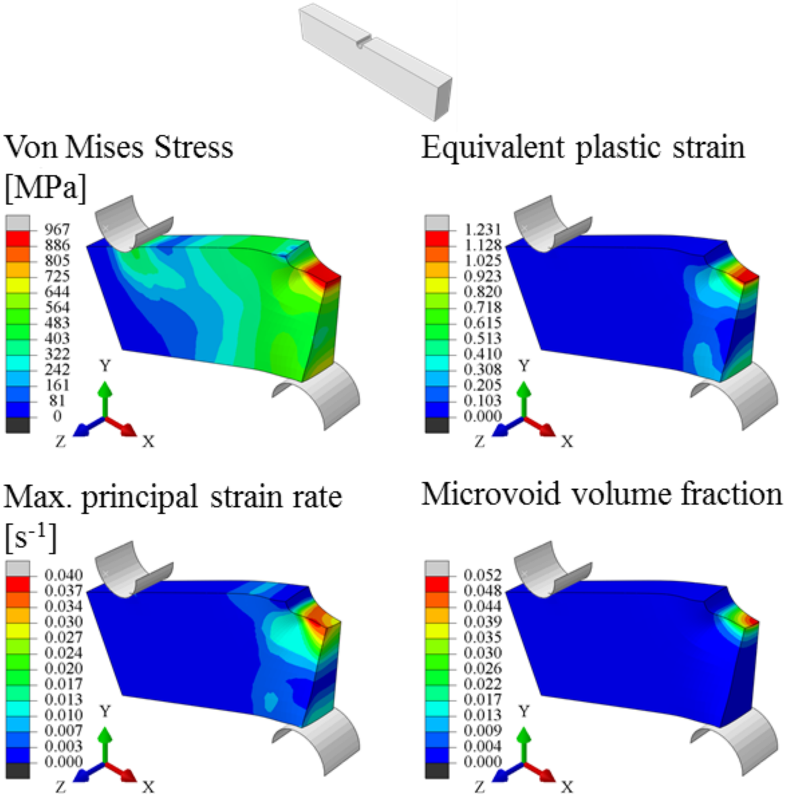

Figure III–101 Magnitude of the von Mises stress, the equivalent plastic strain, the maximum principal strain rate, and the microvoid volume fraction for a miniaturized specimen tested with the 3-point bending test at a displacement of 1.5mm.

The simulation shows that the magnitude of the stress and the plastic strain is considerably higher at the bottom of the notch and that there is a considerably large zone where the stress and the plastic strain are non-null. For instance, almost the totality of the sample is under non-zero stress. Furthermore, the zone of plastic deformation generated by the tensile stress in the bottom of the notch extends to the centre of the sample following an arc and eventually joining the plastic zone generated by the compressive stress in the bottom of the sample.

Moreover, the strain rate values at this test point are in the same order of magnitude as observed in the SPT samples at the fracture point. The microvoid volume fraction values are slightly higher in this simulation, as the sheet used to extract the bending specimens has a higher yielding point than that used for the SPT specimens.

III.12. Discussion and conclusions on the FEM

The results of the FEM of the different mechanical tests agree with the experimental observations. In the case of the SPT modelling, there is a good match between the calculated and the experimental force-displacement curves since the experimental setup displacement was measured and subtracted. The bending test simulations present lower displacement values than the experimental curves since the setup displacement was not subtracted from these last. Nevertheless, the calculated deformation contours match the experimental observations. Although, the FEM differs from the experimental observation after the fracture initiation point since the FEM does not consider any fracture.

Contrasting the results of the FEM of the different SPT specimens, the notched specimens seem to be more suitable for studying the LME of alpha brass by the EGaIn. The notched specimens presented a smaller volume with high-stress values, a consequence of the stress concentration in the notch. The notch also affected the microvoid formation in a smaller area near the crack initiation zone. On the contrary, the standard sample presents high stress and microvoid volume values in a larger sample volume.

In the case of the bending tests, the FEM confirmed the inadequacy of the 4-point bending test on the miniaturized samples used in this work. This inadequacy comes from the low magnitude of plastic deformation in the sample centre at the late stages of the test, despite the notch. Instead, there is high plastic deformation in the volumes near the supports of the sample. Nevertheless, since there is a considerable concentration of plastic deformation in the volume between the supports at the early stages of the test, this test could be suitable for testing materials that do not present high plastic deformation at fracture.

On the other hand, the 3-point bending test is pertinent to the samples used in this work since the plastic deformation concentrates in the notch at all test stages. The test presents a practical limit in the extent of deformation it can apply to the sample. This limit arrives when the sample touches the setup, and the supports cannot continue applying any displacement, which occurs when the sample bends beyond 340°. For instance, this happened experimentally on the bending test of the Cu-15 wt.%Zn alloy at displacement rates of 0.05 mm/min or higher.

A comparison of the FEM of the STP and the 3-point bending test shows that the calculated strain rate varies among the different zones of the samples. All specimens' strain rate values are higher in the zone where the fracture initiates, except for the standard SPT samples. The calculated strain rates at the moment of fracture for a displacement rate of 5 mm/min at the zone of the fracture are around 0.02, 0.1, and 0.05 s^{-1} on the standard, the longitudinally notched, and the laterally notched SPT samples, respectively. While the 3-point bending test at the same conditions presents a strain rate of 0.04 s^{-1}. These values present the same order of magnitude, so their difference cannot account for a considerable effect on the mechanical behaviour of the samples. The strain rate values allow us to compare better the different mechanical tests done at the different displacement rates. Figure 102 summarizes the conditions at which there was LME, which allows better visualization of the tendencies previously discussed in section III.7., i.e. higher LME susceptibility at higher hardness values, higher strain rates, and higher Zn content.

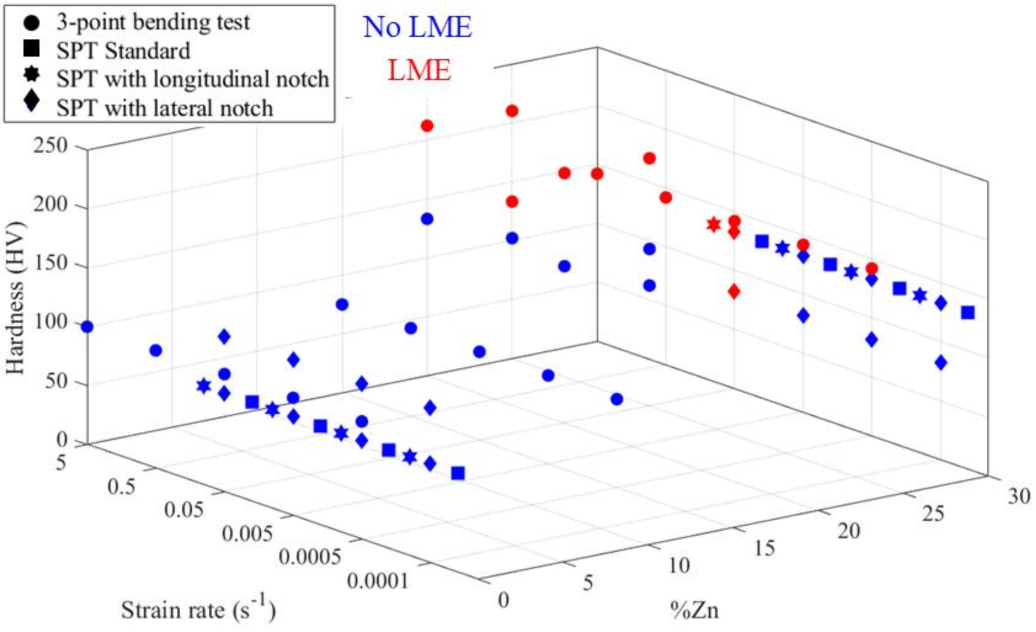

Figure 102 Summary of the conditions at which LME occurred on materials tested by the different SPT and the 3-point bending test in contact with the liquid EGaIn.

Another critical magnitude that can play a role in the fracture of the samples is triaxiality since a high triaxiality value can promote the apparition of a brittle fracture. Figure III–103 shows the calculated triaxiality for each test; for clarity, the colour spectrum is the same for all specimens, and the negative values are excluded (plotted in black).

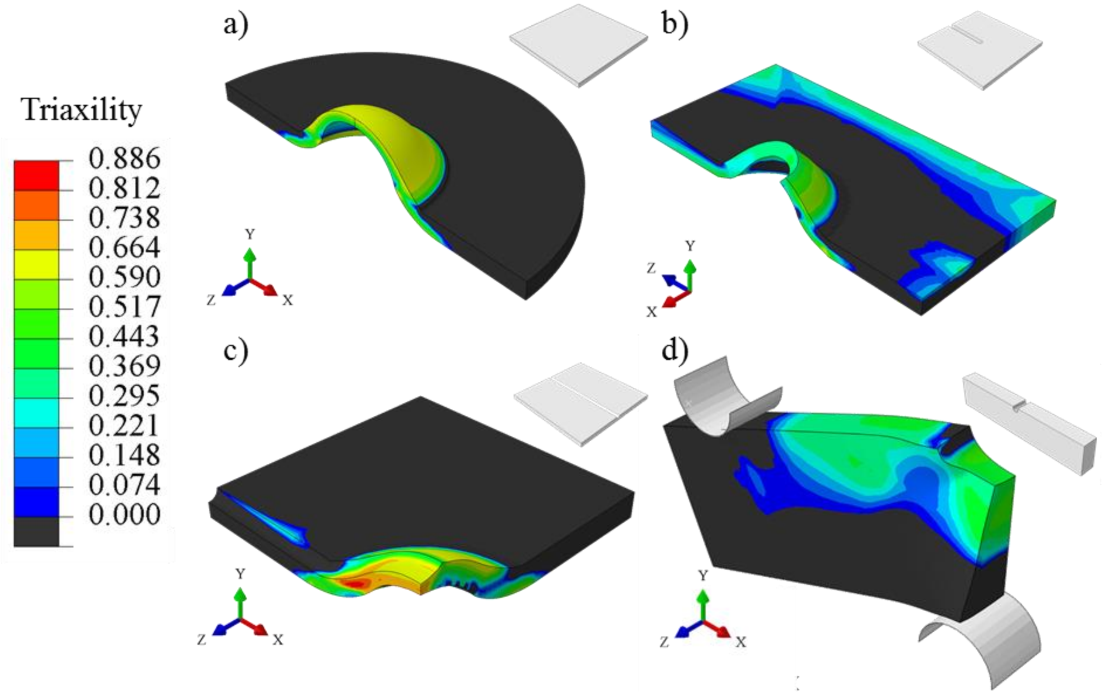

Figure III–103 Triaxiality at the fracture initiation of the a) standard SPT specimen, b) laterally notched SPT specimen, c) longitudinally notched SPT specimen, and d) 3-point bending test specimen.

The values of the triaxiality in the fracture zone are similar between the different samples. Furthermore, there appears to be no relation between the triaxiality values and the apparition of the brittle fractures on the samples tested in contact with the EGaIn. For instance, the standard SPT sample presents higher triaxiality in its surface than the 3-point bending test sample, but this last sample presents LME when the Cu-30%Zn samples break in contact with the EGaIn.

No significant differences exist in the magnitudes of the strain rate, strain, stress, and triaxiality between the notched SPT and the bending tests. However, experimentally, there are some significant differences in their sensitivity to the LME. For instance, while the standard SPT presented LME at any displacement rate, the 3-point bending test shows clear signs of embrittlement. Moreover, the notched SPT samples present a displacement rate dependency of the LME sensitivity, which does not occur in the 3-point bending test samples, despite the similar strain rate magnitude.

The lack of differences in the mechanical states among the specimens indicates that the differences in their sensitivity to LME may come from the differences in the samples' metallurgical states. Both batches used to machine the samples present similar hardness, 133 ± 8 and 142 ± 4 HV for the SPT and bending tests samples, respectively. However, their grain size is 16 ± 2 µm for the SPT specimens and 39 ± 7 for the bending tests samples. These differences in grain size could account for the changes in the LME sensitivity.

On the other hand, the FEM is useful to analyse the fracture initiation and propagation in the case of the 3-point bending tests. For this, Figure III–104a presents the principal stress components for this test. In this representation, the maximum principal stress in the centre of the sample is parallel to the X-axis, and the other two principal stresses have small values. Practically, the stress state corresponds to a state of traction/compression along the central volume of the sample. Furthermore, Figure III–104b presents the field of the maximum principal stress components.

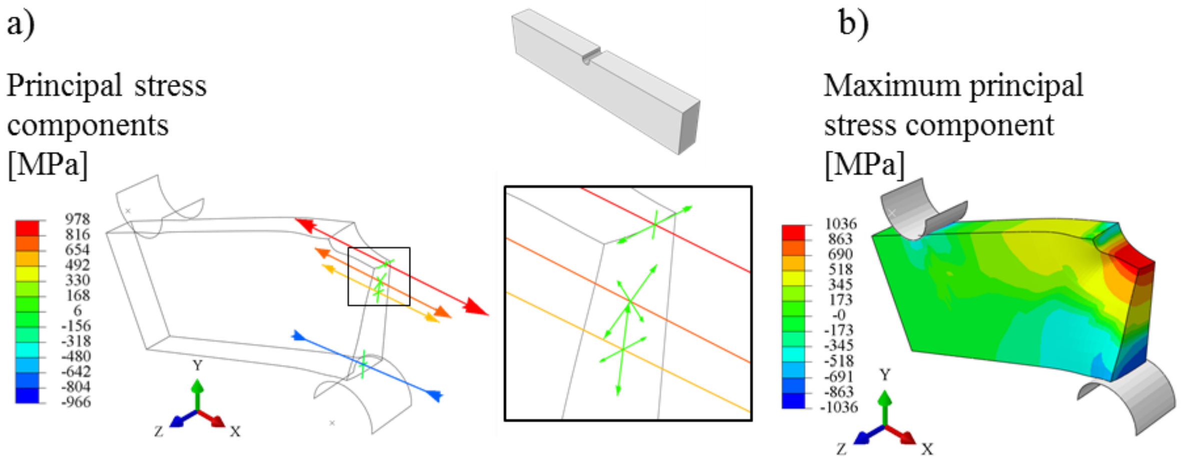

Figure III–104 a) Principal stress components for the central volume of the 3-point bending test sample and b) magnitude of the maximum principal stress component across the sample.

There is a change from a ductile fracture to a brittle fracture on the Cu-30%Zn samples tested in contact with the EGaIn (see Figure III–46 in section III.5.3.). This change could relate to the transition from tension to a compressive state or the microvoid formation. Figure III–104b shows the sample volumes in tension and under compression. For better identification of the transition point, Figure III–105 shows the calculated profiles of these two parameters in a central line of the sample.

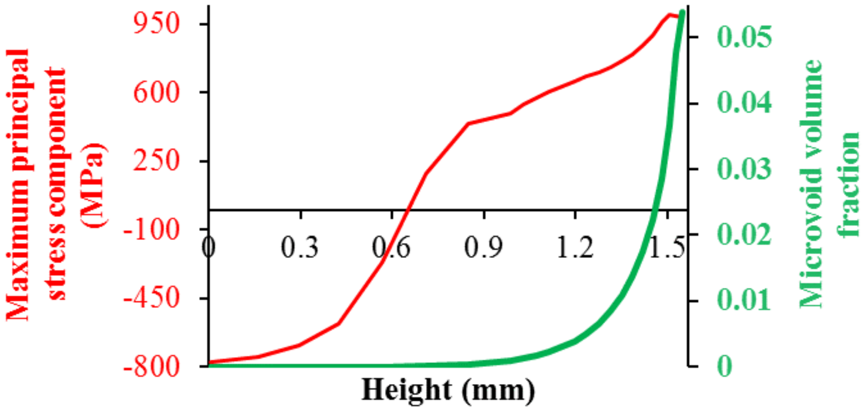

Figure III–105 Values of the maximum principal stress and the microvoid volume fraction along the centre of a 3-point bending test specimen.

The stress profile shows that the transition point from negative to positive stress values is around 0.7 mm, far from where the fracture changes its mode. Else, the transition from a volume in tension to a volume in compression is not the cause of the change in the fracture behaviour. Contrary to the stress profile, the calculated microvoid volume fraction decays rapidly to half its maximum value in the first tenth of a millimetre, which agrees with the size of the ductile fracture.

Moreover, as discussed in section III.7., there should be a ductile fracture for the liquid EGaIn to enter contact with a fresh strained Cu-30%Zn surface. The brittle fracture occurs after considerable damage has already appeared in the sample; when the brittle fracture starts, there are ductility dimples at the beginning of the fracture, and these dimples are present on the fractographies of the Cu-30%Zn samples tested in contact with the EGaIn. Figure III–106b contrasts the calculated microvoid volume fraction with a transversal cut of a brittle fracture (Figure III–106a); the calculated microvoid volume fraction profile matches the experimental observations of the fracture mode transition.

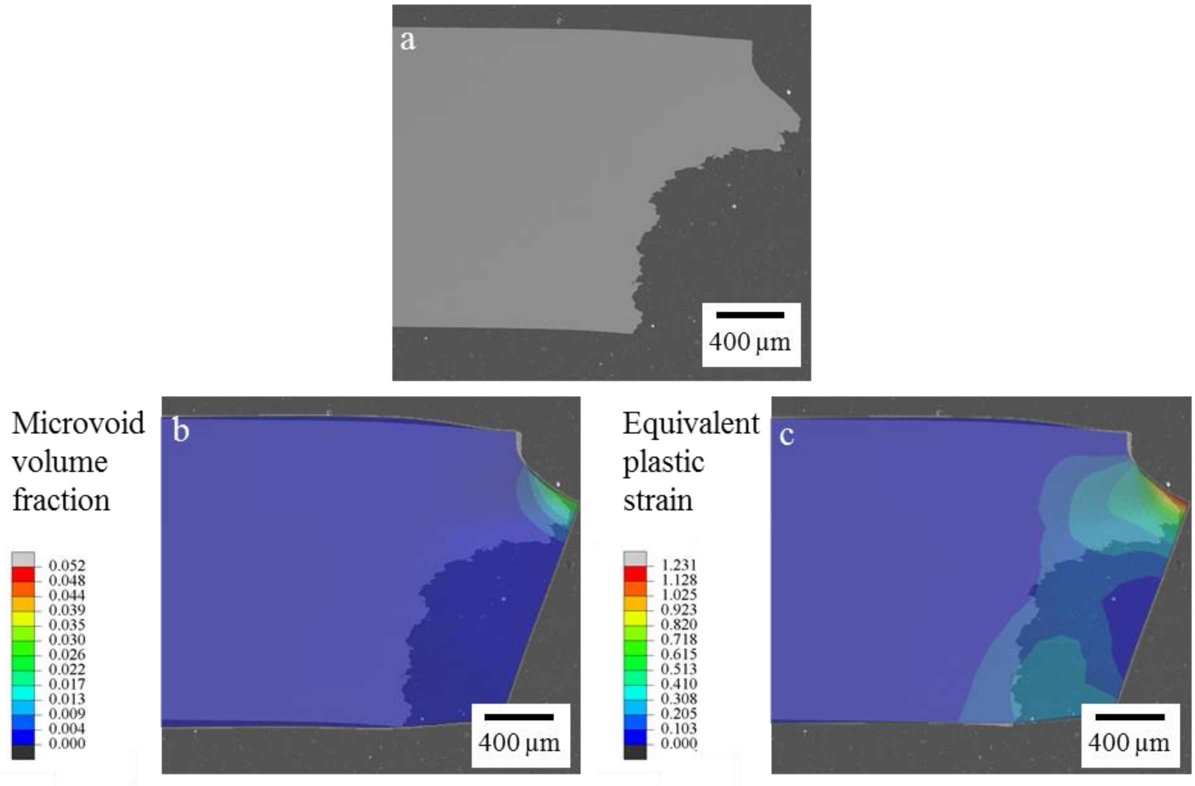

Figure III–106 a) Fracture of a Cu-30%Zn sample tested in contact with the EGaIn, b) the calculated microvoid volume fraction, and c) the calculated equivalent plastic strain.

Also, Figure III–106c compares the calculated plastic strain with the experimental fracture of a Cu-30%Zn sample tested in contact with the EGaIn. The comparison shows that the brittle fracture's propagation matches the zones of higher plastic strain. This association reinforces the idea that once the brittle fracture initiates, the plastic strain of the sample controls its propagation. At the end of the bending tests in contact with the EGaIn, the Cu-30%Zn samples presented a drastic force drop, which indicates no significant resistance of the material during the propagation of the fracture. This little resistance matches the fact that there is already a considerable plastic deformation on the sample, so for the fracture propagation, there is no need for much extra energy from further deformation.

Since the planes of fracture initiation are different for the ductile and the brittle fractures, the stress components associated with their respective loading mode are different. In the case of the ductile fracture, the loading mode corresponds to mode I (opening), which corresponds to the σ_{xx} stress component. On the contrary, the σ_{xx} stress does not contribute to the brittle fracture initiation since the plane of brittle fracture propagation is perpendicular to the x-plane. Depending on the loading mode I, II, or III, the σ_{yy}, σ_{xy}, and σ_{xz} would be their respective stress components. Figure III–107 shows the magnitudes of these stress components in the centre of a 3-point bending test sample. The only stress that has a significant magnitude in the zone where the brittle fracture initiates is the σ_{yy} component, indicating that the brittle fracture's loading mode corresponds to mode I (opening). This loading mode corresponds only to the beginning of the fracture; later, the fracture changes its direction, and the FEM used in this work cannot calculate the stress state at those conditions.

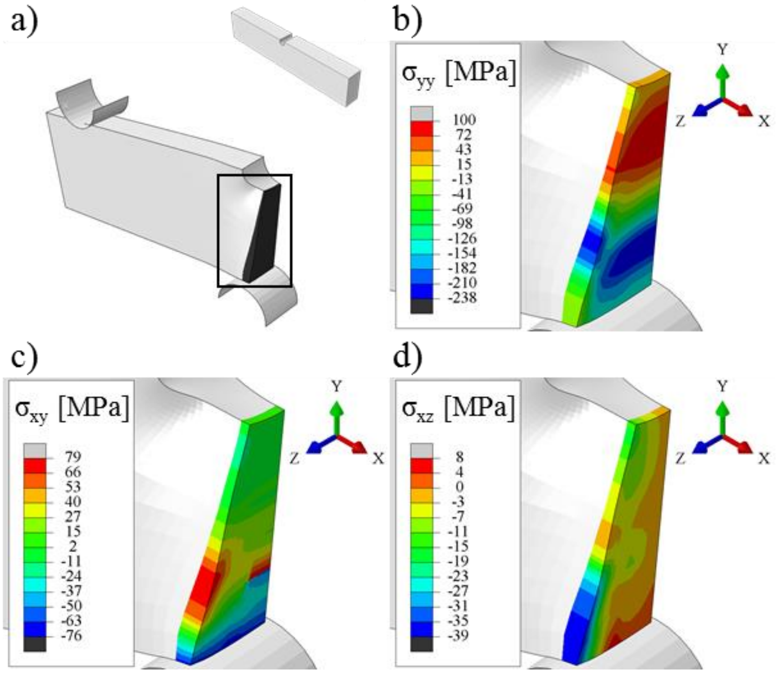

Figure III–107 a) FEM of the 3-point bending test and the corresponding magnitudes of the b) σ_{yy}, c) σ_{xy}, and d) σ_{xz} along the centre of the sample.

Another factor that may influence the plane and direction of the brittle fracture initiation is the deformation of the grains previous to the start of the brittle fracture. Before the brittle fracture occurs, considerable plastic deformation (see Figure I–46) produces the once equiaxed grains to become elongated in the x-axis direction. The brittle fracture presents an intergranular nature and would propagate in the minor tortuous direction, corresponding to the x-axis direction. This explanation is compatible with the previous comparison of plastic deformation with fracture (Figure III–106). Later, the fracture propagates and arrives at zones when the grains are no longer significantly elongated; hence, the fracture can propagate into a different plane.

With the implementation of the FEM, the quantification of the LME is possible by calculating the fracture toughness. The following chapter address this calculation.

III.13. References

[1] M. Bruchhausen *et al.*, “European standard on small punch testing of metallic materials,”

Ubiquity Proc., vol. 1, no. S1, p. 11, Sep. 2018.

[2] S. Arunkumar, “Overview of Small Punch Test,” *Met. Mater. Int.*, vol. 26, no. 6, pp. 719–738, 2020.

[3] M. Abendroth and S. Soltysiak, “Assessment of Material Properties by Means of the Small Punch Test,” *Recent Trends Fract. Damage Mech.*, pp. 127–157, 2016.

[4] S.-H. Chi, J.-H. Hong, and I.-S. Kim, “Evaluation of irradiation effects of 16 MeV proton-irradiated 12Cr-1MoV steel by small punch(SP) tests,” *Scr. Metall. Mater.*, vol. 30, no. 12, pp. 1521–1525, Jun. 1994.

[5] S. Haroush, D. Moreno, I. Silverman, A. Turgeman, R. Shneck, and Y. Gelbstein, “The mechanical behavior of HAVAR foils using the small punch technique,” *Materials (Basel).*, vol. 10, no. 5, 2017.

[6] D. Moreno, S. Haroush, A. Turgeman, and I. Silverman, “Small punch technique used to evaluate the radiation damage in SS316L thin foils due to proton bombardment,” *Ubiquity Proc.*, vol. 1, no. S1, p. 36, 2018.

[7] T. Auger, I. Serre, G. Lorang, Z. Hamouche, D. Gorse, and J.-B. Vogt, “Role of oxidation on LME of T91 steel studied by small punch test,” *J. Nucl. Mater.*, vol. 376, no. 3, pp. 336–340, Jun. 2008.

[8] O. Hamdane, I. Proriol Serre, J. B. Vogt, and N. Nuns, “ToF-SIMS analyses of brittle crack initiation of T91 steel by liquid sodium,” *Mater. Chem. Phys.*, vol. 145, no. 1–2, pp. 243–249, 2014.

[9] I. Serre and J. B. Vogt, “Heat treatment effect of T91 martensitic steel on liquid metal embrittlement,” *J. Nucl. Mater.*, vol. 376, no. 3, pp. 330–335, 2008.

[10] C. Ye, J.-B. Vogt, and I. Proriol Serre, “Liquid metal embrittlement of the T91 steel in lead bismuth eutectic: The role of loading rate and of the oxygen content in the liquid metal,” *Mater. Sci. Eng. A*, vol. 608, pp. 242–248, Jul. 2014.

[11] I. Serre and J. B. Vogt, “Liquid metal embrittlement of T91 martensitic steel evidenced by small punch test,” *Nucl. Eng. Des.*, vol. 237, no. 7, pp. 677–685, 2007.

[12] I. Proriol Serre, I. Diop, N. David, M. Vilasi, and J. B. Vogt, “Mechanical behavior of coated T91 steel in contact with lead-bismuth liquid alloy at 300°C,” *Surf. Coatings*

Technol., vol. 205, no. 19, pp. 4521–4527, 2011.

[13] P. Patel and B. K. Patel, “The Small Punch Test a Viable Alternate for In-service Components Preserved Strength Estimation,” *J. Inst. Eng. Ser. C*, vol. 103, no. 1, pp. 121–133, 2022.

[14] W. Wang, T. Xu, J. Zhong, K. Guan, Y. Shang, and X. Zhang, “Specimen size effect on evaluation of strength properties of 3Cr1MoV and Incoloy 800H using small punch test,” *Mater. Sci. Eng. A*, vol. 832, p. 142400, 2022.

[15] Z. Cheng *et al.*, “Comparative Study between Small Punch Tests and Finite Element Analysis of Miniature Steel Specimens,” *J. Mater. Eng. Perform.*, vol. 30, no. 12, pp. 9094–9107, 2021.

[16] J. Zhong *et al.*, “Use of database and small punch test to estimate true stress-plastic strain curve of steels,” *Int. J. Press. Vessel. Pip.*, vol. 191, p. 104370, 2021.

[17] J. Peng, V. D. Vijayanand, D. Knowles, C. Truman, and M. Mostafavi, “The sensitivity ranking of ductile material mechanical properties, geometrical factors, friction coefficients and damage parameters for small punch test,” *Int. J. Press. Vessel. Pip.*, vol. 193, p. 104468, 2021.

[18] I. Peñuelas, I. I. Cuesta, C. Betegón, C. Rodriguez, and F. J. Belzunce, “Inverse determination of the elastoplastic and damage parameters on small punch tests,” *Fatigue Fract. Eng. Mater. Struct.*, vol. 32, no. 11, pp. 872–885, Nov. 2009.

[19] E. Martínez-Pañeda, I. I. Cuesta, I. Peñuelas, A. Díaz, and J. M. Alegre, “Damage modeling in Small Punch Test specimens,” *Theor. Appl. Fract. Mech.*, vol. 86, pp. 51–60, Dec. 2016.

[20] V. D. Vijayanand *et al.*, “A novel methodology for estimating tensile properties in a small punch test employing in-situ DIC based deflection mapping,” *J. Nucl. Mater.*, vol. 538, p. 152260, 2020.

[21] K. Li, J. Peng, and C. Zhou, “Construction of whole stress-strain curve by small punch test and inverse finite element,” *Results Phys.*, vol. 11, pp. 440–448, 2018.

[22] Y. Li, K. Matocha, R. Hurst, P. Čižek, K. Turba, and P. Stevens, “Experimental verification to determine fracture toughness from the small punch test using ‘Local approach,’” *Theor. Appl. Fract. Mech.*, vol. 102, pp. 16–29, 2019.

[23] J. C. Chica, P. M. Bravo Díez, and M. Preciado Calzada, "Improved correlation for elastic modulus prediction of metallic materials in the Small Punch Test," *Int. J. Mech. Sci.*, vol. 134, no. 1, pp. 112–122, Dec. 2017.

[24] E. Priel, B. Mittelman, S. Haroush, A. Turgeman, R. Shneck, and Y. Gelbstein, "Estimation of yield and ultimate stress using the small punch test method applied to non-standard specimens: A computational study validated by experiments," *Int. J. Mech. Sci.*, vol. 135, pp. 484–498, 2018.

[25] T. E. García, C. Rodríguez, F. J. Belzunce, and C. Suárez, "Estimation of the mechanical properties of metallic materials by means of the small punch test," *J. Alloys Compd.*, vol. 582, pp. 708–717, Jan. 2014.

[26] F. Lacalle, R., García, J., Álvarez, J. A., & Gutiérrez-Solana, "Obtención mediante el ensayo small punch de las propiedades de tracción de materiales metálicos," *An. Mecánica la Fract.*, vol. 2, no. 26, pp. 501–506, 2009.

[27] J. Autillo, M. A. Contreras, C. Betegón, C. Rodríguez, and F. J. Belzunce, "Utilización del Ensayo Miniatura de Punzonamiento (Small Punch test) en la Caracterización Mecánica de Aceros," *An. la mecánica la Fract.*, vol. 1, pp. 77–83, 2006.

[28] X. Mao and H. Takahashi, "Development of a further-miniaturized specimen of 3 mm diameter for tem disk (ø 3 mm) small punch tests," *J. Nucl. Mater.*, vol. 150, no. 1, pp. 42–52, Sep. 1987.

[29] S. R. Ghodke, B. K. Dutta, and P. V. Durgaprasad, "Analytical development and experimental verification of empirical correlations to determine mechanical properties of copper alloys using small punch test data," *Fusion Eng. Des.*, vol. 159, p. 111786, Oct. 2020.

[30] M. F. Moreno, "Effects of thickness specimen on the evaluation of relationship between tensile properties and small punch testing parameters in metallic materials," *Mater. Des.*, vol. 157, pp. 512–522, 2018.

[31] S. Haroush *et al.*, "Evaluation of the mechanical properties of SS-316L thin foils by small punch testing and finite element analysis," *Mater. Des.*, vol. 83, pp. 75–84, 2015.

[32] J. Calaf-Chica, P. M. Bravo Díez, M. Preciado Calzada, and M. J. Garcia-Tarrago, "Optimization of the t/10 offset correlation method to obtain the yield strength with the

Small Punch Test," *J. Nucl. Mater.*, vol. 534, pp. 1–9, 2020.

[33] M. Madia, S. Foletti, G. Torsello, and A. Cammi, "On the applicability of the small punch test to the characterization of the 1CrMoV aged steel: Mechanical testing and numerical analysis," *Eng. Fail. Anal.*, vol. 34, pp. 189–203, 2013.

[34] T. D. Shikalgar, B. K. Dutta, and J. Chattopadhyay, "Determination of J-initiation toughness using pre-cracked small punch test specimens," *Procedia Struct. Integr.*, vol. 14, pp. 529–536, 2019.

[35] T. E. García, C. Rodríguez, F. J. Belzunce, and I. I. Cuesta, "Development of a new methodology for estimating the CTOD of structural steels using the small punch test," *Eng. Fail. Anal.*, vol. 50, pp. 88–99, Apr. 2015.

[36] J. M. Alegre, R. Lacalle, I. I. Cuesta, and J. A. Álvarez, "Different methodologies to obtain the fracture properties of metallic materials using pre-notched small punch test specimens," *Theor. Appl. Fract. Mech.*, vol. 86, pp. 11–18, Dec. 2016.

[37] E. Martínez-Pañeda, T. E. García, and C. Rodríguez, "Fracture toughness characterization through notched small punch test specimens," *Mater. Sci. Eng. A*, vol. 657, pp. 422–430, Mar. 2016.

[38] J.-B. Ju, J. Jang, and D. Kwon, "Evaluation of fracture toughness by small-punch testing techniques using sharp notched specimens," *Int. J. Press. Vessel. Pip.*, vol. 80, no. 4, pp. 221–228, Apr. 2003.

[39] R. Lacalle, J. A. Álvarez, and F. Gutiérrez-Solana, "Use of Small Punch Notched Specimens in the Determination of Fracture Toughness," in *Volume 6: Materials and Fabrication, Parts A and B*, 2008, pp. 1363–1369.

[40] K. Turba, B. Gülçimen, Y. Z. Li, D. Blagoeva, P. Hähner, and R. C. Hurst, "Introduction of a new notched specimen geometry to determine fracture properties by small punch testing," *Eng. Fract. Mech.*, vol. 78, no. 16, pp. 2826–2833, Nov. 2011.

[41] I. I. Cuesta and J. M. Alegre, "Determination of the fracture toughness by applying a structural integrity approach to pre-cracked Small Punch Test specimens," *Eng. Fract. Mech.*, vol. 78, no. 2, pp. 289–300, Jan. 2011.

[42] P. J. L. Fernandes and D. R. H. Jones, "The effects of microstructure on crack initiation in liquid-metal environments," *Eng. Fail. Anal.*, vol. 4, no. 3, pp. 195–204, 1997.

[43] A. Legris, G. Nicaise, J.-B. Vogt, J. Foct, D. Gorse, and D. Vançon, “Embrittlement of a martensitic steel by liquid lead,” *Scr. Mater.*, vol. 43, no. 11, pp. 997–1001, Nov. 2000.

[44] A. Hojná, F. Di Gabriele, J. Klecka, and J. Burda, “Behaviour of the steel T91 under uniaxial and multiaxial slow loading in contact with liquid lead,” *J. Nucl. Mater.*, vol. 466, pp. 292–301, 2015.

[45] J. E. Norkett, M. D. Dickey, and V. M. Miller, “A Review of Liquid Metal Embrittlement: Cracking Open the Disparate Mechanisms,” *Metall. Mater. Trans. A*, vol. 52, no. 6, pp. 2158–2172, Jun. 2021.

[46] O. Hamdane, J. Bouquerel, I. Proriol-Serre, and J.-B. Vogt, “Effect of heat treatment on liquid sodium embrittlement of T91 martensitic steel,” *J. Mater. Process. Technol.*, vol. 211, no. 12, pp. 2085–2090, Dec. 2011.

[47] J. Siegl, P. Haušild, A. Janča, and R. Kopřiva, “Fractographic Aspects of Small Punch Test Results,” *Procedia Mater. Sci.*, vol. 3, pp. 912–917, 2014.

[48] J. Van den Bosch and A. Almazouzi, “Compatibility of martensitic/austenitic steel welds with liquid lead bismuth eutectic environment,” *J. Nucl. Mater.*, vol. 385, no. 3, pp. 504–509, Apr. 2009.

[49] B. Long, Z. Tong, F. Gröschel, and Y. Dai, “Liquid Pb–Bi embrittlement effects on the T91 steel after different heat treatments,” *J. Nucl. Mater.*, vol. 377, no. 1, pp. 219–224, Jun. 2008.

[50] Y. Dai *et al.*, “Assessment of the lifetime of the beam window of MEGAPIE target liquid metal container,” *J. Nucl. Mater.*, vol. 356, no. 1–3, pp. 308–320, Sep. 2006.

[51] O. Hamdane, “Étude des mécanismes de plasticité et d’endommagement de l’acier martensitique T91 en présence de sodium liquide,” Université de science et technologies de Lille 1, 2012.

[52] R. D. Bert Verlinden, Julian Driver, Indradev Samajdar, *Thermo-Mechanical Processing of Metallic Materials*, 1st ed. Elsevier Ltd, 2007.

[53] Y. H. Zhao, X. Z. Liao, Y. T. Zhu, Z. Horita, and T. G. Langdon, “Influence of stacking fault energy on nanostructure formation under high pressure torsion,” *Mater. Sci. Eng. A*, vol. 410–411, pp. 188–193, 2005.

[54] E. El-Danaf, S. R. Kalidindi, and R. D. Doherty, "Influence of grain size and stacking-fault energy on deformation twinning in fcc metals," *Metall. Mater. Trans. A Phys. Metall. Mater. Sci.*, vol. 30, no. 5, pp. 1223–1233, 1999.

[55] A. L. Gurson, "Continuum Theory of Ductile Rupture by Void Nucleation and Growth: Part I—Yield Criteria and Flow Rules for Porous Ductile Media," *J. Eng. Mater. Technol.*, vol. 99, no. 1, pp. 2–15, Jan. 1977.

[56] V. Tvergaard and A. Needleman, "Analysis of the cup-cone fracture in a round tensile bar," *Acta Metall.*, vol. 32, no. 1, pp. 157–169, Jan. 1984.

[57] A. Needleman and V. Tvergaard, "An analysis of ductile rupture in notched bars," *J. Mech. Phys. Solids*, vol. 32, no. 6, pp. 461–490, 1984.

[58] D. S. SIMULIA, "23.2.9 Porous Metal Plasticity," in *ABAQUS 6.13 User's manual*, 2013.

[59] B. K. Dutta, S. Guin, M. K. Sahu, and M. K. Samal, "A phenomenological form of the q2 parameter in the Gurson model," *Int. J. Press. Vessel. Pip.*, vol. 85, no. 4, pp. 199–210, Apr. 2008.

IV. Measurement of the fracture toughness of Cu-30%Zn brass in contact with the liquid EGaIn

For the study of the liquid metal embrittlement (LME) phenomenon, its impact on the mechanical properties of the solid metal should be quantified with a pertinent parameter. Since the main effect of the LME on a solid metal is the reduction of its energy to fracture and the change of its fracture mode, fracture toughness appears to be the most suitable parameter to quantify this phenomenon. This parameter allows defining the conditions of propagation of a brittle crack by taking into account the stresses applied locally

This chapter presents the fracture toughness measurement of the Cu-30 wt.%Zn brass in contact with the eutectic Ga-In (EGaIn), considering the intermetallic formation. First, section IV.1. presents the fracture toughness measurement from a macroscopic approach using some of the results obtained in section III.4. Section IV.2. presents a short review of the fracture toughness measurement using micromechanical tests. Sections IV.3. and IV.4. present the results and calculation of the fracture toughness measurements using micro-bending tests.

IV.1. Macroscopic approach for the fracture toughness calculation of Cu-30%Zn brass in contact with the liquid EGaIn

The results presented in Chapter III showed that the 3-point bending test is suitable for studying the sensitivity to liquid metal embrittlement (LME) of the Cu-30 wt.%Zn alloy in contact with the eutectic Ga-In (EGaIn). This test allowed the observation of the change of the fracture mode whenever the Cu-Zn alloys were in contact with the EGaIn under the appropriate conditions.

The common use of the 3-point bending test is the calculation of materials' fracture toughness. This measurement can be done by using an analytical formula derived using linear elastic fracture mechanics, here presented in Eq. (22) and Eq. (23) [1].

$$K_Q = \frac{S\,F}{B\,w^{\frac{3}{2}}}\,g_1\left(\frac{a}{w}\right) \tag{22}$$

$$g_1\left(\frac{a}{w}\right) = \frac{3\left(\frac{a}{w}\right)^{0.5}\left[1.99 - \frac{a}{w}\left(1 - \frac{a}{w}\right)\left(2.15 - 3.93\frac{a}{w} + 2.7\frac{a^2}{w^2}\right)\right]}{2\left(1 + 2\frac{a}{w}\right)\left(1 - \frac{a}{w}\right)^{1.5}} \tag{23}$$

where a is the length of the notch, F is the force, S is the distance between the supports, w is the height of the sample, and B is the thickness of the sample.

Using the value of the force at failure in Eq. (22) and Eq. (23), the resistance of a material to crack extension can be calculated. Moreover, if the sample is under plane strain conditions, this value corresponds to $K_{IC,}$ considered a size-independent material parameter.

With Eq. (24), the minimum thickness of a 3-point bending test sample can be calculated using the plane strain fracture toughness of the material and its yield strength.

$$B_{min} = 2.5\left(\frac{K_{Ic}}{\sigma_Y}\right)^2 \tag{24}$$

where B_{min} is the minimum thickness value for a 3-point bending test sample to present plane strain conditions, and σ_Y is the yield strength of the material.

The correspondent fracture toughness can be calculated using the results from the bending tests of the Cu-30%Zn alloy when tested in air and in contact with the EGaIn. For this calculation, the maximum force values at each displacement rate tested are used, and the values of the dimensions of the samples correspond to a= 0.3 mm, L=8 mm, w=10 mm, and B=1 mm. Table IV–1 presents the results for the different testing conditions. The table also includes the minimum thickness value for the plane strain, calculated using Eq. (3) with the corresponding K_Q value and the yield strength of the material previously determined with a tensile test in section III.9., which is 324 MPa.

Table IV–1 Values of K_Q of Cu-30%Zn tested at different conditions and their corresponding minimum thickness value for plane strain conditions.

Displacement rate	**Environment**	**K_Q**	**B_{min}**
(mm)		**(MPa $m^{1/2}$)**	**(mm)**
5	Air	25.35 ± 0.79	15.32 ± 0.94
	EGaIn	24.91 ± 0.71	14.79 ± 0.84
0.5	Air	25.10 ± 0.20	15.00 ± 0.24
	EGaIn	24.69 ± 0.85	14.54 ± 1.01
0.05	Air	25.18 ± 0.46	15.10 ± 0.55
	EGaIn	24.64 ± 0.63	14.46 ± 0.74
0.005	Air	25.62 ± 0.74	15.64 ± 0.90
	EGaIn	24.39 ± 1.16	14.19 ± 1.35
0.0005	Air	23.51	13.16
	EGaIn	21.75 ± 1.84	11.32 ± 1.9

The fracture toughness values do not present considerable variations; they all fall between 19.83 and 26.14 MPa $m^{1/2}$ regardless of the displacement rate used and if the material was tested in air or in contact with the liquid EGaIn. Moreover, the minimum thickness for the plane strain condition is more than ten times higher than the actual thickness of the samples, so the fracture toughness calculated by this method does not correspond to the plane strain fracture toughness K_{IC}; hence this value is size-dependent.

Another method that can be used for the fracture toughness measurement is the calculation of the J-Integral [1], which is derived from elasto-plastic fracture mechanics and is defined in Eq. (25):

$$J = \int_{\Gamma} (w \, dy - T_i \frac{\partial u_i}{\partial x} ds) \tag{25}$$

where Γ is an arbitrary path around the crack, w is the density of strain energy, T_i are the traction components, u_i are the displacement components, and ds is the incremental length along Γ.

Using the value of the J-Integral, the value of the fracture toughness can be then approximated using Eq. (26)

$$K = \sqrt{E^* J} \tag{26}$$

where E^* equates to the Young Modulus (E) in the case of plane stress, and in the case of plane strain, E^* is defined by Eq. (27).

$$E^* = \frac{E}{1 - v^2} \tag{27}$$

where v is the Poisson's ratio.

The J-integral calculation is implemented in the ABAQUS software, so the finite element modelling (FEM) presented in section III.11. allows calculating the J-integral at the point of the 3-point bending test when the material fractures. The J-integral was calculated on 30 different contours around the notch on 11 different zones along the thickness of the samples. Figure IV–1 shows the 17th contour and the 11 zones across the thickness.

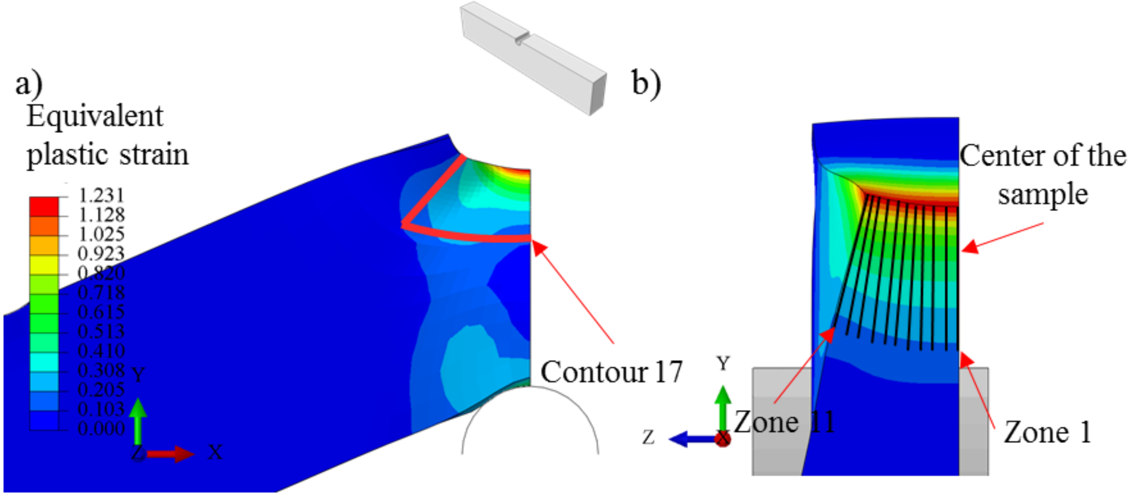

Figure IV–1 Contours used for the calculation of the J-integral.

A displacement of 1.5 mm was chosen for the calculation of the J-integral. Figure IV–2a shows the calculated values for each contour; the red point corresponds to the average of all zones in one contour, and the error bars correspond to their standard deviation. The values deviation is related to the deformation in the Z-direction that is considerably higher in the zones near the sample's surface. Moreover, the J-integral values vary significantly among the first contours, then the value of the J-integral is relatively constant from the 10th to 17th contour, and then the value varies significantly on the further contours. The plastic deformation in the zones near the notch and the opposite zone causes these variations. Moreover, Figure IV–2b presents the evolution of the J-integral during the test in the 13th contour along the most central zone of the sample; the red lines indicate the J-integral value at the fracture point.

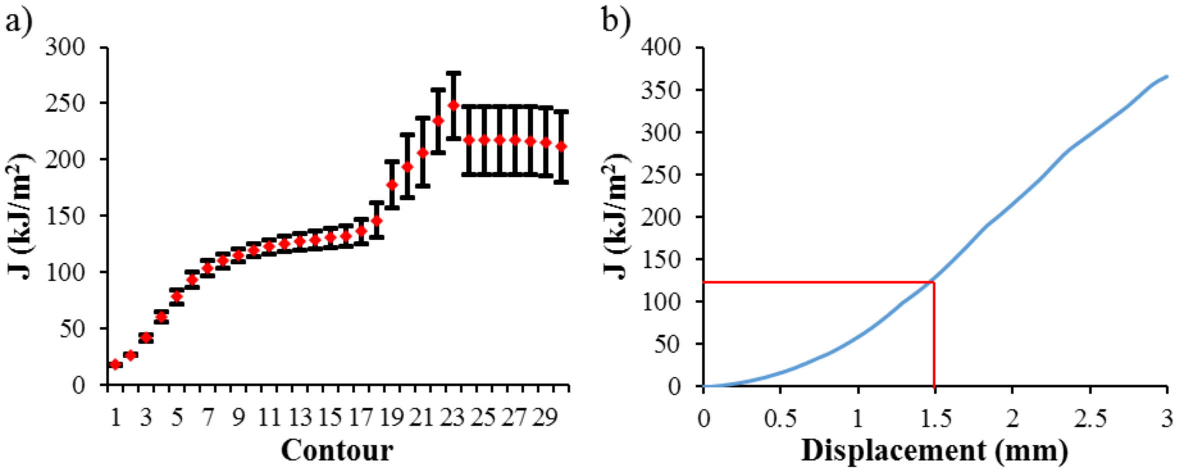

Figure IV–2 a) Values of the J-integral along the different contours at a displacement of 1.5 mm, and b) evolution of the J-integral value in the 13th contour.

The average of the values of the J-integral from contour 10 to 17 is 127.90 ± 9.28 kJ/m^2. With this value, Young's modulus (99,7 GPa) and Poisson's ratio (0.33), a stress intensity factor (K_I) value of 118.87 ± 4.02 MPa·m$^{1/2}$ was obtained with Eq. (26). For comparison, to the knowledge of the author, the only K_{IC} value available in the literature for a Cu-30%Zn alloy is 76 MPa·m$^{1/2}$ [2]. The reported value is in the same order of magnitude as the value obtained in this work. Moreover, there is no information on the sample's metallurgical state nor the testing conditions that allow us to correctly compare it with our material.

Since linear elastic fracture mechanics are not used here to measure the fracture toughness, Eq. (24) does not need to be satisfied. However, there is another criterion that must be satisfied when using elasto-plastic fracture mechanics [3], and is defined in Eq. (28):

$$\left\{ \begin{matrix} B \\ W-a \end{matrix} \right\} > 10\frac{J}{\sigma_y} \tag{28}$$

According to this formula, the value of J = 127.90 kJ/m^2 would correspond to a minimum sample thickness of 3.82 mm, which is higher than the actual dimension of the sample. Therefore, the value obtained by this method cannot be used to calculate K_{IC}.

As discussed in the previous chapter, the mechanical conditions at fracture of the Cu-30%Zn are the same when tested in air and in contact with the EGaIn. We proposed that the $CuGa_2$ intermetallic layer causes this effect by impeding the contact between the liquid EGaIn and the Cu-30%Zn alloy. The K_Q values are practically the same for the testes performed in air and those performed in contact with the EGaIn, which supports the proposed intermetallic effect. Since the fracture initiates under the same mechanical conditions, the fracture toughness calculated here corresponds to the Cu-30%Zn without embrittlement. Moreover, even if the FEM incorporates the ductile crack propagation in its formulation to obtain the mechanical conditions when the brittle crack initiates, the calculated fracture toughness of this crack would be overestimated since the value of the stress components would be greater than the minimum values of brittle crack initiation. A different mechanical test must be designed to correctly calculate the fracture toughness linked with the LME of Cu-30%Zn by EGaIn.

In this work, a micrometric test was specially designed to find the fracture toughness of Cu-30%Zn in contact with the EGaIn by avoiding intermetallic formation before the crack initiation. For the design of this test, literature on the measurement of fracture toughness using micromechanical tests was assessed.

IV.2. Literature on the use of micromechanical tests to obtain the fracture toughness

In recent years, there have been several studies on the use of micromechanical tests to measure fracture toughness. In particular, an article by Jaya et al. raised the question: "Can microscale fracture tests provide reliable fracture toughness values?" [4]. They tried to answer by comparing four different geometries to test the fracture toughness of Si (100). Figure IV–3 presents these tests and the corresponding K_{IC} value.

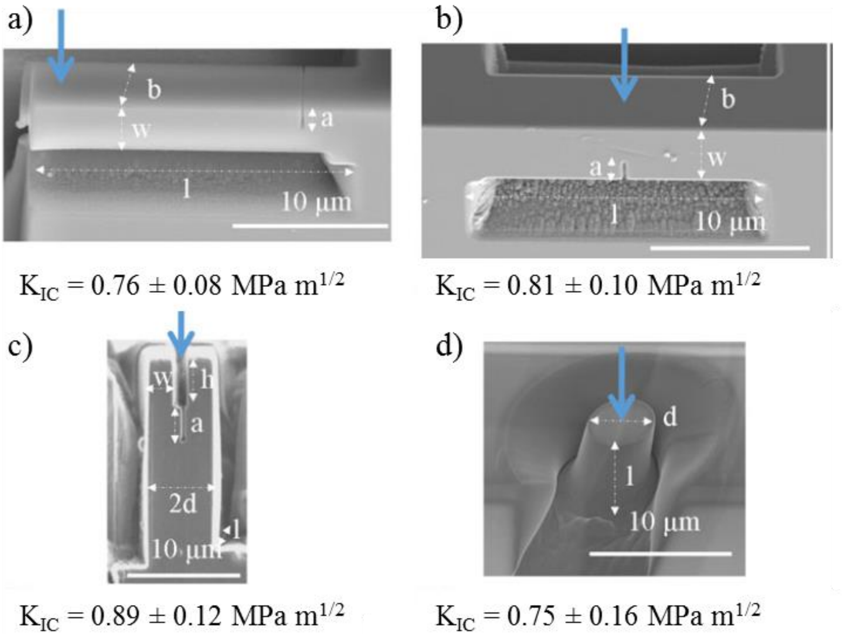

$K_{IC} = 0.76 \pm 0.08$ MPa $m^{1/2}$

$K_{IC} = 0.81 \pm 0.10$ MPa $m^{1/2}$

$K_{IC} = 0.89 \pm 0.12$ MPa $m^{1/2}$

$K_{IC} = 0.75 \pm 0.16$ MPa $m^{1/2}$

Figure IV–3 Four different geometries selected for fracture toughness testing at the small scale: (a) single cantilever bending, (b) clamped beam bending, (c) double cantilever bending, and (d) pillar splitting. All samples were machined and notched using the focus ion beam on a straight edge of Si (100) [4].

Jaya et al. found a good agreement between the values obtained with these micromechanical tests and those reported in the literature (0.7-1.3 MPa $m^{1/2}$). They calculated the fracture toughness using analytical formulas, except for the clamped beam bending, for which they used an extended FEM because there is no analytical formula for this geometry. It must be noted that Si is a low fracture toughness material with a yield stress of 500 MPa, which means that according to Eq. (24), this material is under plane strain conditions even with microscopic dimensions. With less brittle systems, the necessary dimensions to avoid plasticity would be higher [4].

Jaya et al. compared the four geometries used in their study and proposed general guidelines for choosing the suitable test; Figure IV–4 presents these guidelines. From these guidelines, to measure the fracture toughness of Cu-30 wt.%Zn in contact with liquid EGaIn, the most suitable tests are the single cantilever bending and the clamped beam bending. The double cantilever bending test is restricted to brittle systems and presents a low success rate, while the pillar splitting is unsuitable for studying interfaces [4].

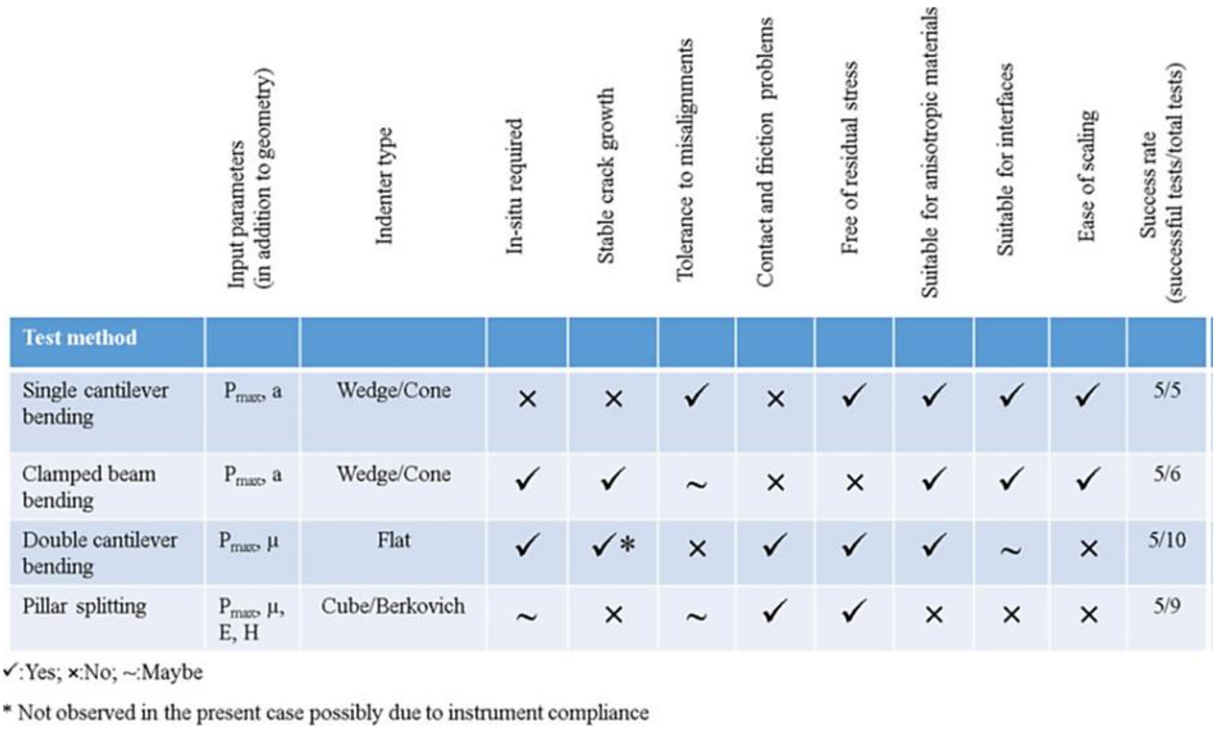

Test method	Input parameters (in addition to geometry)	Indenter type	In-situ required	Stable crack growth	Tolerance to misalignments	Contact and friction problems	Free of residual stress	Suitable for anisotropic materials	Suitable for interfaces	Ease of scaling	Success rate (successful tests/total tests)
Single cantilever bending	P_{max}, a	Wedge/Cone	×	×	✓	×	✓	✓	✓	✓	5/5
Clamped beam bending	P_{max}, a	Wedge/Cone	✓	✓	~	×	×	✓	✓	✓	5/6
Double cantilever bending	P_{max}, μ	Flat	✓	✓*	×	✓	✓	✓	~	×	5/10
Pillar splitting	P_{max}, μ, E, H	Cube/Berkovich	~	×	~	✓	✓	×	×	×	5/9

✓:Yes; ×:No; ~:Maybe

* Not observed in the present case possibly due to instrument compliance

Figure IV–4 General guidelines for choosing a fracture toughness test geometry at the micrometre scale [4].

On the other hand, Saxena et al. presented a workflow with recommendations for calculating fracture toughness at a micrometric scale [5]. From these recommendations, we highlight the choice of the sample size to complain with Eq. (24) to apply linear elastic fracture mechanics or in its defect to Eq. (28) to apply elasto-plastic fracture mechanics. In addition, to avoid the overestimation of the fracture toughness of materials using elasto-plastic fracture mechanics, Saxena et al. recommend the use of notches through all the thickness of the sample, instead of bridge notches, which are partial notches that are fabricated only in a central volume of the sample. They also suggest using cantilevers five times longer than their width and height to avoid the influence of shear stress.

Another available method for the measurement of the fracture toughness at the micrometric scale is the micro-tensile tests on notched specimens. For instance, Arnaud et al. studied thin nitride compound layers using this method to extract their elastic modulus, Poisson's ratio and fracture toughness simultaneously [6]. For the fracture toughness calculation, they used a FEM instead of the analytical formulation to account for the effect of the notch radius and the roughness in calculating the fracture toughness.

When using micrometric mechanical tests, some size effects can modify the material's behaviour. Motz et al. studied some of these effects on the mechanical properties of Cu by performing single cantilever tests with variable dimensions [7]. They reported an increase in the yielding point from 250 to 1000 MPa when they reduced the sample's thickness from 7.5 to 1 µm. For reference, the bulk yielding point of their material is 227 MPa. They explained the size effect with two phenomena: the limitation of available dislocation sources and the dislocation pile-up at the centre of the beam.

Another work that observes similar size effects is that of Fleck et al. [8], in which they reported that under a torsional test, a Cu wire with a 170 µm diameter has less resistance than a Cu wire with a diameter of 12 µm. However, they did not find significant differences when testing both wires with a tensile test.

Similarly, Weiss et al. performed tensile tests on Cu foils with thicknesses from 50 to 250 µm and on Cu wires with diameters ranging from 50 to 122 µm [9]. The yield strength of these samples is similar regardless of the dimensions of the samples, which coincides with the results from Fleck et al. Furthermore, Weiss et al. reported a fracture strain reduction from 36 to 15 % when reducing the Cu foil thickness from 250 to 50 µm and a fracture strain reduction from 16 to 12 % when reducing the Cu wire diameter from 122 to 50 µm. Fleck et al. did not address the effect of the size on the fracture strain [8]

According to Kiener et al., three promising models explain the size effects on the mechanical properties: dislocation starvation, dislocation nucleation, and dislocation pile-up [10].

Whenever the sample is too small, there is a higher surface/volume ratio, which promotes that dislocations move to the surface and then disappear; the dislocations that leave the crystal do not contribute to the multiplication by cross-slip or to interactions with other dislocations, this effect is known as dislocation starvation. Additionally, when the volume is too small, the dislocation sources are limited, activating unfavourable glide systems or of unfavourable size; this is referred to as dislocation nucleation. Lastly, obstacles, such as regions of high internal stress gradients like the neutral axis of a cantilever, can cause the concentration of dislocation pile-ups on a few glide systems due to the limited number of dislocation sources; hence these dislocation pile-ups affect the dislocation sources by strong back stress [10].

One thing to consider for using the focus ion beam (FIB) to fabricate samples for measuring fracture toughness is the possible effect of ion bombarding on the studied material. For instance, J. Michael studied the effect of the Ga^+ on the behaviour of Cu films [11]. In his research, he evaporated films of Cu and then irradiated them with 30 kV Ga^+ ions. In fine-grained Cu films bombarded with a dose of 3.4×10^{17} ion/cm^2, Michael observed the apparition of "dark" grains due to microstructural modification via the formation of new grains and the formation of 50 nm thick intermetallic Cu_3Ga, which is not a stable compound at room temperature. He reported that these phenomena were not present on Cu samples with a grain size of 100 µm.

Similarly, Kiener et al. studied the damage of Ga^+ ion bombardment on polycrystalline Cu and found a concentration as large as ∼20 at.% close to the surface and penetration depths up to ∼50 nm for 30 keV Ga^+ ions [12]. They propose that the possible consequence of this Ga penetration is the increase in the stress of the material due to solution and precipitation hardening.

For the micro-mechanical tests necessary to study the LME of Cu-30%Zn in contact with the EGaIn, it is necessary to test a grain boundary to account for the intergranular brittle mode of fracture observed in the macroscopic tests. Growing bi-crystal is a possible method to characterize the mechanical properties of a grain boundary, but it is time-consuming and expensive. A better alternative is a micro-scale mechanical test on a polycrystalline material [13]. For this, micro-scale cantilever samples have been used to study the embrittlement of Cu grain boundaries by Bi [13] and the study of the oxidized grain boundaries of a Ni-based alloy [14].

IV.3. *In-situ* micrometric tests on Cu-30%Zn in contact with EGaIn

The single cantilever bending and the clamped beam bending tests were chosen considering the information available in the literature. The tests were carried out in the Cu-30 wt.%Zn alloys, which is the alloy that presented the most conditions of embrittlement by the EGaIn. Moreover, since the Cu-30%Zn brittle fractures had an intergranular nature, the tests were designed to test grain boundaries in contact with the EGaIn. A W-layer was applied to the sample to obtain contact between the liquid EGaIn and the Cu-30%Zn alloy only after the alloy was under plastic deformation. The following section presents a more detailed description of the methodology.

IV.3.1. Methodology for the micrometric tests

The micromechanical tests were done at Mécanique des Sols, Structures et Matériaux laboratory (MSSMAT) in an FEI Helios Nanolab 660 equipped with an electron beam and an ion beam. This machine fabricated the samples and performed the observations during the micromechanical tests. Like standard scanning electron microscopes, the electron beam of the Helios Nanolab 660 is oriented vertically, while the ion beam is tilted 52° from the electron beam. The electron source is a Schottky thermal field emitter, and the ions used for the milling and observations are Ga^+. This machine is equipped with an easylift micro-manipulator with a W needle. Figure IV–5 shows an image of the Helios Nanolab 660 along with the positioning of the electron beam, the ion beam, and the micro-manipulator.

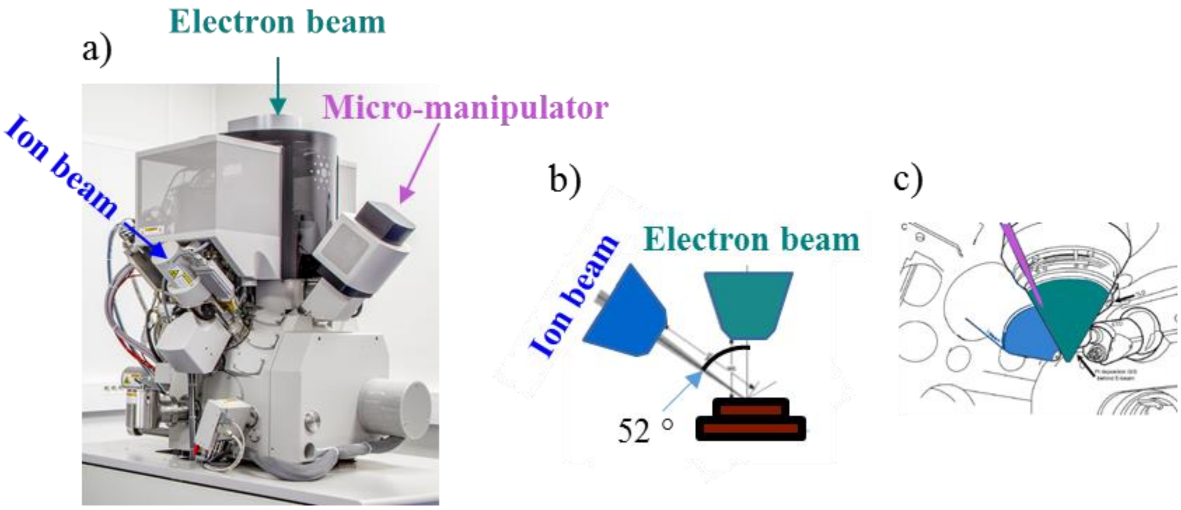

Figure IV–5 Photography of the Helios Nanolab 660 (taken by F. Armand), and two schemas of the position of the ion and electron beams.

Figure IV–6 shows the machine used to carry out the *in-situ* micromechanical test, which was developed in the MSSMat (now LMPS) laboratory with the collaboration of Framatome [6], [15]. The machine has piezoelectric motors that control the movement of the sample and its alignment with the needle in three perpendicular axes, a load cell that registers the force applied in traction and compression to the sample, a needle that is used to apply force to the sample, and a rotation motor that rotates the needle.

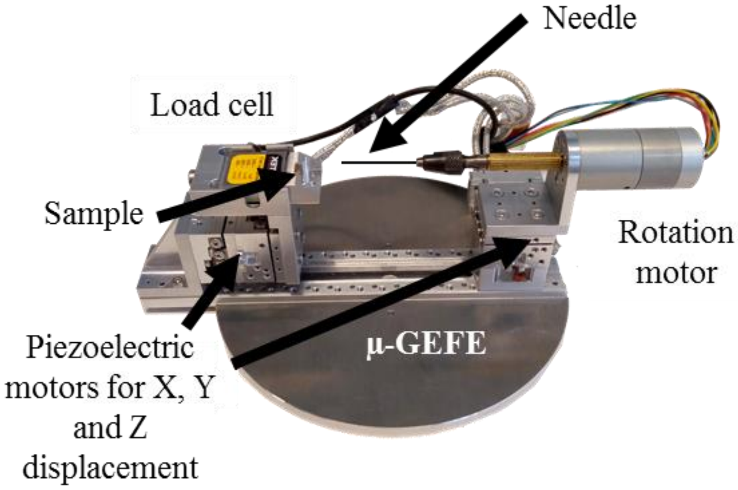

Figure IV–6 In-situ *machine used for micromechanical testing* [15].

The sample used for these tests corresponds to the Cu-30%Zn batch with an initial thickness of 2 mm, i.e., with a grain size of 39 ± 7 µm and a hardness of 142 ± 4 HV. A piece of the sample was cut and mechanically polished to obtain a sample of 9×4×0.8 mm.

A W-layer was applied by electron beam-induced deposition into the zone of the solid sample that enters in contact with the EGaIn to inhibit the intermetallic formation that would impede the contact between the liquid metal and the solid metal. The objective is to have a layer impeding the contact between the Cu-30%Zn and the EGaIn when there is still no plastic deformation on the solid. Otherwise, the intermetallic formation would impede the contact between the liquid and the solid and deplete the liquid metal by reacting with a significant part of the sample. Due to the brittleness of W, the layer breaks during the sample's deformation, and contact between the solid and the liquid becomes possible.

IV.3.2. Single cantilever bending

The single cantilever bending test was chosen as the geometry for the test because it presents a higher success rate, is suitable for studying embrittled grain boundaries, and is easily scalable [4], [13].

IV.3.2.1. Sample preparation

Before preparing the cantilever, the suitable milling parameters for the fabrication of the notches were determined, and the notch radius was measured. Figure IV–7 shows two of these notches, their dimensions and radii. The form of the notch was chosen to be able to introduce the liquid EGaIn in it.

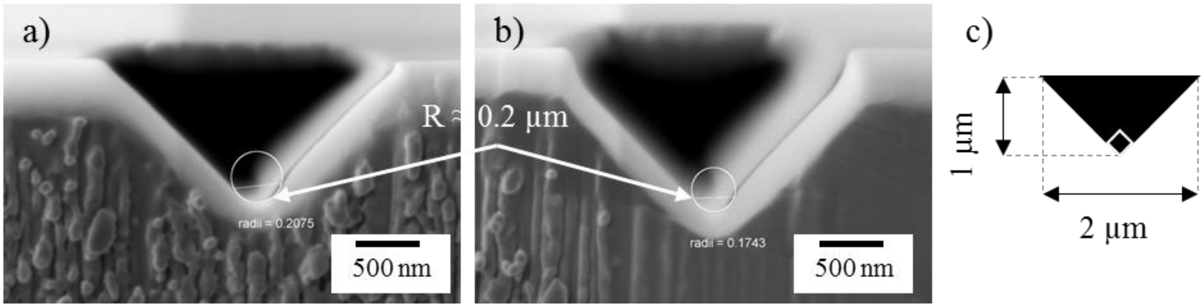

Figure IV–7 Notches milled with the FIB with different parameters.

The best parameters of the ion beam for milling the notch were 30kV and 80 pA. In addition, different parameters of W deposition were tested; Figure IV–8 shows some examples of notches with a W-layer. These layers were deposited using 5 kV and 3.2 nA; their thicknesses are 50, 65, 100, 150 and 150 nm, in the order of apparition in Figure IV–8; their dwell time was 1.4 ms, except for the last layer, which was done with a dwell time of 140 µs. The parameters of the W depositions are essential since the W-layer must be thick enough for the liquid EGaIn to not react with the Cu-30%Zn, and it must be thin enough to brake during the test.

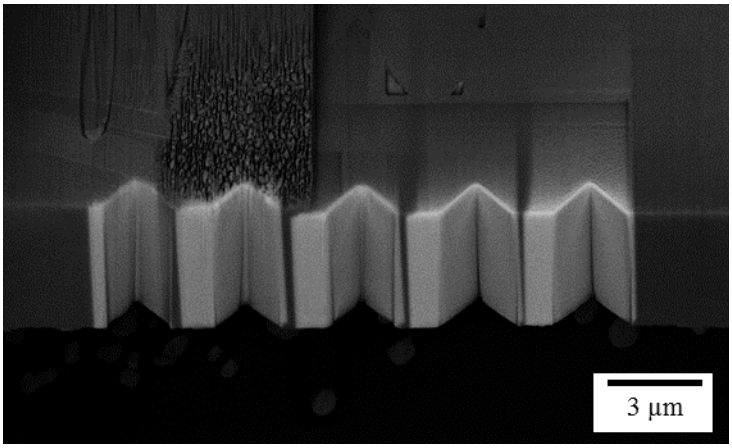

Figure IV–8 Examples of W-layers applied on notches.

Drops of liquid metal were deposited in the notch to test the effectiveness of the W-layers. For this deposition, the micro-manipulator needle was soaked in liquid EGaIn to obtain a dispersion of drops at its extreme, and then the needle was inserted into the Helios Nanolab 660. Then, using the easylift micro-manipulator, the needle was approached to the sample. Once the needle was close to the notch, the ion beam was used to break the oxide layer of the EGaIn drop and spread the liquid metal inside the notch. Figure IV–9 illustrates this process.

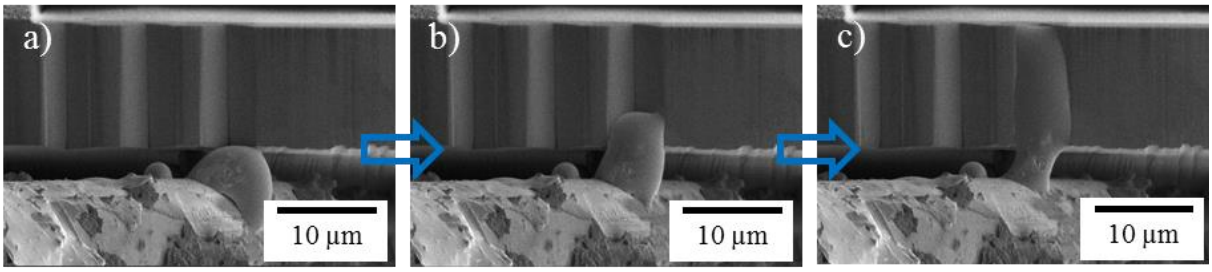

Figure IV–9 Process for the deposit of an EGaIn drop on a notch.

The filled notches were observed with a backscattered electron (BSE) detector to distinguish better the W, the Cu-30%Zn alloy, and the EGaIn. Figure IV–10 shows an example of this observation where the drop of EGaIn stays in the notch and does not overflow to the other face of the sample. The chosen parameters of the electron beam for the W deposition were 5 kV, 3.2 nA, a dwell time of 140 µs, and a thickness of 150 nm. The last value is a parameter of the deposit and does not indicate the layer's actual thickness. The actual thickness value depends on several parameters, such as the surface inclination and the dwell time, and it could not be measured due to its small size.

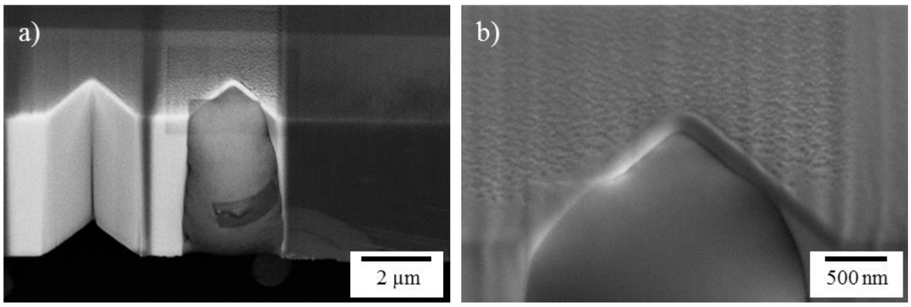

Figure IV–10 Observation of a notch filled with the EGaIn.

The cantilever sample was milled from the sample using continuously decreasing ion beam intensities ranging from 65 nA to 80 pA, with a constant voltage of 30 kV. The observations with the ion beam were limited to avoid Ga^+ contamination, and they were done using an intensity of 40pA. Figure IV–11 shows a simplified step-by-step milling of the sample with some of the intensities used for the ion beam. The intensities used were 65 nA to mill the zone in Figure IV–11a, 9.3 nA to do the mills between Figure IV–11b and Figure IV–11c, and 2.5 nA to do the mills between Figure IV–11e and Figure IV–11f. For the finishing steps, a tilt of 2° was applied to account for the beam deviation.

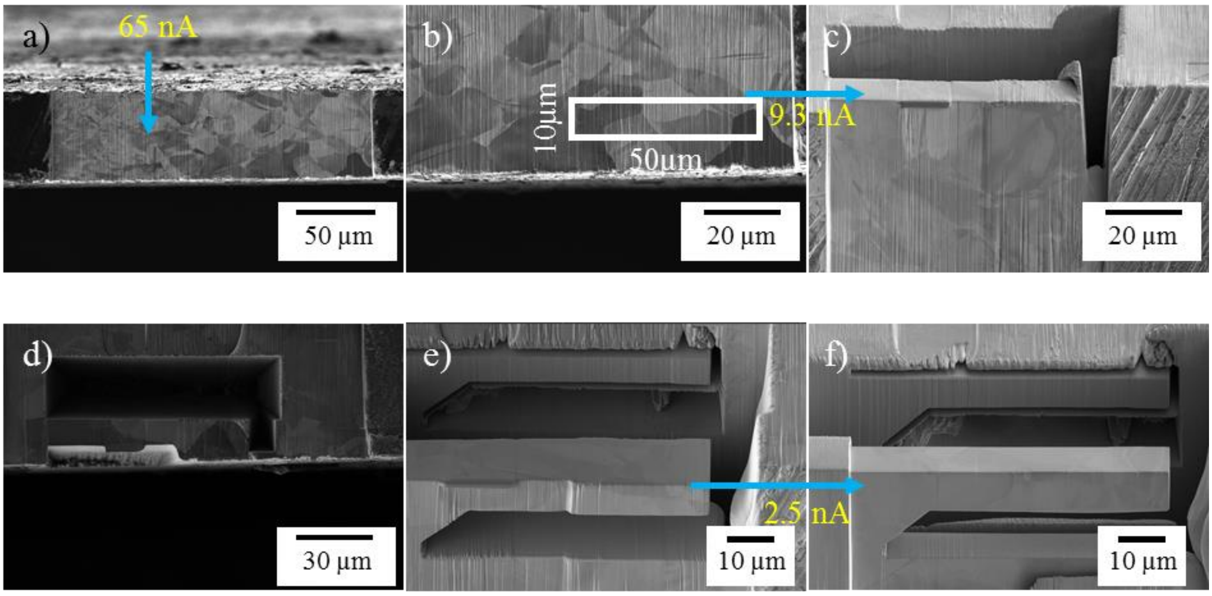

Figure IV–11 Process of fabrication of the cantilever sample using the Ga$^+$ ion beam.

The choice of the zone to fabricate the cantilever was made to have a grain boundary correctly aligned to the notch, i.e., a grain boundary oriented vertically in both planes. A great area was milled to find the suitable grain boundary (Figure IV–11a), and a vertical grain boundary with the correct dimensions was chosen (Figure IV–11b). Then transversal mills were done to assess if the grain boundary was well oriented in the other plane. Once a suitable grain boundary was found, the cantilever sample was milled around this zone (Figure IV–11f). Then, the notch was milled into the sample, and the W-layer was applied to this notch. Figure IV–12 shows the last steps of the process and the cantilever's approximate dimensions.

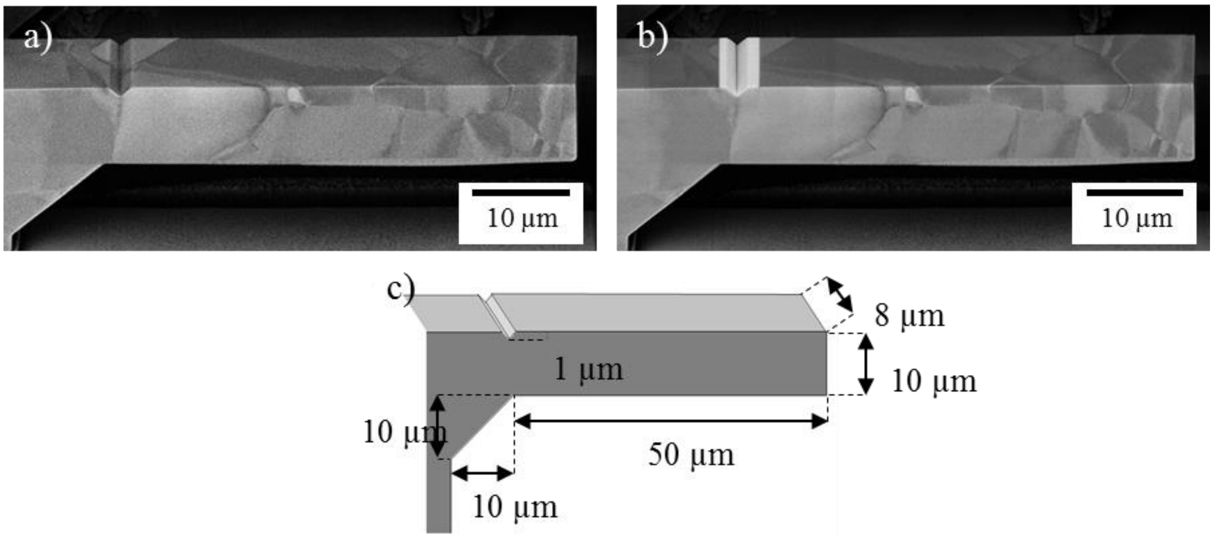

Figure IV–12 BSE images of the final cantilever sample a) without the W-layer and b) with the W-layer. c) Final dimensions of the sample.

The liquid metal was introduced into the notch with the micro-manipulator using the methodology previously exemplified in Figure IV–9. Figure IV–13 shows the drop while being placed in the cantilever and the final filled notch.

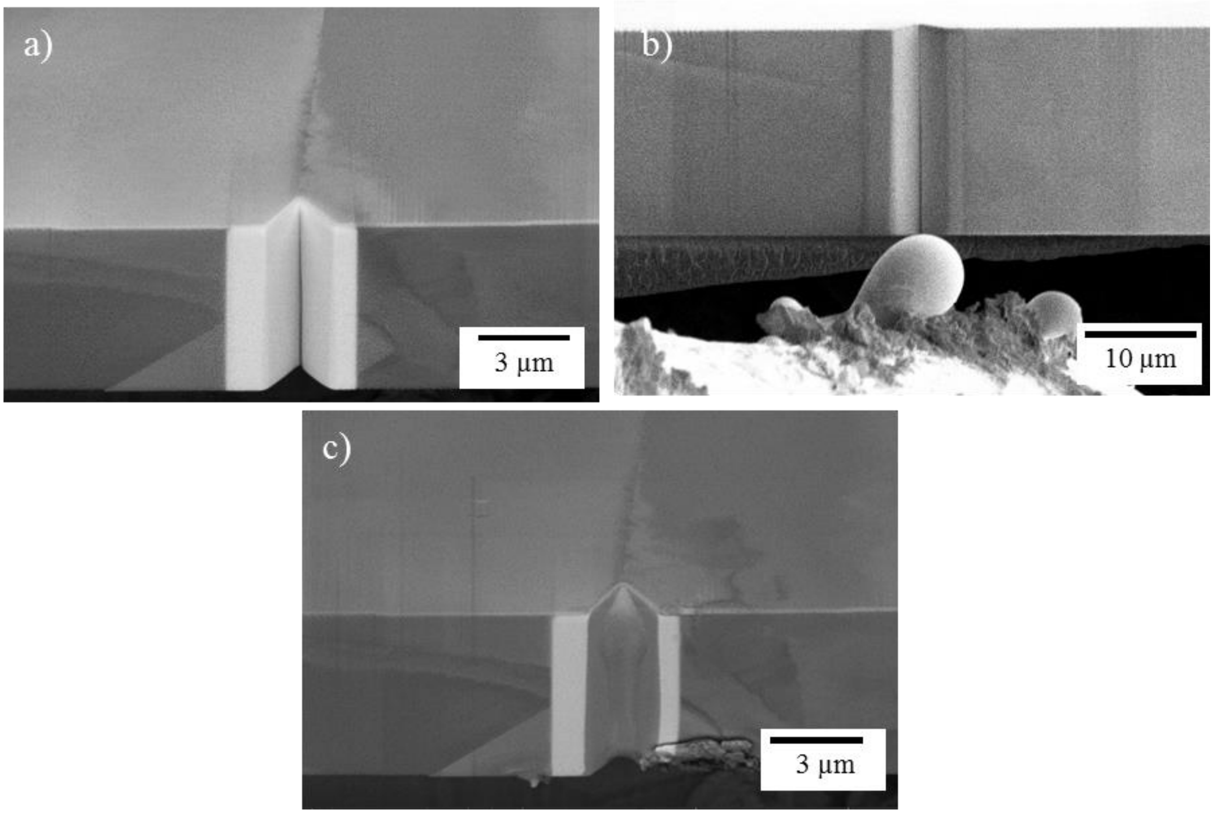

Figure IV–13 Placement of the EGaIn drop on the cantilever sample.

The sample was mounted into the *in-situ* testing machine, and the needle was approached and aligned with the sample. Figure IV–14 shows the setting before the start of the test. An electron beam corresponding to 10 kV and 1.6 nA was employed for the observation, and the signals were collected using two different detectors. One of the signals is that of the secondary electrons (SE), which gives information related to the sample's surface since its interaction volume is small. The other corresponds to that of backscatter electrons (BSE), which interact more deeply with the matter. Using the outer zone of the BSE detector, the obtained image contains crystallographic aspects, i.e., it gives a contrast that depends on the orientation of the crystal lattice. The SE images allow observation of the needle contour, the sample contour, and the liquid metal in the notch; these images correspond to Figure IV–14a and Figure IV–14b. The BSE images allow the observation of the slip bands, the disorientation of the grains, and the grain boundaries; these images correspond to Figure IV–14d and Figure IV–14e. Observing the slip bands is especially important since these indicate when the material undergoes plastic deformation. The micrographs of both detectors are obtained simultaneously.

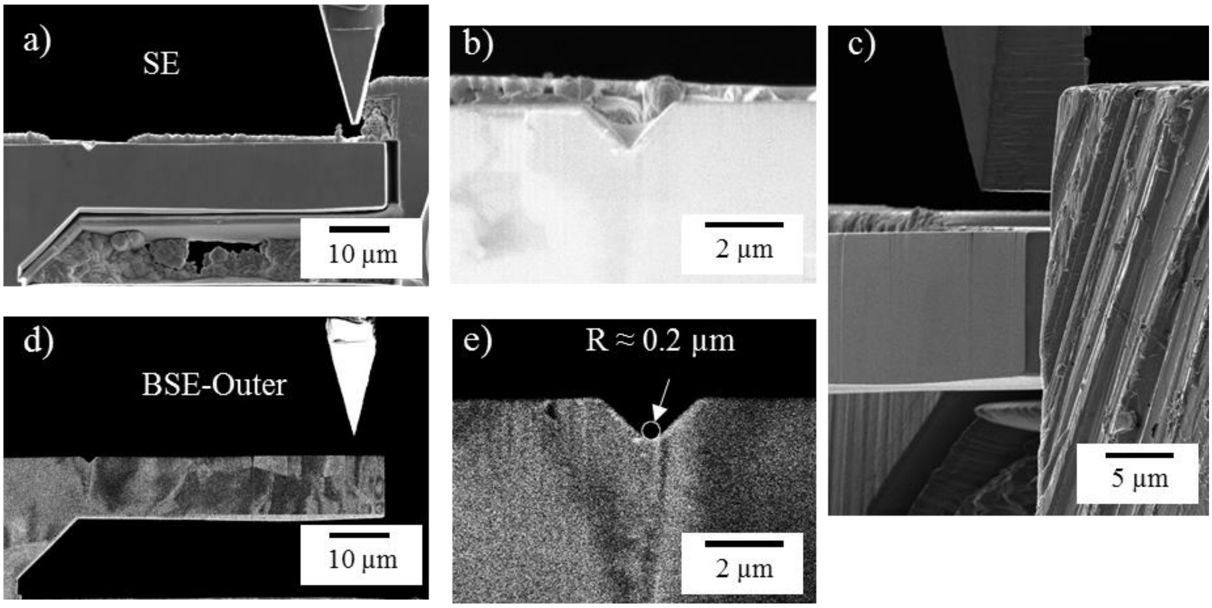

Figure IV–14 Setting before the single cantilever bending test.

As seen in Figure IV–14e, the radius of the notch was estimated to be 0.2 µm with the BSE images. Additionally, the needle was aligned with the thickness of the sample by observations done with the ion beam. The needle alignment is critical since misalignment could lead to only partially applying the force in the sample, creating unexpected force components.

IV.3.2.2. Test

The test was carried out in various steps. The needle was advanced at a defined distance by commanding the piezoelectric motors, and then micrographs of the totality of the samples were taken using the SE and BSE-outer detectors, followed by closer micrographs of the zone near the notch. This process was repeated until the failure of the sample.

Figure IV–15 shows the initial and the last step of the first stage of the test, and Figure IV–16 shows a closer look into the notch at the corresponding moments of the test. The BSE images show slip bands concentrated around the notch, a sign of plastic deformation in these zones.

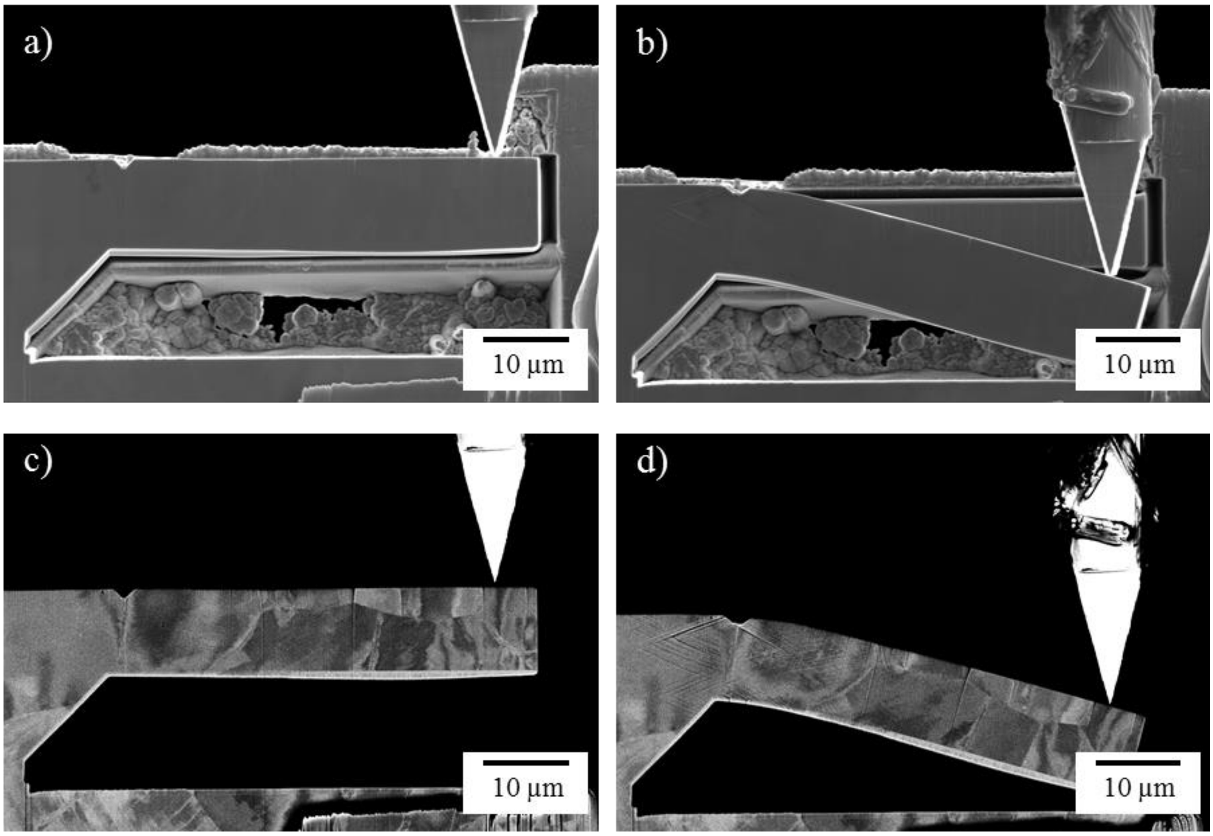

Figure IV–15 a, b) SE and c, d) BSE images of the first stage of the single cantilever bending test.

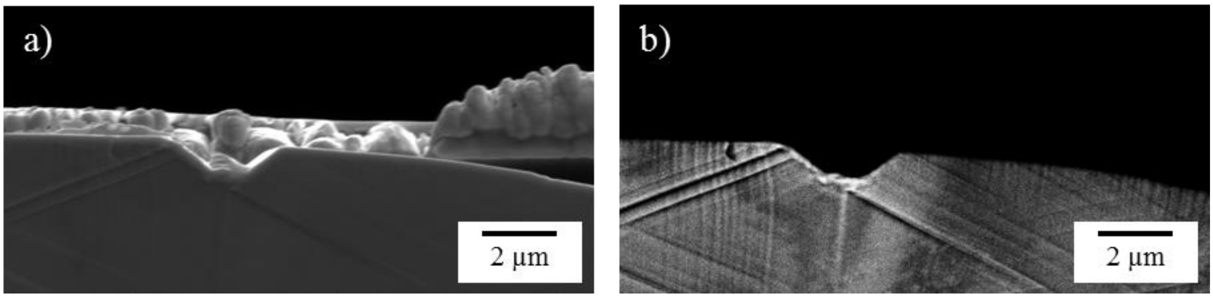

Figure IV–16 a, b) SE and c, d) BSE images of the notch at the end of the first stage of the single cantilever bending test.

Unfortunately, at the end of this stage, no additional space was available for the cantilever deformation. The cantilever was milled to shorten its span length to continue testing the sample. The stress state changes by doing this, i.e., a smaller span length propitiates the apparition of shear stress that adds to the tensile test in the notch.

Figure IV–17 and Figure IV–18 show the continuation of the test with the modified sample. The sample could be deformed considerably in this stage of the test. Furthermore, the BSE image of the last part of the stage shows a fracture in the bottom of the notch. The respective

SE image shows that the EGaIn entered this fracture. However, the tests could not be continued due to the same limitation encountered during the first stage.

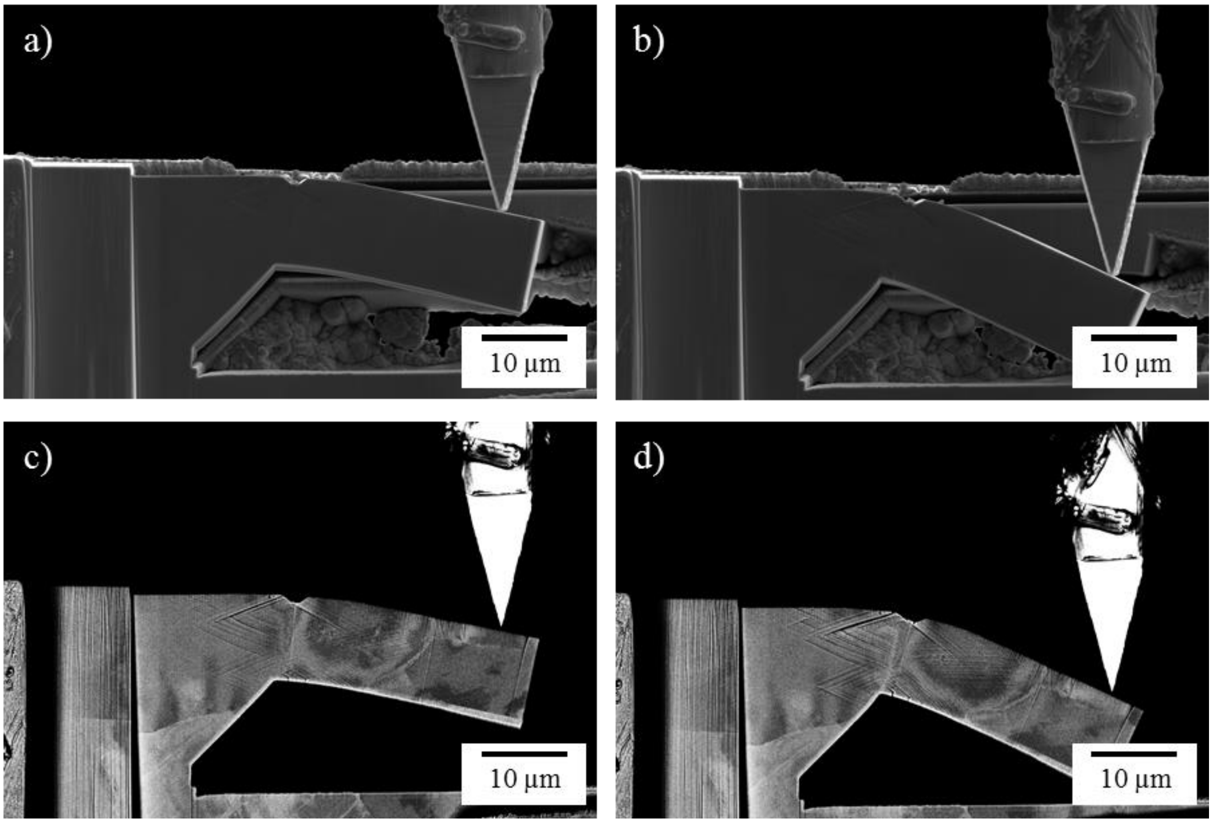

Figure IV–17 a, b) SE and c, d) BSE images of the second stage of the single cantilever bending test.

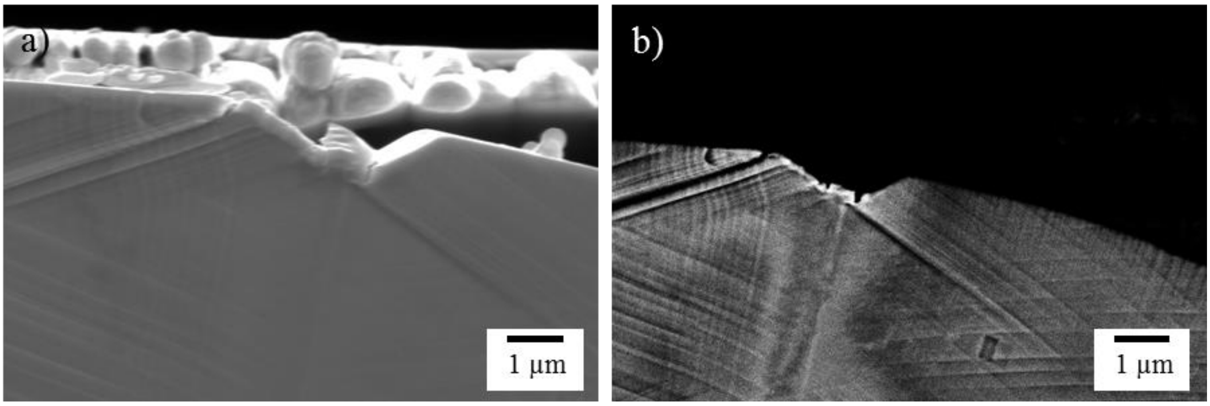

Figure IV–18 a) SE and b) BSE images of the notch at the end of the second stage of the single cantilever bending test.

The test was resumed into a third stage by cutting the sample again; Figure IV–19 shows this last stage of the test. Cutting the sample could apply some more deformation, although not significantly. This time, the sample could not be further deformed due to another practical limitation: since the cantilever bent significantly, the needle orientation with the beam provoked the needle to start removing material from the sample and slip to the extreme of the cantilever.

The SE image in Figure IV–19 illustrates this limitation. Moreover, the excessive bending of the cantilever also restricts the force that the needle could apply to the sample on the vertical axis, and instead, the needle applies considerable force on the horizontal axis.

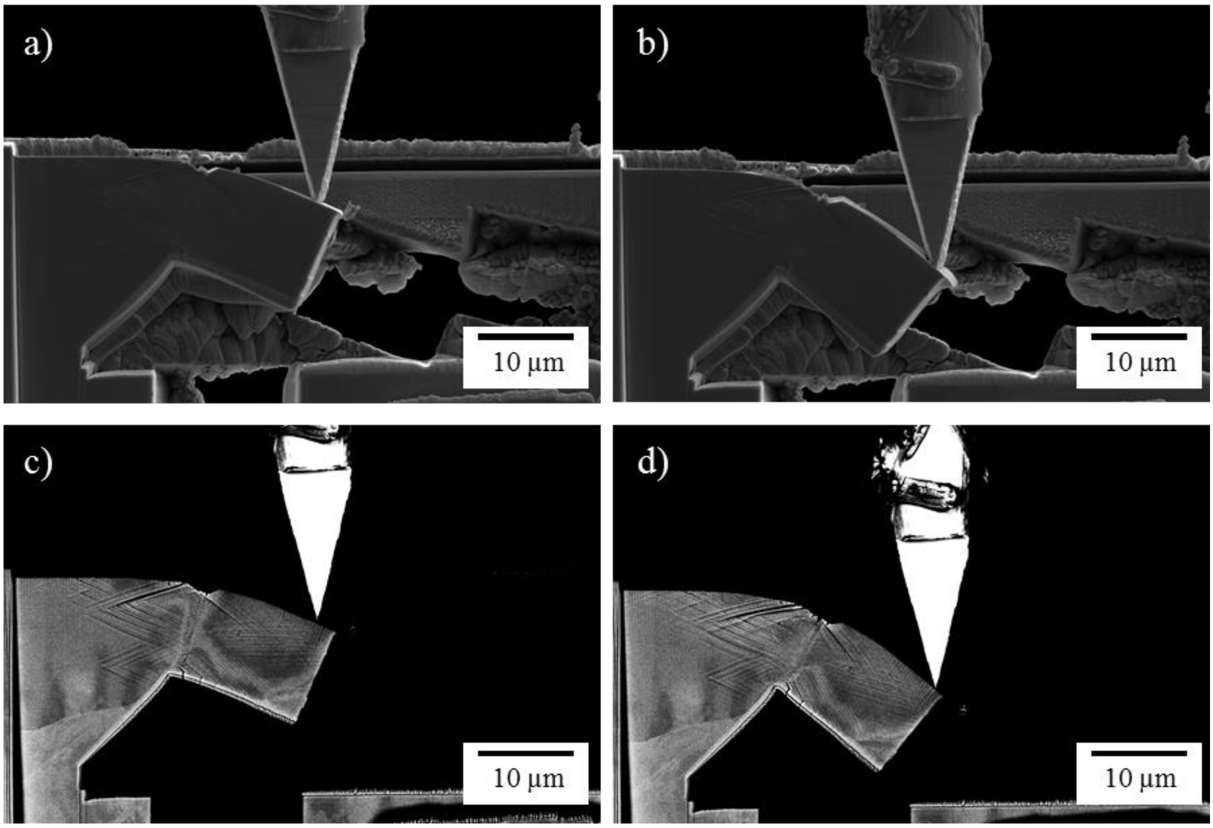

Figure IV–19 a, b) SE and c, d) BSE images of the second stage of the single cantilever bending test.

Figure IV–20a shows the force-displacement curves of the single cantilever bending test, the force is obtained from the load cell, and the displacement is measured from the SE images. Furthermore, for a better comparison of the three stages, Figure IV–20b shows the longitudinal stress at the notch position vs displacement curves of the single cantilever bending test. The stress was estimated using an analytical formula (Eq. (29)). The obtained stress is only approximate since it does not consider the notch geometry and is not meant to be used as a quantitative comparison.

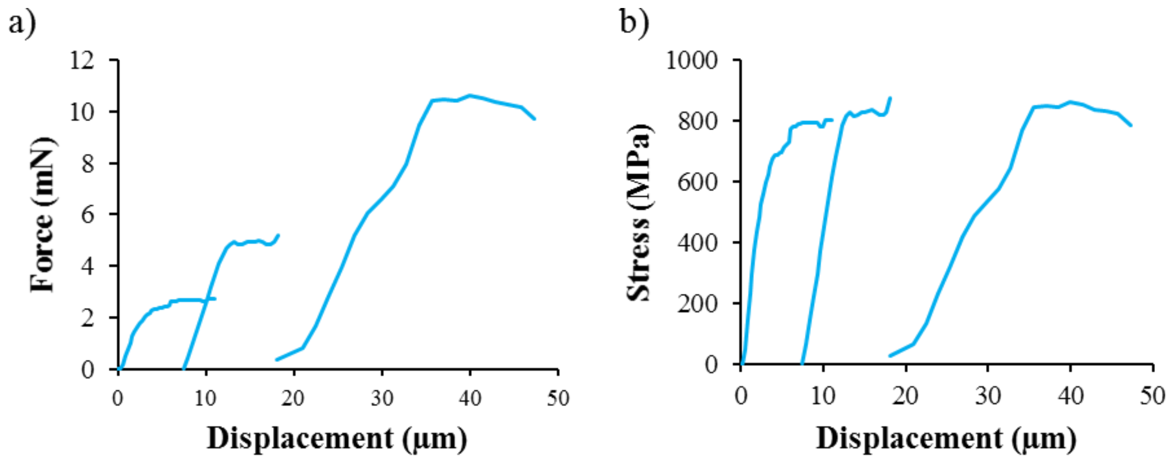

Figure IV–20 a) Force-displacement and b) Stress v displacement curves of the three stages of the single cantilever bending test.

$$\sigma_x = -\frac{12\,F\,d\,y}{b\,h^3} \qquad (29)$$

where *F* is the applied force; *d* is the distance of the applied force from the notch, which is 44, 25 and 12 µm for each stage, respectively; *y* is the distance from the neutral axis, in this case, considered as 4.5 µm; *b* is the thickness of the beam, which is 8 µm; and *h* is the height of the beam, which is 10 µm.

The fact that the slope in the elastic regime is considerably lower in the third step of the test confirms that there was a fracture initiation during the second step.

IV.3.2.3. Analysis post-test

After the test, the sample was unmounted, and the zone near the notch was observed. Figure IV–21 presents images of the notch after the test, where the W-layer and the zone below it completely fractured. Also, on the sample side that was not observed during the test, the fracture was more extended, which indicates that the fracture may have started earlier. No trace of liquid EGaIn was observed, which confirms that it entered into contact with the solid sample during the test.

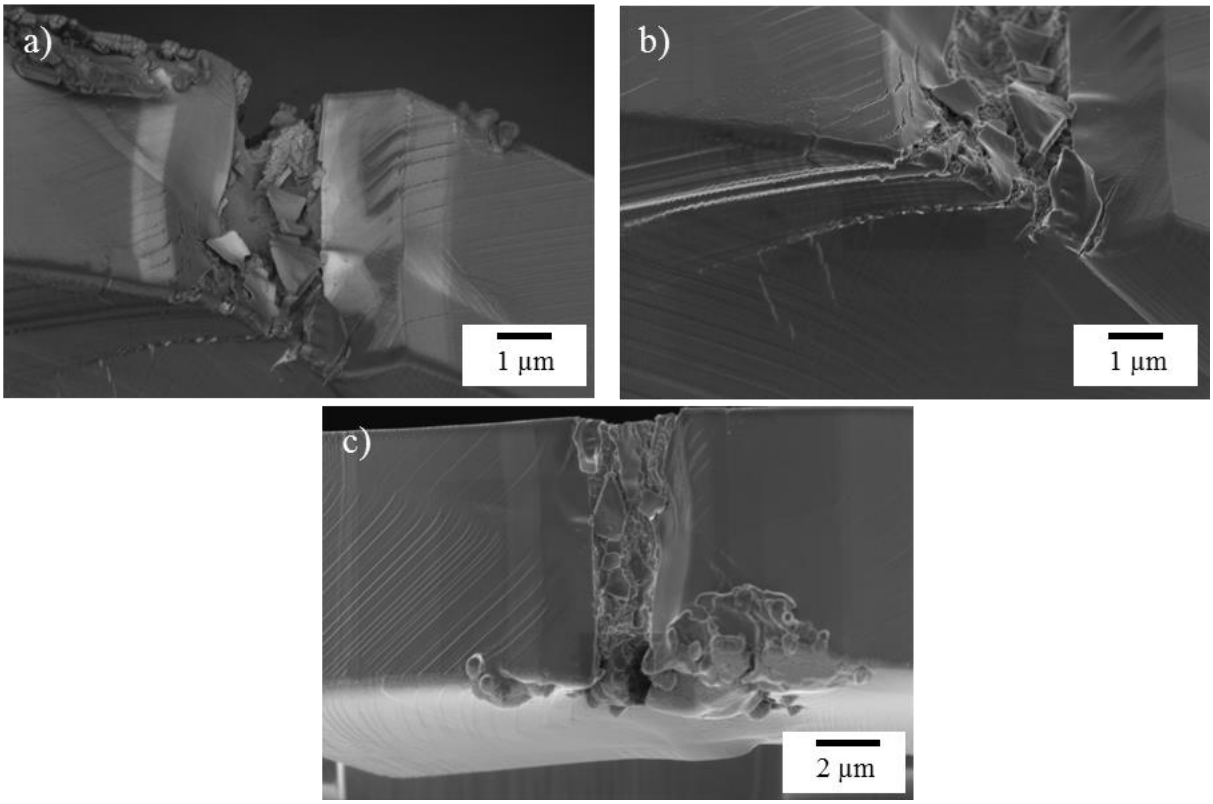

Figure IV–21 Fractured notch of the single cantilever bending test sample.

In addition, the ion beam was used to mill the sample to obtain a transversal cut of the fracture. This cut was observed and analyzed using energy-dispersive X-ray spectroscopy (EDS). Figure IV–22 presents the micrographs and EDS analysis of this cut. These analyses show that the fracture initiation zone corresponds to the sample's grain boundary and that there is Ga in that zone. In a close zone, there is a W-layer and Ga around it, which indicates that Ga went below the layer. No presence of In was detected.

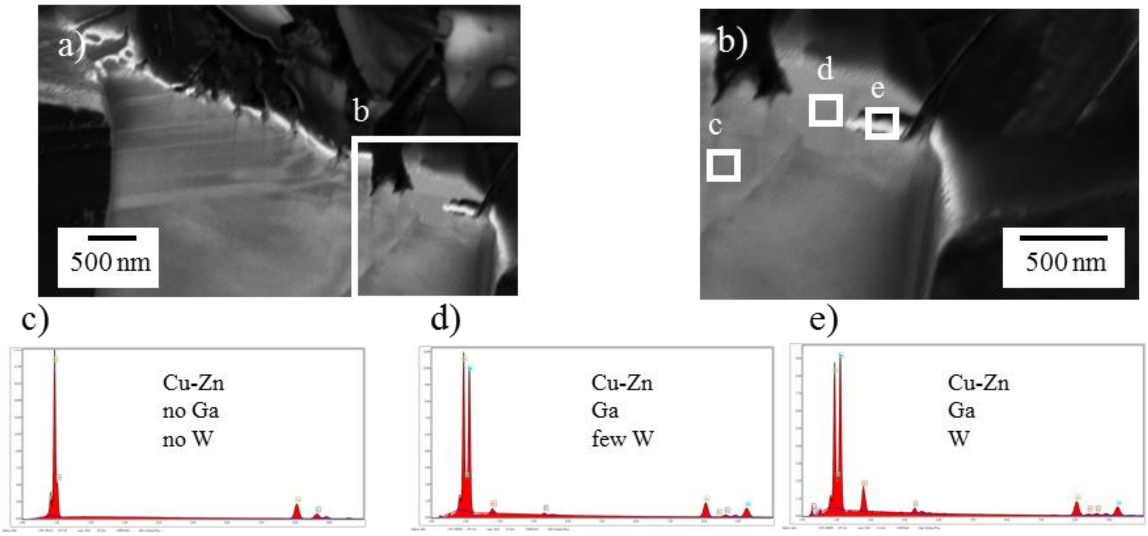

Figure IV–22 Transversal cut of the fracture and the correspondent EDS analysis.

The fact that this test could not be carried out without cutting the sample made interpreting the results not straightforward. However, even if these complications were avoided by milling a deeper space for the sample to deform, the test would undergo a critical practical limit in the quantity of deformation it can apply to the sample. The sample showed that it could be plastically deformed significantly before the apparition of the first fracture, which traduced in a significant bending of the cantilever bend. This bending would prevent the needle from applying a correct vertical force to the cantilever; additionally, the needle could glide to the edge of the sample until it no longer touches the cantilever.

In comparison, the clamped beam bending does not present this limit, and the needle could continue the sample deformation virtually indefinitely.

IV.3.3. Clamped beam bending

IV.3.3.1. Preparation of the sample

The same sample of the Cu-30 wt.%Zn alloy was used to prepare the clamped beam bending test. The sample preparation followed the methodology used for the single cantilever bending test. First, a zone with a grain boundary correctly oriented in both planes is chosen. Figure IV–23a presents a significant sample volume milled to find a suitable zone with a vertical grain boundary. Once this zone was spotted, a perpendicular mill was done to observe if the grain boundary was relatively straight in the other face. Figure IV–23b shows the two faces of a grain boundary that fulfils these conditions; hence, the sample was milled in this zone. Moreover, Figure IV–23c shows an Electron Backscatter Diffraction (EBSD) measurement in this zone to verify that the grain boundary is not a special grain boundary, such as a twin.

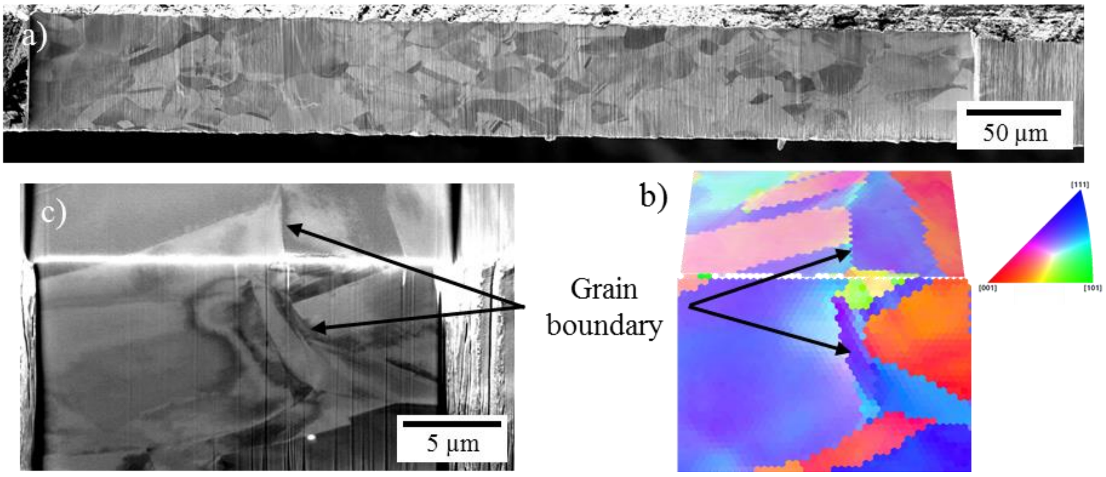

Figure IV–23 a) Microstructure of the sample observed by ion milling, b) grain boundary chosen for the sample milling, and c) EBSD of the zone around the grain boundary.

With the zone defined, the sample was milled around it. Figure IV–24 shows a simplification of the milling process. Figure IV–24b shows the milled clamped beam, which is then notched (Figure IV–24c). Figure IV–24d shows the W-layer applied to the notch following the same parameters as the previous test.

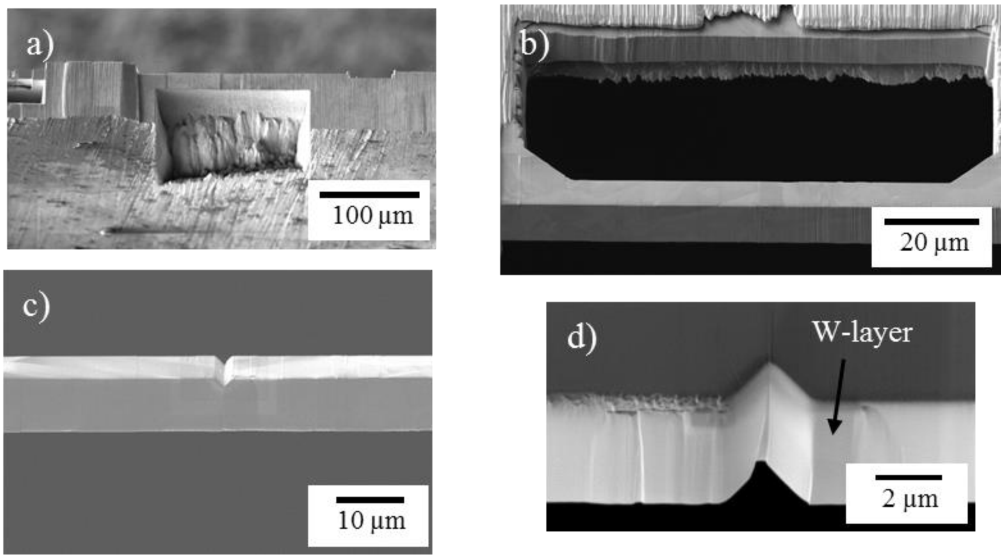

Figure IV–24 Process of the clamped beam bending test sample milling.

Figure IV–25 presents the final sample with its dimensions and the results of an EBSD done in the totality of the sample.

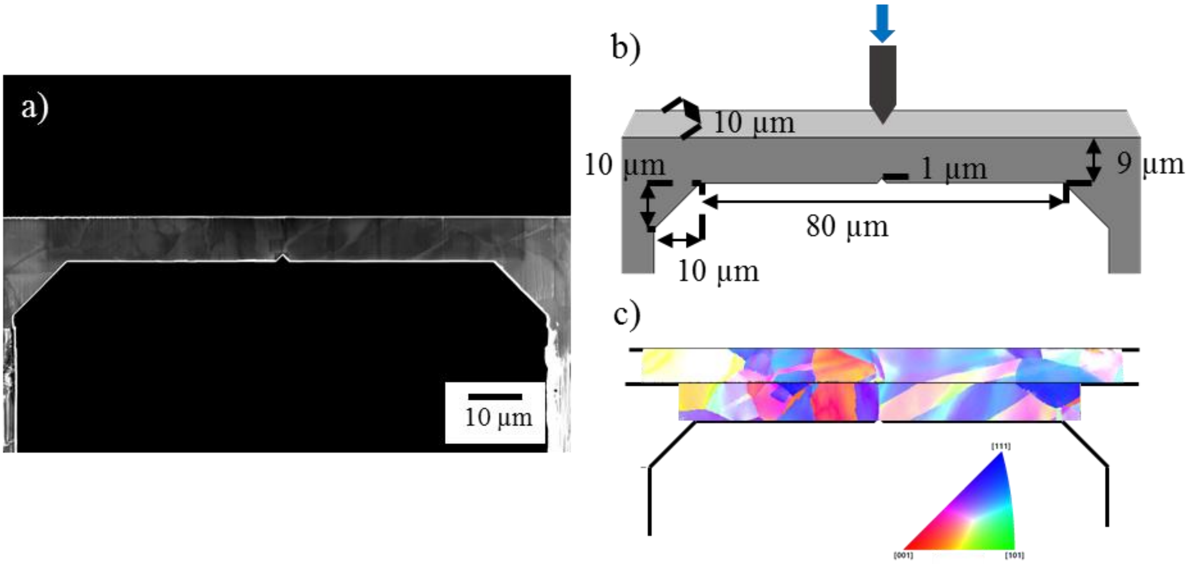

Figure IV–25 a) Final clamped beam bending test sample, b) sample dimensions and c) EBSD of the sample.

Then, the micro-manipulator deposited a drop of EGaIn into the notch. Figure IV–26 shows the process of drop deposition with two different views obtained with the electron beam and the ion beam, respectively. We recall that for the drop to enter the notch, the ion beam was used to break the oxide layer of the EGaIn and spread the liquid metal into the notch. The EGaIn drop successfully entered the sample notch but overflowed to zones of the sample that were not covered with the W-layer.

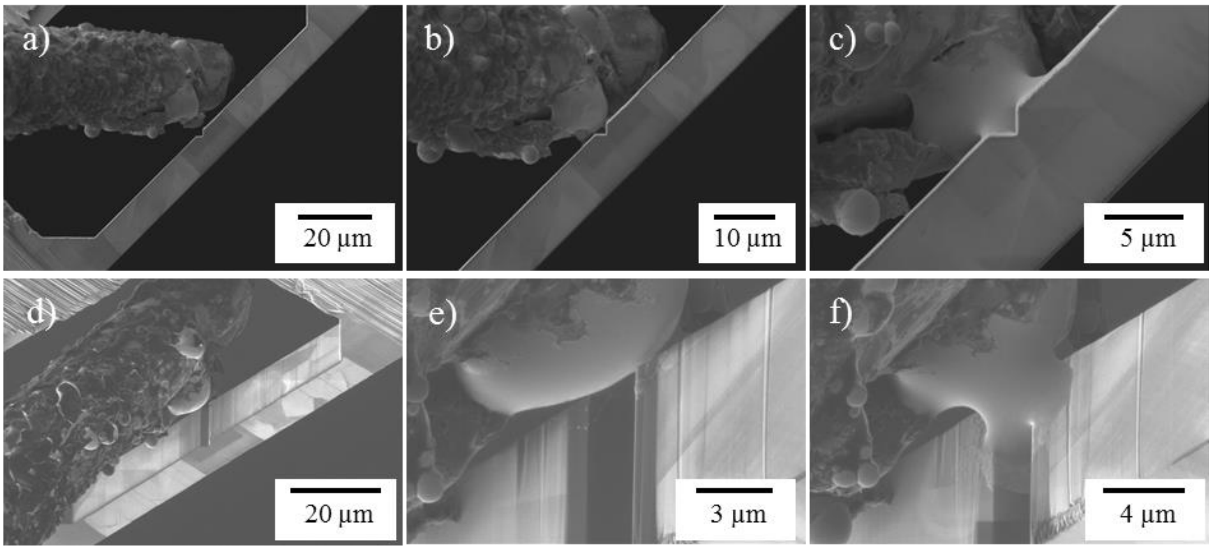

Figure IV–26 Deposition of the EGaIn drop on the clamped beam bending test sample. a to c) are SE images and d to f) are ion images.

The overflow of the EGaIn generated a reaction between the liquid EGaIn and the Cu-30%Zn, most probably to create the $CuGa_2$ intermetallic. Figure IV–27a and Figure IV–27d show the notch filled with the EGaIn and the reaction between the EGaIn and the Cu-30%Zn. Figure IV–27b and Figure IV–27e show the evolution of this interface after 12 minutes. Moreover, Figure IV–27c and Figure IV–27f show the sample after 20 hours of contact. There were no considerable changes in the interface after the first minutes of contact, which indicates that the EGaIn reacted with the Cu-30%Zn to form an intermetallic, but this reaction eventually stopped before the EGaIn completely depleted, i.e., there is EGaIn available for the test.

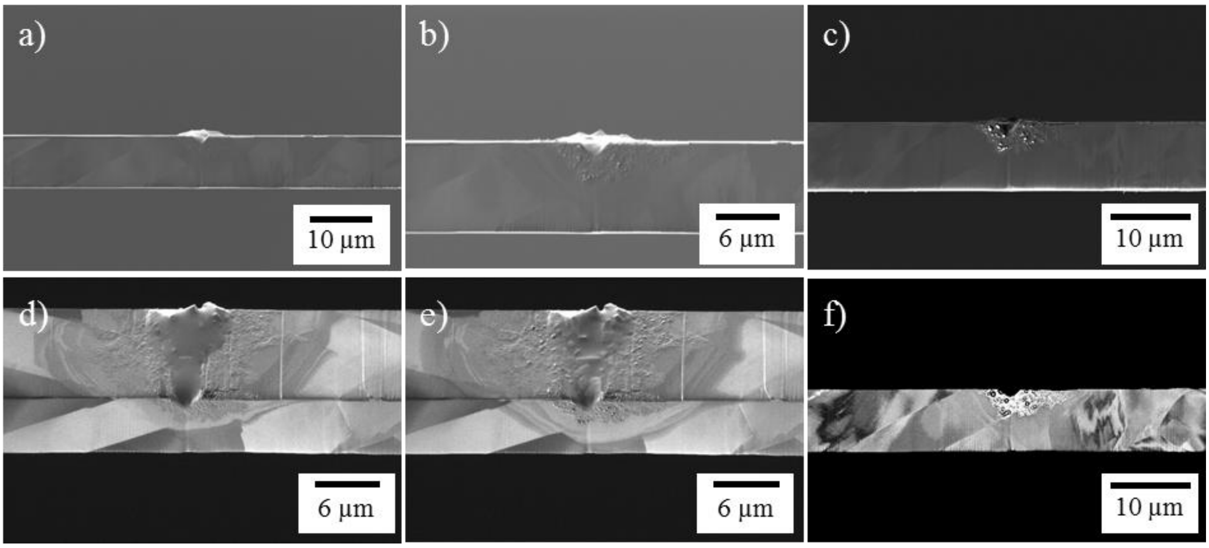

Figure IV–27 Evolution of the interface liquid EGaIn/Cu-30%Zn after the start of the reaction. a to c) are SE images, d, e) are ion images, and f) is a BSE image.

The sample was mounted into the *in-situ* micromechanical testing machine, and the machine was mounted into the Helios Nanolab 660. Figure IV–28a shows the machine inside the chamber of the Helios Nanolab 660, and Figure IV–28b shows the alignment of the needle with the sample.

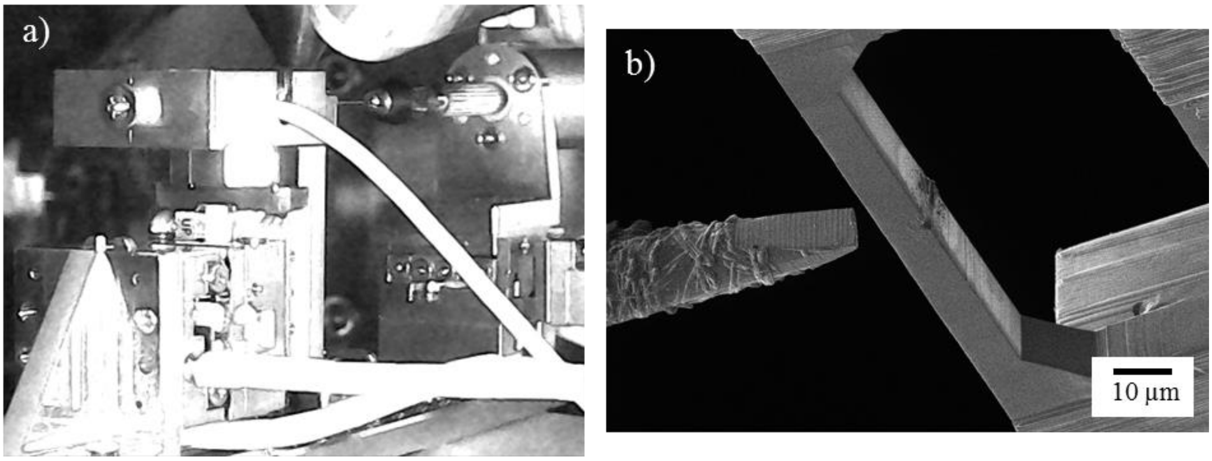

Figure IV–28 a) In-situ *micromechanical testing machine inside the Helios Nanolab 660 and b) needle alignment before the bending test.*

IV.3.3.2. Test

Like the single cantilever bending test, the clamped beam bending test was performed in various interrupted steps. Between these interruptions, the micrographs were taken. Figure IV–29 and Figure IV–30 show some images taken at four test moments using the SE and BSE-Outer detectors, respectively. The images correspond to the beginning of the test, the apparition of the first sample's fracture before the sample's final failure, and the sample's final failure, in that order.

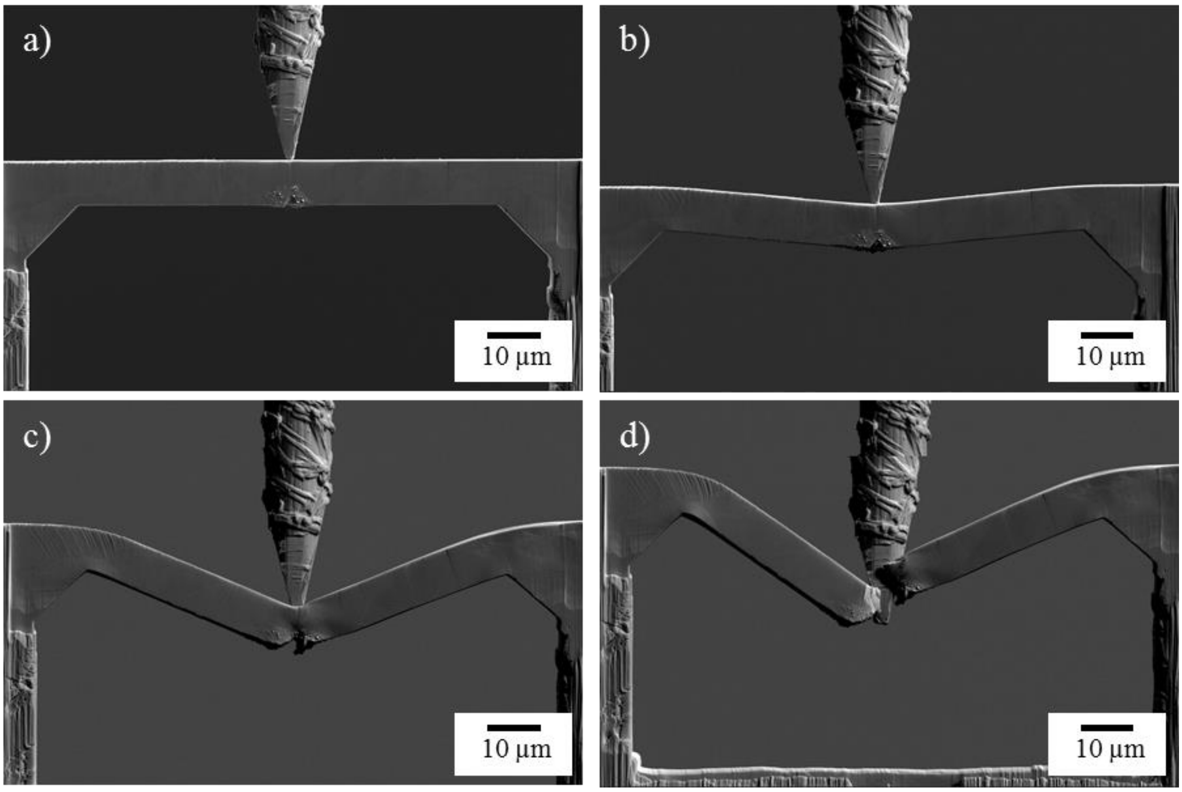

Figure IV–29 SE images of the clamped beam bending test.

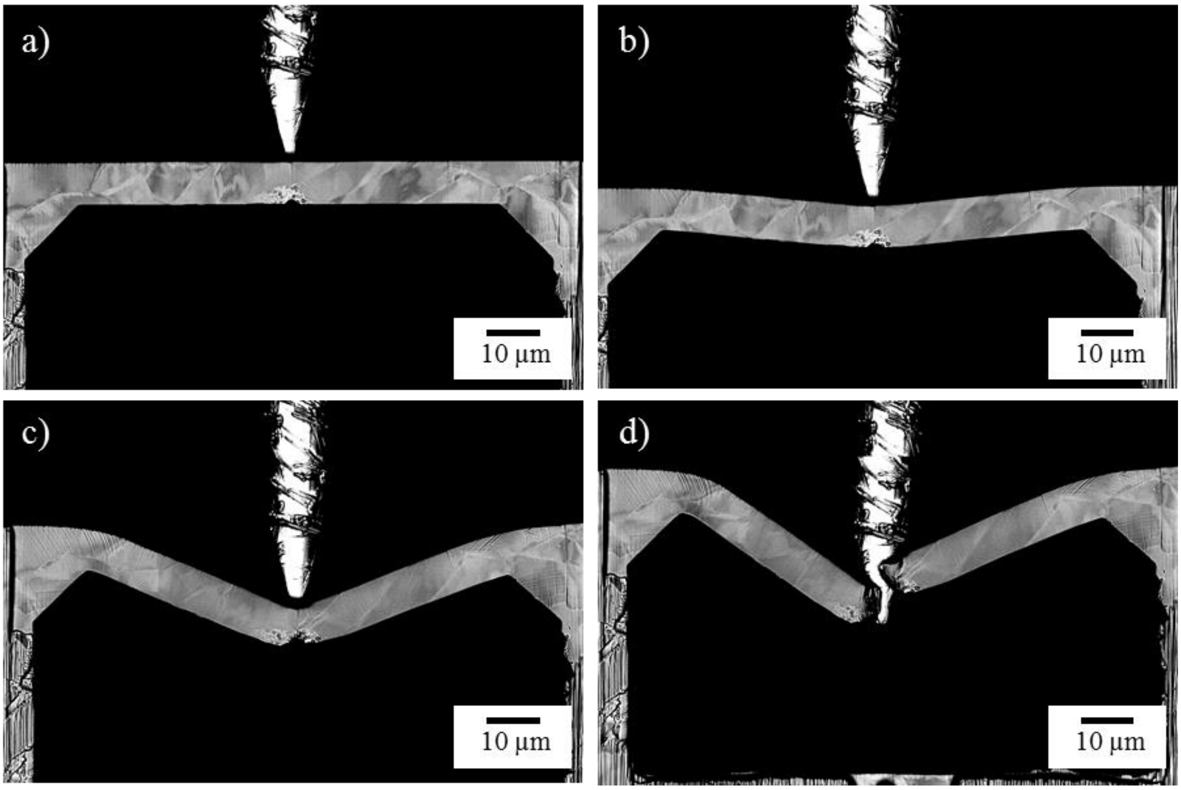

Figure IV–30 BSE-outer images of the clamped beam bending test.

The final failure of the sample occurred while taking the photo of the corresponding step. While the electron beam was performing the scan, the needle moved due to the recovery of the elastic deformation of the sample after it failed, and it caused the apparent discontinuity of the needle observed in Figure IV–29d and Figure IV–30d.

Figure IV–31 presents a closer view of the sample. Figure IV–31a and Figure IV–31b correspond to the moment of the apparition of the first fracture. Figure IV–31c and Figure IV–31d correspond to the step before the final failure of the sample. The fracture initiation is clearer within the BSE image, while the SE image lets us observe that the EGaIn entered the notch. In addition, various fractures appeared near the notch at later stages of the test.

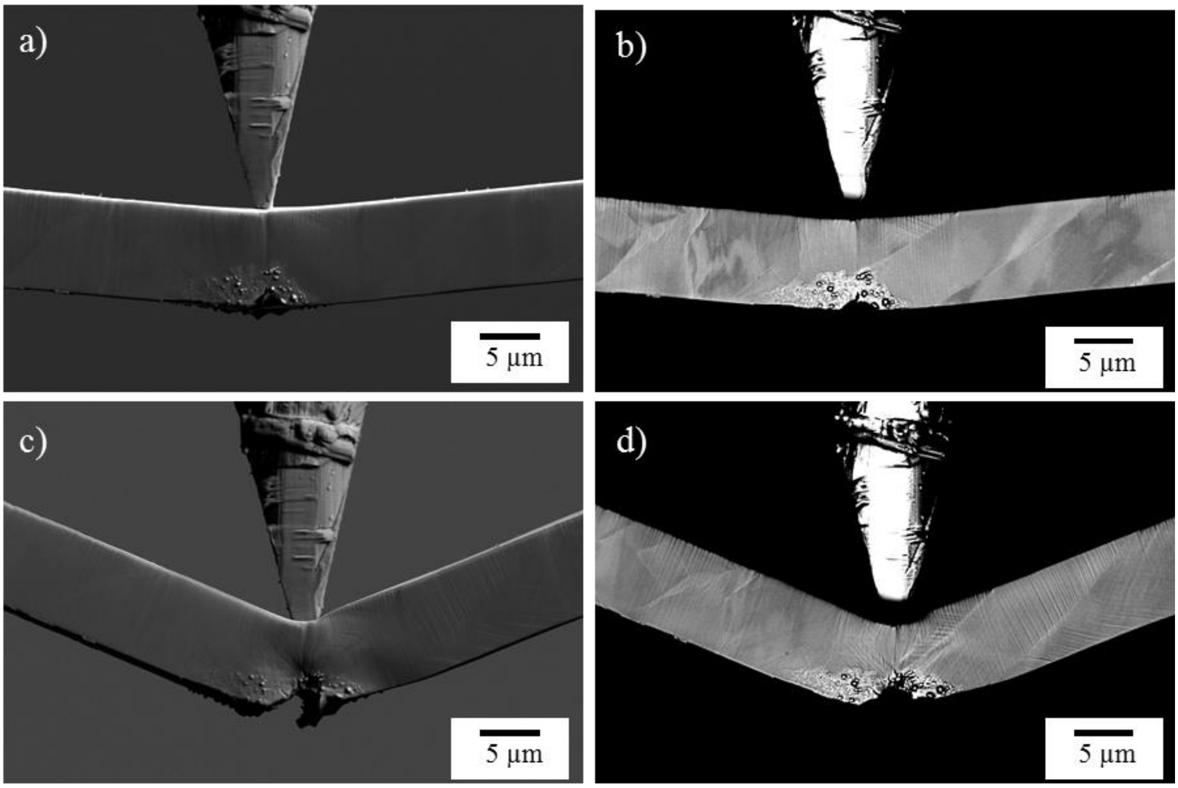

Figure IV–31 a, c) SE and b, d) BSE-outer images of the clamped beam bending test showing the fracture of the sample.

Figure IV–32 presents the force-displacement curve of the clamped beam bending test; in this curve, a red rhombus indicates where the first fracture appeared.

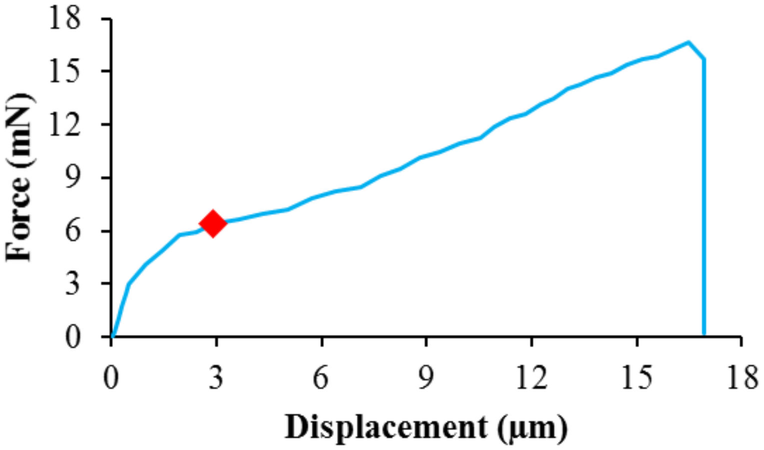

Figure IV–32 Force-displacement curve of the clamped beam bending test.

IV.3.3.3. Analysis post-test

After the final sudden failure of the sample, the elastic deformation of the sample and the whole setup recovered. Unfortunately, because of this, the needle damaged almost the totality of the fracture surface of the sample. Figure IV–33 presents some observations post-mortem of the fracture surfaces. In the intact zones of the fracture, the W-layer broke, and the fracture occurred homogeneously across the sample thickness.

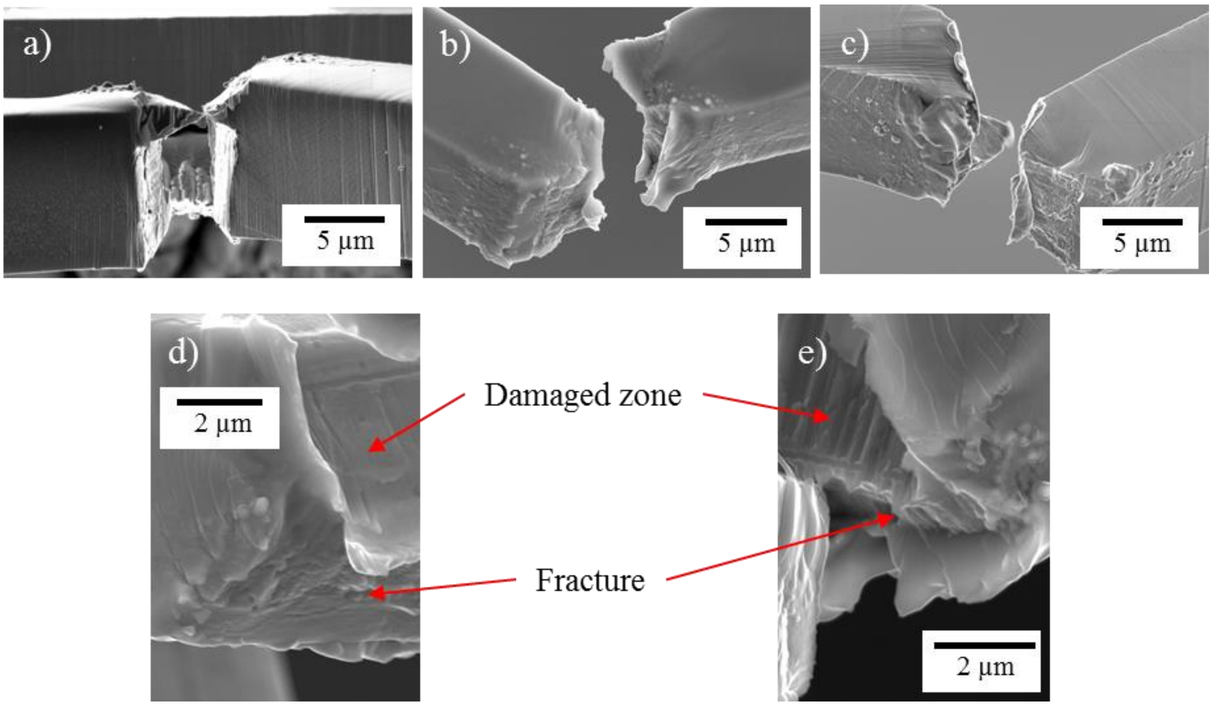

Figure IV–33 Observation of the fracture surface of the double clamped bending test sample.

Moreover, an EDS analysis was carried out to detect the presence of the EGaIn on the fracture surfaces. Figure IV–34 shows the principal results of this analysis. There is Ga in the sample notch and some Ga in the analyzable fracture zone. The little appearance of Ga in the fracture surface does not discard the possibility of the LME since very few liquid metal is necessary to embrittle a grain boundary, and this small quantity may not be detectable under these analysis conditions. Due to the irregular shape of the sample, the surface of interest could not be placed perpendicular to the electron beam, which impedes a more detailed EDS analysis.

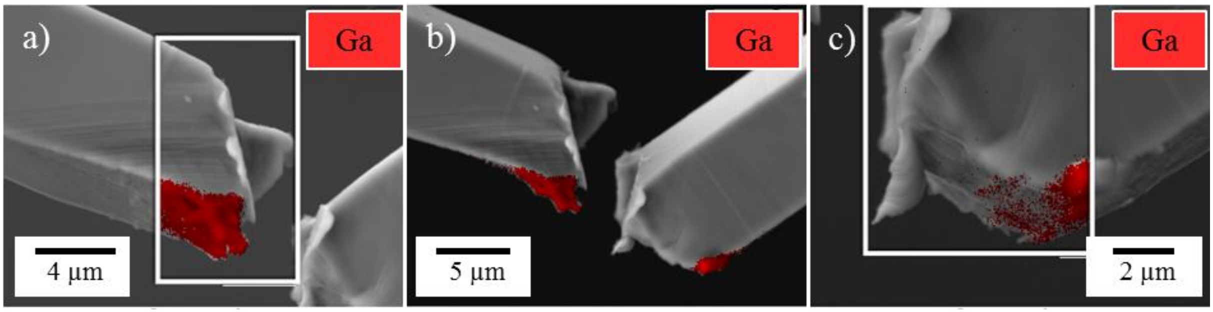

Figure IV–34 EDS analysis on the fracture of the clamped beam bending test sample.

The clamped beam bending test is suitable for studying the embrittlement of Cu-30%Zn in contact with the EGaIn and does not present any practical limitation on the degree of the deformation it can excerpt to the sample. Nevertheless, due to the recovery of the elastic deformation after the sample failed, the needle considerably damaged the fracture surface of the sample, which led to a limited *post-mortem* analysis. The best test would be one that does not present a limitation on the quantity of deformation applied to the sample, allows the preservation of the fracture surfaces after the test, and does not present complex stress states. An alternative clamped beam bending test was designed to fulfil all these requirements.

IV.3.4. Alternative clamped beam bending

The alternative clamped beam bending proposed in this work consists of a sample with a notch located away from the sample centre to avoid damage to the fracture surface. The notch location corresponds to a zone where the stresses are of the same magnitude as the centre of the sample and present a similar stress state. This zone corresponds to a zone that is close to the supports.

IV.3.4.1. Test preparation

This test's preparation is similar to that of the previous micro-bending tests. Figure IV–35a presents the alternative test geometry where the notch does not locate in the sample's centre but in a zone near one of the supports. Figure IV–35b indicates the grain boundary that presents the suitable orientation, i.e., vertical in both sample planes. Figure IV–35c shows the final beam, and Figure IV–35d shows the correspondent EBSD analysis.

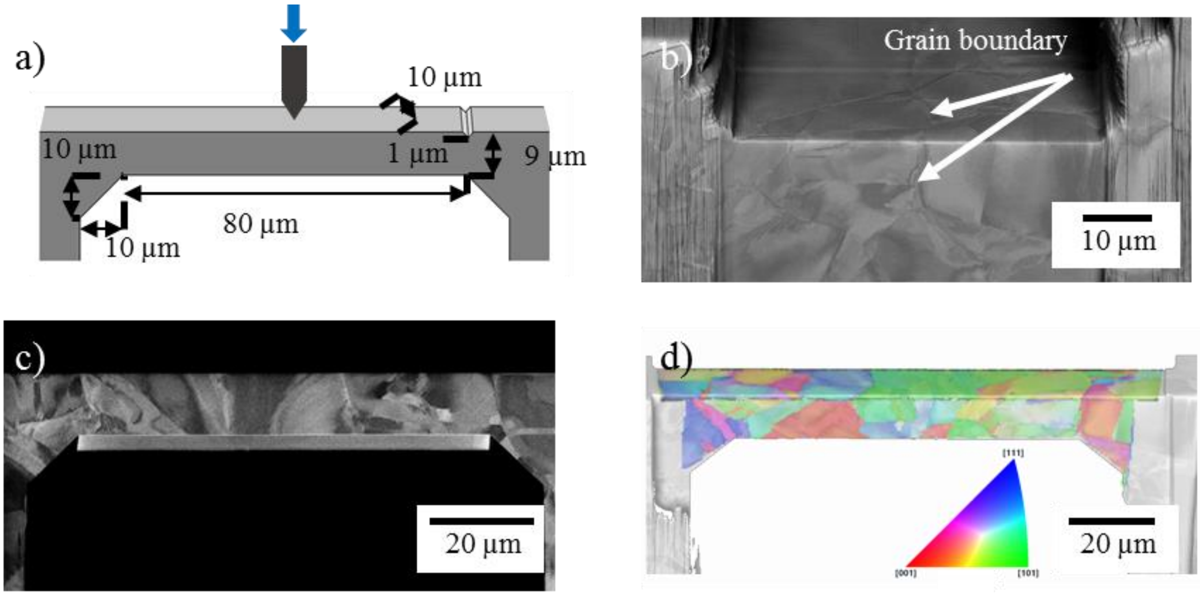

Figure IV–35 Summary of the fabrication of the alternative clamped beam bending test sample.

Moreover, Figure IV–36a illustrates the notch of the sample and the correspondent grain boundary, and Figure IV–36b shows the W-layer applied to the notch. For this test, the zone where the W-layer was deposited was more extensive than the previous tests to avoid possible overflows of the EGaIn drop. In addition, Figure IV–36c displays the notch filled with the EGaIn, which shows no signs of reaction with the solid. Finally, Figure IV–36d illustrates the needle's alignment with the sample's thickness.

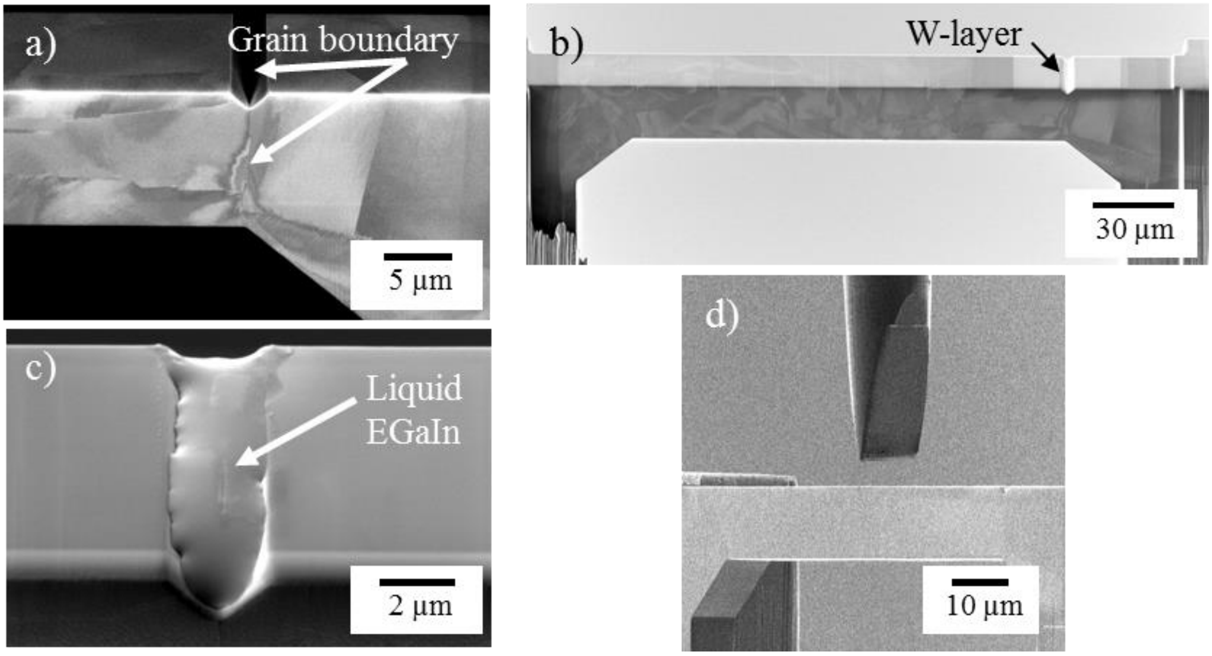

Figure IV–36 Summary of the alternative clamped beam bending test sample preparation.

IV.3.4.2. Test

Figure IV–37 and Figure IV–38 show the images taken with the SE and the BSE detectors at three moments of the test: the initial point, the moment before the final sample failure, and after the final failure of the sample. Unfortunately, the sample broke in the middle of the sample instead of the notch. An excessive indentation of the needle during the test could have caused significant plastic deformation around the point of contact that propitiates the failure of the sample in this area.

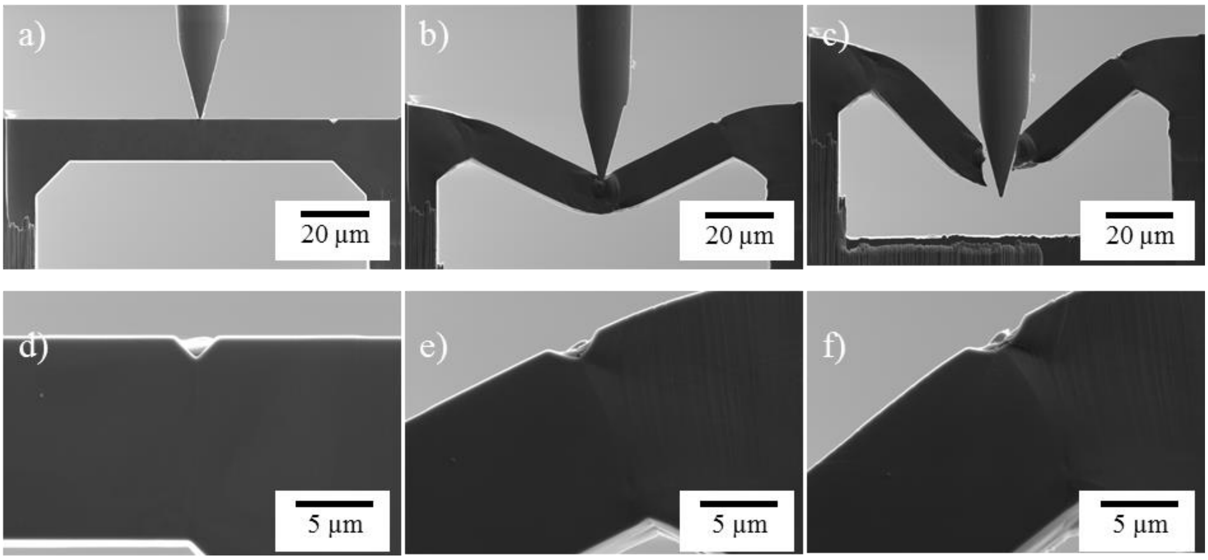

Figure IV–37 SE images of the alternative clamped beam bending test.

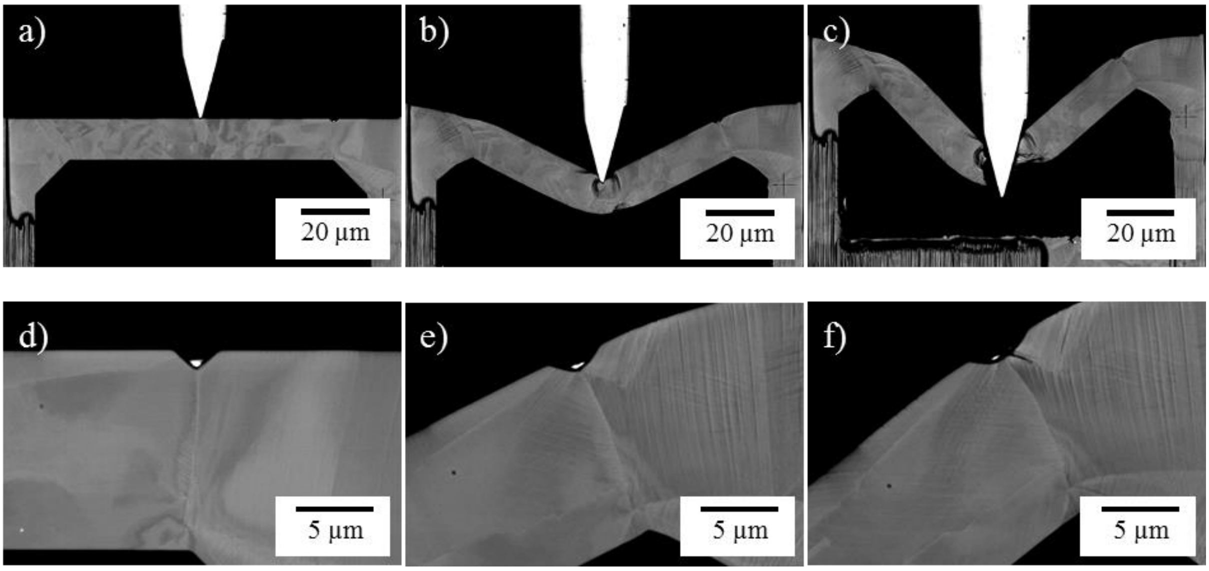

Figure IV–38 BSE images of the alternative clamped beam bending test.

During the same step where the sample's final failure happened, a fracture appeared in the zone near the notch. This fracture did not appear in the grain boundary but in an interface created during the sample's deformation.

Furthermore, Figure IV–39 presents the corresponding force-displacement curve.

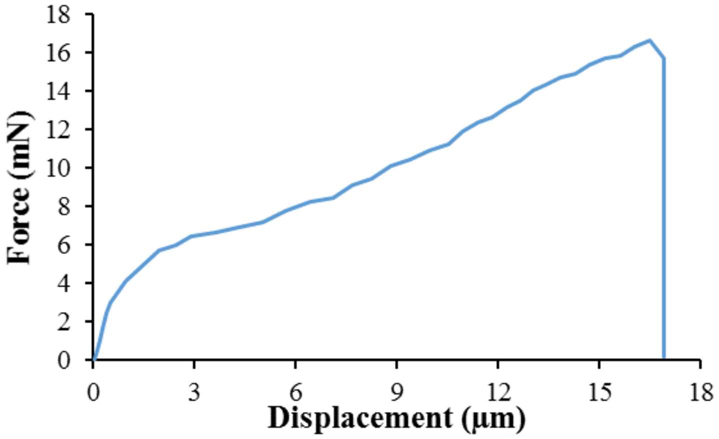

Figure IV–39 Force-displacement curve of the alternative clamped beam bending test.

The material's fracture toughness can be calculated with the experimental results from these micromechanical tests.

IV.4. Microscopic approach for the calculation of the fracture toughness of Cu-30%Zn in contact with the EGaIn

The FEM of each micro-bending test was implemented, and the methodology used in section IV.1. was used for the fracture toughness calculation. In the same way, the material's behaviour was defined by using the macroscopic material law. In addition, a preliminary FEM of the clamped beam test using a crystal plasticity finite element model (CPFEM) is presented, which would better describe the material's response at this scale.

IV.4.1. Modelling using the macroscopic behaviour of the material

For the first approach, the macroscopic material behaviour used for the previous FEM was used, i.e., the material behaviour obtained from the tensile tests described in section III.9. Figure IV–40 shows the assembly of the three FEM, with their corresponding mesh and boundary conditions. For the three FEM, the needle was considered a rigid body, and the friction was supposed to be zero. The symmetric conditions of the samples were exploited to reduce the calculation times.

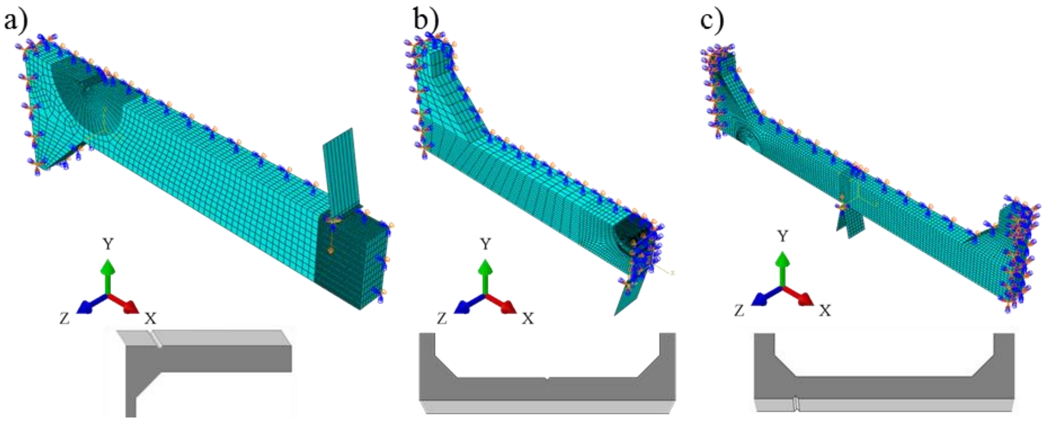

Figure IV–40 Assemblies, boundary conditions and mesh for the a) single cantilever, b) clamped beam, and c) alternative clamped beam bending tests.

One possible improvement that could be applied to these FEM is the notch correction to account for the roughness generated by the ion beam, following the work of Arnaud et al. [6]. However, the deposition of a W layer tampers the effect of the FIB milling, and the roughness does not seem to be significantly high inside the notch; moreover, the exact roughness of the notch could not be measured.

Figure IV–41 compares the simulation with the experimental curves by contrasting their corresponding force-displacement curves. Due to the irregularities of the single cantilever bending test, it is not possible to directly compare with the simulations, except for the first part of the test. In all three cases, the curves match relatively well.

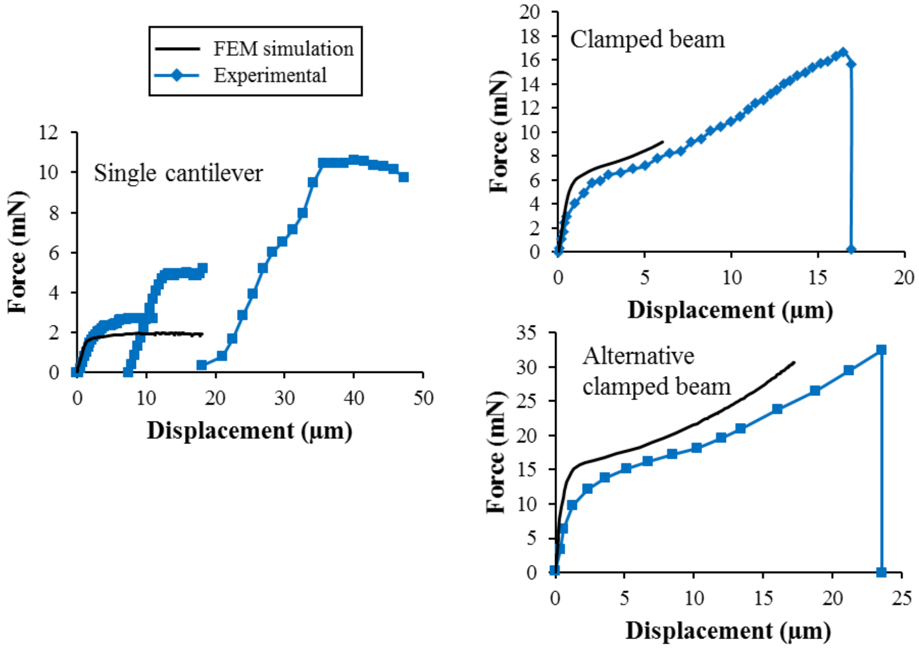

Figure IV–41 Comparison of the experimental and the calculated force-displacement curves for the micro-bending tests.

For instance, Figure IV–42 shows the 15th contour over the plastic deformation field. Some contours go beyond the plastic deformation zone; hence, these could be valid for the J-integral calculation.

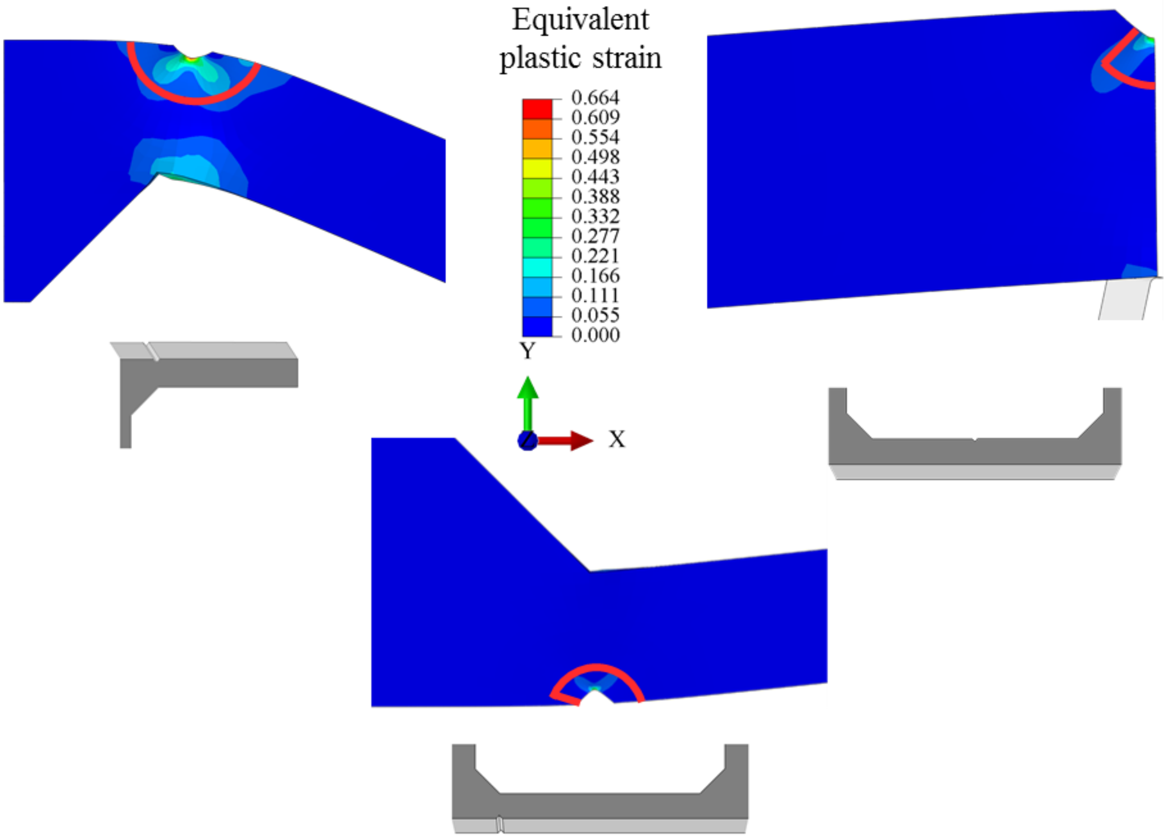

Figure IV–42 15th contour used for calculating the J-integral for each micro-bending test geometries.

Figure IV–43 shows the calculated values for the J-integral for each test and its evolution across the different contours. The J-integral was calculated at a displacement corresponding to the fracture initiation moment near the notch. As for the previous FEM in section IV.1., various zones across the sample thickness were used for the J-integral calculation for each contour. In Figure IV–43, the rhomboids indicate the average for each contour, and the error bars represent the standard deviation.

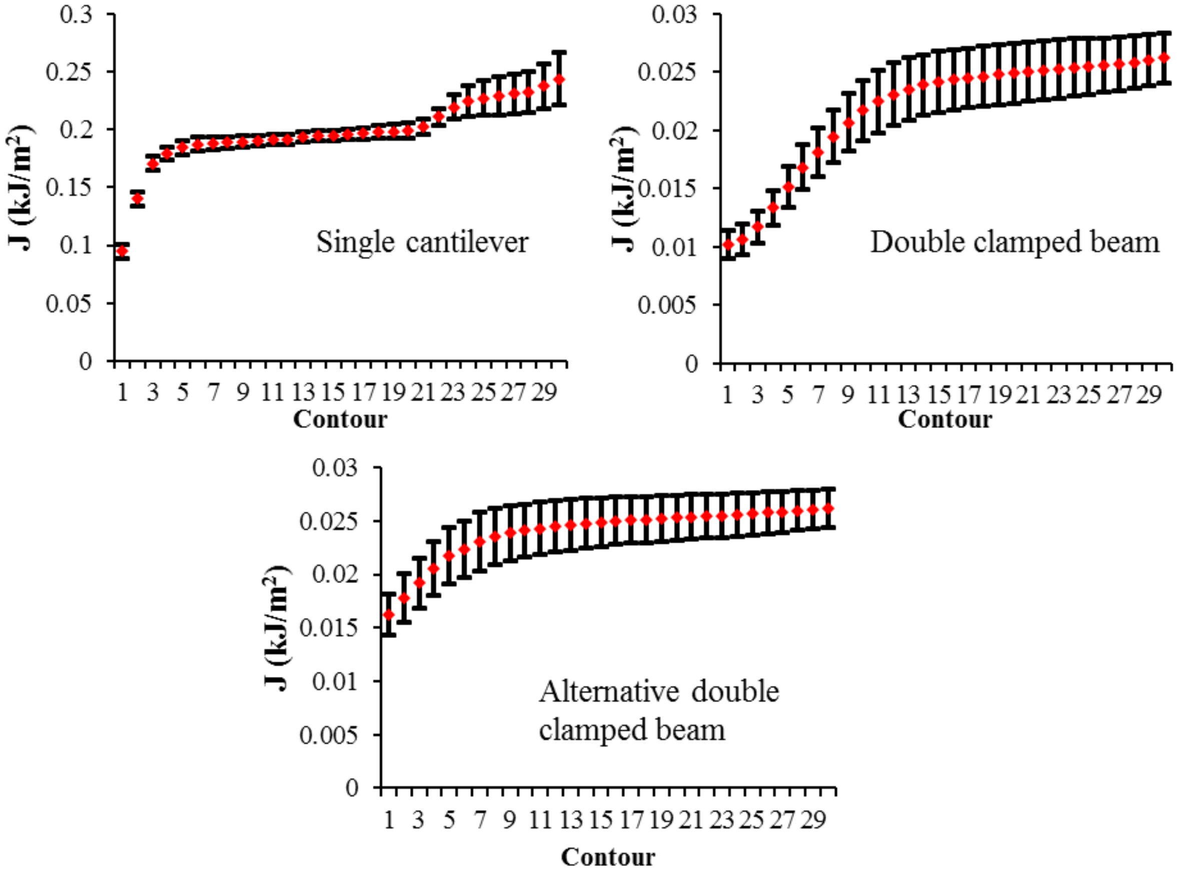

Figure IV–43 Values of the J-integral across the different contours for the three bending tests.

The values of the J-integral tend to converge for the contours located away from the zone where the plastic deformation is high. The values of the ten contours with less variation were used for calculating the K_{IC}, using Eq. (5). Table IV–2 indicates the calculated values for each bending test along with the minimum thickness value derived from Eq. (28).

Table IV–2 Values of the fracture toughness for the three bending tests geometries.

	Single cantilever	**Double clamped cantilever**	**Alternative double clamped cantilever**
K_{IC} (MPa m$^{1/2}$)	4.41 ± 0.06	1.57 ± 0.08	1.6 ± 0.06
B_{min} (μm)	6.02	0.77	0.79

The fracture toughness values are practically the same for both double clamped cantilever samples, while it is higher for the single cantilever, although they are all in the same order of magnitude. Nevertheless, the difference in the values is expected due to the execution of the single cantilever test, which led to significant differences in the stress state with the simulated sample. According to the calculated minimum thickness value of the three tests, the dimensions of the micro-bending test samples compel the conditions for measuring the fracture toughness.

IV.4.2. Preliminary modelling using a crystal plasticity model

On the other hand, the clamped beam bending test was modelled using a crystal plasticity finite element model (CPFEM) define the material behaviour. For these simulations, it was necessary to simplify the FEM of the test. This simplification was achieved by only modelling the central part of the specimen and imposing displacements as boundary conditions instead of modelling the needle and its contact with the sample. These displacements were derived from the displacement fields calculated using the previous simulation (see Figure IV–40) and are coherent with the displacement observed by SEM. The y-axis displacements correspond to the movement executed by the needle in the sample's lower face, and the x-axis displacements correspond to that imposed by the sample extremes during its deformation. There are no boundary conditions on the z-axis.

Figure IV–44a shows the central part of the modelled clamped beam specimen divided according to the grain boundaries measured with the EBSD presented in Figure IV–44b. Figure IV–44c shows the mesh, and Figure IV–44d presents the boundary conditions applied to this FEM.

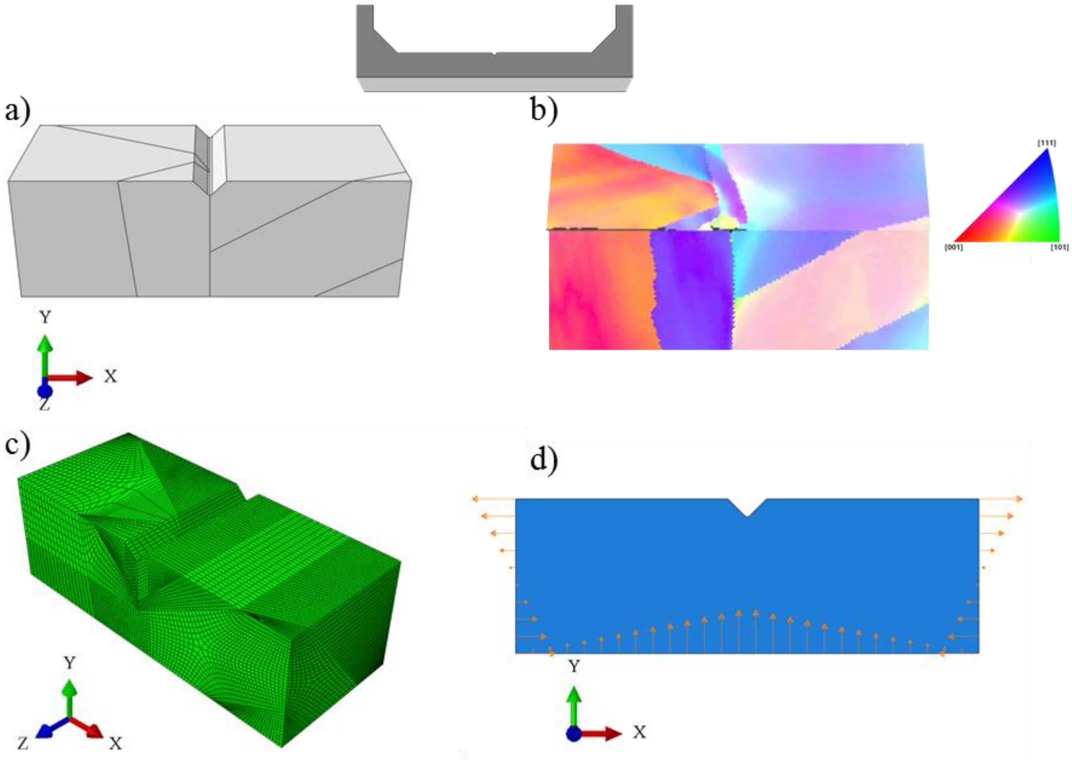

Figure IV–44 Simplified FEM of the clamped beam bending test.

These mesh and boundary conditions were also used with the macroscopic material behaviour to compare the effect of FEM simplification. For instance, Figure IV–45 presents the 15th contour used for calculating the J-integral and the field of plastic deformation obtained from the simulation using the macroscopic material's behaviour. Due to the distribution of the mesh elements, the contour follows a twisted path.

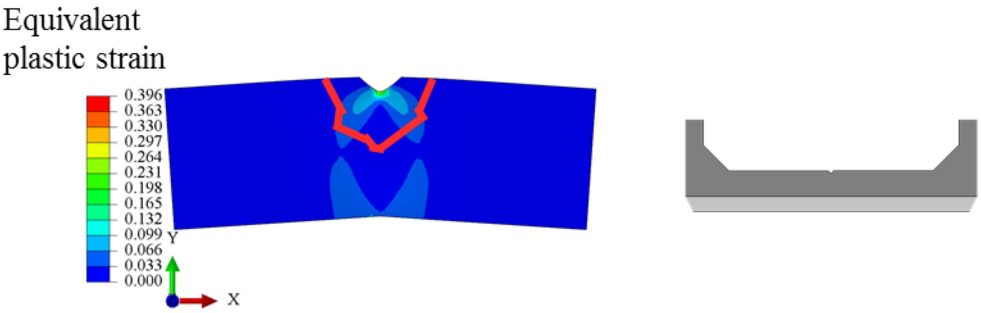

Figure IV–45 15th contour used for calculating the J-integral on the simplified FEM of the clamped beam bending test.

The CPFEM was implemented following the same methodology used by Plancher et al. [16], which consists of using a User Subroutine UMAT to implement the constitutive laws. The constitutive laws define critical shear stress (τ_c^s) [17], the rate-dependent slip rate ($\dot{\gamma}^s$) [18], and the rate of evolution of the stored dislocation density ($\dot{\rho}^s$) [19]. Equations (30), (31), and (32) express these relations, respectively.

$$\tau_c^s = \tau_0 + \mu b \sqrt{\sum_{u=1,12} a^{su} p^{u}} \tag{30}$$

$$\dot{\gamma}^s = \begin{cases} \dot{\gamma}_0 \left(\dfrac{|\tau^s|}{\tau_c^s} \right)^n sign(\tau^s), & |\tau^s| > \tau_c^s \\ 0, & \text{otherwise} \end{cases} \tag{31}$$

$$\dot{\rho}^s = \frac{|\dot{\gamma}^s|}{b} \left[\frac{\sqrt{\sum_{u \neq s} \rho^u}}{K} - 2 y_c \rho^s \right] \tag{32}$$

where τ_0 is the lattice friction stress, μ the isotropic shear modulus, b the norm of the Burgers vector, a^{su} is the interaction matrix between the slip systems s and u, $\dot{\gamma}_0$ is a reference shear rate, n is the stress sensitivity parameter, and K and y_c are material parameters to fit.

The elastic constants and the Burgers vector correspondent to Cu-30 wt.%Zn were taken from the work of Jia et al. [20] and are C_{11}=147 GPa, C_{12}=111 GPa, C_{44}=72 GPa, and b=2.56×10^{-7} mm. The rest of the parameters were fit by simulating a polycrystalline material and finding the suitable parameters that describe the experimental material's behaviour. This simulation was done using an aggregate of 100 grains with different orientations, which was generated using the open-source software package for polycrystal generation and meshing Neper [21]. A FEM of the aggregate was implemented with the aggregate under tensile stress using initial parameters, the stress-strain was averaged, and a stress-strain curve was traced. This curve was compared with the macroscopic stress-strain curve, then the pertinent parameters were adjusted, and a new simulation was launched. This process was iteratively repeated until reaching a good agreement between the simulated and the experimental stress-strain curve; Figure IV–46 compares these two, and Table IV–3 lists the final parameters for Cu-30%Zn.

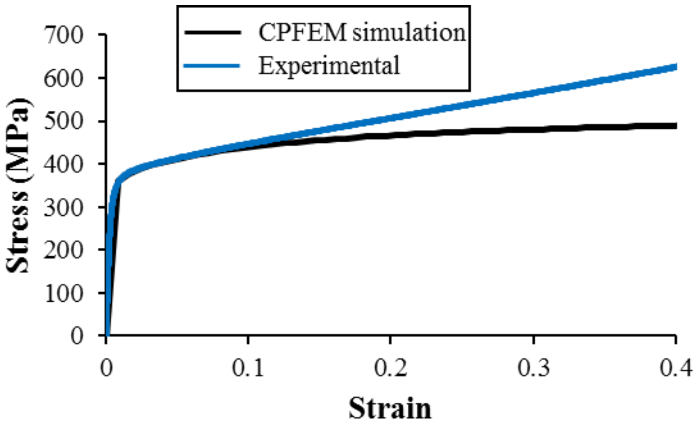

Figure IV–46 Stress-strain curves of the experimental Cu-30%Zn and the material simulated by CPFEM.

Table IV–3 Parameters for the CPFEM of the Cu-30 wt.%Zn.

$\dot{\gamma}_0$ (s^{-1})	n	y_c (mm)	K	ρ_0 (mm^{-2})	b (mm)	$a0$	$a1$	$a2$	$a3$
10^{-4}	40	1.5×10^{-5}	100	1000	2.56×10^{-7}	0.02	0.08	0.18	0.3

The experimental and the simulated curves match at the early stages of the curve, and then the simulated material presents a lower strain hardening than the actual material. This difference may come from the twinning effect on Cu-30%Zn, which is promoted at high strain levels and is not considered in the current CPFEM.

Figure IV–47 summarizes the results of calculating the J-integral using the 30 contours for the FEM using the macroscopic material's behaviour and the CPFEM. Table IV–4 shows the calculated values of K_{IC} and the minimum thickness to comply with elasto-plastic fracture mechanics.

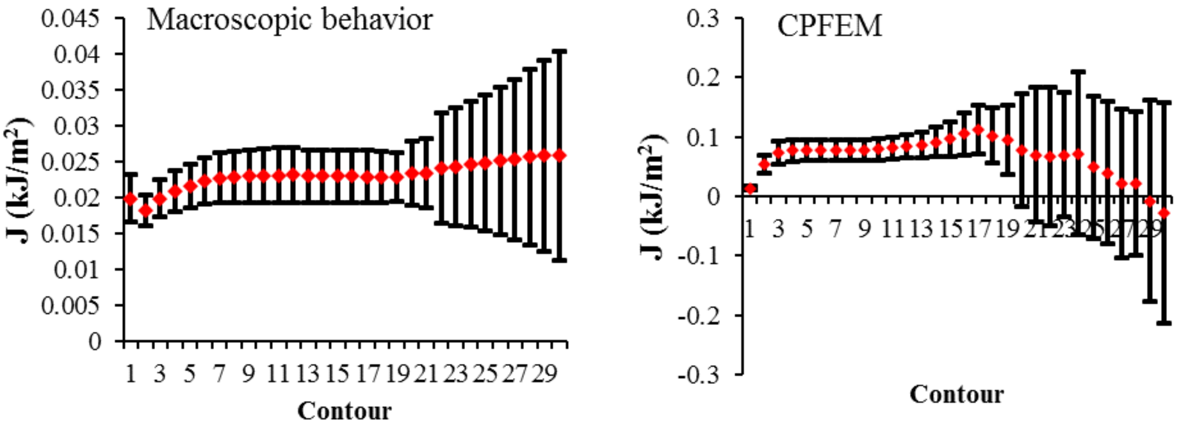

Figure IV–47 Values of the J-integral across the different contours for the simplified clamped beam bending test using the macroscopic material behaviour and the crystal plasticity model.

Table IV–4 Values of the fracture toughness for the simplified clamped beam bending test using the macroscopic material behaviour and the crystal plasticity model.

	Macroscopic behaviour	**CPFEM**
K_{IC} (MPa m$^{1/2}$)	2.49 ± 0.20	2.82 ± 0.34
B_{min} (µm)	2.12	2.49

These results indicate that the simplification of the FEM affects the calculation of the fracture toughness, but its value is of the same order of magnitude as that obtained when implementing the macroscopic material behaviour in the FEM, 1.57 ± 0.08 MPa m$^{1/2}$. Moreover, the implementation of CPFEM also gave a similar fracture toughness value. Implementing this CPFEM could be further refined and exploited in other works. For example, to compare the activation of the glide systems predicted by the model vs the experimental *in-situ* observations.

IV.5. Conclusions

The mechanical behaviour of the Cu-30 wt.%Zn alloy in contact with the EGaIn at a micrometric scale was studied using micromechanical bending tests. The plastic deformation of the alloy was observed via the apparition of slip bands.

In the three micro-bending tests, the alloy presented a considerable degree of plastic deformation before the apparition of the first crack. The plastic deformation was observed in large sample zones, although it was more concentrated in the zones near the notch. The high degree of plastic deformation complicated the measurement of the fracture toughness at the micrometric scales since the micrometric test should be able to highly deform the sample, maintaining the correct stress state in the notch.

In the case of the single cantilever bending test, the test was stopped due to insufficient space for the cantilever to deform. However, even with enough space for the cantilever deformation, the needle could not have applied a vertical force in the cantilever due to its excessive bending. For the clamped beam bending test, the recovery of the elastic deformation when the beam fails generates that the needle damaged almost the totality of the fracture surface, making the post-mortem observation of the fracture surface impossible. When using the alternative clamped beam bending test proposed in this work, the high degree of plastic deformation needed in the sample propitiated the indentation of the needle into the sample. This indentation generated a heavily deformed and damaged zone in the sample's centre, and this caused the failure to appear in this zone instead of the notch.

In contrast, these micro-bending tests allow for observing the crack propagation since there is stable crack growth in these geometries. The only test that presented a sudden failure without a noticeable crack initiation was that of the alternative clamped beam cantilever. This sudden failure was caused by the indentation of the needle in the centre of the sample, which induced a high degree of plastic deformation across its height and thickness, so when the zone started failing, its failure was abrupt. A sudden failure does not occur whenever the failure initiates near a notch since the deformation concentrates at the outermost surface.

Given the micro-bending test results, using a tensile test to measure the fracture toughness at this scale seems more appropriate. However, the tensile tests present a stress state different from the macroscopic bending tests used in this work; hence, comparing these could be more complex. In addition, using two notches like the work of Arnaud et al. [6] could lead to a more complex situation of crack initiation. For instance, in contrast with the bending tests, the crack propagation in a tensile test cannot be controlled and would be more challenging to observe. Nevertheless, this test does not present any limitations on the plastic deformation it can excerpt into the material, making it suitable for studying other aspects of the LME phenomenon.

With the methodology used in this work, the liquid and solid metals are in contact for several hours before the start of the test. Considering that the EGaIn can react with the Cu-30%Zn to form a $CuGa_2$ intermetallic layer of approximately 1 µm in 5 hours (section II.3.), the W-layer is essential to carry out this experiment. In the three micro-bending tests, the W-layer effectively blocked the intermetallic formation in the volume under the notch. Additionally, as intended, the W-layer broke during the test, allowing the liquid EGaIn to come into contact with the strained Cu-30%Zn surface.

Contrary to other studies, we choose not to carry out an image correlation to measure the deformation of the sample. If an image correlation is to be done, the sample should have an artificial pattern that allows a good contrast for measuring the deformation. This pattern is made by depositing an element with a different atomic number and observing with the BSE detector for good contrast. However, the contrast from the crystallographic features in the BSE images could not be exploited by doing this. For instance, the slip bands would be hard to observe, and it would not be easy to follow the grain boundaries during the test.

With the FEM implementation of these tests, the fracture toughness values were estimated by calculating the J-integral at the point where the fracture initiation was observed. The fracture toughness values of the micro-bending tests are considerably lower than that of the macroscopic bending tests. This difference indicates that there could be a brittle crack initiation on the Cu-30%Zn sample caused by the contact with the EGaIn. Moreover, the values obtained in this work agree with those presented in Clement and Auger's recent work, which presented the simulation of a Cu-30%Zn alloy crack tip on a monocrystal and calculated a value K_I=0.47 MPa $m^{1/2}$ when the crack tip emits a dislocation [22]; Figure IV–48 sums these values.

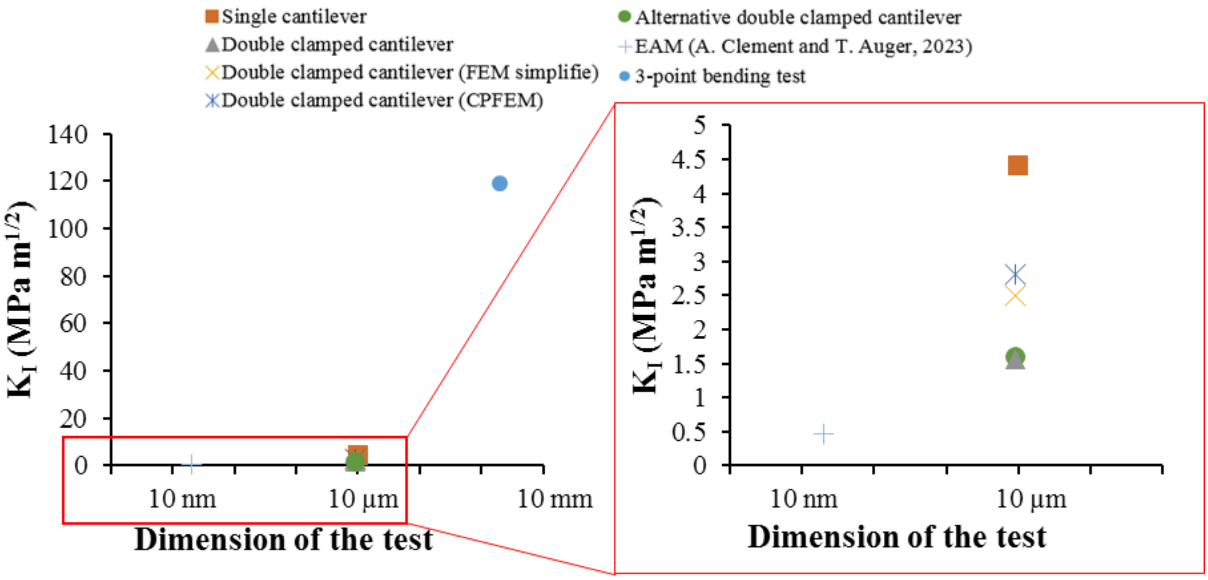

Figure IV–48 Summary of the fracture toughness values obtained in this work for the Cu-30%Zn alloy in contact with the EGaIn, along with the reported value for a dislocation emission for Cu-30%Zn [22].

One possible error source in our micro-bending test is the W-layer, which may have delayed the crack initiation. For the LME to occur, the liquid EGaIn should be in contact with the Cu-30%Zn under plastic deformation. If the W-layer did not break when the Cu-30%Zn is under sufficiently plastic deformation, the EGaIn could not enter in contact, and hence there would not be any LME, i.e., there would not be any fracture. This effect could lead to an overestimation of the fracture toughness.

Due to the dimensions of our samples, there is the possibility that the mechanical behaviour of the Cu-30%Zn sample is affected by the same phenomena that lead to size effects on micrometric pure Cu samples [7], [9], [10]. Since in most areas of the samples, there are only one or two grains across the thickness; the dislocations can leave the sample before they can interact with any obstacle and multiply, which propitiates the dislocation starvation phenomenon. Additionally, the stress gradient in the bending tests could have concentrated the dislocation on a few glide systems and generated dislocation pile-ups that create strong back stresses, such as for the bending tests reported by Motz et al. [7].

Since the material studied in this work is an alloy and not a pure metal, the magnitude of the effect of the size effects could be different from pure Cu. The principal effect of Zn in the Cu-30%Zn alloy is to generate solid solution strengthening via the blocking of the dislocation movement. The solid solution strengthening would increase the effect of the dislocation starvation and the dislocation pile-ups since the few available dislocations would have difficulty moving due to the stress fields generated by the Zn atoms. In contrast, adding Zn decreases the stacking fault energy (SFE), enhancing the dislocation emission and probably decreasing the effect of limiting the dislocation sources.

If the micro-bending tests presented in this work suffer from any size effects previously observed when testing pure Cu [7], [10], they could have altered the mechanical response of the Cu-30%Zn and would lead to an underestimation of the material's fracture toughness. In contrast with the mechanical tests on pure Cu reported by Motz et al. and Kiener et al. [7], [10], the number of dislocation sources in the sample tested in this work is not limited. In their work, Motz et al. and Kiener et al. tested single-crystal Cu samples, but the samples tested in this work were polycrystalline. The grain boundaries are important dislocation sources, evidenced during the micro-bending test by the apparition of multiple slip bands that nucleated from the grain boundaries. Moreover, the grain boundary under the samples' notch is a significant source of dislocations that can sustain the plastic deformation in this zone. In addition, a significant number of slip bands also nucleated from the surface. According to Motz et al., the pile-up effect vanishes if abundant dislocation sources are available since the dislocations can be distributed more or less uniformly [7].

Furthermore, in terms of the yield strength, the tests did not present a considerable difference with the macroscopic behaviour of the alloy, which is evidenced by the fact that the macroscopic material behaviour could effectively describe the yield strength when implementing the correspondent FEM. This lack of size effect on the yield strength could be due to the availability of dislocation sources in the sample.

If there is any size effect on the mechanical properties, it will manifest during a late stage of the test with the incapacity of the material to accommodate further deformation due to dislocation starvation. A possible consequence of this effect is the apparition of slip bands in a second direction at the late stages of the tests, which indicates the activation of a second slip plane. This second slip plane's apparition was observed for the three specimens. Nevertheless, the activation of a second slip plane can also be due to the lowering of the SFE by the Zn solutes and to the high degree of plastic deformation exerted on the sample.

There is no clear evidence suggesting the apparition of any size effect on the micro-bending tests of Cu-30%Zn in contact with the EGaIn, which indicates that these micro-bending tests are suitable for the study of the mechanical properties at this scale.

Additional tests should be done without any liquid EGaIn to confirm that the low value of fracture toughness of the micro-bending tests is due to the LME and not because of the size effects.

IV.6. References

[1] D. François, “Essais de mesure de la ténacité - Mécanique de la rupture,” *Techniques de l’ingénieur - M 4 166*. pp. 1–21, 2007.

[2] A. Gopichand, Y. Srinivas, and A. V. N. . L. Sharma, “Computation of stress intensity factor of brass plate with edge crack using J-integral technique,” *Int. J. Res. Eng. Technol.*, vol. 01, no. 03, pp. 261–266, Mar. 2012.

[3] J. Ast, M. Ghidelli, K. Durst, M. Göken, M. Sebastiani, and A. M. Korsunsky, “A review of experimental approaches to fracture toughness evaluation at the micro-scale,” *Mater. Des.*, vol. 173, p. 107762, Jul. 2019.

[4] B. N. Jaya, C. Kirchlechner, and G. Dehm, “Can microscale fracture tests provide reliable fracture toughness values? A case study in silicon,” *J. Mater. Res.*, vol. 30, no. 5, pp. 686–698, 2015.

[5] A. K. Saxena, S. Brinckmann, B. Völker, G. Dehm, and C. Kirchlechner, “Experimental conditions affecting the measured fracture toughness at the microscale: Notch geometry and crack extension measurement,” *Mater. Des.*, vol. 191, p. 108582, Jun. 2020.

[6] P. Arnaud *et al.*, “Micromechanical tensile test investigation to identify elastic and toughness properties of thin nitride compound layers,” *Surf. Coatings Technol.*, vol. 421, p. 127303, Sep. 2021.

[7] C. Motz, T. Schöberl, and R. Pippan, “Mechanical properties of micro-sized copper bending beams machined by the focused ion beam technique,” *Acta Mater.*, vol. 53, no. 15, pp. 4269–4279, 2005.

[8] N. A. Fleck, G. M. Muller, M. F. Ashby, and J. W. Hutchinson, “Strain gradient plasticity: Theory and experiment,” *Acta Metall. Mater.*, vol. 42, no. 2, pp. 475–487, Feb. 1994.

[9] B. Weiss *et al.*, “Characterization of mechanical and thermal properties of thin Cu foils and wires,” *Sensors Actuators A Phys.*, vol. 99, no. 1–2, pp. 172–182, Apr. 2002.

[10] D. Kiener, C. Motz, T. Schöbert, M. Jenko, and G. Dehm, “Determination of mechanical properties of copper at the micron scale,” *Adv. Eng. Mater.*, vol. 8, no. 11, pp. 1119–1125, 2006.

[11] J. R. Michael, “Focused Ion Beam Induced Microstructural Alterations: Texture Development, Grain Growth, and Intermetallic Formation,” *Microsc. Microanal.*, vol. 17, no. 3, pp. 386–397, Jun. 2011.

[12] D. Kiener, C. Motz, M. Rester, M. Jenko, and G. Dehm, “FIB damage of Cu and possible consequences for miniaturized mechanical tests,” *Mater. Sci. Eng. A*, vol. 459, no. 1–2, pp. 262–272, Jun. 2007.

[13] D. E. J. Armstrong, A. J. Wilkinson, and S. G. Roberts, “Micro-mechanical measurements of fracture toughness of bismuth embrittled copper grain boundaries,” *Philos. Mag. Lett.*, vol. 91, no. 6, pp. 394–400, 2011.

[14] H. Dugdale, D. E. J. Armstrong, E. Tarleton, S. G. Roberts, and S. Lozano-Perez, “How oxidized grain boundaries fail,” *Acta Mater.*, vol. 61, no. 13, pp. 4707–4713, Aug. 2013.

[15] G. Ben Salem, E. Héripré, P. Bompard, S. Chapuliot, A. Blouin, and C. Jacquemoud, “Mechanical Behavior Characterization of a Stainless Steel Dissimilar Metal Weld

Interface : In-situ Micro-Tensile Testing on Carburized Martensite and Austenite," *Exp. Mech.*, vol. 60, no. 8, pp. 1037–1053, Oct. 2020.

[16] E. Plancher *et al.*, "Validity of Crystal Plasticity Models Near Grain Boundaries: Contribution of Elastic Strain Measurements at Micron Scale," *Jom*, vol. 71, no. 10, pp. 3543–3551, 2019.

[17] P. Franciosi, "The concepts of latent hardening and strain hardening in metallic single crystals," *Acta Metall.*, vol. 33, no. 9, pp. 1601–1612, Sep. 1985.

[18] D. Peirce, R. J. Asaro, and A. Needleman, "Material rate dependence and localized deformation in crystalline solids," *Acta Metall.*, vol. 31, no. 12, pp. 1951–1976, Dec. 1983.

[19] C. Teodosiu, J. L. Raphanel, and L. Tabourot, "Finite element simulation of the large elastoplastic deformation of multicrystals," in *Large Plastic Deformations*, London: Routledge, 1991, pp. 153–168.

[20] N. Jia, F. Roters, P. Eisenlohr, C. Kords, and D. Raabe, "Non-crystallographic shear banding in crystal plasticity FEM simulations: Example of texture evolution in α-brass," *Acta Mater.*, vol. 60, no. 3, pp. 1099–1115, Feb. 2012.

[21] R. Quey, P. R. Dawson, and F. Barbe, "Large-scale 3D random polycrystals for the finite element method: Generation, meshing and remeshing," *Comput. Methods Appl. Mech. Eng.*, vol. 200, no. 17–20, pp. 1729–1745, Apr. 2011.

[22] A. Clement and T. Auger, "An EAM potential for α-brass copper–zinc alloys: application to plasticity and fracture," *Model. Simul. Mater. Sci. Eng.*, vol. 31, no. 1, p. 015004, Jan. 2023.

Conclusions and perspectives

This work presents the study of the Liquid Metal Embrittlement (LME) phenomenon on alpha brasses by the liquid eutectic Ga-In (EGaIn). The study focuses on three broad aspects of the LME: first, the interface between the liquid EGaIn and the alpha brasses with different Zn content; then, the mechanical parameters controlling the LME sensitivity of these alpha brasses in contact with the EGaIn; and finally, the quantification of the LME by calculating the fracture toughness using micro-bending tests.

Whenever there is contact between the alpha brasses and the liquid EGaIn, the liquid metal reacts with the solid to create the $CuGa_2$ intermetallic. This intermetallic forms homogenously across the surface relatively fast: a layer of around 0.5 µm after 20 seconds of contact and a $CuGa_2$ layer of around 1 µm after 5 hours. Moreover, during this contact, the Cu and Zn dissolve into the liquid EGaIn. The dissolved Cu reacts with Ga while the dissolved Zn stays in the liquid phase. There are no significant traces of In in the intermetallic, and there is no apparent effect of the Zn content in the formation of the intermetallic.

There is partial wettability of the EGaIn on all the alpha brasses studied with a relatively low contact angle. This contact angle decreases as the Zn content in the alloys increases, going from a value of 49 ± 5° for pure Cu to 36 ± 5° for the Cu-30 wt.%Zn alloy. A further study on the impact of the $CuGa_2$ reaction on the wettability is of interest.

To study the sensitivity of the Cu-30%Zn brass to the LME by the EGaIn, we used the Small Punch Tests (SPT) and the 3-point bending tests. The test conditions play an essential role in the apparition of the embrittlement by the EGaIn on the alpha brasses. For instance, the Cu-30%Zn alloy presented liquid metal embrittlement when tested by the 3-point bending test in contact with the EGaIn, but the liquid metal did not affect the mechanical behaviour of the same alloy when tested using the standard SPT. One possible explanation for the difference in the LME sensitivity is the stress states of these tests. However, the tests' finite element modelling (FEM) showed that the values of strain rate, von Mises stress, equivalent plastic strain and triaxiality are similar under the same displacement rates. Therefore, these values cannot explain the differences in the LME sensitivity.

These differences derive from the particular crack initiation in this system, which is always ductile and not induced by the liquid metal. For instance, the embrittled 3-point bending test samples systematically presented a fracture that started ductile and became brittle intergranular. In contrast, the standard SPT samples presented a ductile fracture because the fracture propagation was minimal and could not develop into a brittle fracture. To account for this crack initiation, alternative pre-notched SPT samples with a more significant fracture propagation path allow the observation of the LME of the Cu-30%Zn alloy by the EGaIn.

This work proposed an explanation for the particular crack initiation in the alpha brasses in contact with the EGaIn. We propose that the $CuGa_2$ intermetallic inhibits the contact between the liquid EGaIn and the alloy surface during the test, which impedes the direct embrittlement of the alloy. Then, during the plastic deformation of the sample, the ductile damage develops until there is a ductile crack initiation, which simultaneously brakes the $CuGa_2$ intermetallic. Consequently, the liquid metal enters into contact with a strained solid surface enabling the LME occurrence. Using the Gurson-Tvergaard-Needleman (GTN) model, the calculated ductile damage matched the experimental observations.

The ductile fracture's propagation differs from that of the brittle fracture. In the 3-point bending test, the ductile fracture propagation matched the zone with the highest tensile stress, while the brittle fracture propagation matched the zones with the highest plastic strain.

The 3-point bending test samples present hardly any dependence of the LME with the strain rate on Cu-30 wt.%Zn, but the Cu-20 wt.%Zn and Cu-25 wt.%Zn alloys presented higher LME sensitivity at higher strain rates. At the same time, the SPT of Cu-30%Zn samples did show a strain rate dependence on the LME occurrence. Additionally, two tendencies of the metallurgical state effect on the LME sensitivity appeared: alloys with higher hardness and higher Zn content presented higher LME sensitivity.

The conditions that enhanced the LME; i.e., higher Zn content, higher hardness, and higher strain rate; point to two possible interrelated phenomena: the inhibition of the dislocation motion and the deformation by twinning. A higher Zn content produces solid solution hardening that pins the dislocations and limits its motion; simultaneously, it reduces the stacking fault energy, propitiating deformation by twinning and planar sliding. In addition, the higher hardness relates to a higher dislocation density, which hinders the dislocation motion via the forest hardening; simultaneously, a higher dislocation density also enhances the deformation by twinning. The brittle crack propagation following zones with the most plastic deformation supports this relation since these zones present higher dislocation densities. Similarly, a higher strain rate promotes twinning and hinders the dislocation motion. Further investigation is needed to corroborate these tendencies using more diverse metallurgical states and strain rates.

Because the crack initiation was ductile, the SPT or the 3-point bending tests could not be used to calculate the fracture toughness of the alpha brasses embrittled by EGaIn. We developed *in-situ* micro-bending tests to overcome this difficulty. These tests incorporated a W-layer to prevent intermetallic formation before the solid undergoes plastic deformation by impeding the contact between the solid and the EGaIn. During the micro-bending tests, the W-layer broke, and the liquid metal could flow into contact with the solid metal under plastic strain, which enabled the LME occurrence. These micro-bending tests allowed the calculation of the fracture toughness of the Cu-30%Zn brass in contact with the liquid EGaIn, which was 1.57 ± 0.08 MPa $m^{1/2}$ determined with the double clamped beam test.

For the first time, this work presented the use of micro-mechanical tests to measure the fracture toughness of a material presenting considerable plasticity. Due to this plastic deformation, the micro-bending tests presented several difficulties. For instance, the single cantilever bending test does not allow for the application of a significant deformation of the sample, the fracture surface of the clamped beam bending test sample was destroyed due to the recovery of the elastic strain, and the alternative clamped beam test sample broke in an unintended zone due to the indentation of the manipulator. A possible improvement for the clamped bending tests is using a smooth manipulator instead of a relatively sharp needle. Alternatively, the implementation of micro-tensile tests would overcome some of the difficulties.

The use of *in-situ* mechanical tests has shown to be suitable for studying LME and enables the observation of diverse phenomena that are impossible to observe with other approaches, such as the apparition of slip bands. Implementing *in-situ* mechanical tests opens the possibility of studying the LME crack initiation mechanisms at a micrometric scale, a novel approach to studying the LME.

Abstract

This work studies the liquid metal embrittlement (LME) phenomenon at room temperature on alpha brasses with different Zn content in contact with the liquid eutectic Ga-In (EGaIn). The liquid EGaIn wets pure Cu partially with a relatively low contact angle of 49 ± 5°, which is lower for the alpha brasses and decreases with the Zn content alloy down to 36 ± 5° for the Cu-30 wt.%Zn alloy. Moreover, the $CuGa_2$ intermetallic forms whenever the liquid EGaIn is in contact with Cu and the alpha brasses, independently of the Zn content. Testing with the 3-point bending test showed that the LME sensitivity by the EGaIn increases at higher strain rates, higher Zn content, and higher hardness. Whenever there is LME, the liquid EGaIn does not affect the fracture initiation but the fracture propagation; hence the samples systematically presented a ductile fracture initiation followed by a brittle intergranular fracture propagation. The $CuGa_2$ intermetallic impedes the brittle fracture initiation by blocking the contact between the EGaIn and the alpha brasses from the early stages of the test. Later, when the intermetallic breaks, the liquid EGaIn comes into contact with the alpha brass making the LME possible if the brass is under sufficient plastic deformation. Due to the ductile fracture initiation, the Cu-30%Zn alloy does not present LME when tested using the standard Small Punch Test (SPT). In contrast, using pre-notched SPT samples enables the observation of this alloy's embrittlement in contact with the liquid EGaIn. Furthermore, due to the ductile fracture initiation, it is impossible to use the bending tests or the SPT to measure the fracture toughness related to the LME phenomenon. In contrast, *in-situ* micro-bending tests with a W protective layer were suitable for the fracture toughness measurement of Cu-30%Zn in contact with the EGaIn; for instance, a fracture toughness value of 1.57 ± 0.08 MPa $m^{1/2}$ was measured with the double clamped beam test.

Keywords: Liquid Metal Embrittlement, intermetallic, *in-situ* micromechanical tests, small punch test, bending tests, fracture toughness, wetting, finite element modelling, alpha brasses, EGaIn.

Résumé

Ce travail présente l'étude de la sensibilité à la fragilisation par les métaux liquides (FML) à température ambiante de laitons alpha contenant différents taux de zinc par l'eutectique liquide In-Ga (EGaIn). Le liquide EGaIn mouille le cuivre pur de manière partielle avec un angle de contact relativement faible de 49 ± 5°. Cet angle est plus faible pour les laitons alpha et décroit avec le pourcentage en zinc. Il est de 36 ± 5° pour le laiton Cu-30%Zn en masse. De plus, l'intermétallique $CuGa_2$ se forme dès le contact avec le liquide EGaIn avec le cuivre et les laitons alpha, indépendamment de la teneur en zinc. Les essais de flexion 3 points montrent que la sensibilité à la FML par l'EGaIn augmente pour des vitesses de déformation élevées, des taux de zinc plus élevés et des duretés plus importantes. Dans les cas de FML, le liquide EGaIn n'affecte pas la phase d'initiation de la fissure mais seulement la propagation de la fissuration. En effet, les faciès de rupture présentent toujours une initiation ductile de la fissure puis une rupture fragile. L'intermétallique $CuGa_2$ empêche l'initiation d'une rupture fragile en limitant le contact entre le métal liquide et le laiton dans les premières phases de l'essai mécanique. Puis l'intermétallique se fissure et ainsi, le liquide EGaIn rentre en contact avec le laiton rendant possible la FML à condition de déformations plastiques suffisamment importantes du laiton. A cause de l'initiation d'une rupture ductile, le laiton Cu-30%Zn ne présente pas de sensibilité à la FML lorsque il est testé par le small punch test (SPT) standard. Cependant l'utilisation d'échantillons de SPT pré-entaillés permet l'observation pour ce laiton de la FML en contact avec l'EGaIn liquide. De plus, du fait de l'initiation d'une rupture ductile, il est impossible à partir des résultats des essais de SPT et de flexion de déterminer une ténacité en présence de métal liquide. C'est pourquoi, des micro-essais de flexion avec observations *in-situ* et présence d'une couche fine protectrice de W ont été mis en oeuvre. Ils ont permis de déterminer en présence d'EGaIn liquide une ténacité de 1,57 ± 0.08 MPa $m^{1/2}$ pour le laiton Cu-30%Zn.

Mots clés : Fragilisation par les Métaux Liquides, intermétallique, essais *in-situ,* essai de small punch test, essai de flexion, mouillage, ténacité, modélisation par éléments finis, laitons alpha, EGaIn.